

Bangor University

DOCTOR OF PHILOSOPHY

Performance assessment of subcarrier multiplexed optical systems implications of laser nonlinearities

Manuel de Castro Faria Salgado, Henrique

Award date:
1993

Awarding institution:
Bangor University

[Link to publication](#)

General rights

Copyright and moral rights for the publications made accessible in the public portal are retained by the authors and/or other copyright owners and it is a condition of accessing publications that users recognise and abide by the legal requirements associated with these rights.

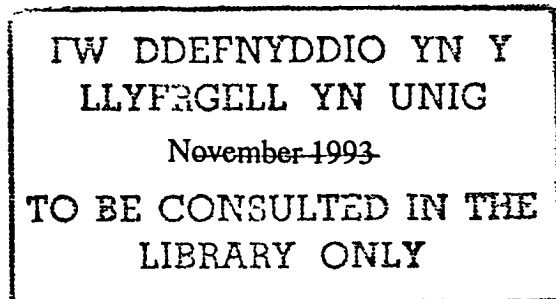
- Users may download and print one copy of any publication from the public portal for the purpose of private study or research.
- You may not further distribute the material or use it for any profit-making activity or commercial gain
- You may freely distribute the URL identifying the publication in the public portal ?

Take down policy

If you believe that this document breaches copyright please contact us providing details, and we will remove access to the work immediately and investigate your claim.

Performance Assessment of Subcarrier Multiplexed Optical Systems: Implications of Laser Nonlinearities

Thesis Submitted in Candidature for the Degree of
Doctor of Philosophy



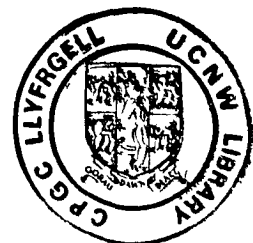
Henrique Manuel de Castro Faria Salgado

School of Electronic Engineering and Computer Systems

University of Wales

Bangor

United Kingdom



Acknowledgments

I am indebted to many people who have helped make this work possible. I wish to express my thanks to Professor John J. O'Reilly for his advice, guidance and motivation throughout the course of this study and for his help in the final preparation of this thesis.

I am also grateful to Instituto de Engenharia de Sistemas e Computadores (INESC-Norte) and University of Wales for the initial financial support and to Junta Nacional de Investigação Científica e Tecnológica (JNICT) for providing my scholarship.

Special thanks go to Dr. A. P. Leite at Faculdade de Ciências, Universidade do Porto whose encouragement and support enabled me to undertake my postgraduate studies. Thanks are also due to my colleagues at the SEECS-Bangor who contributed to my work with numerous fruitful discussions. A special mention to Paulo Moreira for introducing me to the optimisation techniques and Izzat Darwazeh for his continuous support.

To the many friends I have made during my stay at Bangor, Carlos Dias, Luis Moura, Amaro de Sousa, Carlos Bastos, Cipriano Lomba and Carlos Mira for their friendship and help that will provide me with good memories for years to come.

Finally, to my wife Maria Antónia and my parents Manuel Tomás and Francelina for their love, encouragement and patience.

Summary

This thesis is concerned with a detailed study of laser nonlinearities and the implications for multichannel subcarrier multiplexed fibre optic systems

In view of the limitations of previously reported analytic treatments of laser nonlinear distortion, a considerable part of the study is dedicated to the development of modelling and analytic techniques suitable for practical system design and optimisation. The single-mode rate equations provide an adequate basis for the analysis of laser intrinsic dynamic distortion and relative intensity noise and their dependence on device parameters and operating conditions. The Volterra series method of nonlinear system theory is then applied and an analytical model is obtained that describes the nonlinearity in the frequency domain by a set of nonlinear transfer functions

This method provides a rigorous analytic nonlinear model that takes into account all the intermodulation products up to third-order as determined by the rate equations. Moreover, the laser response to the important case of a sum of narrow-band signals is considered and under certain conditions, which are valid for the majority of systems of interest, the intermodulation power spectral density of the distortion products is determined. This enables an accurate evaluation of the impact on the overall system performance of laser intrinsic distortion and optimum overall performance is identified after including the noise introduced in the detection process. The relative importance of laser intrinsic distortion and clipping-distortion is also examined

Finally, the analytic model is used to investigate design constraints and the overall system performance of relevant SCM systems. Case studies are considered that demonstrate the applicability of the method devised

Contents

1	Introduction	1
1.1	Background and motivation	1
1.2	Thesis organisation	2
1.3	Contributions	3
2	Semiconductor laser modelling	7
2.1	Introduction	7
2.2	Basic laser characteristics	8
2.2.1	Recombination mechanisms	8
2.2.2	Gain and stimulated emission	10
2.2.3	Lasing characteristics	13
2.2.4	Laser structures	15
2.3	Single-mode rate equation model	19
2.3.1	Rate equations	19
2.3.2	Influence of carrier diffusion and nonlinear gain	20
2.3.3	Steady-state characteristics	22
2.4	Numerical solution of the rate equations	23
2.4.1	Normalization	23
2.4.2	Steady-state solution	24
2.4.3	Transient response	26
2.5	Intensity noise characteristics	28
2.5.1	Langevin formulation	28
2.5.2	Intensity noise definition	29
2.5.3	Analysis of RIN using the stochastic rate equations	29

2.5.4	Requirements of RIN for intensity modulated systems	31
2.6	Summary	32
3	Nonlinear distortion in semiconductor lasers	33
3.1	Introduction	33
3.2	Intermodulation distortion in SCM systems	34
3.3	Origins of laser nonlinear distortion	36
3.4	High-frequency modulation characteristics	38
3.4.1	Small-signal response	38
3.4.2	Relaxation oscillation damping	40
3.4.3	High frequency limits	40
3.5	Laser characterization and extraction of model parameters	41
3.5.1	Package and chip parasitics model	42
3.5.2	Determination of parasitics and laser intrinsic parameters	43
3.6	Analysis of laser nonlinear distortion	47
3.6.1	Perturbation solution of the rate equations	47
3.6.2	Bessel function expansion	53
3.7	Summary	56
4	Volterra series analysis	58
4.1	Introduction	58
4.2	Volterra series: frequency domain analysis	59
4.3	Determination of laser transfer functions	61
4.4	Laser response to a sum of narrow-band signals	65
4.4.1	General theory	65
4.4.2	Multitone input case	67
4.5	Series expansion of nonlinear transfer functions	68
4.6	Analytic and simulation results	69
4.6.1	Model validity	69
4.6.2	Dependence of intermodulation products on frequency spacing	75
4.7	Summary	77

5	System performance assessment	78
5.1	Introduction	78
5.2	Intermodulation power spectral density	79
5.3	Series expansion of H_n and implications for single-tone modulation	81
5.4	Carrier-to-intermodulation ratio	85
5.5	Overall system performance	87
5.6	Receiver design considerations	90
5.7	Clipping distortion implications	93
5.8	Summary	95
6	SCM system case studies	97
6.1	Introduction	97
6.2	FM broadcast systems	98
6.2.1	Introduction	98
6.2.2	Intermodulation power spectral density	98
6.2.3	Carrier-to-intermodulation ratio	101
6.2.4	Results	103
6.3	AM CATV systems	110
6.3.1	Introduction	110
6.3.2	Intermodulation power spectral density	110
6.3.3	Intermodulation noise	113
6.3.4	Carrier-to-intermodulation ratio	117
6.3.5	System results	119
6.4	FSK Fibre-Radio return link	124
6.4.1	Introduction	124
6.4.2	System description	125
6.4.3	Intermodulation power spectral density	125
6.4.4	Carrier-to-intermodulation ratio	127
6.4.5	Worst case condition	129
6.4.6	System results	132
6.5	Summary	135

7	Concluding remarks	137
	Appendices:	
A	Clipped distortion power of an octave bandwidth FM system	141
B	Power spectral density of third-order two-tone IMP of an AM-SSB system	144
C	Intermodulation power spectral density of CPFSK	148
	Bibliography	155

List of Figures

2.1	Transition of an electron from E_1 to E_2 by the absorption of a photon of energy $E_2 - E_1$. The quasi-Fermi levels for the valence and conduction bands are F_v and F_c , respectively.	9
2.2	Calculated stimulated gain coefficient versus photon energy $E = h\nu$	12
2.3	Cross section of three InGaAsP semiconductor laser structures: (a) Oxide-stripe laser; (b) Channeled-substrate planar waveguide; (c) Etched-mesa buried heterostructure. The active layer material (shaded area) has a smaller band gap and lower refractive index than the surrounding cladding layers.	17
2.4	Normalized steady-state electron density as a function of current density. . .	25
2.5	Normalized steady-state photon density as a function normalized current density for two values of β . Above threshold p_0 is a linear function of j_0	25
2.6	Laser large-signal turn-on response to a current step at $t = 0$ with 100 ps rise time and an amplitude of $2I_{th}$. (a) $I_{off}/I_{th} = 0.98$, (b) $I_{off}/I_{th} = 1.1$	27
2.7	Relative intensity noise spectra at several bias currents: (1) $I_0/I_{th} = 1.5$, (2) $I_0/I_{th} = 2$, (3) $I_0/I_{th} = 3$. Laser parameters taken from Reference [31]. . .	31
3.1	Intermodulation products and harmonics generated by a three-tone modulation of a laser diode.	34
3.2	Total number of third-order intermodulation products as a function of channel number with the number of channels, N as a parameter.	35
3.3	Small-signal transfer function of a ridge-waveguide laser [31], with ω_0/ω_d as a parameter.	39
3.4	Magnitude of the resonance peak height (M_p) for a InGaAsP ridge-waveguide laser	41
3.5	Equivalent circuit model of package and chip parasitics	43

3.6	Measured and simulated results of (a) reflection coefficient (S_{11} -parameter) and (b) input impedance of parasitics equivalent circuit in the frequency range of 1–8 GHz.	45
3.7	Frequency response of the laser package and chip parasitics.	46
3.8	Measured and modelled small-signal frequency response of the laser diode Ortel-1510B.	46
3.9	Second harmonic and intermodulation distortion levels for a ridge-waveguide laser [31] with $\tau_p = 1$ ps, $\epsilon/g_0 = 20$ ps and $f_0 = \omega_0/(2\pi) = 3$ GHz: comparison between the exact solution of the perturbation technique, eqn. (3) of [15] and eqn. (3.33).	51
3.10	Effect of neglecting nonradiative mechanisms in the laser model: the difference is less than 0.4 dB. Parameters were taken from [21] with $m = 0.3$, $f_1 = 2$ GHz, $f_2 = 2.2$ GHz and $f_3 = 2.4$ GHz.	52
3.11	Numerical solution of the set of equations (3.42)–(3.43) and (3.47)–(3.48).	54
3.12	Fundamental and second harmonic amplitudes: comparison between eqn. (3.45), eqn. (3.50), perturbation analysis and direct simulation.	55
4.1	Diagram block of the semiconductor laser	61
4.2	First-order laser transfer function $H_1(f_1)$: comparison between analytical and simulation results when the laser is modulated by three carriers for two values of the laser bias current I_0 ($m(0) = 0.13$).	73
4.3	Second-order laser transfer function $H_2(f_1, f_2)$: comparison between analytical and simulation results when the laser is modulated by three carriers for two values of the laser bias current I_0 ($f_2 = f_1 + 0.2$ GHz and $m(0) = 0.13$)	73
4.4	Third-order laser transfer function $H_3(f_1, f_2, -f_3)$: comparison between analytical and simulation results when the laser is modulated by three carriers for two values of the laser bias current I_0 ($f_2 = f_1 + 0.2$ GHz, $f_3 = f_1 + 0.7$ GHz and $m(0) = 0.13$)	74
4.5	Amplitude of second and third-order intermodulation products relative to the carrier at f_1 for a laser bias current of (a) $I_0 = 40$ mA and (b) $I_0 = 60$ mA ($f_1 = 2.1$ GHz, $f_2 = 2.3$ GHz and $f_3 = 2.8$ GHz).	74

4.6	Third-order intermodulation distortion versus f_1 for constant f_2 and f_3 ($f_3 - f_2 = 200$ MHz, $m = 20\%$, $I_0 = 50$ mA and $f_0 = 3.3$ GHz)	76
4.7	Third-order intermodulation distortion versus f_2 for constant f_1 ($f_3 - f_2 = 200$ MHz, $m = 20\%$, $I_0 = 50$ mA and $f_0 = 3.3$ GHz)	76
5.1	Block diagram of a directly modulated subcarrier multiplexed system.	78
5.2	Single-tone modulation with frequency f_m in a AM upper-sideband system	82
5.3	Approximation error on the evaluation of the second harmonic distortion resulting from taking the second-order transfer function constant over the channel band. AM single-tone modulation with frequency $f_m = 6$ MHz using a DFB-BH laser, parameters given in table 6.1	83
5.4	Approximation error on the evaluation of the third harmonic distortion resulting from taking the third-order transfer function constant over the channel band. FM single-tone modulation with frequency $\Delta f = 11.25$ MHz using a DFB-BH laser, parameters given in table 6.1	84
5.5	Sensitivity as a function of carrier-to-noise ratio using a PIN detector for two circuit noise levels. Parameters are $R_0 = 0.8$ A/W, $N = 62$, $B = 36$ MHz, $RIN = -155$ dB/Hz and $D_{111} = 0.02$	91
5.6	Sensitivity as a function of carrier-to-noise ratio using an APD with the same assumptions of figure 5.5: $R_0 = 0.8$ A/W, $x = 0.7$, $N = 62$, $B = 36$ MHz, $RIN = -155$ dB/Hz and $D_{111} = 0.02$	92
5.7	Optimum avalanche gain and optimum modulation depth associated with the curves of figure 5.6.	92
5.8	Contribution of clipping distortion and intermodulation distortion due to laser resonance distortion to the total carrier-to-noise ratio: $D_{111} = 0.02$, $D_{11} = 0$, $\Lambda = 1/4$ and $N = 62$	95
6.1	Diagram of the multiplex structure	103
6.2	First-order transfer function (—) and parasitics response (---) for a DFB-BH laser diode.	105
6.3	Relative intensity noise (RIN) for a DFB-BH laser diode.	105
6.4	Carrier-to-intermodulation ratio for channels 1, 31 and 62	106

- 6.5 Maximum of the third-order distortion coefficient D_{111} as a function of laser bias current for constant input amplitude (—) and constant modulation depth (---) among all the channels. The numbers in the plot, for each curve, indicate the channel suffering maximum distortion ($\max(D_{111})$) 106
- 6.6 Optimum modulation depth per channel (m_{opt}) for three values of CNR (16.5, 18.5 and 20.5 dB). 107
- 6.7 Sensitivity of an APD based receiver with APD gain ≥ 1 : 62 channel FM system with RIN= -150 dB/Hz and $I_0 = 50$ mA 108
- 6.8 Sensitivity of a PIN based receiver: 62 channel FM system with RIN= -150 dB/Hz and $I_0 = 50$ mA 108
- 6.9 Distribution of (a) second-order distortion products and third-order products of type (b) $f_i + f_j - f_k$ and (c) $2f_i - f_k$ for a 42 channel system. The short markers on the top of (a) show the frequency location of the carriers. 114
- 6.10 Power spectral density of second-order intermodulation products and their location within the band of channel at 157 MHz for a 42 channel AM system with the frequency plan of figure 6.9. The grey areas represent the fraction of the intermodulation power that falls in the channel band. 116
- 6.11 Power spectral density of third-order intermodulation products of type $f_i + f_j - f_k$ and their location within the band of channel at 157 MHz, for a 42 channel AM system with the frequency plan of figure 6.9. The grey areas represent the fraction of the intermodulation power that falls in the channel band. 118
- 6.12 Carrier-to-intermodulation ratio of channels 1, 21 and 42 for two values of the laser bias current. 120
- 6.13 Second and third-order distortion coefficients of a 42 channel AM system: frequency plan of figure 6.9 and channel bandwidth of 6 MHz 120
- 6.14 Distortion levels as a function of the laser bias current: modulation depth is $m = 0.1$. The distortion minimum occurs at lower bias currents for channels at the lower frequencies. 121

6.15	Carrier-to-intermodulation ratio as a function of the optimum r.m.s modulation depth, μ_{opt} , for two values of bias current, $I_0 = 21.7$ mA and $I_0 = 50$ mA, corresponding to two cases where laser intrinsic distortion and clipping distortion are dominant, respectively.	122
6.16	Block diagram of a frequency division multiple access (FDMA) fibre/radio return link.	124
6.17	Power spectral density of input signal and of third-order intermodulation products. The frequency deviation is $f_d T = 0.5$ corresponding to minimum shift keying.	128
6.18	Carrier-to-intermodulation ratio; DFB-BH laser with a bias current of 50 mA and the channels have equal amplitudes. The optical modulation depth is (4.5%) for channel 29 (reference channel).	130
6.19	Multiplex frequency plan of a 50 channel CPFSK system.	132
6.20	Third-order distortion coefficients D_{111} (—) and D_{21} (---).	133
6.21	Dependence of the optimum modulation depth (m_{opt}) with laser bias current.	133
6.22	Sensitivity of a PIN based receiver: (—) $I_0=60$ mA, $RIN=-151$ dB/Hz; (---) $I_0 = 50$ mA, $RIN=-148$ dB/Hz	134
6.23	Various noise contributions and dependence of CNR with received optical power: $\langle I_r^2 \rangle = 4$ pA/ $\sqrt{\text{Hz}}$, $RIN=-148$ dB/Hz and laser bias 50 mA. Optimum performance is obtained for $m \approx 4.9\%$ and the dynamic range is achieved for a mean optical power of -10 dBm.	135
A.1	Normalized clipped distortion spectrum, $y(x)$	142

List of Tables

3.1	Linearity requirements of typical subcarrier multiplexed systems.	36
3.2	Parasitic element values for the equivalent circuit of figure 3.5.	44
3.3	Parameter values for the laser diode Ortel-1510B.	47
3.4	Driving terms; C^ω equals zero for $\omega = \omega_{1,2,3}$ and D^ω for the other cases. $c_1 = 1 - 2\epsilon p_0$, $c_2 = n_0 - n_{0m}$. $i, j, k = 1, 2, 3$ and $i \neq j \neq k$	50
4.1	Driving terms: C_n equals zero for $n = 1$ and D_n for the other cases	64
4.2	Amplitude of third-order IMPs	68
4.3	Parameter values for a Buried-Heterostructure laser	71
4.4	Package and chip parasitics elements values for a BH laser (for a diagram of the equivalent circuit see Reference [31]).	71
6.1	Parameter values for a DFB-BH laser.	104

Chapter 1

Introduction

1.1 Background and motivation

This thesis is concerned with an investigation of the impact of source nonlinearity on the performance of multichannel subcarrier multiplexed optical fibre systems. There has been much interest recently in the capabilities of subcarrier multiplexing (SCM) as a means of realising economically multichannel systems which can be deployed in the short to medium term to support a wide range of analogue and digital services [1, 2, 3, 4].

The attractive feature of SCM is that it provides a way of exploiting the multi-gigahertz bandwidth potential of high speed lasers [5, 6] using conventional and already established microwave techniques. Also they are very flexible being capable of simultaneously transmitting conventional baseband and microwave signals with the same fibre and detector [7, 8]. Moreover, SCM systems can be combined with coherent techniques [9, 10, 11] and wavelength division multiplexing [12, 13] to fully utilize the tens of terahertz capacity of single-mode fibre.

The performance of such systems can be impaired very significantly by nonlinearities associated with the laser diode source. Realisation of the full system capabilities calls for detailed modelling and analysis of the nonlinearities and the associated intermodulation distortion with a view to practical system optimisation through an appropriate balance between signal induced distortion and noise effects.

At the commencement of this study much was already known about the basic distortion-producing phenomena but such analytical treatments as had been presented concentrated on supporting experimental observations relating to relatively simple (two-tone and three-

tone modulation) distortion measurements [14, 15, 16]. There had been little work aimed at providing rigorous yet tractable design and analysis tools and techniques appropriate for assessing systems of the kind and complexity being envisaged for planned deployments. Indeed, as subsequently proved to be the case, it seemed likely that some of the methods extant in the literature were such as to not be realistically extensible to such cases of practical interest [17, 18]. It was these observations which motivated the present study, the aim being to obtain and demonstrate the applicability of tools and techniques appropriate for practical systems design and optimisation. As a basis for this, it has been necessary to direct significant attention to the refinement of models for laser diodes in order to appropriately accommodate some of the more subtle aspects of induced signal distortion. To achieve this, whilst retaining a realistic level of tractability, recourse has been made to the Volterra series method of nonlinear system theory [19], the applicability of the methods devised being demonstrated via a set of systems case studies. With this brief introduction we may now proceed to a discussion of the organisation of the thesis.

1.2 Thesis organisation

Following this introduction, chapter 2 will provide a review of the basic principles and characteristics of semiconductor lasers. We will focus on the physical mechanisms responsible for stimulated emission and the associated optical gain, with the aim of introducing the single-mode rate equations that govern the laser dynamics operation. Numerical solutions of the rate equations are then examined. Additionally, a Langevin formulation of the rate equations is described from which the laser intensity noise characteristics are investigated.

In chapter 3 the problem of modelling the laser nonlinear distortion is addressed. The impact of laser distortion on typical SCM systems and their requirements are discussed and the mechanisms which give rise to laser nonlinearity are examined. Since the laser intrinsic distortion is intimately related to the modulation characteristics the frequency response of the laser diode is examined in some detail using a small-signal analysis of the rate equations. This is complemented by measurements of device characteristics and extraction of laser parameters for a commercial laser diode. Existing methods for the analysis of laser nonlinearity are then analysed: the perturbation technique is extended to include the three tone intermodulation

products of type $f_i + f_j - f_k$ and a technique based on Bessel functions expansion, offering promising results, is shown not to predict adequately the levels of distortion of the laser diode.

The limitations of these methods, that their inapplicability to the performance assessment of practical systems of interest, is overcome by the application of a Volterra series analysis. The general theory of this method is described in chapter 4. The nonlinear transfer functions which describe the nonlinearity in the frequency domain are determined from the rate equations and the laser response to the relevant case of a sum of narrow-band signals is considered. Analytic and simulation results are compared that validate our theoretical model.

This model is used in chapter 5 to assess the performance of directly modulated SCM systems. The general method for calculating the intermodulation power spectral density is detailed permitting an accurate evaluation of the impact of laser intrinsic distortion on system performance. The overall system performance is then determined by inclusion of relative intensity noise, receiver shot and thermal noise. By balancing the signal dependent and independent noise contributions optimum performance is identified. Receiver design considerations as well as clipping-induced distortion effects are discussed.

The results of chapter 5 are applied in chapter 6 to study three important SCM systems namely: FM video broadcast, AM-CATV and a Fibre-Radio system having a wide-dynamic range of power levels. Finally, chapter 7 concludes the thesis by summarising the main achievements and identifying areas of further research.

1.3 Contributions

The research reported here has sought to provide a detailed and comprehensive assessment of the performance of multichannel SCM fibre optic systems, emphasis being placed on the implications of laser nonlinearities. A major objective has been to provide tractable, accurate modelling and analysis techniques applicable to the performance assessment of practical systems and this constitutes the primary contribution of this thesis. In order to achieve this it has been necessary to produce new derivations and means of analysis, relating both to specific impairments and their combined influence on system performance. The main contributions of this research work may be summarized as follows:

- Extension of the perturbation technique to include three-tone third-order distortion products of type $f_i + f_j - f_k$ which dominate for a large number of channels.
- Deficiencies in a previously published method for the analysis of laser distortion was identified. The technique, based on the expansion of Bessel functions, was extended to allow for laser relaxation resonance effects and modified to predict adequately second and higher-order harmonics.
- A theoretical nonlinear laser model was developed based on the Volterra series analysis of distortion which includes all the intermodulation products up to third-order, for a laser nonlinearity as determined from the rate equations and for an arbitrary number of channels. This model is able to predict the laser response to a sum of narrow-band signals and takes into account key parameters such as bias current and frequency (channel) allocation.
- The intermodulation power spectral density was determined for relevant modulation formats enabling one to assess accurately the impact of laser distortion by taking the fraction of intermodulation power that falls in the channel band.
- A suitable performance assessment strategy was identified that may be used for the optimisation of SCM systems prior to implementation. This analysis was applied to study two important SCM applications: FM video broadcast and AM-CATV systems.
- Identification of the relative importance of clipping and laser intrinsic distortion on different types of SCM practical systems.
- A method was developed to enable the optimisation of SCM systems in applications requiring a wide-dynamic variation of power levels, based on a worst case condition. One possible application was studied consisting of a FSK Fibre-Radio return link.
- Development of “software tools” implemented in MATLAB and SIMULINK for system simulation and optimisation.

The contributions of this research work have led to the following publications:

1. H. M. Salgado and J. J. O'Reilly, "Nonlinear distortion characteristics of semiconductor lasers," *Digest of 2nd Bangor Symposium on Communications*, pp. 211–214, (Bangor, U.K.), 23–24 May 1990.
2. J. J. O'Reilly and H. M. Salgado, "Distortion analysis of semiconductor lasers: A caution," *Electron. Lett.*, vol. 27, pp. 946–947, May 1991.
3. H. M. Salgado and J. J. O'Reilly, "Tractable models of laser distortion in subcarrier multiplexed optical systems," *Digest of 3rd Bangor Symposium on Communications*, pp. 23–25, (Bangor, U.K.), 29–30 May 1991.
4. H. M. Salgado and J. J. O'Reilly, "Modelling laser distortion in subcarrier multiplexed systems," *Digest of IEEE Lasers and Electro-Optics Society: Annual Meeting*, (San Jose, CA), 4–7 Nov. 1991.
5. H. M. Salgado and J. J. O'Reilly, "Volterra series analysis of distortion in semiconductor laser diodes," *IEE Proc.-J*, vol. 138, pp. 379–382, Dec. 1991.
6. J. J. O'Reilly and H. M. Salgado, "Performance assessment of optical subcarrier multiplexing systems: Implications of laser distortion," *Proc. IEEE Global Telecommunications Conference*, pp. 1845–1848, (Phoenix, USA), 2–5 Dec. 1991.
7. H. M. Salgado and J. J. O'Reilly, "Effect of laser distortion on the performance of AM SCM optical systems," *Digest of 4th Bangor Symposium on Communications*, pp. 226–229, (Bangor, U.K.), 27–28 May 1992.
8. J. J. O'Reilly, P. M. Lane, M. H. Capstick, H. M. Salgado, R. Heidmann and R. Hofstetter, "Remote delivery of video services using mm-waves and optics," *OFC'93-Workshop on Options for Video Delivery*, (San Jose, USA), 21–26 Feb. 1993.
9. H. M. Salgado and J. J. O'Reilly, "Modelling laser nonlinear distortion in multichannel analogue optical systems," *OFC'93-Workshop on Theory and Modelling of Lightwave Networks*, (San Jose, CA), 21–26 Feb. 1993.
10. J. J. O'Reilly, P. M. Lane, M. H. Capstick, H. M. Salgado, R. Heidmann, R. Hofstetter and H. Schmuck, "MODAL: An enabling technology for wireless access," *Proc. of 4th*

IEE Conference on Telecommunications, (Manchester, U.K), Apr. 1993.

11. H. M. Salgado and J. J. O'Reilly, "Performance assessment of subcarrier multiplexed fibre/radio systems," *Digest of 5th Bangor Symposium on Communications*, pp. 92–95, (Bangor, U.K.), 2–3 Jun. 1993.
12. J. J. O'Reilly, P. M. Lane, M. H. Capstick and H. M. Salgado, "Wireless connection using mm-waves and fibre," *Digest of Int. Symp. on Subscriber Loops and Services*, (Vancouver, Canada), Sep. 1993.
13. J. J. O'Reilly, P. M. Lane, M. H. Capstick, H. M. Salgado, R. Heidmann, R. Hofstetter and H. Schmuck, "RACE R2005–microwave optical duplex antenna link." *IEE Proc.-J*, in Press.
14. H. M. Salgado and J. J. O'Reilly, "Performance assessment of broadcast FM optical subcarrier multiplexed systems." *IEE Proc.-J Special Issue on Analogue Optical Fibre Communications*, in Press.

Chapter 2

Semiconductor laser modelling

2.1 Introduction

In subcarrier multiplexed applications the laser diode has a great impact on system performance due to several degradation factors: relative intensity noise (RIN), nonlinear distortion and the increased RIN levels through optical reflections. Modelling of the semiconductor laser is thus required to obtain an accurate representation of its characteristics under dynamic operation. This subject is addressed here, the model presented being used for later studies of laser nonlinearity. The theoretical basis for this is well developed, although new refinements are constantly being introduced.

We start by reviewing the key ideas and principles of the semiconductor laser. The degradation factors mentioned above are ultimately determined by the intrinsic laser diode characteristic, which is a semiconductor device where the stimulated emission is achieved by means of current injection through a forward biased $p-n$ junction. The recombination mechanisms responsible for laser action are considered and stimulated emission is related to the optical gain. The effect of laser structure on laser characteristics is also addressed. The study of laser dynamics in the following sections is based on a set of coupled rate equations. These are introduced in section 2.3. In section 2.4 the numerical solution of the laser diode steady-state and transient responses are examined. Finally the intensity noise characteristics are investigated.

2.2 Basic laser characteristics

Stimulated emission is a phenomena that can occur when electromagnetic radiation interacts with matter. In stimulated emission, a photon interacts with an electron causing an emission of an additional identical photon. A laser is formed by providing feedback of some of this emission. The Einstein relations can be used to relate the rate of spontaneous and stimulated emission to the optical gain. This approach only provides the small-signal gain and so saturation effects can not be treated. These will be discussed separately.

Although different classes of lasers are based on this same principle there are some aspects that are unique to injection semiconductor lasers: the optical transitions, which take place in the active region of the p - n junction, are between a continuous distribution of electronic states within the conduction and valence bands, and the injected electrons of the excitation current are directly converted to photons with a high quantum efficiency.

2.2.1 Recombination mechanisms

A high quantum efficiency requires dominance of radiative over non-radiative recombination. The optical processes associated with radiative transitions are photon emission, spontaneous emission and stimulated emission. In figure 2.1 an electron transition is shown. The transition is from a state E_1 in the valence band to a state E_2 in the conduction band, with the absorption of a photon of energy $E = E_2 - E_1 = h\nu$. In addition to being absorbed these photons can also stimulate the emission of a similar photon by the transition of an electron from E_2 to E_1 . The net rate of stimulated emission, $r_{st}(E)$, i.e. stimulated emission minus absorption rate, is found from the Einstein relations. If the transitions are defined with respect to the interaction with photons of a single oscillation state the final result is ¹[20]

$$r_{st}(E) = B(E_1, E_2)\rho_c(E_2)\rho_v(E_1)[f_c(E_2) - f_v(E_1)] \quad (2.1)$$

where B is the transition probability, ρ_c and ρ_v are the electron density states in the conduction and valence bands, respectively, and f_c , f_v are the corresponding electron occupation probabilities, which follow a Fermi-Dirac distribution with quasi-Fermi level F_c and F_v . Hence, the

¹The units of $r_{st}(E)$ are number of photons per unit time, per unit energy interval and per photon in the oscillation state considered.

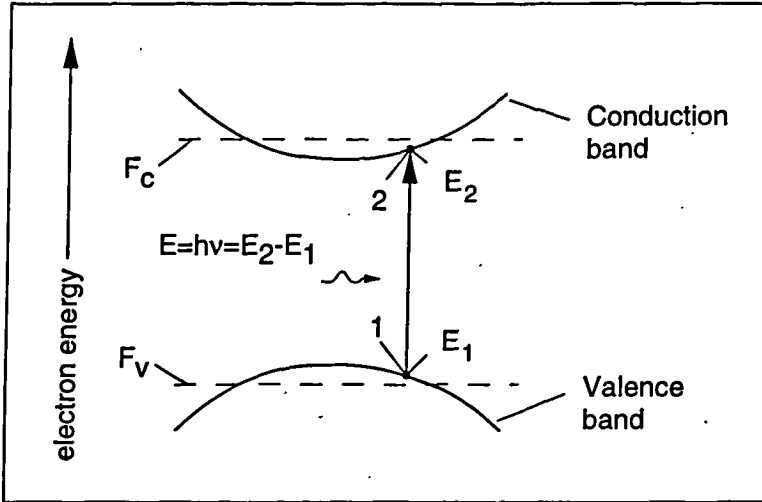


Figure 2.1: Transition of an electron from E_1 to E_2 by the absorption of a photon of energy $E_2 - E_1$. The quasi-Fermi levels for the valence and conduction bands are F_v and F_c , respectively.

net stimulated emission and thus the optical gain is positive only if the occupation probability in the conduction band at E_2 is larger than the occupation probability in the valence band at E_1 ($f_c(E_2) > f_v(E_1)$). This condition, known as population inversion, is achieved only for strong carrier injection into the active region yielding a shift of the quasi-Fermi levels F_c , F_v into the conduction and valence bands, respectively. The condition for stimulated emission $r_{st} > 0$ reduces to

$$F_c - F_v > E \quad (2.2)$$

This is a necessary, but not sufficient, condition for laser action in semiconductors. In order to achieve lasing the net stimulated emission rate must also be sufficient to overcome various loss mechanisms in the device.

The total spontaneous emission rate, which occurs without external stimulation, is proportional to the product of the electron concentration in the conduction band, N , with the hole concentration in the valence band, P_h ,

$$R_{sp} = BN P_h \quad (2.3)$$

where B is a constant of the order of $10^{-10} \text{ cm}^3 \text{ s}^{-1}$ for GaAlAs and InGaAsP devices. For undoped material $N = P_h$ and the total spontaneous emission rate is proportional to N^2 , which is often denoted as bimolecular recombination. For a p -type material, for example, with a doping level P_{h0} one has $R_{sp} = BN(N + P_{h0})$. In the case of low carrier injection (or high

doping levels) such that $N \ll P_{h0}$ the spontaneous recombination varies linearly with N with a proportionally constant BP_{h0} .

So far we have only considered radiative combination. Nonradiative recombinations also exists in actual devices. For GaAlAs devices the nonradiative recombination is usually small but for InGaAsP it has to be taken into account. The most probable process is an Auger transition [21] involving four particle states (three electrons and one hole, two electrons and two holes and so forth). The Auger recombination rate for lightly doped material can be approximately written as

$$R_{Auger} = CN^3 \quad (2.4)$$

where the recombination coefficient C is if the order of $1 \dots 3 \times 10^{-29} \text{ cm}^6\text{s}^{-1}$. Auger recombination exceeds spontaneous emission for $CN > B$ which is verified for carrier densities larger than $3 \times 10^{18} \text{ cm}^{-3}$. These carrier densities are required for laser operation, especially at high temperatures. Therefore the large temperature dependence of the threshold current for InGaAsP lasers is expected to be due to significant contribution of Auger recombination. Other nonradiative mechanisms include recombination at defects and surface recombination. In general terms, defects in a p - n junction produce a continuum of states in a localized region. Electrons and holes situated within a diffusion length from the edge of the defect may recombine nonradiatively. In addition, in a injection laser a surface can be considered as a perturbation of the crystal lattice, creating many dangling bonds that can absorb impurities from the ambient. When modelling the semiconductor laser, the defects and surface recombination are considered together with a recombination rate given by

$$R_d = A_{nr}N \quad (2.5)$$

with a typical value for A_{nr} of $1 \times 10^8 \text{ s}^{-1}$.

2.2.2 Gain and stimulated emission

The interaction of photons and electrons in the solid may be related to a macroscopic effect: the amplification an optical wave if the stimulated emission is sufficiently large.

The emission rate considered in the previous section represents transitions between the energy levels E_1 and E_2 . In a semiconductor there is a continuum of states in the conduction

and valence bands. Therefore, the rate of stimulated emission R_{st} is the integral of r_{st} over all energy levels separated by $E = h\nu$

$$R_{st}(E) = \int_{-\infty}^{\infty} B(E_2, E) \rho_c(E_2) \rho_v(E_1) [f_c(E_2) - f_v(E_1)] dE_2 \quad (2.6)$$

If S is the number of photons in the laser cavity in one specific oscillation state, the net stimulated rate which tells us how many photons are generated per unit of time per existing photon, yields a generation rate of new photons dS/dt according to

$$\frac{dS}{dt} = R_{st} S. \quad (2.7)$$

The resulting stimulated gain coefficient relates to the stimulated emission coefficient R_{st} by [20]

$$\begin{aligned} g_{st} &= \frac{\text{power emitted per unit volume}}{\text{power crossing a unit area}} \\ &= \frac{R_{st}}{v_g} = \frac{R_{st} \bar{\mu}}{c} \end{aligned} \quad (2.8)$$

where v_g is the group velocity, c is free-space velocity of light and $\bar{\mu}$ is the group refractive index of the material taking dispersion into account: $\bar{\mu} = \mu + \nu d\mu/d\nu$. Thus the factors influencing the gain spectrum are the transition probabilities, the density of states and the occupation probabilities. In particular, it follows from (2.2) that the gain is only positive for photon energies less than the separation of the quasi-Fermi levels, $F_c - F_v$.

The calculation of gain coefficient requires knowledge of the transition probability $B(E)$ which determines the transition rate of electrons. B is expected to depend on various properties of the system that relate the interaction of electrons in the solid with the electromagnetic radiation. This requires the techniques of time-dependent perturbation theory and the transition probability is given by Fermi's "Golden Rule" [22, 23]. The actual calculations depend on the \mathbf{k} -selection rule used. For transitions between parabolic band states the initial and final particles obey the \mathbf{k} -selection rule, that is, the allowed transitions are between initial and final states of the same wave vector \mathbf{k} . In the lasing situation the high density of carriers (or high doping levels) modifies the density of states by the creation of band-tail states [21]. For these states the conservation of momentum is not satisfied, i.e., the \mathbf{k} -selection rule does not apply. For heavily doped semiconductors a sophisticated model of transitions involving band-tail

states was developed first for GaAs by Casey and Stern [24] and later applied to $1.3 \mu\text{m}$ by Dutta [25]. Figure 2.2 shows the gain spectra for different carrier concentrations, as calculated from the latter model. This data can be used to relate the gain and carrier density.

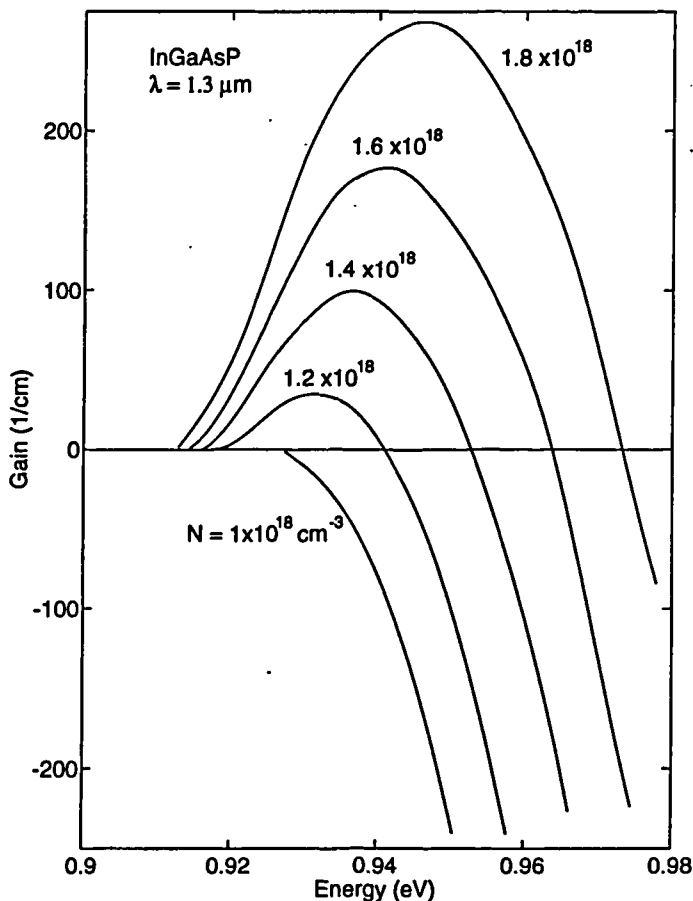


Figure 2.2: Calculated stimulated gain coefficient versus photon energy $E = h\nu$

A simple empirical formula for the gain is obtained by assuming a linear dependence on electron concentration and a parabolic variation with wavelength λ

$$g_{st} = a(N - N_{0m}) - b(\lambda - \lambda_p)^2 \quad (2.9)$$

where b is related to the gain spectral width, N_{0m} is the 'transparency' electron density (for which $g_{st} = 0$ at $\lambda = \lambda_p$) and a is the gain coefficient. A further refinement is to include the

shift of peak wavelength with N in the form

$$\lambda_p = \lambda_0 + (N - N_{0m}) \frac{d\lambda}{dN} \quad (2.10)$$

Values of $a = 2.7 \times 10^{-16} \text{ cm}^2$, $N_{0m} = 1 \times 10^{18} \text{ cm}^{-3}$ and $d\lambda/dN = -2.7 \times 10^{-17} \text{ nm cm}^3$ were obtained by fitting equations (2.9) and (2.10) to measured gain spectra [26].

Confinement factor

The considerations so far have been for a bulk laser active material. However, the active region of a double heterostructure laser is rather thin and the optical field is only partly confined to the active region where positive optical gain exists. If the active region with thickness d and refractive index μ_1 is surrounded by heterolayers with refractive index $\mu_2 < \mu_1$ a dielectric waveguide is formed. The fundamental mode of this waveguide will exhibit a gain

$$g = \Gamma g_{st} \quad (2.11)$$

where Γ is the confinement factor defined as the fraction of the mode power within the active layer. For the symmetric three-layer waveguide and for a thin active layer the confinement factor is approximately given by [22]

$$\Gamma = \frac{1}{1 + [2\pi^2(\mu_1^2 - \mu_2^2)(d/\lambda)^2]^{-1}} \quad (2.12)$$

for the predominantly TE-polarized mode. A typical active layer thickness of $0.1 \dots 0.2 \mu\text{m}$ thick and for $\mu_1 \simeq 3.6$, $\mu_2 \simeq 3.4$ and $\lambda = 1.1 \dots 1.65 \mu\text{m}$ yields a confinement factor of $\Gamma = 0.2 \dots 0.6$.

2.2.3 Lasing characteristics

Threshold conditions

In order to cause the gain medium to oscillate, regenerative feedback must be provided. The simplest semiconductor laser structure employs a Fabry-Perot (FP) cavity formed by cleaved facets at each end of the device. The high refractive index of the semiconductor ($\mu = 3.5$ for InGaAsP) gives sufficient reflectivity $\approx 30\%$ at the facets to produce a resonant cavity. The threshold gain is defined as the gain required to sustain the optical field after travelling one

round trip in the cavity. Assuming the optical gain is constant over the whole length of the laser this leads to the condition

$$R_1 R_2 e^{2(g_{th} - \alpha_s)L} = 1 \quad (2.13)$$

where R_1 , R_2 are the facets power reflectivities, α_s is the cavity loss per unit length and L is the length of the cavity. Equation (2.13) yields the threshold gain as

$$g_{th} = \alpha_s + \frac{1}{2L} \ln \frac{1}{R_1 R_2} \quad (2.14)$$

The second term is defined as the mirror loss α_m . This equation shows that the gain per unit length must be sufficient to cancel out the optical losses and the losses due to light emission. Since the contribution of spontaneous emission in this simple analysis has not been considered, the actual gain will be slightly lower than the threshold gain.

The concept of gain cancelling out the losses applies not only at the threshold current but at all currents above threshold. However, as the current is increased saturation effects start to reduce the gain in some parts of the laser compared with others, so that there is no longer the exact balance between gain and loss at all points along the laser but the loop gain must still be unity.

Dynamic characteristics

The description of laser operation is complete once the carrier density N is related to the pump parameter, the current density J . This is accomplished through a rate equation that incorporates all the mechanisms by which the carriers are generated or lost inside the active region. The continuity equation which describes the rate of change of carriers in its general form is

$$\frac{\partial N}{\partial t} = D(\nabla^2 N) + \frac{J}{qd} - \gamma_e(N)N - R_{st}P \quad (2.15)$$

The first term accounts for carrier diffusion, with D the diffusion coefficient. The second term governs the rate at which the carriers, electrons or holes, are injected into the active layer because of external pumping (q is the value of the electron charge). The third term takes into account the carrier loss owing to various recombination processes: spontaneous emission and non-radiative. A suitable form for the carrier recombination rate $\gamma_e(N)$, for lightly doped

InGaAsP, as described in section 2.2.1, is

$$\gamma_e(N) = A_{nr} + BN + CN^2 \quad (2.16)$$

The last term of equation (2.15) is due to stimulated emission recombination that leads to coherent emission of light. Depending on the device geometry, diffusion effects may be neglected. This is the case for strongly index guided lasers [21] as discussed in section 2.2.4.

A corresponding rate equation for the photon density can be obtained from Maxwell's equations using a classical approach [27, 20]. By a simple bookkeeping of the supply, annihilation and creation of carriers and photons inside the laser cavity, gives

$$\frac{dP}{dt} = P(\Gamma R_{st} - \frac{1}{\tau_p}) + \beta\Gamma R_{sp} \quad (2.17)$$

in which the photon lifetime is defined by

$$\tau_p^{-1} = v_g \left[\alpha_s + \frac{1}{2L} \ln \left(\frac{1}{R_1 R_2} \right) \right] \quad (2.18)$$

Equation 2.18 states that the rate of increase in photon density is equal to the photon generation by stimulated emission $\Gamma R_{st}P$ less the loss rate of photons $-P/\tau_p$ (as characterized by the photon lifetime τ_p), plus the rate of spontaneous emission into the photon mode βR_{sp} , where β is the fraction of the total spontaneous emission coupled into the laser mode.

Equations (2.15) and (2.17) represent the basic relations for describing the dynamic characteristics of laser diodes, as long as the noise sources may be omitted. Laser intensity noise will be discussed in section 2.5.

2.2.4 Laser structures

Gain-guided and index-guided lasers

The carrier density required for laser operation is rather high. In order to achieve high carrier densities at low currents it is necessary to confine the recombining carriers to as small a volume as possible. The confinement of carriers perpendicular to the layer structure can be achieved very effectively by the use of a double heterojunction. This structure provides a well defined region, the active layer, where recombination occurs and the injected carriers are prevented from travelling far to other regions by the potential barriers at the heterointerfaces. Laser

performance is thus improved by confining the carriers to the active layer. Another effect of the structure arises from the fact that the refractive index of the cladding layer is lower than that of the active region, and this leads to good optical confinement of the laser mode. For stable fundamental mode operation with a low threshold current, additional confinement of the optical mode along the junction plane is required. Several laser structures realize the lateral confinement in different ways. These can in general be classified into two groups: gain-guided and index-guided and are shown in figure 2.3. In the gain-guided structure, the current injection is restricted to a narrow region along the junction plane, where optical gain exists. The width of the optical mode along this plane is mainly determined by the width of the optical gain region, thus yielding a gain-guide. Since variations of the gain and the refractive index are related to one another, a large gain corresponds to low refractive index [20], the gain-guided mechanism is accompanied by an anti-guiding action with respect to the refractive index. In index-guided lasers, a narrow central region of relatively higher refractive index in the junction plane confines the lasing mode to that region yielding a waveguide not only perpendicular to the active layer but also parallel to it. The index-guided lasers can be divided in two subgroups, weakly and strongly index guided. In weakly index guided lasers, the active region is continuous and an effective index discontinuity is provided by a cladding layer of varying thickness. The laser structure is modified so as to introduce an effective refractive index step of $\approx 10^{-2}$, which is larger than the carrier-induced reduction $\approx 5 \times 10^{-3}$. A number of structures, known as ridge waveguide, rib waveguide, plano-convex waveguide and channeled-substrate planar waveguide have been used [21]. A stronger lateral waveguide is obtained in strongly index guided lasers employing a buried heterostructure (BH). The active region is buried in higher bandgap layers (e.g., InP) on all sides. The lateral index step along the junction plane is ≈ 0.2 in these structures which is larger than the carrier-induced effects by two orders of magnitude. The BH structure, in addition, provides tight lateral carrier confinement.

Because of the better lateral optical confinement index-guided lasers have lower threshold currents which may be of the order of 10 mA for tight optical and electrical confinement, such as the BH-laser, compared with 100–150 mA for gain-guided. Also they are capable of operating in the fundamental lateral mode up to high powers. The superior performance of BH-lasers make them prime candidates for high-performance applications. However, bandwidth

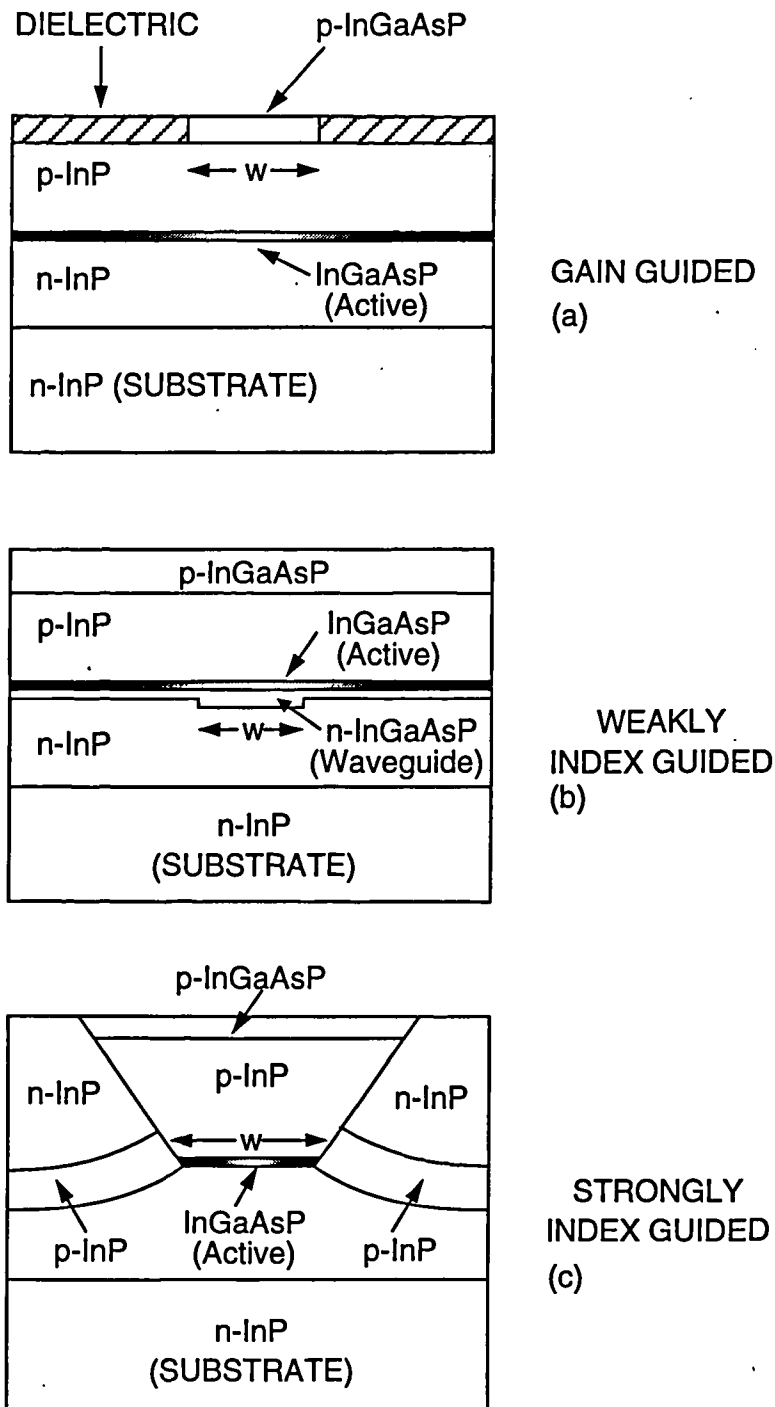


Figure 2.3: Cross section of three InGaAsP semiconductor laser structures: (a) Oxide-stripe laser; (b) Channelled-substrate planar waveguide; (c) Etched-mesa buried heterostructure. The active layer material (shaded area) has a smaller band gap and lower refractive index than the surrounding cladding layers.

limitation due to parasitics is a problem in BH-lasers, particularly for high speed modulation, such as microwave applications. This subject will be further discussed in section 3.5.

DFB lasers

In a Fabry-Perot laser the feedback is provided by the facet reflections whose magnitude remains the same for all longitudinal modes. The only longitudinal-mode discrimination is provided by the gain spectrum itself which is usually much wider than the mode spacing. As a result the mode discrimination is poor. This means that there are several modes exhibiting a gain only slightly smaller than the threshold gain of equation (2.14). Therefore, even if the laser is single-mode in CW-operation, such as the strongly-index guided laser, it may exhibit a multimode spectrum under modulation. In distributed feedback lasers (DFB) the mode selectivity is improved by making the feedback frequency dependent so that the cavity loss is different for different longitudinal modes. This is achieved through the use of a grating etched so that the thickness of one layer (in the heterostructure) varies periodically along the cavity length. This leads to a periodic perturbation of the refractive index which provides feedback by successively reflections of an optical travelling wave in the opposite direction. Mathematically, the reflection at the grating is considered by means of coupled wave equations. This analysis takes into account the coupling between forward and backward travelling waves [28] by introducing a coupling factor κ that determines the amount of feedback due to the grating structure. The threshold gain may be expressed in a similar way as for the Fabry-Perot laser

$$g_{th} = \alpha_m + \alpha_s \quad (2.19)$$

with the scattering loss α_s as in (2.14) and α_m is the cavity loss accounting for the power leaving the laser cavity. It has been shown that a DFB laser with a coupling strength of $\kappa L = 2$ (L is the cavity length) has the same threshold gain as a FP laser with facet reflectivities $R = 0.25$ [29]. The DFB laser may then be described by the rate equation approach derived in section 2.2.3. In fact the rate equations (2.15) and (2.17) are adequate for single-mode lasers but only describe the general behaviour of a multimode laser. These should be modified if phenomena such mode hopping and mode partition noise is to be studied [20, 21].

2.3 Single-mode rate equation model

2.3.1 Rate equations

The single-mode rate equations were introduced when discussing the dynamics of the semiconductor laser in section 2.2.3. Neglecting carrier diffusion these equations are:

$$\frac{dN}{dt} = \frac{J}{qd} - R_{st}P - \gamma_e N \quad (2.20)$$

$$\frac{dP}{dt} = \left[\Gamma R_{st} - \frac{1}{\tau_p} \right] P + \beta \Gamma R_{sp} \quad (2.21)$$

where R_{st} is the rate of stimulated emission at the peak value of the gain since the longitudinal mode closest to the peak gain reaches threshold first. Using a linear approximation (section 2.2.2), we get

$$R_{st} = g_0(N - N_{0m}) \quad (2.22)$$

with $g_0 = ac/\bar{\mu}$. The other symbols were introduced in the previous section. The effect of carrier diffusion and nonlinear gain will be discussed in the next section, R_{st} will then be modified accordingly.

These rate equations are sometimes written in the simple form [30, 31, 32, 33]

$$\frac{dN}{dt} = \frac{J}{qd} - R_{st}P - \frac{N}{\tau_s} \quad (2.23)$$

$$\frac{dP}{dt} = \left[\Gamma R_{st} - \frac{1}{\tau_p} \right] P + \beta \Gamma \frac{N}{\tau_s} \quad (2.24)$$

where τ_s is the spontaneous recombination lifetime. These equations are obtained based on the following approximations:

$$R_{sp} \simeq \frac{N}{\tau_s} \quad (2.25)$$

$$\gamma_e N = \frac{R_{sp}}{\eta_i(N_{th})} \simeq \frac{N}{\tau_s} \quad (2.26)$$

where the internal quantum efficiency, η_i , represents the fraction of injected carriers that recombine radiatively and generate photons given by the ratio of radiative to the total recombination rates. Strictly, equations (2.23) and (2.24) are valid for high doping levels compared to the injection levels ($R_{sp} \propto N$), as discussed in section 2.2.1, and when Auger recombina-

tion may be neglected in which case $\eta_i(N_{th}) \simeq 1$. The reasons for using the set of equations (2.23)–(2.24) are twofold. First, much of the work on laser nonlinear distortion modelling has been done using these equations [14, 15, 34]. Secondly, equations (2.20)–(2.21) are already a simplified model of a complex device, the semiconductor laser. Further simplification is justifiable if they do not lead to appreciably different results. It is not clear at the moment whether this is the case since the approximations involve neglecting a nonlinear dependence of the carrier recombination rate on the carrier density. If, however, τ_s is taken as the inverse of the carrier recombination rate at threshold $\tau_s^{-1} = \gamma_e(N_{th})$ the results obtained do not differ significantly, as shown in the next chapter, due to the carrier clamping effect above threshold. Although these equations may be slightly inaccurate below threshold they still provide a general description of the laser behaviour in this region. Whenever necessary we will refer back to equations (2.20) and (2.21).

Equations (2.20) and (2.21) describe the laser dynamics in a most basic manner. More detailed explanations of laser modulation can be obtained by addition and/or modification of the terms in these equations. Although extensively used the rate equations (2.20) and (2.21) are approximate equations that do not take into account the fact that the light actually propagates and bounces back and forth inside the laser cavity. The analysis of laser kinetics involving the coupled rate equations [35] leads to the conclusion that in the simple rate equations (2.20) and (2.21), N and P should be understood as spatially average quantities; they are valid if the electron density is uniform along the cavity length which holds for reflectivities larger than 0.2 [36, 35]. Common InGasAs Fabry-Perot lasers have a reflectivity of about 0.3 and are thus well within this limit. Another factor that can render the spatially uniform assumption invalid is when fast phenomena occurring on the time scale of the cavity transit time are considered. In the semiconductor laser the cavity length is typically 300 μm corresponding to a transit time of about 3.5 ps. The usual rate equations are therefore not applicable in describing phenomena shorter than about 5 ps or at modulation frequencies higher than 60 GHz.

2.3.2 Influence of carrier diffusion and nonlinear gain

As will be shown later, the laser exhibits a resonance in its modulation response. Several mechanisms are responsible for the damping of the resonance peak, one of which is the spontaneous emission factor β . It has been shown [35] that lasers with a tight optical confinement

in the transverse direction (strongly index-guided), such as the buried heterostructure, have a high value for β and consequently have a relatively weak relaxation oscillation. However, typical values of β around 10^{-4} are not sufficient to explain the damping observed experimentally. Therefore other mechanisms must be involved, and these include carrier diffusion and gain nonlinearities due to spectral hole burning, which can not be explained by the rate equations (2.20) and (2.21).

Lateral carrier diffusion

Tucker has shown [37] that a narrow strip laser, of width w , with strong carrier confinement with an effective diffusion length $L_{eff} > w$, which has a nonuniform electron density, can be reduced to an equivalent laser with uniform electron density but exhibiting optical gain saturation or compression. The gain may be written as

$$g_{st} = a(N - N_{0m})(1 - \epsilon P) \quad (2.27)$$

where ϵ is the gain compression factor given by

$$\epsilon = \frac{\Gamma g_0 \tau_s}{2 \left[1 + \left(\frac{2\pi L_{eff}}{w} \right)^2 \right]} \quad (2.28)$$

Assuming $L_{eff} = 3 \mu\text{m}$, $\tau_s = 2\text{ns}$, $\Gamma = 0.2$ and $g_0 = 2.2 \times 10^{12} \text{ m}^3\text{s}^{-1}$ yields

$$\epsilon = 5.4 \times 10^{-24} \text{ m}^3 \quad (2.29)$$

Nonlinear gain

The nonlinear gain may be understood as the gain difference between the gain at threshold, above which the carrier density should be clamped, and the actual gain under lasing conditions. For dynamic single-mode lasers (e.g. DFB lasers) spectral hole burning is an important phenomena responsible for the saturation of the dominant mode. To explain this effect consider a laser diode with nearly single-mode emission. The emission wavelength $\lambda_0(\nu_0)$ corresponds to a stimulated emission transition from the conduction band to the valence band with $h\nu_0 = E_2 - E_1$ (figure 2.1). The electron state 2 will then be depleted and the gain at the frequency ν_0 is reduced, yielding a gain depression around $\lambda = \lambda_0$. Spectral hole burning has been shown

to be stronger for InGaAsP than for GaAs. In Reference [38] a factor of 4 has been reported. Although the hole burning itself is relative weak small variations of gain affect considerably the dynamic characteristics and so gain suppression should be considered.

In [20] it is shown that equation (2.27) is also adequate for describing gain compression due to spectral hole burning. For InGaAsP lasers ϵ is now of the order of

$$\epsilon = 1 \times 10^{-23} \dots 10 \times 10^{-23} \text{ m}^3 \quad (2.30)$$

which is higher than the gain compression due to carrier diffusion as given by equation (2.28). The influence of carrier diffusion on laser dynamics is thus relatively low for very narrow stripe lasers. In any case the two effects can be included in the single-mode rate equations in the form of a gain compression. The rate equations (2.23) and 2.24) with gain compression in the form given by equation (2.27) will then constitute the basis for our laser modelling.

2.3.3 Steady-state characteristics

When a 'dc' current is applied to the laser, after some possible transient effects the laser will reach a steady-state in which fluctuations of the electron and photon densities are eliminated. Then $dN/dt = 0$, $dP/dt = 0$ and the steady-state populations N_0 and P_0 are reached. Neglecting gain compression the rate equation (2.21) yields the following photon density

$$P_0 = \frac{\beta \Gamma R_{sp}(N_0)}{1/\tau_p - \Gamma R_{st}(N_0)} \quad (2.31)$$

This equation states that the spontaneously emitted photons provide the noise input that is amplified in the presence of gain by the injected carriers. It is important to note that $R_{st}(N_0)$ cannot equal or be greater than $1/\tau_p$ because the photon density would be infinite negative. This means that the required optical gain is slightly below the cavity loss and approaches its asymptotic value $1/\tau_p$ as the output power increases. The carrier density at threshold is defined as the value of N for which the gain equals the loss

$$N_{th} = N_{0m} + 1/\Gamma g_0 \tau_p \quad (2.32)$$

If the injection current is not sufficient to yield this required gain, then the photon population must be very low. The threshold current may be estimated from (2.20) with $N = N_{th}$ and

$P = 0$. Neglecting spontaneous emission we get

$$I_{th} = qVN_{th}\gamma_e(N_{th}) \quad (2.33)$$

V being the cavity volume. The threshold current is required to obtain the threshold electron density N_{th} and any further current does not yield a further increase in the electron density, so that N may be considered to be clamped at N_{th} for $I > I_{th}$. Therefore, any injected electrons above threshold must contribute to the stimulated emission. The internal quantum efficiency must be very close to unity and the photon density becomes proportional to $(I - I_{th})$

$$P = \eta_i \frac{\Gamma \tau_p}{qV} (I - I_{th}) \quad (2.34)$$

The quantity of interest, the optical power emitted from each facet, may be obtained from the photon density by noting that photons escape the laser cavity at a rate $v_g \alpha_m$

$$P_{out} = \frac{h\nu v_g \alpha_m V P}{2\Gamma} \quad (2.35)$$

$$= \frac{V \eta_d h\nu P}{2\Gamma \eta_i \tau_p} \quad (2.36)$$

where h is Planck's constant and η_d is the differential quantum efficiency defined as

$$\eta_d = \eta_i \left[1 + \frac{2\alpha_s L}{\ln(1/R_1 R_2)} \right]^{-1} \quad (2.37)$$

2.4 Numerical solution of the rate equations

2.4.1 Normalization

In this section some solutions of the rate equations are discussed. It is convenient to normalize the various quantities in the rate equations (2.23) and (2.24) as follows:

$$t \equiv t/\tau_s \quad (2.38)$$

$$p = g_0 \tau_s P \quad (2.39)$$

$$n = g_0 \tau_p N \quad (2.40)$$

$$n_{0m} = g_0 \tau_p N_{0m} \quad (2.41)$$

$$j = g_0 \tau_s \tau_p (J/qd) \quad (2.42)$$

$$\varepsilon = \varepsilon/(g_0 \tau_s) \quad (2.43)$$

$$\gamma = \tau_s/\tau_p \quad (2.44)$$

We use the same letter t for the time variable but it is supposed to be a normalized variable as given by (2.38) when used in conjunction with the normalized variables n , p and j . Accordingly, equations (2.23) and (2.24) become

$$\frac{dn}{dt} = j - n - (n - n_{0m})(1 - \varepsilon p)p \quad (2.45)$$

$$\frac{dp}{dt} = \gamma \left[(\Gamma(n - n_{0m})(1 - \varepsilon p) - 1)p + \Gamma\beta n \right] \quad (2.46)$$

In terms of the normalized variables the steady-state solution corresponding to equation (2.31) becomes

$$p_0 = \frac{\beta n_0}{1/\Gamma + n_{0m} - n_0} \quad (2.47)$$

and the current and carrier population at threshold are

$$j_{th} \equiv n_{th} = 1/\Gamma + n_{0m} \quad (2.48)$$

2.4.2 Steady-state solution

The numerical solution of the steady-state rate equations will now be considered. Eliminating n_0 in equations (2.45) and (2.46) with $dn/dt = 0$ and $dp/dt = 0$ a third-order polynomial in p_0 is obtained

$$-p_0^3\varepsilon/\Gamma + [1/\Gamma + (j_0 - (1 - \beta)n_{0m})\varepsilon]p_0^2 + [1/\Gamma - j_0 + (1 - \beta)n_{0m}]p_0 - j_0\beta = 0 \quad (2.49)$$

which gives the dependence of p_0 with device current j_0 . Numerical results give three solutions with only one being physically meaningful. Once p_0 is found, n_0 can be determined by the relation

$$n_0 = \frac{j_0 - p_0/\Gamma}{1 - \beta} \quad (2.50)$$

Figure 2.4 shows the carrier density n_0/n_{th} as a function of j_0/j_{th} for a 1.3 μm InGaAsP laser with $\beta = 10^{-4}$, $\Gamma = 0.4$, $\varepsilon = 6.25 \times 10^{-3}$ and $n_{0m} = 2.4$ [31]. It is clear that when $j = j_{th}$ the normalized density n_0 is close to its asymptotic value. The variation of the photon density with j is shown in figure 2.5. Near threshold there is a rapid increase in the photon density. This sudden change indicates the stimulated emission has taken over the spontaneous emission. The sharpness of the transition, however, depends on β being sharper for lower

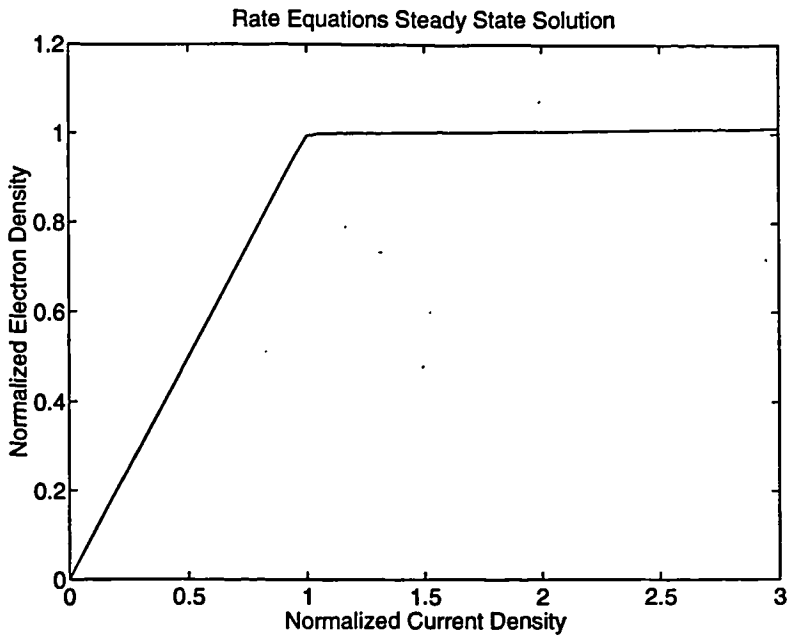


Figure 2.4: Normalized steady-state electron density as a function of current density.

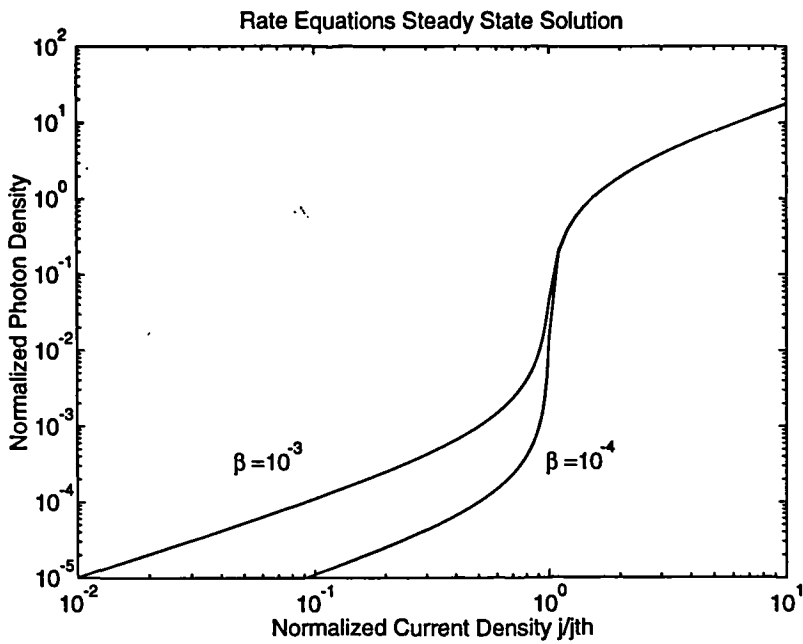


Figure 2.5: Normalized steady-state photon density as a function normalized current density for two values of β . Above threshold p_0 is a linear function of j_0

values of β . Comparing figures 2.4 and 2.5 it is seen that when the gain is close to the loss a small change in n can nonetheless produce a large change in p .

2.4.3 Transient response

Transient phenomena occur because of the time required for the electron and photon populations to come into equilibrium. Theoretical analysis shows how the large signal switching speed can be related directly to the small-signal bandwidth [32]. The rate equations can be used to model large-signal dynamic response but the complexity of this task often requires a numerical solution. Figures 2.6a and 2.6b show the transient response of a 1.3 μm BH laser to a current step. The laser parameters as in the previous section were taken from Reference [31]. The significance of the gain compression term of the laser response is also illustrated in figure 2.6b, which shows the laser response when gain compression is neglected.

These figures indicate that as the current initial value I_{off} is increased, the turn-on delay t_d , is reduced and the amplitude of the oscillations become smaller. If I_{off} is well below threshold the electron density is much smaller than the threshold density N_{th} and the photon density is small. The carrier density then satisfies the rate equation

$$\frac{dN}{dt} = \frac{I}{qV} - \gamma_e(N)N \quad (2.51)$$

The delay time depends on the functional form of the recombination rate $\gamma_e(N)$. In the presence of Auger recombination γ_e is a second-order polynomial and a closed form expression for t_d is difficult to obtain. In the simple approximation where γ_e is constant the result is [39]

$$t_d = \tau_s \ln \left(\frac{I_{on} - I_{off}}{I_{on} - I_{th}} \right) \quad (2.52)$$

In [40] an analytic expression for t_d is given when $\gamma_e = A_{nr} + BN$. This turn-on delay on the order of several nanoseconds, may be avoided if the laser is biased above threshold. In this case the turn-on time t_{on} is defined as the time required for the photon density to reach the final value P_{on} (figure 2.6b). Neglecting spontaneous emission ($\beta = 0$) and gain compression, which is valid for low and moderate output power, the turn-on time is [41, 32]

$$t_{on} = \frac{\sqrt{2}}{\omega_0} \left[\ln \left(\frac{P_{on}}{P_{off}} \right) \right]^{1/2} \quad (2.53)$$

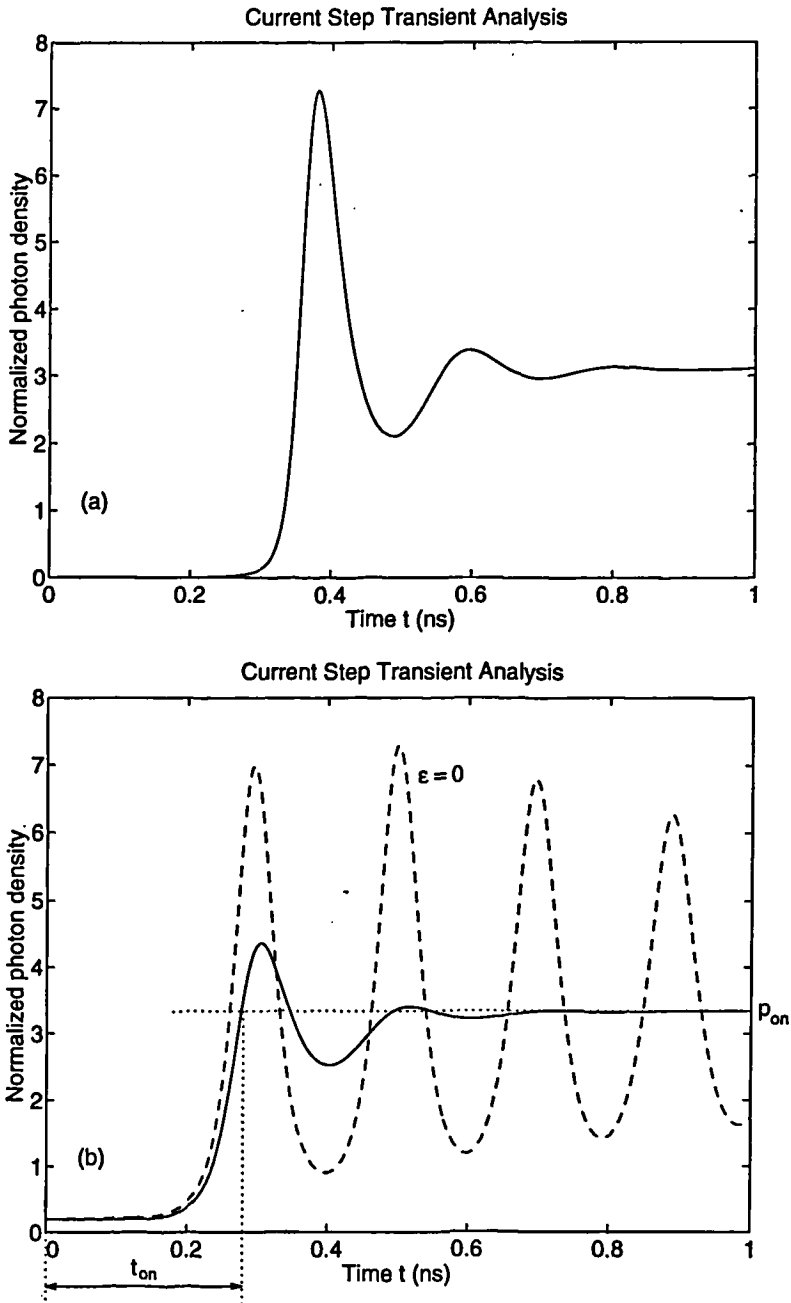


Figure 2.6: Laser large-signal turn-on response to a current step at $t = 0$ with 100 ps rise time and an amplitude of $2I_{th}$. (a) $I_{off}/I_{th} = 0.98$, (b) $I_{off}/I_{th} = 1.1$

with

$$\omega_0^2 = \frac{g_0}{\tau_p^2} (P_{on} - P_{off}) \quad (2.54)$$

being the relaxation resonance frequency at the on level. Usually, $P_{on} \gg P_{off}$ so that ω_0 can be approximated by

$$\omega_0 = \sqrt{g_0 P_{on} / \tau_p} \quad (2.55)$$

For a relaxation resonance $\omega_0/2\pi = 5$ GHz and an on-off ratio $P_{on}/P_{off} = 10$, one obtains $t_{on} = 70$ ps, which shows that low switching times are attainable if the laser diode is biased above threshold.

2.5 Intensity noise characteristics

In subcarrier multiplexed applications there are two important sources of noise that originate at the laser: relative intensity noise (RIN) and intermodulation distortion. The latter will be considered in the next chapter. Intensity noise embedded in a received signal directly degrades signal quality and thus system performance. An analysis of RIN is therefore required and will be here given.

2.5.1 Langevin formulation

At the most fundamental level, the origin of the laser intensity fluctuations lies in the quantum nature of the lasing process itself. An adequate description of this phenomena requires a quantum mechanical formulation of the rate equations [42, 43, 44, 45]. In the semiclassical approach, fluctuations arising from the spontaneous emission process and carrier-generation-recombination process are incorporated into the single-mode rate equations by adding a Langevin noise source [46]. Equations (2.20)–(2.21) then become

$$\frac{dN}{dt} = \frac{J}{qd} - R_{st}P - \gamma_e N + F_N(t) \quad (2.56)$$

$$\frac{dP}{dt} = \left[\Gamma R_{st} - \frac{1}{\tau_p} \right] P + \beta \Gamma R_{sp} + F_P(t) \quad (2.57)$$

In the presence of Langevin noise sources, N and P become random and these equations are called the stochastic rate equations. Physically F_N has its origin in the discrete nature of the carrier generation and recombination process (shot noise) whereas F_P arises from

spontaneous emission. Assuming the correlation time of the noise sources is much shorter than the relaxation times τ_p and γ_e^{-1} the Langevin noise sources satisfy the general relations [46, 47]

$$\langle F_P(t)F_N(t + \tau) \rangle = -2\beta R_{sp}(N_0)P_0\delta(\tau) \quad (2.58)$$

$$\langle F_N(t) \rangle = 0, \quad \langle F_P(t) \rangle = 0 \quad (2.59)$$

$$\langle F_N(t)F_N(t + \tau) \rangle = 2\left(\beta R_{sp}(N_0)P_0/\Gamma + \gamma_e(N_0)N_0/V\right)\delta(\tau) \quad (2.60)$$

$$\langle F_P(t)F_P(t + \tau) \rangle = 2\beta\Gamma R_{sp}(N_0)P_0\delta(\tau) \quad (2.61)$$

where $\langle \rangle$ denotes ensemble average and N_0 and P_0 are steady-state average values of the carrier and photon populations.

2.5.2 Intensity noise definition

The emitted optical power is assumed to exhibit noise, so that the time dependent photon density around the steady-state value P_0 is

$$P(t) = \langle P(t) \rangle + \delta P(t) \quad (2.62)$$

For a stationary signal $P_0 = \langle P(t) \rangle$ is time independent and $\langle \delta P(t) \rangle = 0$. The intensity noise at a given frequency is characterized by the relative intensity noise (RIN) defined as

$$RIN = \frac{S_p(\omega)}{P_0^2} \quad (2.63)$$

where $S_p(\omega)$ is the spectral density of the random process $\delta P(t)$

$$S_p(\omega) = \int_{-\infty}^{\infty} \langle \delta P(t + \tau)\delta P(t) \rangle e^{-i\omega\tau} d\tau \quad (2.64)$$

2.5.3 Analysis of RIN using the stochastic rate equations

In the small-signal analysis the rate equations with Langevin noise sources (2.56)–(2.57) are perturbed by a small amount δN and δP around the stationary values P_0 and N_0 . The rate equations are then linearized by neglecting the quadratic and higher powers of δN and δP which gives

$$\frac{d(\delta N)}{dt} = -\Gamma_N \delta N - (R_{st,0} + R_{st,P} P_0) \delta P + F_N(t) \quad (2.65)$$

$$\frac{d(\delta P)}{dt} = \Gamma_P \delta P + \Gamma (R_{st,N} P_0 + \beta R_{sp,N}) \delta N + F_P(t) \quad (2.66)$$

In obtaining the above equations the variables $R_{st}(N, P)$, $R_{sp}(N)$ and $\gamma_e(N)$ are expanded in a Taylor series

$$R_{st}(N, P) = R_{st,0} + R_{st,N} \delta N + R_{st,P} \delta P \quad (2.67)$$

$$R_{sp}(N) = R_{sp,0} + R_{sp,N} \delta N \quad (2.68)$$

$$\gamma_e(N) = \gamma_{e,0} + \gamma_{e,N} \delta N \quad (2.69)$$

where the notation $Y_{a,N(P)} = \partial Y_a(N, P) / \partial N(P)$, $Y_{a,0} = Y_a(N_0, P_0)$, has been used and

$$\Gamma_N = \gamma_{e,0} + \gamma_{e,N} N_0 + R_{st,N} P_0 \quad (2.70)$$

$$\Gamma_P = \Gamma (\beta R_{sp,0} / P_0 - R_{st,P} P_0) \quad (2.71)$$

are the small-signal decay rates of the photon and carrier populations, respectively. The solution of the linear set of equations (2.65)–(2.66) for the Fourier component $\bar{\delta}P(\omega)$ is

$$\bar{\delta}P(\omega) = \frac{(i\omega + \Gamma_N) \bar{F}_P + (R_{st,N} P_0 + \Gamma \beta R_{sp,N}) \bar{F}_N}{(i\omega + \Gamma_P)(i\omega + \Gamma_N) + (R_{st,N} P_0 + \Gamma \beta R_{sp,N})(R_{st,0} + R_{st,P} P_0)} \quad (2.72)$$

from which the spectral density may be calculated by the relation

$$S_P(\omega) = \langle |\bar{\delta}P(\omega)|^2 \rangle \quad (2.73)$$

Substituting equation (2.72) in (2.73) and using the relations (2.58)–(2.61) we obtain

$$RIN \simeq \frac{2\beta R_{sp,0} [(\omega^2 + \Gamma_N^2)\Gamma + R_{st,N}^2 P_0^2 (1/\Gamma + \gamma_{e,0} N_0 / \beta R_{sp,0} P_0 V)]}{P_0 [(\omega^2 - \omega_0^2)^2 + \omega^2 (\Gamma_N + \Gamma_P)^2]} \quad (2.74)$$

where

$$\omega_0^2 = (R_{st,N} P_0 + \Gamma \beta R_{sp,N})(R_{st,0} + R_{st,P} P_0) \quad (2.75)$$

$$\simeq \left(\frac{1 + \Gamma g_0 N_{0m} \tau_p}{\tau_s \tau_p} \right) \left(\frac{I_0}{I_{th}} - 1 \right) \quad (2.76)$$

Figure 2.7 shows the intensity-noise spectra at several bias currents for a 1.3 μm InGaAsP

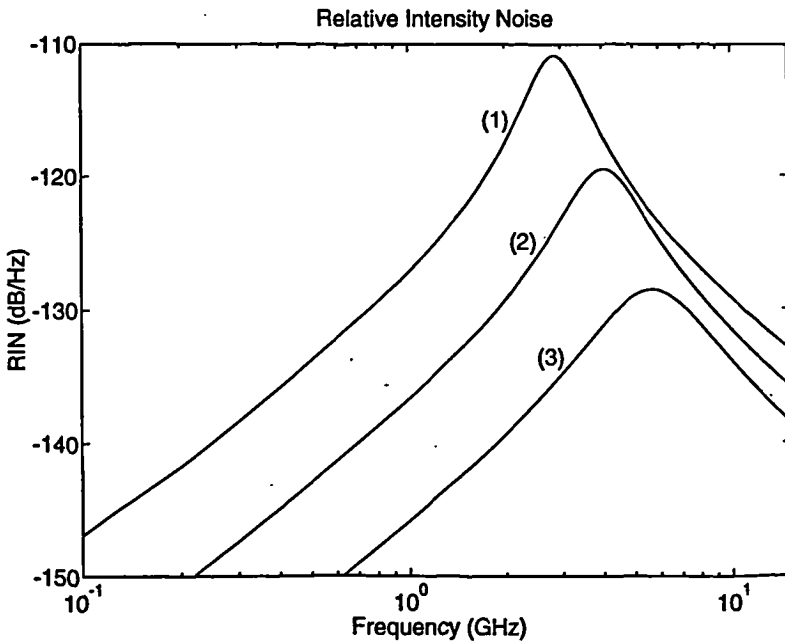


Figure 2.7: Relative intensity noise spectra at several bias currents: (1) $I_0/I_{th} \approx 1.5$, (2) $I_0/I_{th} = 2$, (3) $I_0/I_{th} = 3$. Laser parameters taken from Reference [31].

laser. The intensity noise is seen to peak at the resonance frequency ω_0 . Away from the resonance and at low power levels RIN decreases according to $RIN \propto P_0^{-3}$ or $RIN \propto (I_0 - I_{th})^{-3}$. At higher bias levels RIN varies more slowly approaching the $(I_0 - I_{th})^{-1}$ dependence.

2.5.4 Requirements of RIN for intensity modulated systems

Consider an analogue sinusoidal modulation with amplitude P_1 and average value P_0 : $P(t) = P_0 + P_1 \sin(2\pi ft)$. The noise is superimposed in the signal and a signal/noise ratio for a modulation bandwidth Δf may be defined as

$$SNR = \frac{P_1^2/2}{\langle \delta P^2 \rangle} = \frac{m^2 P_0^2}{2 \langle \delta P^2 \rangle} = \frac{m^2}{RIN \Delta f} \quad (2.77)$$

with $m = P_1/P_0$ the optical modulation depth. An improved SNR ratio is obtained with increasing modulation depth m . The maximum value for m will be limited by nonlinear distortion (chapter 3). Assuming a high quality TV (AM) transmission with a signal/noise ratio of 56 dB (electrical dB after the photodetector, $SNR = 10^{56/10}$), $m = 0.08$ and $\Delta f = 5$ MHz this yields a $RIN = -145$ dB/Hz. As seen in the previous section RIN is bias dependent and peaks at the resonance frequency. However, such a value for RIN is a stringent requirement

for laser diodes. Moreover RIN can be increased significantly in the presence of reflections, from fibre discontinuities (fibre connectors/splices), back to the laser or by multiple reflections between fibre discontinuities [48]. These phenomena can increase RIN by 10–20 dB, and so in analogue intensity modulated systems care must be taken to minimize these effects.

2.6 Summary

In this chapter the laser model, which will be used in subsequent chapters, was examined in some detail. The basic principles of laser diode operation were first presented. The radiative and non-radiative recombination mechanisms inside the laser cavity were discussed and the optical gain (stimulated emission) was related to the carrier density. The laser dynamic characteristics were then examined and the important aspects of laser structures were addressed. It was seen that the model should strictly be applied to strongly-index guided single-mode lasers. The model, can however, be applied to predict the general behaviour of multimode lasers. This model was further refined by considering gain compression. It was shown that carrier diffusion in strongly-index guided lasers and symmetric nonlinear gain (spectral hole burning) in dynamic single-mode lasers are some of the physical phenomena responsible for gain compression. Its effect on the transient response was noted. In the next chapter it will be shown that gain compression is an important factor in determining the damping of the relaxation oscillation resonance.

Finally, it was shown that laser relative intensity noise, due to spontaneous emission and the discrete nature of the carriers, is an important source of noise in analogue intensity modulated optical systems. To account for this noise in our model the rate equations have to be modified by the introduction of Langevin noise sources. An analytic procedure for the calculation of RIN from the stochastic single-mode rate equations was outlined which shows that RIN peaks at the resonance frequency and decreases with increasing bias level. Typical requirements of RIN for intensity modulated systems was also discussed. Another source of noise of great importance in subcarrier multiplexed systems is intermodulation distortion due to laser nonlinearity which will be discussed in the next two chapters.

Chapter 3

Nonlinear distortion in semiconductor lasers

3.1 Introduction

The direct modulation of the semiconductor laser is very attractive for the conversion of electrical analogue signals to optical. The reasons are its simplicity and the possibility to extend this conversion process to the microwave region. However, since the laser dynamics described by the rate equations are intrinsically nonlinear, harmonic and intermodulation distortion occurs during this process which limits system performance. Modelling of the semiconductor laser diode in such a way as to render tractable the accurate computation of intermodulation products (IMPs) is thus of importance for the design and dimensioning of such systems. In section 3.2 the impact of the intermodulation distortion in typical SCM systems is assessed and the origins of laser distortion will be presented in section 3.3. The frequency modulation characteristics of the laser diode will be first discussed (section 3.4) as they are intimately related to the nonlinear distortion. The same mechanism responsible for the intrinsic nonlinearity also gives rise to a resonance in the small-signal response. This is complemented by measurements of device characteristics using a commercially available laser diode. Model parameters are also extracted by fitting the measured data to the simulated results. In section 3.6 analytic techniques for the analysis of laser distortion based on the rate equation model will then be discussed. Perturbation analysis has been applied to the single-mode rate equations to obtain approximate expressions for second order IMPs and third order IMPs of the type $2f_i - f_j$ [14, 15]. Here the perturbation technique is extended to include the three-tone IMPs of type $f_i + f_j - f_k$ which dominate for a large number of

channels. The technique is then applied to assess laser nonlinear distortion. An alternative analytic approach has been reported [49] offering simple results accommodating an arbitrary number of carriers, although computational results have not been presented. In section 3.6.2 we extend this analysis to allow for laser relaxation resonance effects and show that to predict adequately the second order distortion a modified analysis must be used [17].

3.2 Intermodulation distortion in SCM systems

In subcarrier multiplexed systems the various electrical subcarriers are combined and used to modulate the laser diode. Because a semiconductor laser is a nonlinear device the various subcarriers are mixed within the laser cavity to form intermodulation products. Second and third-order distortion products are generated by every combination of two and three input frequencies, respectively. The interference resulting from source nonlinearity then depends strongly on the number of channels and the distribution of channel frequencies. Let us consider transmission of three channels (figure 3.1) with subcarrier frequencies f_1 , f_2 and f_3 . The third-

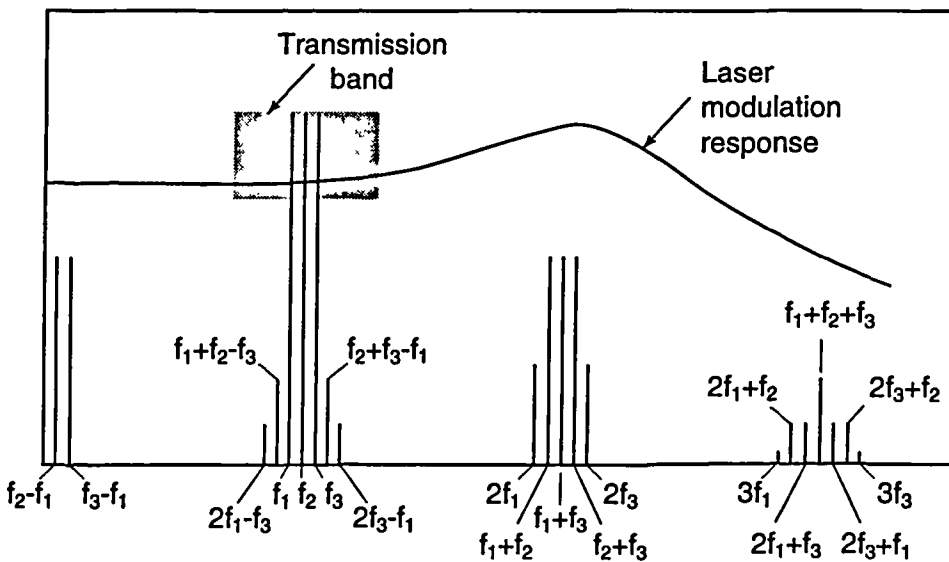


Figure 3.1: Intermodulation products and harmonics generated by a three-tone modulation of a laser diode.

order intermodulation distortion products (IMPs) at frequencies $f_i + f_j - f_k$ and $2f_i - f_j$ will certainly lie within the transmission band leading to interchannel interference. For a N channel system with uniform frequency spacing the number of IMPs, IM_{2i}^N and IM_{11i}^N of type

$2f_i - f_j$ and $f_i + f_j - f_k$, respectively, coincident with channel r are given by [50]

$${}_rIM_{21}^N = \frac{1}{2} \left\{ N - 2 - \frac{1}{2} [1 - (-1)^N (-1)^r] \right\} \quad (3.1)$$

$${}_rIM_{111}^N = \frac{r}{2} (N - r + 1) + \frac{1}{4} [(N - 3)^2 - 5] - \frac{1}{8} [1 - (-1)^N] (-1)^{N+r} \quad (3.2)$$

Figure 3.2 shows the total number of third-order IMPs as a function of channel number each curve representing a different number of channels. For large N , ${}_rIM_{111}^N$ approaches the asymptotic value of $3N^2/8$ for the central carrier. For SCM systems occupying a bandwidth of more than one octave, the second-order nonlinear distortion will also have to be considered in which the most important terms are of type $f_i \pm f_j$.

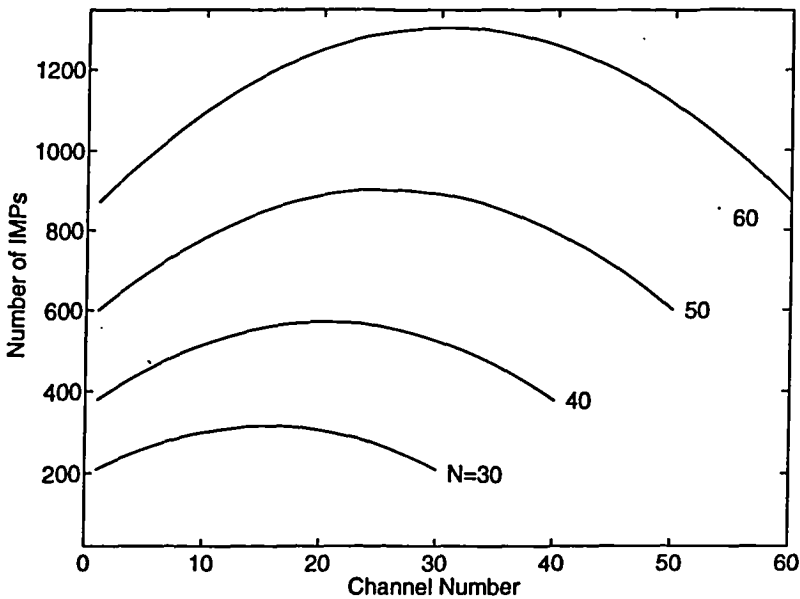


Figure 3.2: Total number of third-order intermodulation products as a function of channel number with the number of channels, N as a parameter.

Table 3.1 compares the number of IMPs and the linearity requirements of typical demonstration SCM systems [51, 2, 52, 3, 53]. Given the number of distortion products and the required carrier-to-noise ratio (CNR) the maximum magnitude of each type of product can be obtained. These numbers, which include a 10 dB margin, should be understood as an estimate because they not include the frequency dependence of the distortion. For directly modulated AM systems the relatively number of second-order products are generally more troublesome than the higher number of third-order products due to their higher amplitude. Also the high

CNR required, 50 dB, compared to 17 dB of the bidirectional and FM systems, imposes greater restrictions on laser linearity. It will be seen in the following chapters that laser distortion peaks at the resonance frequency and so AM systems should operate at low frequencies where the linearity is greater.

	Bidirectional System (FSK)	FM Video	AM-VSB Video
# channels	8x180 Mb/s	60x30 MHz	42x4 MHz
Bandwidth (MHz)	280	30	4
Freq. Range (GHz)	2.5-5.0	2.4-4.8	0.05-0.40
Max. Product Count			
$f_i \pm f_j$	0	0	27
$f_i \pm f_j \pm f_k$	15	1276	576
CNR Required (dB)	17	17	50
Linearity Required (dB)			
$f_i \pm f_j$	-	-	-74
$f_i \pm f_j \pm f_k$	-39	-58	-88

Table 3.1: Linearity requirements of typical subcarrier multiplexed systems.

3.3 Origins of laser nonlinear distortion

In the semiconductor laser, distortion can be divided in two types: static and intrinsic dynamic nonlinearity. Usually one type of nonlinearity is dominant depending on the system frequency range of operation. For low modulation frequencies, below a few hundreds of megahertz, distortions are introduced mainly due to the imperfect linearity of the static light-power versus current (L-I) characteristic. This nonlinearity can be caused by leakage currents [21, 54] and is usually modelled using a power series expansion of the laser curve around the bias point [3]. The optical power of a second and third-order IMP relative to the fundamental carrier are then proportional to (d^2L/dI^2) and (d^3L/dI^3) , respectively. The leakage current effects can also be included in the rate equations by making the current through the active layer

a nonlinear function of the total injected current. This requires accurate modelling of the electrical equivalent circuit of the laser chip [4, 55]. The advantage is to have a complete model which includes both static and dynamic nonlinearity.

With increasing modulation frequency the distortion increases rapidly caused by the nonlinear interaction between the photons and the injected carriers. This same nonlinear coupling is responsible for the relaxation oscillation resonance and so this distortion is denoted as intrinsic dynamic distortion or resonance distortion. This effect is well described by the rate equations as given in the previous chapter. Using a small-signal analysis of the rate equations (section 3.6.1) Lau and Yariv [14, 56] have calculated the two-tone third-order IMPs $2f_i - f_j$. Their results were later extended to InGaAsP lasers [15] and measurements have been given that show good agreement with theory [16]. The results given are however restricted to two closely spaced microwave carriers. However, as shown previously, for a larger number of channels the three-tone IMPs $f_i + f_j - f_k$ are dominant. Analytic techniques are therefore required that enable us to assess these distortion products for an arbitrary number of channels. Here the perturbation technique will be extended to include the three-tone distortion products. A reported alternative technique based on the expansion of Bessel functions will also be considered [49].

Recently it has been shown that spatial hole burning in DFB lasers may play an important role in determining the nonlinear distortion at low frequencies [57]. Spatial hole burning is caused by the coupling between the DFB grating and the active region creating a non-uniform distribution of the light intensity along the laser axis, which is power dependent [58]. This effect has been shown to be responsible not only for an additional nonlinearity of the laser curve but also for the gain and loss (threshold gain) above threshold becoming power dependent [59, 60]: that is modulation of the photon-lifetime, τ_p , occurs. The single-mode rate equations are then modified by the introduction of additional gain and loss suppression factors in a similar way as has been done in section 2.3.2 for the case of spatial hole burning. These factors however are themselves power dependent, resulting in additional distortion. For directly modulated SCM systems operating in the high frequency region (> 1 GHz), such as the FM systems, only the intrinsic dynamic nonlinearity of the laser needs to be considered since it is the dominant nonlinear mechanism. For directly modulated lasers at frequencies operated by AM systems (table 3.1) leakage current and SHB should be considered, by modification of

the single-mode rate equations. Finally, if the L-I nonlinearity is eliminated and the dynamic resonance frequency is infinite, then the allowed modulation depth is limited by clipping. Below the threshold current the light output is zero and larger excursions in the modulation current produce distortion which limits the modulation depth per channel to about 5% for a carrier-to-noise ratio of 55 dB [61].

3.4 High-frequency modulation characteristics

The same mechanism responsible for the intrinsic nonlinearity also gives rise to the relaxation oscillations of figure 2.6. Since the photon and carrier lifetimes differ by about three orders of magnitude ($\tau_p \ll \tau_s$), considerable oscillation occurs. These oscillations set an upper limit for the modulation bandwidth of semiconductor lasers. Here the important small-signal characteristics of directly modulated lasers will be discussed and in section 3.6 these will be related to the laser nonlinear distortion.

3.4.1 Small-signal response

The small-signal response can be obtained from the the normalised single-mode rate equations (2.45)–(2.46). A laser diode is considered with a sinusoidal modulation of the injected current around the bias level j_0 according to

$$j(t) = j_0 + j^\omega e^{i\omega t} \quad (3.3)$$

where $\omega = 2\pi f$ is the angular frequency. Note that since t is here normalised by τ_s , ω must also be normalised relative to $1/\tau_s$. Under the small-signal condition ($j^\omega \ll j_0$) the rate equations may be linearized and the electron and photon densities also vary harmonically

$$n(t) = n_0 + n^\omega e^{i\omega t} \quad (3.4)$$

$$p(t) = p_0 + p^\omega e^{i\omega t} \quad (3.5)$$

The laser response is conveniently described by the transfer function $H_1(\omega)$ defined as the ratio of the photon density p^ω to the perturbed current j^ω . After substitution of (3.3)–(3.5) into (2.45)–(2.46) and solving for the ratio p^ω/j^ω the transfer function $H_1(\omega)$ can be expressed

approximately as [32]

$$\frac{H_1(\omega)}{H_1(0)} = \frac{\gamma(1 - \epsilon p_0)p_0}{(i\omega)^2 + i\omega(\gamma\Gamma\beta j_{th}/p_0 + \gamma\epsilon p_0) + \gamma(1 - \epsilon p_0)p_0} \quad (3.6)$$

$$= \frac{1}{\left(\frac{i\omega}{\omega_0}\right)^2 + \frac{i\omega}{\omega_d} + 1} \quad (3.7)$$

Important parameters can now be identified, such as ω_0 the relaxation oscillation frequency, the damping frequency ω_d and the damping coefficient δ which completely determine the laser modulation characteristics

$$\omega_0^2 = \gamma(1 - \epsilon p_0)p_0 \simeq \gamma p_0 \quad (3.8)$$

$$\omega_d = \omega_0^2/\delta \quad (3.9)$$

$$\delta = \gamma\Gamma\beta j_{th}/p_0 + \gamma\epsilon p_0. \quad (3.10)$$

In order to obtain a large modulation bandwidth the relaxation resonance should be as large as possible which may be achieved for large p_0 . For sufficiently large photon density the damping

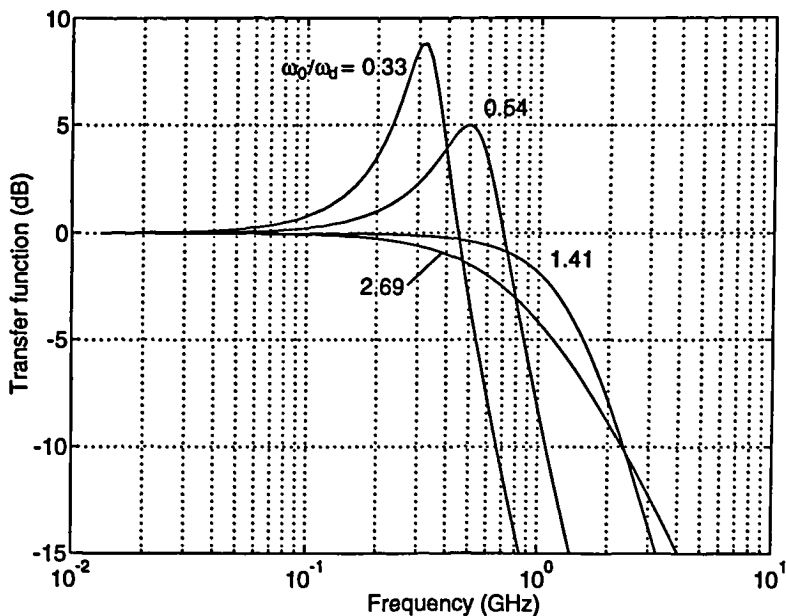


Figure 3.3: Small-signal transfer function of a ridge-waveguide laser [31], with ω_0/ω_d as a parameter.

frequency is nearly independent of p_0 since the damping coefficient becomes $\delta \simeq \gamma\epsilon p_0$

yielding for ω_d

$$\omega_d = 1/\epsilon \quad (3.11)$$

Figure 3.3 illustrates the general form of the transfer function against frequency with ω_0/ω_d as parameter. The frequency of the resonance peak is ω_p , the height of the peak is $M_p = H_1(\omega_p)/H_1(0)$ and the 3 dB roll-off frequency is ω_{-3dB} . At low and moderate output power levels $\omega_0/\omega_d < 0.5$ a resonance peak occurs at $\omega_p \simeq \omega_0$. With increasing ω_0/ω_d this resonance peak is less pronounced and disappears at $\omega_0 = \sqrt{2}\omega_d$. At this point, ω_{-3dB} saturates at its maximum value of $\sqrt{2}\omega_d$ yielding a maximum flat response (second-order Butterworth). Further increase in ω_0 slowly decreases ω_{-3dB} resulting in a -3 dB-bandwidth of $\omega_{-3dB} = \omega_d$. The maximum achievable bandwidth is therefore $\sqrt{2}\omega_d$.

3.4.2 Relaxation oscillation damping

The damping coefficient δ controls the damping of the resonance. If the damping coefficient is small the height of the resonance peak is large and the frequency ω_p is close to ω_0 . If the damping coefficient is large the height of the peak is reduced and $\omega_p \neq \omega_0$. The first term in the damping coefficient $\gamma\Gamma\beta j_{th}/p_0$ arises from spontaneous emission and the second term $\gamma\epsilon p_0$ from gain compression. Figure 3.4 shows the magnitude of the peak height M_p as a function of bias current for a InGaAsP ridge-waveguide laser [31]. At low bias (low p_0) the resonance peak is small due to the dominant spontaneous emission term in the damping coefficient. For bias currents above $I_0/I_{th} \simeq 1.2$, the peak height decreases due to increasing gain compression. In between, a maximum enhancement of the relaxation oscillation occurs. Also shown in figure 3.4 is the peak height for zero gain compression ($\epsilon = 0$). At high bias M_p now rises to a value of 25 dB indicating that gain compression is an important factor in determining the damping of the laser resonance.

3.4.3 High frequency limits

The ultimate modulation bandwidth of a laser diode is limited by the damping frequency when driven considerably above threshold. According to 3.11 and in terms of unnormalised variables we get

$$\omega_d = \frac{g_0}{\epsilon} \quad (3.12)$$

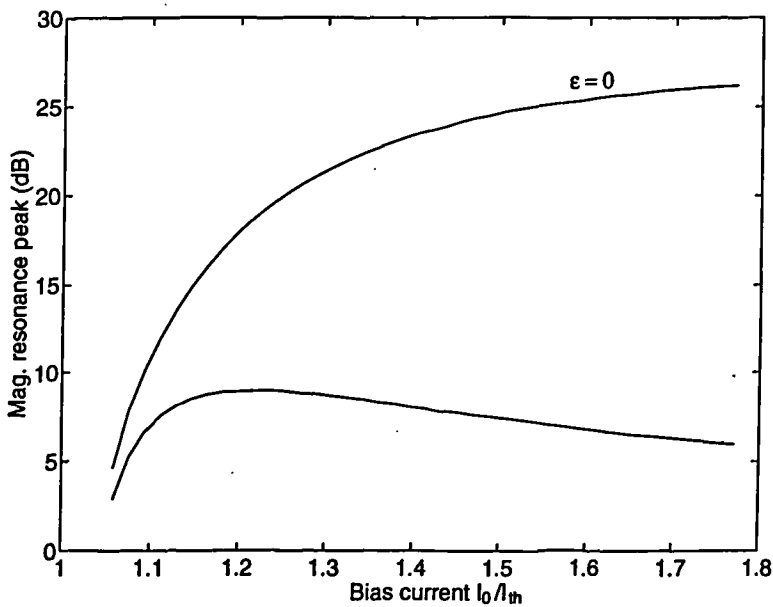


Figure 3.4: Magnitude of the resonance peak height (M_p) for a InGaAsP ridge-waveguide laser

This equation represents a fundamental limitation for laser diode modulation, since it involves only material properties of the laser active region. Assuming $g_0 = 2.9 \times 10^{-12} \text{ m}^3 \text{ s}^{-1}$ and $\epsilon = 2.5 \times 10^{-23} \text{ m}^3$ [33] equation (3.12) yields

$$f_d = \omega_d/2\pi \approx 18 \text{ GHz} \quad (3.13)$$

which represents an estimate for the maximum modulation frequency of dynamic single-mode lasers. Modulation bandwidths of about 13 GHz have been obtained for DFB lasers [62]. Larger bandwidths may be obtained for a lower gain compression which may occur for multimode lasers [63]. Another possibility is the increase of g_0 by operating the laser diode at low temperatures [30] or by using quantum well laser structures [21].

3.5 Laser characterization and extraction of model parameters

So far the problem of modelling the semiconductor laser has been addressed and its modulation characteristics have been given. An important aspect is the extraction of parameters capable of predicting measured data. Laser parameters are commonly extracted from the small-signal

frequency response [31, 33, 48]. Here parameters will be obtained for a $1.3 \mu\text{m}$ multimode laser diode (Ortel 1510B) designed for microwave applications. If the package and chip parasitics are small enough to not become band-limiting, only the intrinsic laser diode model need be used. The laser is specified to operate above 6 GHz and at these frequencies the parasitics have to be considered.

3.5.1 Package and chip parasitics model

When dealing with high frequency electronics the frequency limits are usually established by the parasitics elements. It is then required to know whether the laser modulation characteristics are due to the laser alone or due to the parasitics elements. For this one must treat the laser as an electrical element and establish an equivalent circuit for it together with the parasitics elements. Characterization of an electrical network at high frequencies is usually done with S-parameters.

Let us consider the equivalent circuit of the intrinsic laser diode. The elements of laser equivalent circuit are derived from the rate equations augmented by the heterojunction voltage-current and space-charge characteristics. The resulting equivalent circuit is a parallel RLC resonant circuit [64, 31]. The carrier density and quasi-Fermi levels are clamped above threshold which manifests in the equivalent circuit as an “ac” short and no voltage can develop. The magnitude of the impedance of the entire circuit $|Z(\omega)|$ is therefore essentially zero at all frequencies except near the relaxation oscillation resonance, where its value does not exceed $\approx 1 \Omega$. For deriving the relation between the total external current I_s and the current through the active region I_a and in comparison to the relatively large external elements, the intrinsic laser diode can be regarded as a short circuit at all frequencies. Under zero bias the intrinsic laser can be modelled by the active layer space-charge capacitance [64].

Chip parasitics vary widely among different laser structures. In practice they take the form of a resistance in series with the intrinsic device combined with a shunt capacitance [32, 30]. An equivalent circuit model of the package and chip parasitics is shown in figure 3.5. R_s is the resistance in series with the active region, C_s the shunt capacitance between the metal contacts and R_{sub} is the substrate resistance. L_{pi} , R_{pi} and C_{pi} are the bond-wire inductance, associated resistance and shunt capacitance to ground. Z_{01} and Z_{02} are the characteristic impedances of the transmission lines with an electrical length $\theta = \pi/2$ at f_{01} and f_{02} , respectively.

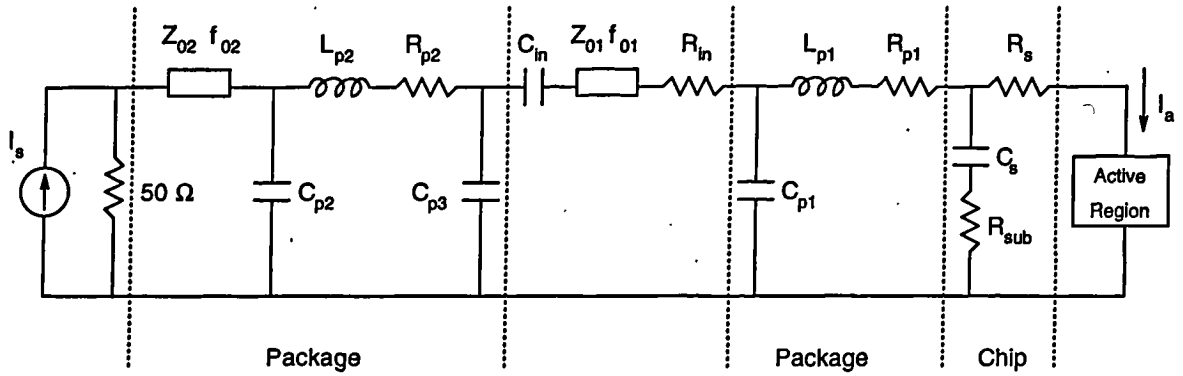


Figure 3.5: Equivalent circuit model of package and chip parasitics

3.5.2 Determination of parasitics and laser intrinsic parameters

With the aim of extracting values for the parasitics of the network of figure 3.5 and intrinsic parameters of the laser diode under consideration, measurements of the microwave S-parameter S_{11} (reflection coefficient) and the modulation frequency response were carried out at various frequencies using the lightwave component analyzer HP8703A. In the second set of measurements care was taken to minimise the light reflected back to the laser by the use of an optical isolator. The intrinsic and parasitic parameters were then obtained by computer-aided fitting of the calculated data to the measured data using the constraint optimization routine (CONSTR) of the Matlab-Optimisation Toolbox software package. The optimisation procedure followed a two step iteration approach now described. First, values for the parasitics were initially estimated and then optimised to match the measured S_{11} data, without consideration of the laser frequency response. Although a good fit for S_{11} may be possible this does not necessarily provide the correct transfer function from the input signal current to the current through the active region I_a/I_s unless the assumed circuit of figure 3.5 contains all the major elements in the right topology. Therefore, the second step consisted in fitting the laser intrinsic parameters to the modulation response for a range of bias currents but allowing C_s , R_s , C_{p1} and L_{p1} to vary simultaneously with the additional constraint that the threshold current given by (2.33) coincided closely with the measured value of 15 mA. Step 1 was then repeated but now fixing the values of C_s , R_s , C_{p1} and L_{p1} obtained in step 2. A final optimisation of $H_1(f)$ was then effected with the parasitic elements all fixed. The result of the optimisation gives the element values and intrinsic laser parameters listed in tables 3.2 and 3.3, respectively. The modelled and measured S_{11} -parameter and input impedance in the frequency range of 1–8 GHz, above

threshold, are shown in figure 3.6. A good fitting is obtained over this frequency range.

Element	Units	Value
C_{p1}	pF	3.0
L_{p1}	nH	0.14
R_{p1}	Ω	1.5
R_{sub}	Ω	1.5
C_s	pF	5.6
R_s	Ω	6
C_{p2}	pF	0.2
L_{p2}	nH	1.3
R_{p2}	Ω	0.5
C_{p3}	pF	0.46
Z_{01}	Ω	48.4
f_{01}	GHz	3.8
Z_{02}	Ω	50.5
f_{02}	GHz	5.13
R_{in}	Ω	58.5
C_{in}	pF	1800

Table 3.2: Parasitic element values for the equivalent circuit of figure 3.5.

The calculated frequency response of the electrical parasitics, shown in figure 3.7, gives the frequency dependence of the current I_a injected into the active region relative to the signal current source I_s . The overall modulation response is obtained by multiplying the intrinsic response of the laser diode by the ratio I_a/I_s . At frequencies below 4 GHz the transfer function of the electrical parasitics I_a/I_s is dominated by the shunt capacitance $C_s = 6$ pF and the series resistance $R_s = 5.6 \Omega$. The RC product is 33.6 ps, which corresponds to a -3 dB cutoff frequency of 4.7 GHz. Therefore, for signal below 4 GHz the electrical parasitics can be neglected. Capacitor C_{p1} and inductor L_{p1} lead to a resonance at 7.7 GHz above which the transfer function falls rapidly with a roll-off of 18 dB/octave.

Figure 3.8 shows the measured and simulated laser frequency response at two bias currents for frequencies up to 10 GHz. A good agreement is obtained between the experimental and modelled data. A feature of the response is the occurrence of a dip at frequencies below

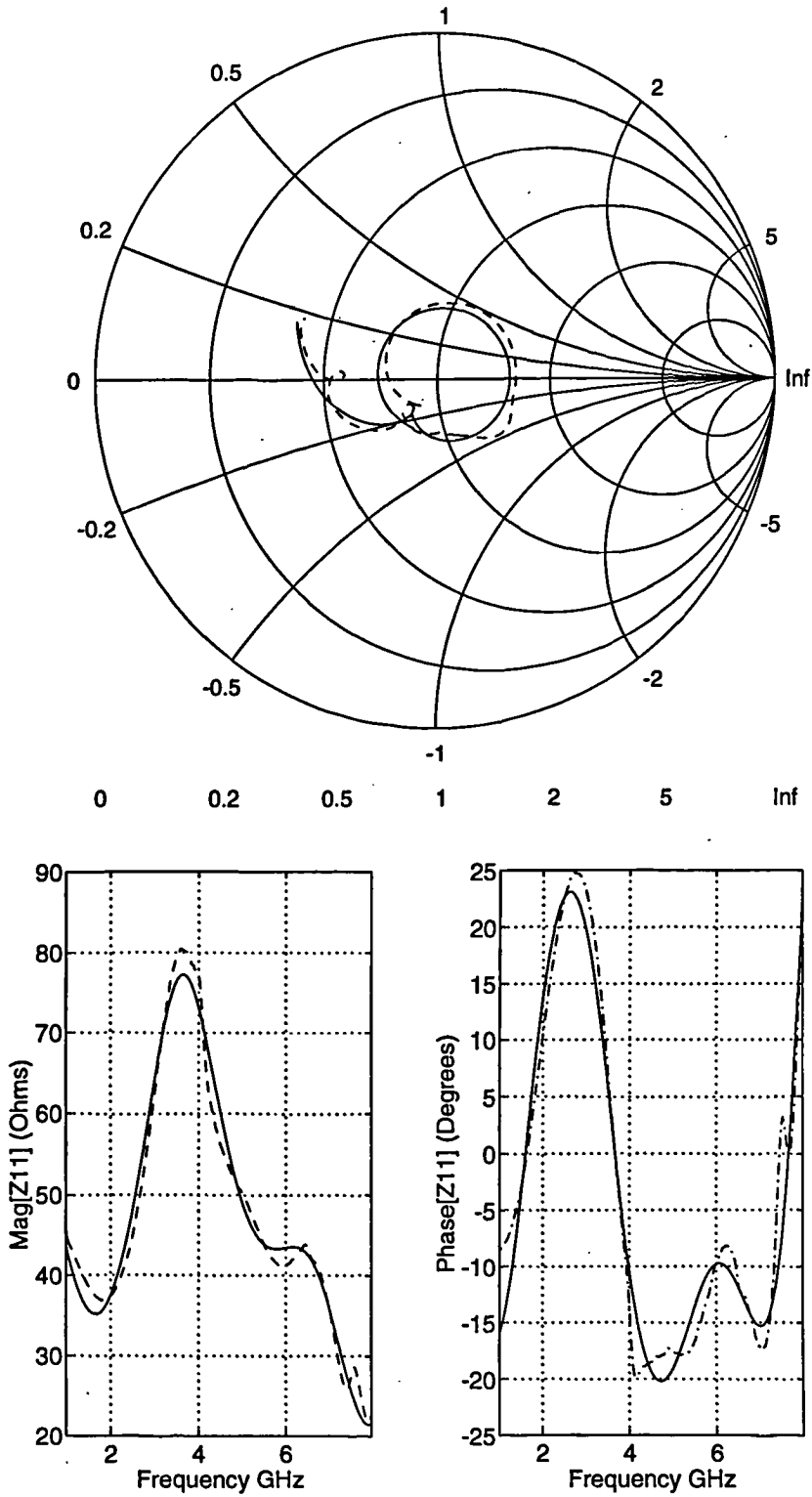


Figure 3.6: Measured and simulated results of (a) reflection coefficient (S_{11} -parameter) and (b) input impedance of parasitics equivalent circuit in the frequency range of 1–8 GHz.

----- Measured
 ——— Simulated

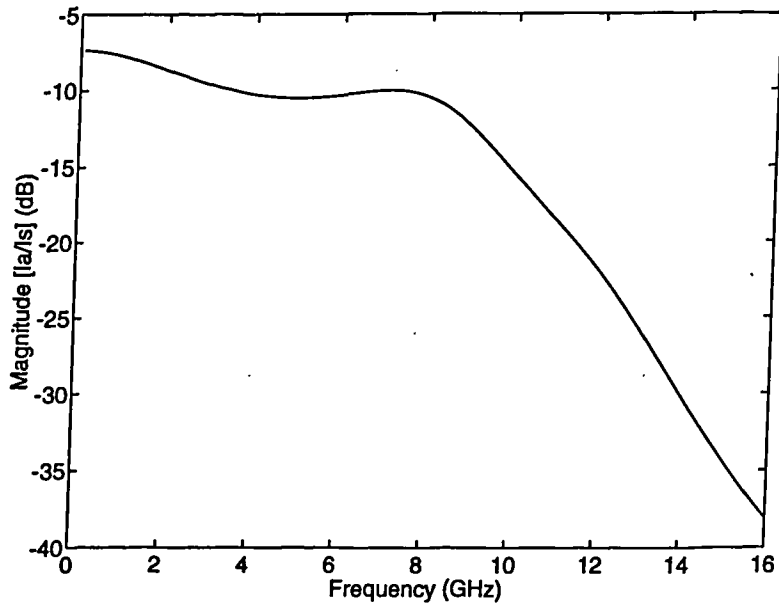


Figure 3.7: Frequency response of the laser package and chip parasitics.

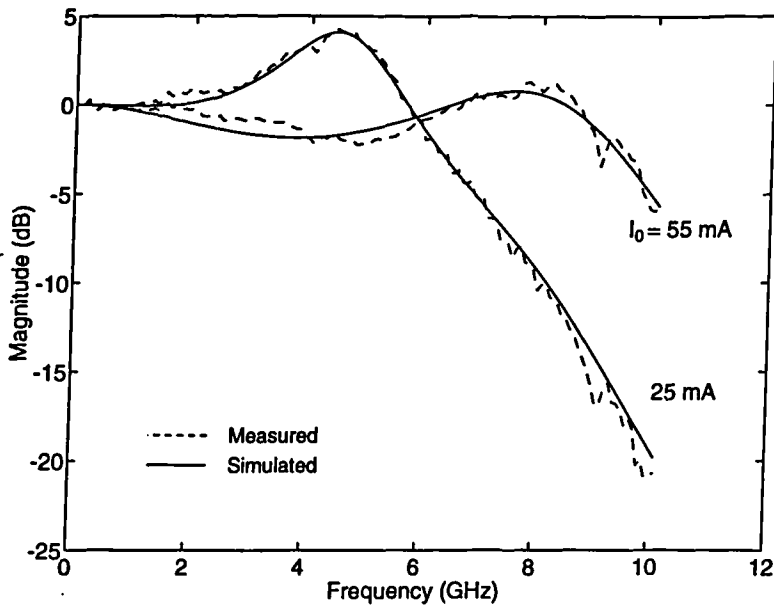


Figure 3.8: Measured and modelled small-signal frequency response of the laser diode Ortel-1510B.

$T = 22^\circ\text{C}$

$I_{th} = 15\text{ mA}$

Parameter	Units	Value
qV	Am^3s	1.28×10^{-35}
β	-	2×10^{-3}
Γ	-	0.36
ϵ	m^3	3.2×10^{-23}
g_0	m^3s^{-1}	3.4×10^{-12}
N_{0m}	m^{-3}	1.27×10^{24}
τ_s	ns	1.65
τ_p	ps	1.0
I_{th}	mA	16

Table 3.3: Parameter values for the laser diode Ortel-1510B.

the resonance frequency which is due to the parasitics. Also a relatively large value for β is obtained which agrees with the multimode nature of the laser [35].

3.6 Analysis of laser nonlinear distortion

The analysis of laser distortion will be based on the rate equation model presented in chapter 2. This model can only predict laser intrinsic distortion and so is valid for frequencies above a few hundreds of megahertz as explained above. The exact region of validity will depend on the location of the laser resonance frequency relative to the system transmission band. However, the analytic techniques given are general. Once the rate equations are modified to include leakage current and spatial hole burning effects, responsible for distortion at lower frequencies, the analysis can be applied to systems operating in this region.

3.6.1 Perturbation solution of the rate equations

Here the normalised rate equations (2.45) and (2.46) will be analysed using a perturbation technique [65]. The input current is considered to be split into a “dc” term and a time varying one. A pair of differential equations for the perturbed electron and photon densities is obtained in terms of the steady-state values. The quantities of interest are written as follows

$$j(t) = j_0 + j_1 \quad (3.14)$$

$$n(t) = n_0 + n_1 + n_2 + n_3 + \dots \quad (3.15)$$

$$p(t) = p_0 + p_1 + p_2 + p_3 + \dots \quad (3.16)$$

where n_0 and p_0 are the steady-state solutions to the “dc” current j_0 , which are assumed to be time independent. The subscripts here refer to the perturbation order. These equations are useful as long as the required number of terms is small. Since we are interested in the laser distortion up to third-order only the first four terms in the expansion are considered. This is valid if the perturbing current, electron and photon densities are small compared to their respective steady-state values, that is, for the small-signal case. Substituting (3.14), (3.15) and (3.16) into the rate equations (2.45) and (2.46) gives for zero order

$$j_0 - n_0 - (n_0 - n_{0m})(1 - \varepsilon p_0)p_0 = 0 \quad (3.17)$$

$$\Gamma(n_0 - n_{0m})(1 - \varepsilon p_0)p_0 - p_0 + \Gamma\beta n_0 = 0 \quad (3.18)$$

The equations of order k can be written compactly as

$$\frac{dn_k}{dt} = -\left\{[(1 - \varepsilon p_0)p_0 + 1]n_k + (n_0 - n_{0m})(1 - 2\varepsilon p_0)p_k + D_k\right\} \quad (3.19)$$

$$\frac{dp_k}{dt} = \gamma\Gamma\left\{[(1 - \varepsilon p_0)p_0 + \beta]n_k + [(n_0 - n_{0m})(1 - 2\varepsilon p_0) - 1/\Gamma]p_k + C_k\right\} \quad (3.20)$$

where C_k and D_k are the driving force terms given by

$$D_1 = -j_1, \quad C_1 = 0 \quad (3.21)$$

$$D_2 \equiv C_2 = (1 - 2\varepsilon p_0)n_1 p_1 - (n_0 - n_{0m})\varepsilon p_1^2 \quad (3.22)$$

$$D_3 \equiv C_3 = (1 - 2\varepsilon p_0)(n_2 p_1 + n_1 p_2) - 2(n_0 - n_{0m})\varepsilon p_1 p_2 - \varepsilon n_1 p_1^2 \quad (3.23)$$

The equations defining the zero-order perturbation determine the steady-state solution previously examined in section 2.4.2. Equations (3.19) to (3.23) can be used to evaluate the time dependence of the electron and photon densities up to third-order.

Intermodulation distortion

The perturbation solution of the rate equations will now be examined when the injected signal current is given by three sinusoids at frequencies ω_1 , ω_2 and ω_3

$$j(t) = j_0 + \text{Re} \left\{ j^{\omega_1} e^{i\omega_1 t} + j^{\omega_2} e^{i\omega_2 t} + j^{\omega_3} e^{i\omega_3 t} \right\} \quad (3.24)$$

The laser output power will contain higher-order harmonics as well as intermodulation products. Neglecting fourth and higher-order terms, the perturbation for the normalised electron and photon densities are written as

$$n_k = \frac{1}{2} \sum_{\omega} \left[n^{\omega} e^{i\omega t} + (n^{\omega})^* e^{-i\omega t} \right] \quad (3.25)$$

$$p_k = \frac{1}{2} \sum_{\omega} \left[p^{\omega} e^{i\omega t} + (p^{\omega})^* e^{-i\omega t} \right] \quad (3.26)$$

$$k = 1, \quad \omega = \omega_1, \omega_2, \omega_3$$

$$k = 2, \quad \omega = 2\omega_1, 2\omega_2, 2\omega_3, \omega_1 \pm \omega_2, \omega_1 \pm \omega_3, \omega_2 \pm \omega_3$$

$$k = 3, \quad \omega = 2\omega_1 - \omega_2, 2\omega_2 - \omega_1, 2\omega_1 - \omega_3, 2\omega_2 - \omega_3, 2\omega_3 - \omega_2, \\ \omega_1 + \omega_2 - \omega_3, \omega_1 + \omega_3 - \omega_2, \omega_2 + \omega_3 - \omega_1.$$

By substitution of (3.24–3.26) into equations (3.19) and (3.20) and equating equal terms in $e^{i\omega t}$, the perturbation analysis gives a set of coupled linear equations corresponding to the seventeen output frequency components

$$i\omega n^{\omega} = - \left\{ [(1 - \varepsilon p_0) p_0 + 1] n^{\omega} + (n_0 - n_{0m})(1 - 2\varepsilon p_0) p^{\omega} + D^{\omega} \right\} \quad (3.27)$$

$$i\omega p^{\omega} = \gamma \Gamma \left\{ [(1 - \varepsilon p_0) p_0 + \beta] n^{\omega} + [(n_0 - n_{0m})(1 - 2\varepsilon p_0) - 1/\Gamma] p^{\omega} + C^{\omega} \right\} \quad (3.28)$$

where the driving terms D^{ω} and C^{ω} are given in table 3.4. Solving (3.27) and (3.28) for p^{ω} the amplitudes of the output components for photon density are obtained

$$p^{\omega} = \begin{cases} \gamma \Gamma [(1 - \varepsilon p_0) p_0 + \beta] / \varphi(\omega), & \text{for } \omega = \omega_1, \omega_2, \omega_3 \\ \gamma \Gamma [i\omega + 1 - \beta] D^{\omega} / \varphi(\omega), & \text{for the other cases} \end{cases} \quad (3.29)$$

where

$$\varphi(\omega) = \psi(\omega) \chi(\omega) + \gamma \Gamma [(1 - \varepsilon p_0) p_0 + \beta] (n_0 - n_{0m}) (1 - 2\varepsilon p_0) \quad (3.30)$$

$$\psi(\omega) = i\omega + (1 - \varepsilon p_0) p_0 + 1 \quad (3.31)$$

$$\chi(\omega) = i\omega - \gamma \Gamma (n_0 - n_{0m}) (1 - 2\varepsilon p_0) + \gamma \quad (3.32)$$

ω	D^ω
ω_i	$-j^{\omega_i}$
$2\omega_i$	$\frac{1}{2}[c_1 n^{\omega_i} p^{\omega_i} - c_2 \varepsilon (p^{\omega_i})^2]$
$\omega_i - \omega_j$	$\frac{1}{2}\{c_1 [n^{\omega_i} (p^{\omega_j})^* + (n^{\omega_j})^* p^{\omega_i}] - 2c_2 \varepsilon p^{\omega_i} (p^{\omega_j})^*\}$
$\omega_i + \omega_j$	$\frac{1}{2}\{c_1 [n^{\omega_i} p^{\omega_j} + n^{\omega_j} p^{\omega_i}] - 2c_2 \varepsilon p^{\omega_i} p^{\omega_j}\}$
$2\omega_i - \omega_j$	$\frac{1}{2}\{c_1 [n^{\omega_i} p^{\omega_i - \omega_j} + n^{\omega_i - \omega_j} p^{\omega_i} + (n^{\omega_j})^* p^{2\omega_i} + n^{2\omega_i} (p^{\omega_j})^*]$ $- [2c_2 \varepsilon p^{\omega_i} p^{\omega_i - \omega_j} + (p^{\omega_j})^* p^{2\omega_i}]$ $- \frac{\varepsilon}{2} [(n^{\omega_j})^* p^{2\omega_i} + 2n^{\omega_i} p^{\omega_i} (p^{\omega_j})^*]$
$\omega_i + \omega_j - \omega_k$	$\frac{1}{2}\{c_1 [n^{\omega_i} p^{\omega_j - \omega_k} + n^{\omega_j} p^{\omega_i - \omega_k} + (n^{\omega_k})^* p^{\omega_i + \omega_j}$ $+ p^{\omega_i} n^{\omega_j - \omega_k} + p^{\omega_j} n^{\omega_i - \omega_k} + (p^{\omega_k})^* n^{\omega_i + \omega_j}]$ $- 2c_2 \varepsilon [p^{\omega_i} p^{\omega_j - \omega_k} + p^{\omega_j} p^{\omega_i - \omega_k} + (p^{\omega_k})^* p^{\omega_i + \omega_j}]$ $- \varepsilon [n^{\omega_i} p^{\omega_j - \omega_k} + n^{\omega_j} p^{\omega_i - \omega_k} + (n^{\omega_k})^* p^{\omega_i + \omega_k}]\}$

Table 3.4: Driving terms; C^ω equals zero for $\omega = \omega_{1,2,3}$ and D^ω for the other cases. $c_1 = 1 - 2\varepsilon p_0$, $c_2 = n_0 - n_{0m}$.
 $i, j, k = 1, 2, 3$ and $i \neq j \neq k$.

From the previous equations it is seen that the same factor $\varphi(\omega)$ responsible for the resonance in the laser modulation response (section 3.4) will also determine the distortion levels. The damping mechanisms of the laser then turn out to be very important. Differences in the distortion levels among different lasers with the same ω_0 have been explained almost entirely by variations in gain compression [15]. Lasers with strong damping will exhibit superior distortion characteristics. However, equation (3) of Reference [15] for the amplitude of the IMP of type $2f_i - f_j$ is valid only for devices in which ε/g_0 is small compared with τ_p [66]. A more accurate expression for two closely spaced frequencies ($\omega_1 \simeq \omega_2 = \omega$) is

$$\frac{p^{2\omega_1 - \omega_2}}{p^{\omega_1}} \simeq m^2 \frac{\left\{ \left[(\omega/\omega_0)^4 - (\omega/\omega_0)^2/2 \right]^2 + \left[(\tau_p + \varepsilon/g_0)\omega^3/\omega_0^2 \right]^2 \right\}^{1/2}}{2H_1(\omega)H_1(2\omega)} \quad (3.33)$$

where m is the optical modulation depth per-channel defined as the ratio of half the peak-to-peak modulated light intensity to the light intensity at bias level. In figure 3.9 we show the second-order harmonic distortion and third-order distortion for a ridge-waveguide laser [31] with $\tau_p = 1$ ps, $\varepsilon/g_0 = 20$ ps and $f_0 = \omega_0/(2\pi) = 3$ GHz. The solid line corresponds to the exact solution of the perturbation technique, the dashed line to equation (3) of [15] and the

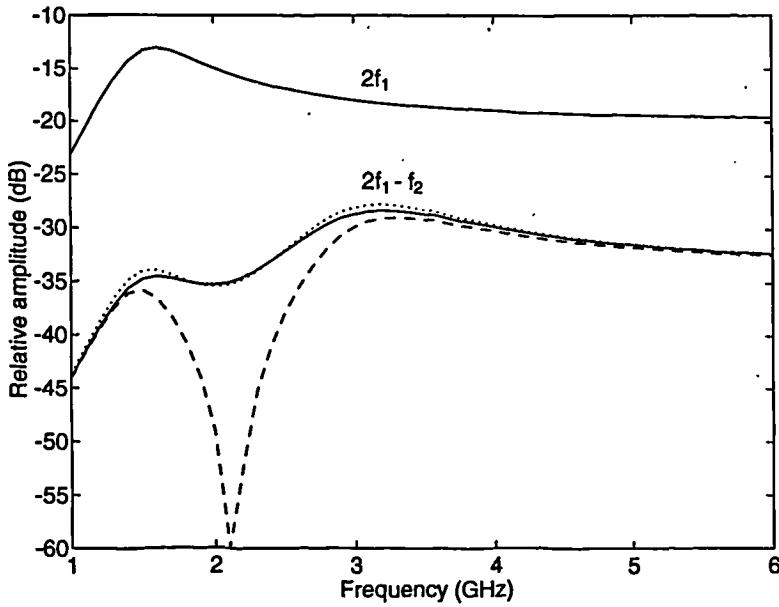


Figure 3.9: Second harmonic and intermodulation distortion levels for a ridge-waveguide laser [31] with $\tau_p = 1$ ps, $\epsilon/g_0 = 20$ ps and $f_0 = \omega_0/(2\pi) = 3$ GHz: comparison between the exact solution of the perturbation technique, eqn. (3) of [15] and eqn. (3.33).

- exact solution
- eqn. (3) of [15]
- eqn. (3.33)

and the dotted line to equation (3.33). Significant differences exist namely a null at 2.1 GHz which would only be observed using (3.33) with a much smaller value of ϵ ($\approx 1.0 \times 10^{-24}$ m³). From figure 3.9 it is seen that both second harmonic and third-order intermodulation distortion have maxima near the resonance frequency, and third-order distortion also peaks at f_0 . For closely spaced frequencies the three-tone IMP ($f_i + f_j - f_k$) is higher than the two-tone IMP ($2f_i - f_j$) by 6 dB. The dependence of the intermodulation distortion on channel spacing will be discussed in the next chapter.

Effect of Auger recombination on nonlinear response

In section 2.3 a simplified rate equation model for the laser diode was given that neglects nonradiative mechanisms the most important of which is the Auger recombination. The affect of this approximation on the laser nonlinear response will now be examined by comparing the more exact solution with the approximated solution. The results given here correspond to a 1.3 μ m BH laser with parameters taken from [21]. The spontaneous lifetime τ_s is now taken

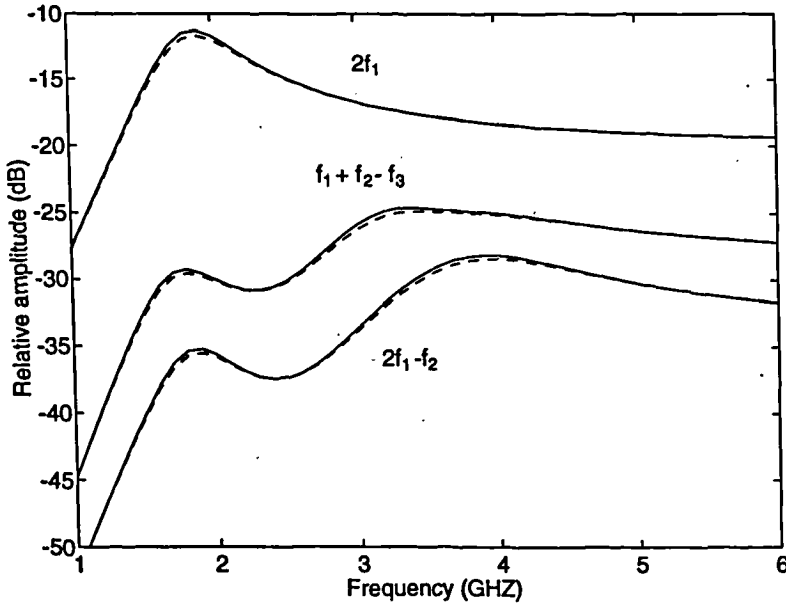


Figure 3.10: Effect of neglecting nonradiative mechanisms in the laser model: the difference is less than 0.4 dB. Parameters were taken from [21] with $m = 0.3$, $f_1 = 2$ GHz, $f_2 = 2.2$ GHz and $f_3 = 2.4$ GHz.

- including Auger recombination
- neglecting nonradiative mechanisms

as the inverse of the carrier recombination rate at threshold

$$\tau_s^{-1} \equiv \gamma_e(N_{th}) = A_{nr} + BN_{th} + CN_{th}^2 \quad (3.34)$$

With $A_{nr} = 1 \times 10^8 \text{ s}^{-1}$, $B = 1 \times 10^{-16} \text{ m}^3 \text{ s}^{-1}$, $C = 3 \times 10^{-41} \text{ m}^6 \text{ s}^{-1}$ and $N_{th} = 2.14 \times 10^{24} \text{ m}^{-3}$ the spontaneous lifetime is $\tau_s = 2.2$ ns. The set of equations (2.20)–(2.21) and (2.23)–(2.24) give slightly different output power levels for the same input current. Since the optical modulation depth is the quantity of interest, in obtaining the results given in figure 3.10 the “dc” current is adjusted so that the mean output power is the same in both cases. $I_0 = 30$ mA for equations (2.20)–(2.21) and $I_0 = 30.2$ mA for the simplified rate equations (2.23)–(2.24) ($I_{th} = 15.8$ mA). The optical modulation depth is 0.3. Figure 3.10 shows that the distortion levels in both cases are almost identical the difference being less than 0.4 dB. Therefore, the simple set of equations (2.23)–(2.24) can be used without loss of accuracy to predict laser nonlinear distortion.

3.6.2 Bessel function expansion

An alternative analytic approach to the perturbation technique has been reported [49] offering simple results accommodating an arbitrary number of carriers, although computation results have not been presented. Here we extend this analysis to allow for laser relaxation resonance effects and show that to predict adequately the second order distortion a modified analysis must be used.

Starting with the normalised rate equations (2.45)–(2.46) the second order differential equation for the photon density is given approximately by

$$\frac{d^2 p}{dt^2} + \frac{dp}{dt} \left[-\frac{1}{p} \frac{dp}{dt} + \gamma \varepsilon p + p + 1 \right] + p \gamma [\Gamma(n_{om} - j) + p + 1] = 0 \quad (3.35)$$

All the symbols have been defined previously. This equation differs from the corresponding equation in Reference [49] only in the term $\gamma \varepsilon p (dp/dt)$ which arises from gain compression. Consider for simplicity a single subcarrier $j(t) = j_0 + j \cos \omega t$ and following Reference [49] by adopting the transformation

$$p = C e^u \quad (3.36)$$

equation (3.35) becomes

$$\frac{d^2 u}{dt^2} + \omega_0^2 \left\{ \frac{du}{dt} \left[\frac{(\gamma \varepsilon + 1) C e^u + 1}{\omega_0^2} \right] + \left[\frac{\gamma C e^u}{\omega_0^2} - 1 \right] - \zeta \cos \omega t \right\} = 0 \quad (3.37)$$

where the following relations have been used:

$$\gamma [\Gamma(j_0 - n_{om}) - 1] \simeq \omega_0^2 \quad (3.38)$$

$$\zeta = \frac{j}{j_0 - j_{th}} \quad (3.39)$$

and j_{th} is the normalised threshold current. Again following [49] an approximate solution of the form

$$u = \alpha_1 \cos(\omega t + \theta_1) \quad (3.40)$$

may be assumed. Substitution of (3.40) in (3.37) yields [67]:

$$C = \frac{p_0}{I_0(\alpha_1)} \quad (3.41)$$

$$\alpha_1 \frac{\omega^2}{\omega_0^2} - 2 \frac{I_1(\alpha_1)}{I_0(\alpha_1)} + \zeta \cos \theta_1 = 0 \quad (3.42)$$

$$\omega \left[\frac{\alpha_1}{\omega_0^2} + 2(\varepsilon + 1/\gamma) \frac{I_1(\alpha_1)}{I_0(\alpha_1)} \right] + \zeta \sin \theta_1 = 0 \tag{3.43}$$

where $I_n(\alpha_1)$ is the modified Bessel function of order n . The photon density is then

$$p = p_0 + \frac{2p_0}{I_0(\alpha_1)} \sum_{m=1}^{\infty} I_m(\alpha_1) \cos(m\omega t + m\theta_1) \tag{3.44}$$

The system of equations (3.42) and (3.43) may be solved in the small signal regime corresponding to α_1 close to zero. Figure 3.11 shows the results of the numerical solution. The parameter values adopted are: laser resonance $f_0 = 4.3$ GHz ($j_0 = 14.04$), $\gamma = 3000$, $\varepsilon = 6.98 \times 10^{-3}$, $\zeta = 0.435$ and $j_{th} = 6.53$. With α_1 determined the harmonic amplitudes

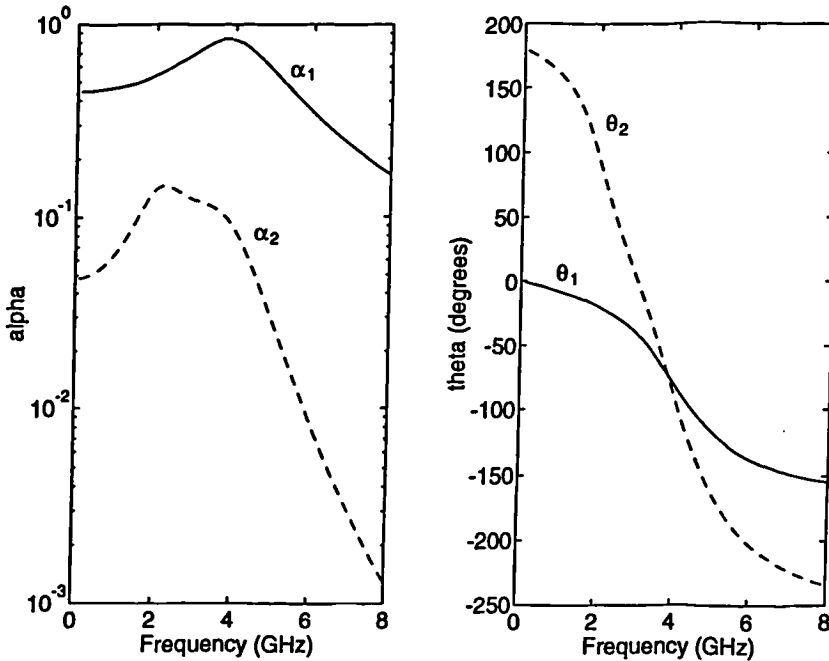


Figure 3.11: Numerical solution of the set of equations (3.42)–(3.43) and (3.47)–(3.48).

may be found from (3.44) as

$$m_{th} \text{ harmonic} = 2p_0 \frac{I_m(\alpha_1)}{I_0(\alpha_1)} \tag{3.45}$$

To assess the adequacy of this analytic approach figure 3.12 provides plots versus frequency of the fundamental and the second harmonic distortion amplitudes, comparing these with values determined by direct simulation and a perturbation analysis.

It is clear that equation (3.40) based on Reference [49], provides only a first-order approximation and so is inappropriate in its present form for performance assessment of multichannel

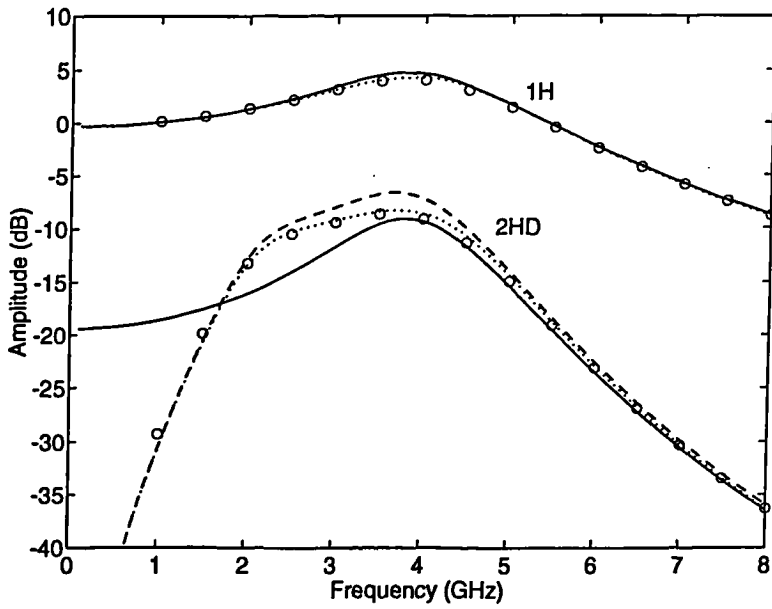


Figure 3.12: Fundamental and second harmonic amplitudes: comparison between eqn. (3.45), eqn. (3.50), perturbation analysis and direct simulation.

- eqn. (3.45)
- - - eqn. (3.50)
- perturbation analysis
- ooo simulation

systems. The approach may be appropriately refined though, by recognising that u must contain higher order terms

$$u = \alpha_1 \cos(\omega t + \theta_1) + \alpha_2 \cos(2\omega t + \theta_2) + \dots \tag{3.46}$$

For simplicity of illustration we will present here only the second-order extension. Analytic manipulation and neglecting terms above second-order yields:

$$2\alpha_2 \frac{\omega^2}{\omega_0^2} + 2\omega \left(\varepsilon + \frac{1}{\gamma} \right) \frac{I_2(\alpha_1)}{I_0(\alpha_1)} \sin(2\theta_1 - \theta_2) - \frac{I_2(\alpha_1)}{I_0(\alpha_1)} \times \cos(2\theta_1 - \theta_2) - \frac{I_1(\alpha_2)}{I_0(\alpha_2)} = 0 \tag{3.47}$$

$$\alpha_2 \frac{\omega}{\omega_0^2} + 2\omega \left(\varepsilon + \frac{1}{\gamma} \right) \left[\frac{I_2(\alpha_1)}{I_0(\alpha_1)} \cos(2\theta_1 - \theta_2) + \frac{I_1(\alpha_2)}{I_0(\alpha_2)} \right] + \frac{I_2(\alpha_1)}{I_0(\alpha_1)} \sin(2\theta_1 - \theta_2) = 0 \tag{3.48}$$

with α_1 and θ_1 still given by equations (3.42), (3.43). Using (3.36) the photon density is then

$$p \simeq p_0 + \frac{2p_0}{I_0(\alpha_1)} \sum_{k=1}^{\infty} I_k(\alpha_1) \cos(k\omega t + k\theta_1) + \frac{2p_0}{I_0(\alpha_2)} \sum_{l=1}^{\infty} I_l(\alpha_2) \cos(2l\omega t + l\theta_2) \quad (3.49)$$

and the second harmonic amplitude, is given by:

$$2\text{HD} = 2p_0 \left\{ \left[\frac{I_2(\alpha_1)}{I_0(\alpha_1)} \cos(2\theta_1) \frac{I_1(\alpha_2)}{I_0(\alpha_2)} \cos(\theta_2) \right]^2 + \left[\frac{I_2(\alpha_1)}{I_0(\alpha_1)} \sin(2\theta_1) + \frac{I_1(\alpha_2)}{I_0(\alpha_2)} \sin(\theta_2) \right]^2 \right\}^{1/2} \quad (3.50)$$

The dashed line of figure 3.12 shows the much improved agreement equation (3.50) provides with direct simulation and perturbation analysis. Since higher-order harmonics and IMPs may be similarly determined, the analytic refinement of [49] presented here represents an appropriate, albeit rather more involved, means of assessing analytically the influence of laser nonlinearities on the performance of multichannel subcarrier multiplexed systems.

3.7 Summary

The modulation and nonlinear distortion characteristics of the semiconductor laser were examined. The frequency modulation response of the laser was obtained in the small-signal case and parameters responsible for the damping of the relaxation oscillation resonance were identified. These parameters, spontaneous emission and gain compression, also determine the distortion levels and so are very important. Characterization of a commercially available laser diode for microwave applications has also been carried out which involved measurements of the reflection coefficient and the laser small-signal response. From these measurements model parameters for the chip and package equivalent circuit and laser intrinsic parameters have been extracted by fitting the measured data to the simulated results.

The problem of modelling laser nonlinear distortion was then addressed. Two analytic techniques were discussed. The perturbation technique was here extended to include the intermodulation products of type $f_i + f_j - f_k$ which were seen to dominate in a system with a large number of channels. A reported analytic technique [49] based on the expansion of Bessel functions was shown to be inappropriate to assess laser distortion, providing only a first-order

approximation. We explain how this analysis must be modified to predict adequately higher-order distortion products. The modified technique, although appropriate for the assessment of laser distortion and the performance of subcarrier multiplexed systems is rather more involved. Tractable analytic techniques that will enable us to assess the performance of complex multichannel SCM system are therefore required. Such a technique will be the subject of the next chapter.

Chapter 4

Volterra series analysis

4.1 Introduction

Signal distortion occurs in communication systems when the amplitude $|H(f)|$ and phase $\phi(f)$ of a linear network transfer function $H(f) = |H(f)|e^{i\phi(f)}$ are frequency dependent functions. This type of distortion is called “linear distortion”. Besides this type of distortion other deviations can occur if the system possesses nonlinear elements. In this case, the system can not be described by a single transfer function as in the linear case; instead the output, $y(t)$, is often expressed as a nonlinear function of the input $x(t)$, that is, $y(t) = T[x(t)]$. The resulting type of distortion is called “nonlinear distortion”.

Another important concept in nonlinear theory is the concept of a “memoryless nonlinearity” which occurs when the output signal is an instantaneous function of its input. As a consequence the distortion is frequency independent, as opposed to a nonlinearity with “memory” where the distortion is frequency dependent. For this latter case and when the distortion is weak, the nonlinearity is best represented by a Volterra functional series.

In the previous chapter it became clear that the frequency dependence of laser nonlinearity relates to the relaxation oscillation resonance and that accurate yet tractable techniques are required to model laser induced distortion in a multichannel system. Here we will show that Volterra series can be applied to assess laser nonlinearity (section 4.2) and that this provides a means of assessing accurately the performance of SCM systems (section 4.4). The nonlinear transfer functions, which completely characterize the semiconductor laser in the frequency domain, are determined in section 4.3. Finally analytic results are compared with direct simulation when the laser is modulated by three carriers; these are shown to match very

closely. The dependence of distortion on channel spacing is also given.

4.2 Volterra series: frequency domain analysis

The response of a linear system to an excitation $x(t)$ can be expressed by the convolution integral

$$y(t) = \int_{-\infty}^{\infty} h(\tau)x(t - \tau) d\tau \quad (4.1)$$

where $h(t)$ is the impulse response. Volterra series provides an extension of this theory to weakly nonlinear systems having small excitations. The conditions imposed ensure that the required number of terms in the expansion is small.

The semiconductor laser is then viewed as a nonlinear system with memory where the output $p = p_0 + p(t)$, the normalised photon density, relates to the input $j = j_0 + j(t)$, the normalised current density, by the functional

$$p(t) = T[j(t)] \quad (4.2)$$

continuous in all values, where p_0 and j_0 are the corresponding steady-state values. This functional can be represented by its Volterra expansion, which is of the form

$$p(t) = \sum_{n=1}^{\infty} p_n(t) \quad (4.3)$$

$$p_n(t) = \int_{-\infty}^{\infty} \cdots \int_{-\infty}^{\infty} h_n(\tau_1, \dots, \tau_n) \prod_{r=1}^n j(t - \tau_r) d\tau_r \quad (4.4)$$

This representation is useful when the required number of terms is small and thus is applicable to the small-signal nonlinear case. In equation (4.4) the multidimensional function $h_n(\tau_1, \dots, \tau_n)$ is the n th-order kernel or the n th-order laser nonlinear impulse response. Just as the linear transfer function is the Fourier transform of $h_1(t)$, the nonlinear transfer function $H_n(f_1, \dots, f_n)$ is the n -dimensional Fourier transform of $h_n(\tau_1, \dots, \tau_n)$

$$H_n(f_1, \dots, f_n) = \int_{-\infty}^{\infty} \cdots \int_{-\infty}^{\infty} h_n(\tau_1, \dots, \tau_n) \prod_{r=1}^n e^{-i2\pi f_r \tau_r} d\tau_r \quad (4.5)$$

The nonlinear impulse responses and nonlinear transfer functions form Fourier transform pairs

and so $h_n(\tau_1, \dots, \tau_n)$ can be obtained from $H_n(f_1, \dots, f_n)$ by inverse Fourier transformation

$$h_n(\tau_1, \dots, \tau_n) = \int_{-\infty}^{\infty} \cdots \int_{-\infty}^{\infty} H_n(f_1, \dots, f_n) \prod_{r=1}^n e^{-i2\pi f_r \tau_r} df_r \quad (4.6)$$

Taking the conjugate of (4.5) the usual Hermitian property is obtained

$$H_n^*(f_1, \dots, f_n) = H_n(-f_1, \dots, -f_n) \quad (4.7)$$

Substitution of (4.6) into (4.4) and carrying out the multiple integrals in τ_1, \dots, τ_n yields

$$p_n(t) = \int_{-\infty}^{\infty} \cdots \int_{-\infty}^{\infty} H_n(f_1, \dots, f_n) \prod_{r=1}^n J(f_r) e^{i2\pi f_r t} df_r \quad (4.8)$$

which expresses the n th-order term of the functional expansion in terms of the input spectrum $J(f)$. The order of each term equals the number of contributing input frequencies when the input signal consists of a sum of individual tones. Note, however, that different order nonlinearities can result in responses at the same frequency and so the frequency of a response is not fully indicative of its order. As an example, the frequency $2f_1 - f_2$ appears to be third-order, that is, $2f_1 - f_2 = f_1 + f_1 - f_2$, but it could also be the fifth-order intermodulation product (IMP) $f_1 + f_1 + f_1 - f_1 - f_2$.

The input-output spectral relation is

$$P(f) = \sum_{n=1}^{\infty} P_n(f) \quad (4.9)$$

where $P_n(f)$ is obtained by Fourier transformation of (4.8)

$$P_n(f) = \int_{-\infty}^{\infty} \cdots \int_{-\infty}^{\infty} H_n(f_1, \dots, f_n) \delta(f - f_1 - \cdots - f_n) \prod_{r=1}^n J(f_r) df_r \quad (4.10)$$

From (4.4) it can be seen that the output $p_n(t)$ is identical for any permutation of the arguments of $h_n(\tau_1, \dots, \tau_n)$. In the following discussion it will be assumed that the impulse response $h_n(\tau_1, \dots, \tau_n)$ and hence the nonlinear transfer functions $H_n(f_1, \dots, f_n)$ are symmetric with respect to their arguments, i.e., that the order of the arguments can be interchanged. In Reference [68] it is shown that $h_n(\cdot)$ and $H_n(\cdot)$ can always be made symmetric. In order to understand the meaning of equation (4.8) an auxiliary multidimensional time function is defined

$$p_n(t_1, \dots, t_n) = \int_{-\infty}^{\infty} \cdots \int_{-\infty}^{\infty} H_n(f_1, \dots, f_n) \prod_{r=1}^n J(f_r) e^{i2\pi f_r t_r} df_r \quad (4.11)$$

and its n -fold Fourier transform

$$P_n(f_1, \dots, f_n) = \int_{-\infty}^{\infty} \dots \int_{-\infty}^{\infty} p_n(t_1, \dots, t_n) \prod_{r=1}^n e^{-i2\pi f_r t_r} dt_r \quad (4.12)$$

so that

$$p_n(t_1, \dots, t_n) = \int_{-\infty}^{\infty} \dots \int_{-\infty}^{\infty} P_n(f_1, \dots, f_n) e^{i2\pi f_r t_r} df_r \quad (4.13)$$

By comparison of the previous equation with (4.8) it follows that

$$P_n(f_1, \dots, f_n) = H_n(f_1, \dots, f_n) J(f_1) \dots J(f_n) \quad (4.14)$$

and

$$P_n(f) = \int_{-\infty}^{\infty} \dots \int_{-\infty}^{\infty} P_n(f_1, \dots, f_n) \delta(f - f_1 - \dots - f_n) df_1 \dots df_n \quad (4.15)$$

which states that the output spectrum is the integral of the multispectral density $P_n(f_1, \dots, f_n)$, subject to the constraint $f = f_1 + \dots + f_n$. This suggests the laser can be represented by the block diagram of figure 4.1.

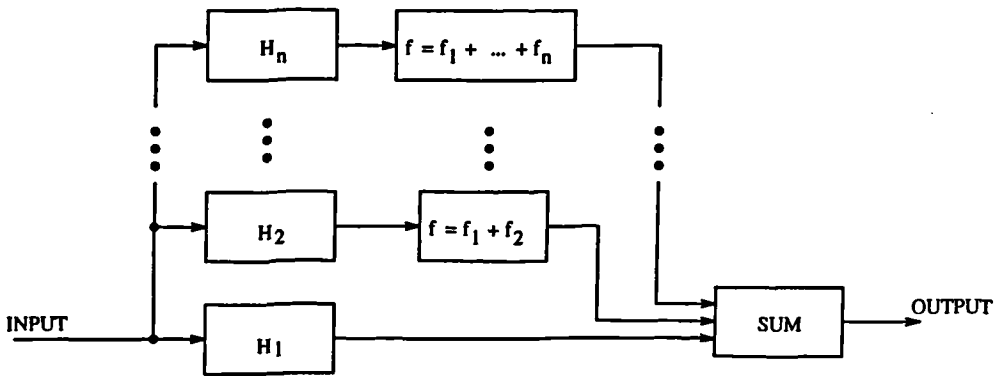


Figure 4.1: Diagram block of the semiconductor laser

The representation of the output by its Volterra expansion, equation (4.8), requires determination of the nonlinear transfer functions $H_n(f_1, \dots, f_n)$. Since the responses up to third-order are of interest $H_1(f)$, $H_2(f_1, f_2)$ and $H_3(f_1, f_2, f_3)$ have to be determined.

4.3 Determination of laser transfer functions

In this section, as in previous sections, it is assumed that the laser is described by the single-mode rate equations and these will be the basis for the determination of the laser transfer

functions. For simplicity of notation and for computational purposes the normalised rate equations are again used, written here for convenience (see chapter 3)

$$\frac{dn}{dt} = j - n - (n - n_{0m})(1 - \varepsilon p)p \quad (4.16)$$

$$\frac{dp}{dt} = \gamma [\Gamma(n - n_{0m})(1 - \varepsilon p)p - p + \Gamma\beta n] \quad (4.17)$$

The method described in Reference [68] to evaluate the transfer functions is called the “probing” or “harmonic input” method because it assumes the input to be given by a sum of exponentials

$$j(t) = e^{i2\pi f_1 t} + e^{i2\pi f_2 t} + \dots + e^{i2\pi f_n t} \quad (4.18)$$

where the frequencies f_r , $r = 1, 2, \dots, n$ are linearly independent, that is, the ratio of all possible pairs of frequencies is a not a rational number. The Fourier transform of (4.18) is a sum of delta functions

$$J(f) = \sum_{k=1}^n \delta(f - f_k) \quad (4.19)$$

After substitution into equation (4.8) the n th-order component of the Volterra expansion becomes

$$p_n(t) = \int_{-\infty}^{\infty} \dots \int_{-\infty}^{\infty} H_n(\xi_1, \dots, \xi_n) \prod_{r=1}^n \sum_{k=1}^n \delta(\xi_r - f_k) e^{i2\pi \xi_r t} d\xi_r \quad (4.20)$$

Expanding the product of the sum and carrying out the multiple integrals yields

$$p_n(t) = \sum_{k_1=1}^n \dots \sum_{k_n=1}^n H_n(f_{k_1}, \dots, f_{k_n}) e^{i2\pi(f_{k_1} + \dots + f_{k_n})t} \quad (4.21)$$

The new frequencies generated, ν , can be written as

$$\nu = m_1 f_1 + \dots + m_n f_n \quad (4.22)$$

where m_i is the number of times the frequency f_i occurs in generating the intermodulation (IM) frequency. Because exactly n terms are generated by a n th-order nonlinearity the set of values of m_i that defines any IM frequency is subject to the constraint

$$\sum_{r=1}^n m_r = n \quad (4.23)$$

In the summations of equation (4.21) it is necessary to determine the number of identical terms at each frequency, except for the permutation of the factors, in order to obtain the correct magnitude of each IM component. For an IM frequency given by (4.22) the number

of terms is given by the multinomial coefficient

$$\frac{n!}{m_1! \cdots m_n!} \quad (4.24)$$

When (4.21) is carried out and identical terms collected, we get

$$p_n(t) = \sum_m \frac{n!}{m_1! \cdots m_n!} H_n(m_1[f_1], \dots, m_n[f_n]) \prod_{r=1}^n e^{i2\pi m_r f_r t} \quad (4.25)$$

where

$$m_r[f_r] = \overbrace{(f_r, \dots, f_r)}^{m_r \text{ times}} \quad (4.26)$$

that is m_r consecutive arguments in $H_n(\cdot)$ having the same frequency f_r ; m under the summation indicates that the sum includes all the distinct sets $\{m_1, \dots, m_n\}$. In this equation there is a term of order n corresponding to $m_1 = \dots = m_n = 1$ given by

$$n! H_n(f_1, \dots, f_n) e^{i2\pi(f_1 + \dots + f_n)t} \quad (4.27)$$

and there are no more terms associated with $e^{i2\pi(f_1 + \dots + f_n)t}$ than this term because f_1, \dots, f_n were assumed to be linearly independent. Therefore the n th nonlinear transfer function $H_n(f_1, \dots, f_n)$ can be determined as the coefficient of $n! e^{i2\pi(f_1 + \dots + f_n)t}$ in the laser output when the input current is the sum of exponentials (4.18). This suggests the use of the perturbation technique [65] to determine all the transfer functions from the single-mode rate equations. The laser is first excited by a single exponential the coefficient of which gives the first-order transfer functions $H_1(f)$ and $G_1(f)$ associated with the photon and electron density, respectively. A sum of two exponentials is then applied yielding $H_2(f_1, f_2)$ and $G_2(f_1, f_2)$ in terms of $H_1(f_1)$ and $G_1(f_1)$. This procedure continues to the required order with one exponential being added at each step. Application of this method to the first, second and third-order differential equations for the perturbed electron and photon densities (section 4.4) gives, for the n th-order, the following system of equations

$$\begin{aligned} i2\pi(f_1 + \dots + f_n)G_n(f_1, \dots, f_n) = & - \{[(1 - \varepsilon p_0)p_0 + 1] G_n(f_1, \dots, f_n) \\ & + (n_0 - n_{0m})(1 - 2\varepsilon p_0)H_n(f_1, \dots, f_n) + D_n\} \end{aligned} \quad (4.28)$$

$$i2\pi(f_1 + \dots + f_n)H_n(f_1, \dots, f_n) = \gamma \{ \Gamma [(1 - \varepsilon p_0)p_0 + \beta] G_n(f_1, \dots, f_n)$$

$$+ [\Gamma(n_0 - n_{0m})(1 - 2\varepsilon p_0) - 1] H_n(f_1, \dots, f_n) + C_n \quad (4.29)$$

where the driving terms C_n and D_n are given in table 4.1. Solving equations (4.28) and (4.29)

n	D_n
1	-1
2	$\frac{1}{2} \{(1 - 2\varepsilon p_0)[G_1(f_1)H_1(f_2) + G_1(f_2)H_1(f_1)] - 2(n_0 - n_{0m})\varepsilon H_1(f_1)H_1(f_2)\}$
3	$\frac{1}{3} \{(1 - 2\varepsilon p_0)[H_1(f_1)G_2(f_2, f_3) + H_1(f_2)G_2(f_1, f_3) + H_1(f_3)G_2(f_1, f_2)$ $+ G_1(f_1)H_2(f_2, f_3) + G_1(f_2)H_2(f_1, f_3) + G_1(f_3)H_2(f_1, f_2)]$ $- (n_0 - n_{0m})2\varepsilon[H_1(f_1)H_2(f_2, f_3) + H_1(f_2)H_2(f_1, f_3) + H_1(f_3)H_2(f_1, f_2)]$ $- \varepsilon[G_1(f_1)H_1(f_2)H_1(f_3) + G_1(f_2)H_1(f_1)H_1(f_3) + G_1(f_3)H_1(f_1)H_1(f_2)]\}$

Table 4.1: Driving terms: C_n equals zero for $n = 1$ and D_n for the other cases

for G_n and H_n gives

$$H_n(f_1, \dots, f_n) = \frac{\gamma \Gamma \{C_n \psi(f_1 + \dots + f_n) - [(1 - \varepsilon p_0) + \beta] D_n\}}{\varphi(f_1 + \dots + f_n)} \quad (4.30)$$

$$G_n(f_1, \dots, f_n) = - \frac{\gamma \Gamma (n_0 - n_{0m})(1 - 2\varepsilon p_0) C_n + \chi(f_1 + \dots + f_n) D_n}{\varphi(f_1 + \dots + f_n)} \quad (4.31)$$

where

$$\psi(f) = i2\pi f + (1 - \varepsilon p_0)p_0 + 1 \quad (4.32)$$

$$\chi(f) = i2\pi f - \gamma \Gamma (n_0 - n_{0m})(1 - 2\varepsilon p_0) + \gamma \quad (4.33)$$

$$\varphi(f) = \psi(f)\chi(f) + \gamma \Gamma [(1 - \varepsilon p_0)p_0 + \beta](n_0 - n_{0m})(1 - 2\varepsilon p_0) \quad (4.34)$$

Equations (4.28) to (4.34) are recursive formulas to calculate H_n as a function of G_{n-1} and H_{n-1} .

Note now that the effect of the chip and package parasitics on the laser response can easily be included in the analysis. The result of the laser parasitics is to divert some of the input current from the active region. If $H_P(f)$ is the transfer function of the parasitics, which gives the frequency dependence of the injected current into the active region, the driving term D_1 should be redefined accordingly, that is, $D_1 = -H_P(f)$. This is equivalent to multiplying the

first-order transfer function of the intrinsic laser by the parasitics transfer function $H_P(f)$

4.4 Laser response to a sum of narrow-band signals

4.4.1 General theory

In SCM systems the input signal to the laser is bandpass and typically narrow-band compared to the carrier frequency. The laser response to a sum of narrow-band components is therefore important and will now be derived. Let the input be a sum of K narrow-band signals each centred at ν_k

$$J(t) = \sum_{k=1}^K J_k(t) \quad (4.35)$$

$$= \sum_{k=1}^K c_k(t) \cos 2\pi \nu_k t - s_k(t) \sin 2\pi \nu_k t \quad (4.36)$$

where $c_k(t)$ and $s_k(t)$ are the in-phase and quadrature components of $J_k(t)$. It is convenient to use an equivalent low-pass representation for the bandpass signals by defining the complex envelope $z_k(t)$ of $J_k(t)$

$$z_k(t) = c_k(t) + i s_k(t) \quad (4.37)$$

With these definitions the input signal can be written as

$$\begin{aligned} J(t) &= \sum_{k=1}^K \operatorname{Re} \left\{ z_k(t) e^{i2\pi \nu_k t} \right\} \\ &= \frac{1}{2} \sum_{k=-K}^K z_k(t) e^{i2\pi \nu_k t} \end{aligned} \quad (4.38)$$

where we have taken $z_k(t)^* = z_{-k}(t)$ and $z_0(t) = 0$. Defining $Z_k(f)$ as the Fourier transform of $z_k(t)$ and denoting $Z_k^*(-f)$ and $-\nu_k$ by $Z_{-k}(f)$ and ν_{-k} , respectively, the spectrum $J_k(f)$ of $J_k(t)$ is

$$\begin{aligned} J_k(f) &= \frac{1}{2} \sum_{k=1}^K [Z_k(f - \nu_k) + Z_k^*(-f - \nu_k)] \\ &= \frac{1}{2} \sum_{k=-K}^K Z_k(f - \nu_k) \end{aligned} \quad (4.39)$$

After substitution of the above equation into (4.8) and performing the product of the input spectra the photon density becomes

$$p(t) = \sum_{n=1}^{\infty} \sum_{k_1=-K}^K \cdots \sum_{k_n=-K}^K 2^{-n} \int_{-\infty}^{\infty} \cdots \int_{-\infty}^{\infty} H_n(f_1, \dots, f_n) \prod_{r=1}^n Z_{k_r}(f_r - \nu_{k_r}) e^{i2\pi f_r t} df_r \quad (4.40)$$

As before there are $n!/(m_{-K}! \cdots m_K!)$ identical integrals for each distinct set $\{k_1, \dots, k_n\}$ with $k_i = -K, \dots, K$ and where $m_i = 0, \dots, n$ is the number of times each k_i occurs in the set, so that

$$\sum_{k=-K}^K m_k = n \quad (4.41)$$

Collecting those integrals, the n th-order term is

$$p_n(t) = \sum_k \frac{n!}{m_{-K}! \cdots m_K!} \int_{-\infty}^{\infty} \cdots \int_{-\infty}^{\infty} H_n(f_1, \dots, f_n) \prod_{r=1}^n Z_{k_r}(f_r - \nu_{k_r}) e^{i2\pi f_r t} df_r \quad (4.42)$$

in which the summation over k includes all the distinct sets $\{k_1, \dots, k_n\}$. Each set $\{\nu_{k_1}, \dots, \nu_{k_n}\}$ must have its symmetric $\{-\nu_{k_1}, \dots, -\nu_{k_n}\}$, except in the case of

$$\sum_{\nu_{k_r}=1}^n \nu_{k_r} = 0.$$

The sum of two such terms in (4.42), which are complex conjugates, is designated as

$$\begin{aligned} p_{n\nu}(t) &= \operatorname{Re} \left\{ \frac{n!2^{-n+1}}{m_{-K}! \cdots m_K!} \left[\int_{-\infty}^{\infty} \cdots \int_{-\infty}^{\infty} H_n(f_1 + \nu_{k_1}, \dots, f_n + \nu_{k_n}) \right. \right. \\ &\quad \left. \left. \times \prod_{r=1}^n Z_{k_r}(f_r) e^{i2\pi f_r t} df_r \right] e^{i2\pi \sum_{r=1}^n \nu_{k_r} t} \right\} \end{aligned} \quad (4.43)$$

so that

$$p_n(t) = \sum_k p_{n\nu}(t) \quad (4.44)$$

Comparing equations (4.38) and (4.43) it can be concluded that when the input current consists of a sum of narrow-band signals the laser generates new narrow-band components centred at all carrier intermodulation frequencies. The n -th order output component, $p_{n\nu}(t)$, centred at frequency

$$\nu = \sum_{r=1}^n \nu_{k_r} = \sum_{k=-K}^K m_k \nu_k \quad (4.45)$$

generated by intermodulation of the input signal components centred at $\nu_{k_1}, \dots, \nu_{k_n}$ is defined as

$$p_{n\nu}(t) = \text{Re} \left\{ q_{n\nu}(t) e^{i2\pi \sum_{r=1}^n \nu_{k_r} t} \right\} \quad (4.46)$$

which has a complex envelope $q_{n\nu}(t)$ given by

$$q_{n\nu}(t) = \frac{n!2^{-n+1}}{m_{-K}! \dots m_K!} \int_{-\infty}^{\infty} \dots \int_{-\infty}^{\infty} H_n(f_1 + \nu_{k_1}, \dots, f_n + \nu_{k_n}) \prod_{r=1}^N Z_{k_r}(f_r) e^{i2\pi f_r t} df_r \quad (4.47)$$

Hence $p_{n\nu}$ is the intermodulation product due to the input signals with carriers at frequencies $\nu_{k_1}, \dots, \nu_{k_n}$. The order of the IMP corresponds to the number of carriers generating this product, with the possibility of n being greater than K and signals intermodulating with themselves. The order of the permutation of the component frequencies $\nu_{k_1}, \dots, \nu_{k_n}$ of ν is irrelevant since it does not affect the IM waveform $p_{n\nu}$. Also, any two sets $\{\nu_{k_i}\}$ are indistinguishable if they differ only by the order of the components within the set. The multinomial coefficient in the integrals (4.43) and (4.47) take into account the number of such indistinguishable sets among all the $(2K)^n$ sets of ν .

In practice there is interest in determining $p_\nu(t)$ the component of $p(t)$ centred on the sum frequency ν

$$p_\nu(t) = \text{Re} \left\{ q_\nu(t) e^{i2\pi \nu t} \right\} \quad (4.48)$$

with complex envelope $q_\nu(t)$. Intermodulation of infinitely many orders and with many different sets of input components $\{\nu_{k_1}, \dots, \nu_{k_n}\}$, can contribute near a particular frequency. Thus $p_\nu(t)$ is the sum of all the $p_{n\nu}(t)$ and $q_\nu(t)$ is the sum over n and ν of all the $q_{n\nu}(t)$ under the constraint (4.45) that they fall at the same frequency ν

$$q_\nu(t) = \sum_{\nu, n=1}^{\infty} q_{n\nu}(t) \quad (4.49)$$

Usually only the first few terms in n of this sum are required. For a large number of channels, however, the sum in ν can contain many terms. As an example, a 62 channel system has over 1000 intermodulation products of type $f_i + f_j - f_k$, ($i \neq j \neq k$) (figure 3.2).

4.4.2 Multitone input case

It is important to consider the multitone case because experimental measurements of distortion are usually performed using two or three-tones. The input will now be assumed to consist of

N carriers located at $\nu_k = f_k$

$$j(t) = \frac{1}{2} \text{Re} \left\{ j_k e^{i2\pi f_k t} \right\} \quad (4.50)$$

The complex envelope spectra of the carriers is

$$Z_k(f) = j_k \delta(f) \quad (4.51)$$

and the complex envelope amplitude, $A(f_{k_1}, \dots, f_{k_n})$ of the n th-order IMP due to carriers at f_{k_1}, \dots, f_{k_n} may be found, from (4.47), to be

$$A(f_{k_1}, \dots, f_{k_n}) = \frac{n! j_{k_1} \cdots j_{k_n}}{2^{n-1} m_{-N}! \cdots m_N!} H_n(f_{k_1}, \dots, f_{k_n}) \quad (4.52)$$

$$k_1, \dots, k_n = \pm 1, \dots, \pm N$$

The amplitudes for three input carriers of typical second and third-order IMPs are listed in table 4.2.

n	m_{-3}	m_{-2}	m_{-1}	m_1	m_2	m_3	Frequency	Amplitude
2	0	0	0	2	0	0	$2f_1$	$\frac{1}{2} j_1^2 H_2(f_1, f_1)$
2	0	0	0	1	1	0	$f_1 + f_2$	$j_1 j_2 H_2(f_1, f_2)$
3	0	1	0	2	0	0	$2f_1 - f_2$	$\frac{3}{4} j_1^2 j_2^* H_3(-f_1, f_2, f_2)$
3	0	0	1	0	2	0	$2f_2 - f_1$	$\frac{3}{4} j_1^* j_2^2 H_3(-f_1, f_2, f_2)$
3	1	0	0	1	1	0	$f_1 + f_2 - f_3$	$\frac{3}{2} j_1 j_2 j_3^* H_3(f_1, f_2, -f_3)$
3	0	1	0	1	0	1	$f_1 - f_2 + f_3$	$\frac{3}{2} j_1 j_2^* j_3 H_3(f_1, -f_2, f_3)$
3	0	0	1	0	1	1	$-f_1 + f_2 + f_3$	$\frac{3}{2} j_1^* j_2 j_3 H_3(-f_1, f_2, f_3)$

Table 4.2: Amplitude of second and third-order IMPs

4.5 Series expansion of nonlinear transfer functions

In the multitone case the laser response is characterized by point values of nonlinear transfer functions at specific frequencies only. When the input channels are modulated each channel occupies a certain bandwidth about its carrier frequency. Unless the transfer functions are

constant across the bandwidth of each input signal, point values at the carrier location are generally inadequate to describe the laser behaviour. Even so, an approximation to the full nonlinear transfer function may be sufficient for a particular input. These approximations, interpreted in terms of suitable signal processing structures, gives rise to a model, designated the “canonic model”. The model described here [68] is based on the multivariate Taylor series expansion of the nonlinear transfer function about its operating frequency. This model is called the “frequency power series canonic model”.

Generally $H_n(f_1 + \nu_{k_1}, \dots, f_n + \nu_{k_n})$ in equation (4.47) can be expanded in a Taylor series about $\nu = (\nu_{k_1}, \dots, \nu_{k_n})$

$$H_n(f_1 + \nu_{k_1}, \dots, f_n + \nu_{k_n}) = \sum_{l=0}^{\infty} \sum_l \frac{f_1^{l_1} f_2^{l_2} \dots f_n^{l_n} \partial^l H_n(f_1, \dots, f_n)}{l_1! l_2! \dots l_n! \partial f_1^{l_1} \partial f_2^{l_2} \dots \partial f_n^{l_n}} \Big|_{f=\nu} \quad (4.53)$$

where the second summation over l includes all the permutations of l_i which satisfy

$$l_1 + l_2 + \dots + l_n = l \quad (4.54)$$

Substitution of the Taylor expansion of H_n in equation (4.47) with some simplification leads to the complex envelope of the n th-order component being written as

$$q_{n\nu}(t) = \sum_{l=0}^{\infty} \sum_l \frac{2^{-n+1} n!}{m_{-K}! \dots m_K! l_1! \dots l_n!} \frac{\partial^l H_n(\nu)}{\partial f_1^{l_1} \dots \partial f_n^{l_n}} \prod_{r=1}^n \frac{z^{(l_r)}(t)}{(2\pi i)^{l_r}} \quad (4.55)$$

in which $z^{(l)}(t)$ represents the l th derivative of $z(t)$. A simplification has occurred since $q_{n\nu}(t)$ now involves only the sum of the weighted products of various derivatives of the input components. The coefficients are the derivatives of the n th-order transfer function evaluated at the frequency set $(\nu_{k_1}, \dots, \nu_{k_n})$. This expansion structures the laser as a series of differentiators ($z^{(l)}(t)$) and multipliers, to apply the proper coefficients, for each term in the sum. The utility of this model is based on the feasibility of a small number of correction terms sufficing. This result will be applied in chapter 6 when assessing the performance of SCM systems.

4.6 Analytic and simulation results

4.6.1 Model validity

To show the applicability of this analysis the intermodulation products were computed and compared with the numerical solution of the rate equations (direct simulation) with the laser

modulated by three carriers

$$f_2 = f_1 + \Delta f \quad (4.56)$$

$$f_3 = f_2 + 7\Delta f/2 \quad (4.57)$$

The input signal amplitude is in general defined in terms of the per-channel optical modulation depth m which relates to the normalised current J_r of the r th-channel by

$$|J_r| = \frac{m(f_r) p_0}{|H_1(f_r)|} \quad (4.58)$$

Note that if J_r is constant $m_r \equiv m(f)$ must be frequency dependent and, according to this definition, the optical modulation depth is a real number

The results given in this section are for a 1.3 μm InGaAsP buried heterostructure laser. The laser intrinsic parameters and parasitics elements, taken from Reference [31] are given in table 4.3 and table 4.4. The parasitics are dominated by the resistance R_s in series with the active region and the shunt capacitance C_s , forming a 1st-order Butterworth filter with a 3 dB bandwidth of 1.1 GHz.

The amplitude and phase of the fundamental and distortion products at f_{k_1} , $f_{k_1} + f_{k_2}$ and $2f_{k_1} - f_{k_2}$ for $k_1, k_2 = 1, 2, 3$ were determined numerically by applying the FFT to the time solution of the rate equations. The time domain solution was obtained using the SIMULINK design block system for simulating dynamic systems. Two cases have been considered: in the first one we obtain the laser transfer functions evaluated at $H_1(f_1)$, $H_2(f_1, f_2)$ and $H_3(f_1, f_2, -f_3)$ by varying the frequency of the carriers over the range of 200 MHz to 7 GHz, in the second the dependence of the IMPs amplitude with the optical modulation depth is examined.

Laser transfer functions

In this case the input signal amplitude, kept constant across the range, is the same for all the carriers and is specified in terms of the optical modulation depth at low frequencies, where the first-order transfer function is flat, which directly relates to the input signal level

$$m(0) = \frac{|J_r|H_1(0)}{p_0} \quad (4.59)$$

Parameter	Value	Units
V: active region volume	1.37×10^{-16}	m^3
g_0 : gain slope constant	2.4×10^{-12}	$\text{m}^3 \text{s}^{-1}$
ϵ : gain compression factor	4.5×10^{-23}	m^3
ϵ : normalised compression factor	6.25×10^{-3}	–
N_{0m} : electron density at transparency	10^{24}	m^{-3}
n_{0m} : normalised electron dens. at transparency	2.4	–
β : spontaneous emission factor	10^{-4}	–
Γ : optical confinement factor	0.4	–
τ_p : photon lifetime	1	ps
τ_s : electron lifetime	3	ns
γ : τ_s/τ_p	3000	–
I_{th} : threshold current	30	mA
j_{th} : normalised threshold current	9.82	–
I_L : leakage current	15	mA

Table 4.3: Parameter values for a Buried-Heterostructure laser

Element	Value
C_P	0.18 pF
L_P	1.1 nH
R_P	1.0 Ω
R_{SUB}	0.5 Ω
C_S	13 pF
R_S	11 Ω
$1/2\pi R_S C_S$	1.1 GHz

Table 4.4: Package and chip parasitics elements values for a BH laser (for a diagram of the equivalent circuit see Reference [31]).

$$\approx \frac{|j_r|}{j_0 - j_{th}}$$

The transfer functions are then calculated from

$$H_n(f_{k_1}, \dots, f_{k_n}) = \frac{m_{-3}! \dots m_3!}{n! 2^{-n+1}} p(f_{k_1}, \dots, f_{k_n}) \left(\frac{H_1(0)}{m(0)p_0} \right)^n \quad (4.60)$$

where $p(f_{k_1}, \dots, f_{k_n})$ represents the IMP at $(f_{k_1}, \dots, f_{k_n})$ obtained by simulation and the relations $j_{k_1} = j_{k_2}$, $j_k^* = j_k$ were used. Figures 4.2, 4.3 and 4.4 show the amplitude and phase of the first, second and third-order laser transfer functions¹, respectively. The transfer functions determined by the method described in section 4.3 are compared with the results of direct simulation for a per-channel modulation depth of $m(0) = 0.13$. Very good agreement is obtained between the analytical and simulation results.

IMPs vs. optical modulation depth

The amplitude of the IMPs relative to the carrier at f_1 are defined as

$$2\text{HD} = \frac{1}{2} m(f_1) p_0 \frac{|H_2(f_1, f_1)|}{|H_1(f_1)|^2} \quad (4.61)$$

$$\text{IMP}_{2,(f_1+f_2)} = m(f_2) p_0 \frac{|H_2(f_1, f_2)|}{|H_1(f_1)H_1(f_2)|} \quad (4.62)$$

$$\text{IMP}_{3,(2f_1-f_2)} = \frac{3}{4} m(f_1)m(f_2) p_0^2 \frac{|H_3(f_1, f_1, -f_2)|}{|H_1^2(f_1)H_1(f_2)|} \quad (4.63)$$

$$\text{IMP}_{3,(f_1+f_2-f_3)} = \frac{3}{2} m(f_2)m(f_3) p_0^2 \frac{|H_3(f_2, f_3, -f_1)|}{|H_1(f_1)H_1(f_2)H_1(f_3)|} \quad (4.64)$$

Figures 4.5(a) and 4.5(b) plot these IMPs as a function of the modulation depth m , for two values of laser bias current 40 mA and 60 mA, respectively. It is seen that this analysis gives good results even for large modulation depths indicating that the third-order model of the laser is adequate. For low values of bias current, although the levels of distortion are higher the Volterra series analysis gives a better approximation to the simulation at large m . This is due to fifth-order terms, which depend on the signal amplitude, becoming important in the series expansion: for the same modulation depth the current signal amplitude is actually higher for increased bias, thereby increasing the impact of these higher-order terms. A consequence of this is that when the laser is operating at large modulation depths an optimum bias current

¹The decibel units used are, as in previous chapters, electrical decibels.

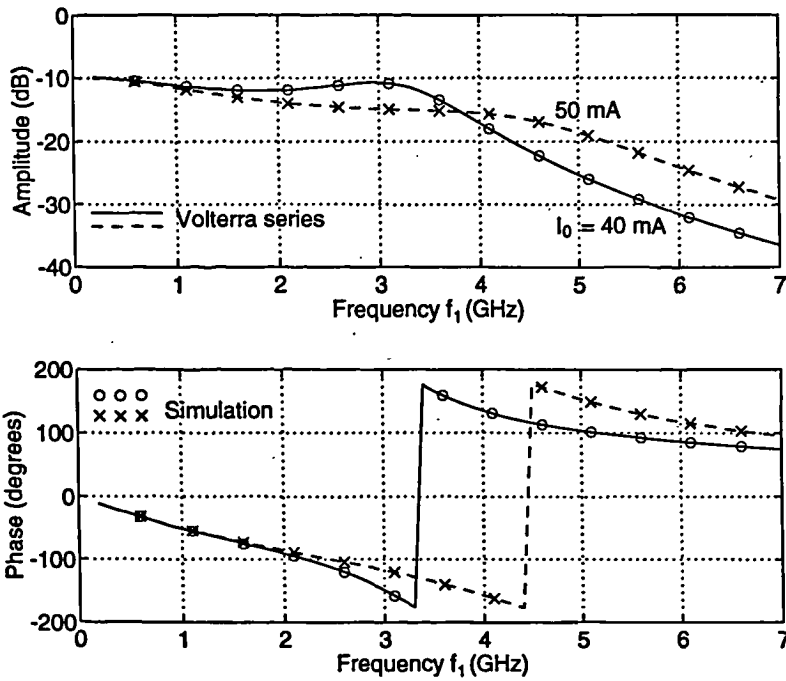


Figure 4.2: First-order laser transfer function $H_1(f_1)$: comparison between analytical and simulation results when the laser is modulated by three carriers for two values of the laser bias current I_0 ($m(0) = 0.13$).

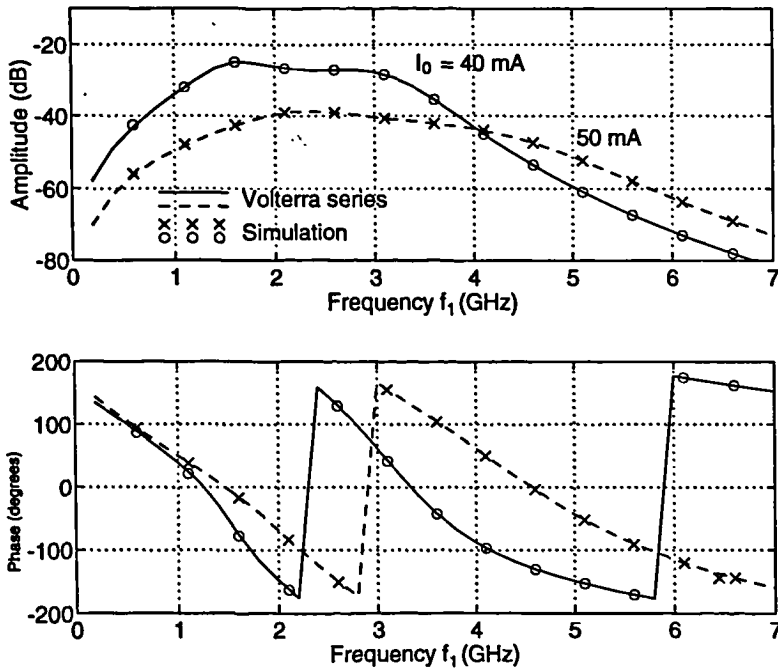


Figure 4.3: Second-order laser transfer function $H_2(f_1, f_2)$: comparison between analytical and simulation results when the laser is modulated by three carriers for two values of the laser bias current I_0 ($f_2 = f_1 + 0.2$ GHz and $m(0) = 0.13$)

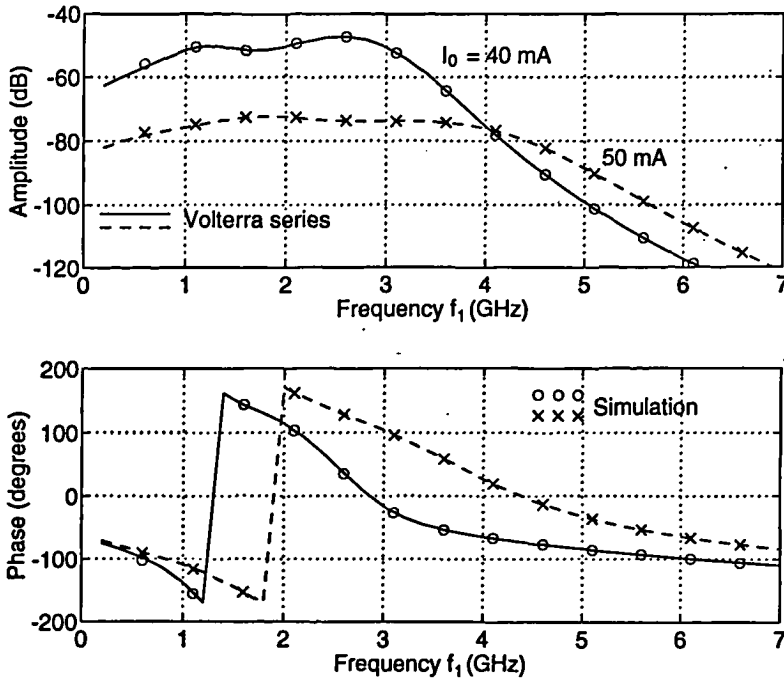


Figure 4.4: Third-order laser transfer function $H_3(f_1, f_2, -f_3)$: comparison between analytical and simulation results when the laser is modulated by three carriers for two values of the laser bias current I_0 ($f_2 = f_1 + 0.2$ GHz, $f_3 = f_1 + 0.7$ GHz and $m(0) = 0.13$)

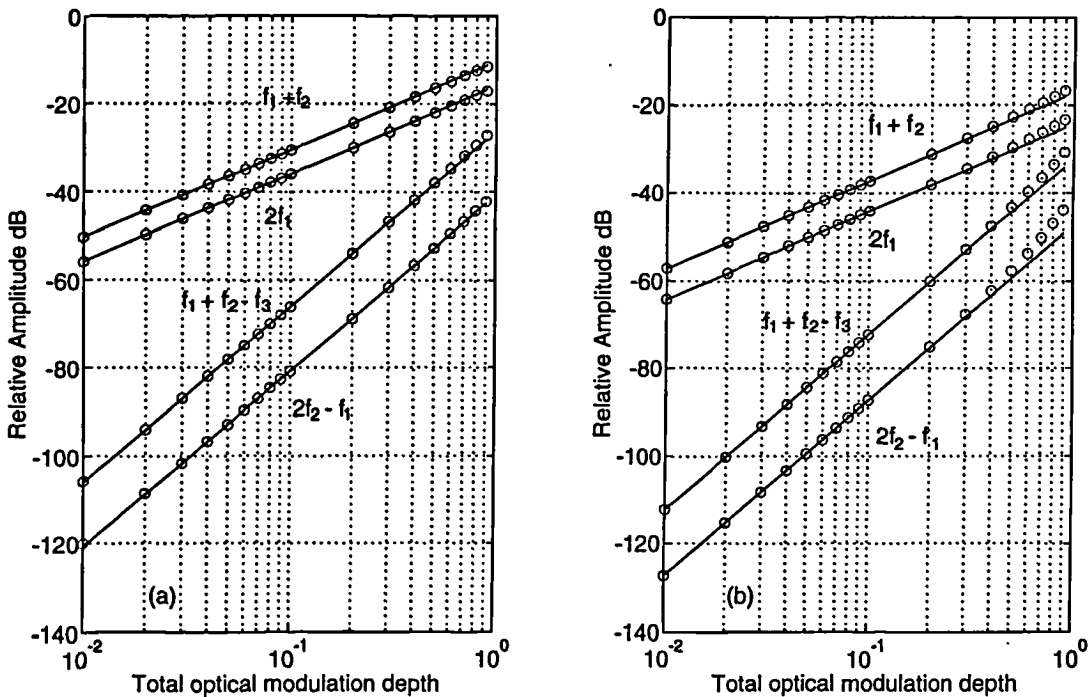


Figure 4.5: Amplitude of second and third-order intermodulation products relative to the carrier at f_1 for a laser bias current of (a) $I_0 = 40$ mA and (b) $I_0 = 60$ mA ($f_1 = 2.1$ GHz, $f_2 = 2.3$ GHz and $f_3 = 2.8$ GHz).

may exist, although an analytical solution is difficult to obtain as it requires determination of 4th and 5th-order transfer functions.

4.6.2 Dependence of intermodulation products on frequency spacing

The determination of intermodulation is usually performed by considering two [14, 15] or three [16] closely spaced frequencies. As shown in Reference [69] this does not describe the interaction of channels with high frequency spacing. In this section we will show that second-order distortion products depend only on the resulting intermodulation frequency, whereas for third-order distortion the position of each modulation frequency must be considered. To find the dependence of $\text{IMP}_{2,(f_1+f_2)}$ with frequency spacing it is assumed all three channels have the same modulation depth $m = m(f_1) = m(f_2) = m(f_3)$. From equation (4.62) and equations (4.30) to (4.34) this distortion product is then written as

$$\text{IMP}_{2,(f_1+f_2)} = \frac{mp_0 [\psi(f_1 + f_2) - B] (1 - 2\epsilon p_0) [\chi(f_1 + f_2) - 2(n_0 - n_{0m})B]}{\gamma \Gamma \varphi(f_1 + f_2) B} \quad (4.65)$$

with $B = (1 - 2\epsilon p_0)p_0 + \beta$, which involves only the sum frequency $f_1 + f_2$ and is therefore independent of the position of f_1 and f_2 . The same is true for second-order distortion products at the difference frequency $f_2 - f_1$, $\text{IMP}_{2,(f_2-f_1)}$.

In contrast to second-order IMPs the third-order IMPs depend on the intermodulation frequency $f_1 + f_2 - f_3$ as well as on each of the modulation frequencies f_1 , f_2 and f_3 . In figure 4.6 the spacing between f_2 and f_3 is fixed with a difference of $f_3 - f_2 = 200$ MHz while the modulation frequency f_1 is varied. The $\text{IMP}_{3,(f_1+f_2-f_3)}$ is therefore located 200 MHz below f_1 . As expected the distortion increases with f_1 reaching a maximum near the relaxation resonance frequency of the laser diode. This maximum occurs when $f_1 + f_2 - f_3$ equals the laser resonance frequency $f_0 = 3.3$ GHz, that is for $f_1 = f_0 + 0.2$ GHz. Yet the distortions are up to 11 dB higher for $f_2 = 0.5$ GHz compared to those for $f_2 = 3$ GHz. This is a result of a small f_3 yielding a large difference frequency $f_1 - f_3$ which is present in the driving term D_3 (table 4.1) and has a maximum at the resonance frequency. This second maximum, at 6.5 GHz for $f_2 = 3$ GHz, is coincident with f_0 for low values of f_2 thereby increasing the levels of distortion when the spacing is large.

To further examine the dependence of third-order distortion on frequency spacing a plot of $\text{IMP}_{3,(f_1+f_2-f_3)}$ is shown in figure 4.7 in which the frequencies f_2 and f_3 are varied while

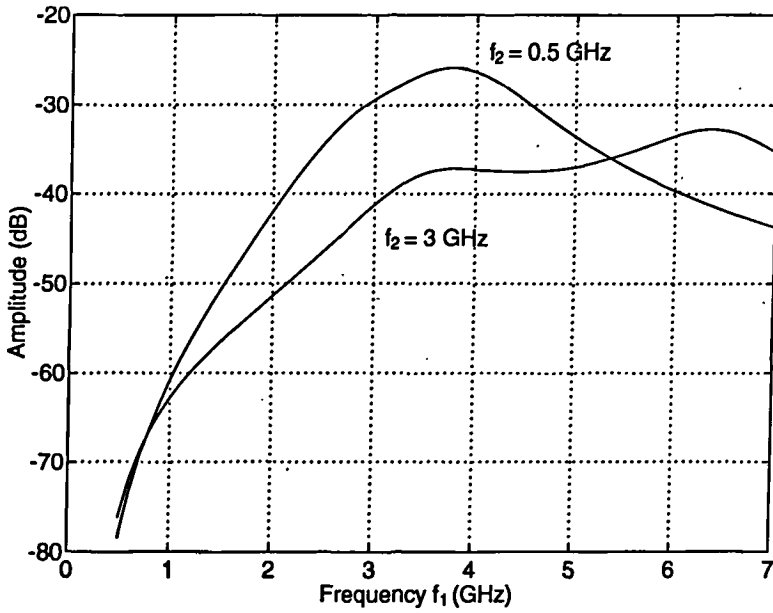


Figure 4.6: Third-order intermodulation distortion versus f_1 for constant f_2 and f_3 ($f_3 - f_2 = 200$ MHz, $m = 20\%$, $I_0 = 50$ mA and $f_0 = 3.3$ GHz)

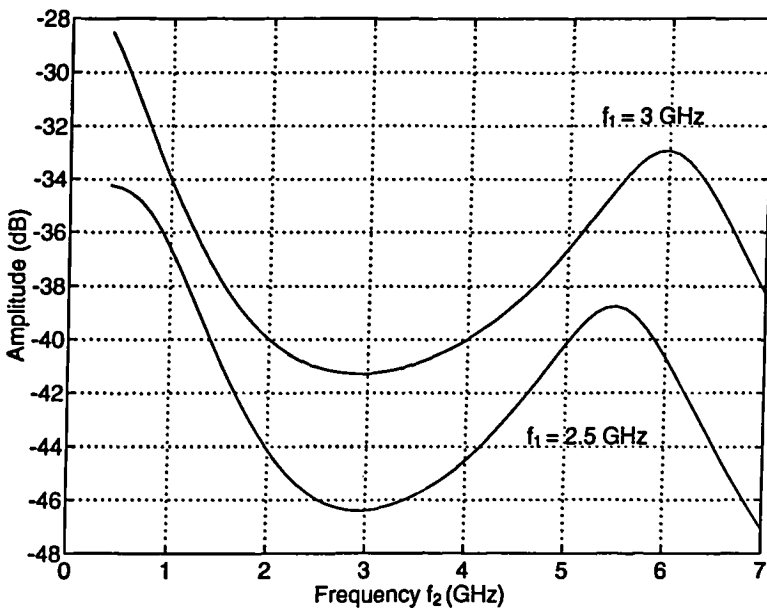


Figure 4.7: Third-order intermodulation distortion versus f_2 for constant f_1 ($f_3 - f_2 = 200$ MHz, $m = 20\%$, $I_0 = 50$ mA and $f_0 = 3.3$ GHz)

keeping f_1 fixed; the difference $f_3 - f_2$ is 200 MHz and the modulation depth is 20% per carrier. It is seen that the distortion levels increase for decreasing f_2 and f_3 . This is explained, once again, by the difference frequency $f_1 - f_3$ which imposes a minimum when $f_1 - f_3 \approx 0$, that is for $f_2 \simeq 3$ GHz and maximum for $f_1 - f_3 = f_0$. The sum frequency $f_1 + f_2$ leads to a maximum at low frequencies ($f_2 = f_0 - f_1 = 0.3, 0.8$ GHz). Hence SCM systems with a large number of channels and correspondingly large transmission bandwidths are expected to suffer higher distortion because of the large frequency spacing between the extreme channels.

4.7 Summary

In this chapter we have developed an analytic nonlinear model for the semiconductor laser. This model is based on the Volterra series analysis which describes the nonlinearity in the frequency domain by nonlinear transfer functions. These transfer functions for the laser diode were determined from the single-mode rate equations and analytic expressions were derived that give the laser response to a sum of narrow-band signals. By comparing the analytic results with simulation we confirmed the accuracy of our model and that its region of validity extends to large optical modulation depths. A preliminary analysis of possible system implications has indicated that an increase in the frequency spacing between the channels adversely affects the third-order distortion products yielding up to 11 dB higher distortion. In the following chapters this model will be applied to assess the performance of multichannel SCM systems.

Chapter 5

System performance assessment

5.1 Introduction

In the previous chapter it was shown that Volterra series provided a tractable analytic technique for the assessment of laser distortion. Here this technique will be applied to assess the performance of directly modulated SCM systems in which laser nonlinear distortion is an important degrading factor. A block diagram of the system being studied is shown in figure 5.1. The electrical signals are modulated onto a subcarrier and the resulting signal is used to modulate the laser diode. At the receiver end the signal is detected and a bandpass filter selects the desired channel.

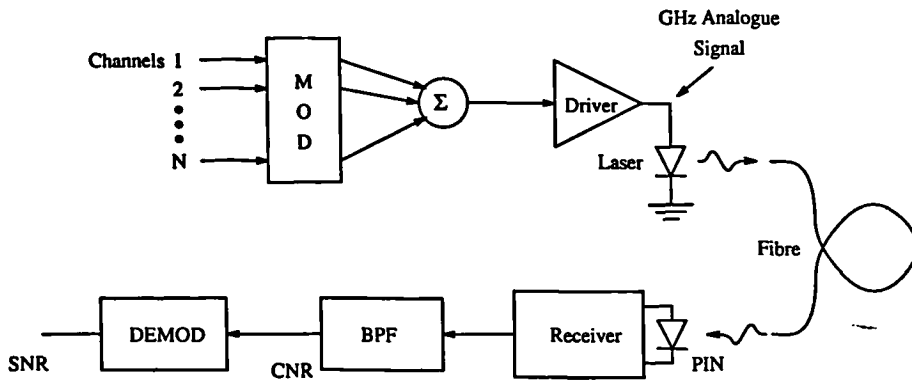


Figure 5.1: Block diagram of a directly modulated subcarrier multiplexed system.

The method for calculating the intermodulation power spectral density is first described (section 5.2) based on the calculation of the autocorrelation of the intermodulation waveform $p_{nv}(t)$. This waveform, however, is difficult to obtain except for simple cases where the system response may be characterized by point values at specific frequencies. The simple case occurs when the transfer functions may be treated as constant over the channel bandwidth.

In section 5.3 the implications of these assumptions, in AM and FM systems under single-tone modulation, are discussed.

The affect of laser distortion on system performance is quantified in terms of the carrier-to-intermodulation ratio (CIR) defined in section 5.4 obtained here for the simple case of unmodulated subcarriers. Distortion coefficients associated with each type of distortion are given that enable one to assess the influence on system performance of key parameters such as bias current and frequency allocation. The overall system performance is then determined (section 5.5) by inclusion of relative intensity noise (RIN), receiver shot and thermal noise. Optimum performance is then identified. The subject of receiver design is discussed in section 5.6 and conditions of operation are identified where APD detectors may be advantageous.

Finally, in section 5.7 the implications of clipping-induced distortion on system performance are examined. Illustrative results are given corresponding to a FM-broadcast system, the case of AM transmission being dealt with in more detail in the next chapter.

In this analysis we take the receiver to be linear although some distortion may be expected with APD receivers and in extreme cases with PIN receivers due to bias fluctuations.

5.2 Intermodulation power spectral density

The power distribution of the multiplexed signal is affected by the laser nonlinearity. In general the power of the intermodulation products (IMPs) spreads over a larger range of frequencies than the original channel bandwidth. The bandpass filter in figure 5.1 then rejects some of this “intermodulation noise”. To assess the impact of laser distortion on system performance it is therefore important to know how the power of the distortion products is distributed over frequency, that is the intermodulation power spectral density.

In this section we will describe the method for calculating the power spectral density of the IMPs. The input laser current is considered to be a sum of N , wide-sense stationary narrow-band processes, with zero mean value, centred at ν_k

$$\begin{aligned}
 j(t) &= \sum_{k=1}^N j_k(t) = \sum_{k=1}^N c_k(t) \cos 2\pi \nu_k t - s_k(t) \sin 2\pi \nu_k t \\
 &= \sum_{k=-N}^N z_k(t) e^{i2\pi \nu_k t}
 \end{aligned} \tag{5.1}$$

where $z_k(t) = c_k(t) + is_k(t)$ is the low-pass complex envelope representation of $j_k(t)$ as defined in the previous chapter. From equation (4.46) the n th-order IMP falling at frequency $\nu = \nu_{k_1} + \dots + \nu_{k_n}$ is

$$p_{n\nu}(t) = \text{Re} \left\{ q_{n\nu}(t) e^{i2\pi\nu t} \right\} \quad (5.2)$$

$$= a(t) \cos 2\pi\nu t - b(t) \sin 2\pi\nu t \quad (5.3)$$

In general the output intermodulation component $p_{n\nu}(t)$ is not stationary [70]. However, stationarity applies to the cases treated in the next chapter and so is assumed hereafter. The stationarity of $p_{n\nu}(t)$ implies that the in-phase and quadrature components of $p_{n\nu}(t)$, $a(t)$ and $b(t)$ respectively, have zero mean values

$$E\{a(t)\} = 0 \quad (5.4)$$

$$E\{b(t)\} = 0 \quad (5.5)$$

and their autocorrelation and cross-correlation functions are also stationary processes satisfying the relations

$$R_a(\tau) = R_b(\tau) \quad (5.6)$$

$$R_{ab}(\tau) = -R_{ba}(\tau) \quad (5.7)$$

The autocorrelation function $R_{p_{n\nu}}(\tau)$ of the intermodulation component $p_{n\nu}(t)$ is then uniquely determined from the autocorrelation $R_{q_{n\nu}}(\tau)$ of the equivalent complex envelope $q_{n\nu}(t)$ and the frequency ν as [71]

$$R_{p_{n\nu}}(\tau) = \frac{1}{2} \text{Re} \left\{ R_{q_{n\nu}}(\tau) e^{i2\pi\nu\tau} \right\} \quad (5.8)$$

Taking the Fourier transform we get

$$G_{p_{n\nu}}(f) = \frac{1}{4} [G_{q_{n\nu}}(f - \nu) + G_{q_{n\nu}}(-f - \nu)] \quad (5.9)$$

which relates $G_{p_{n\nu}}(f)$, the power spectral density of the intermodulation component $p_{n\nu}(t)$, with the power spectral density of the equivalent low-pass process $G_{q_{n\nu}}(f)$. Whenever possible we will use the low-pass representation.

5.3 Series expansion of H_n and implications for single-tone modulation

The method outlined is based on the knowledge of $q_{nv}(t)$ which is difficult to calculate except for simple cases where the system response may be characterized by point values at specific frequencies. In chapter 4 it was shown that Taylor series expansion of the transfer functions provides a simplified model replacing the multiple integration in $q_{nv}(t)$, equation (4.47), by a sum of weighted products involving the various derivatives of the input components. In the next chapter, case studies are considered where the nonlinear transfer functions are treated as constant about any set of frequencies $\nu = (\nu_{k_1}, \dots, \nu_{k_n})$. Let this constant value be equal to $H_n(\nu_{k_1}, \dots, \nu_{k_n})$ which we shall write as $H_n(\nu)$. In such cases, the Fourier transforms in equation (4.47) can all be carried out giving

$$q_{nv}(t) = \frac{n! 2^{-n+1}}{m_{-N}! \dots m_N!} H_n(\nu) \prod_{r=1}^n z_{k_r}(t) \quad (5.10)$$

so that the complex envelope of each IMP becomes simply the product of n intermodulation components with a suitable complex coefficient. If a frequency ν_k appears m_k times in the intermodulation product then

$$\prod_{r=1}^n z_{k_r}(t) = \prod_{k=-N}^N z_k^{m_k}(t) \quad (5.11)$$

where m_k can be any integer from 0 to n and $\sum_{r=-N}^N m_r = n$. Given the complex envelope it follows that the intermodulation waveform due to inputs at $(\nu_{k_1}, \dots, \nu_{k_n})$ is

$$p_{nv}(t) = \frac{n! 2^{-n+1}}{m_{-N}! \dots m_N!} \operatorname{Re} \left\{ H_n(\nu) \prod_{k=-N}^N z_k^{m_k}(t) e^{i2\pi m_k \nu_k t} \right\} \quad (5.12)$$

A great simplification has occurred but how accurate this approximation is depends on the type of system being studied. We will now show that for practical systems and specifically for the systems considered in the following chapter, this is a reasonable approximation. This will be done for the AM-SSB and FM systems by taking another term, ($l = 0, 1$) in the series expansion of $H_n(\nu)$ of equation (4.53). It is not our aim to preview here the calculations of the next chapter but simply to obtain an error estimate and so we consider one channel with tone modulation.

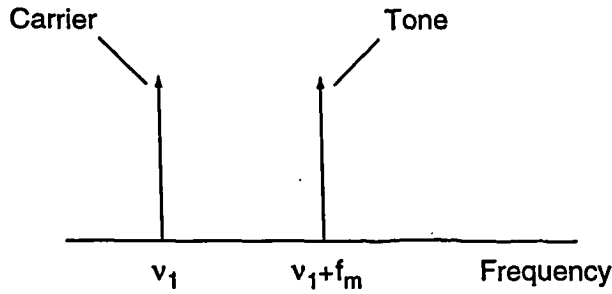


Figure 5.2: Single-tone modulation with frequency f_m in a AM upper-sideband system

AM system

Let us start by considering the AM system. For one channel only with tone modulation the complex envelope of the input signal is

$$z(t) = \cos 2\pi f_m t + i \sin 2\pi f_m t = e^{i2\pi f_m t} \quad (5.13)$$

where f_m is the maximum frequency of the baseband signal. In figure 5.2 a diagram is shown representing the location of the carrier and signal. For further simplicity denote the first derivative $dz(t)/dt = z^{(1)}(t)$ by $\dot{z}(t)$. The second-order harmonic term at twice the original carrier frequency $\nu = 2\nu_1$ is written as

$$q_{2\nu}(t) = \frac{1}{2} \left[H_2(\nu) z^2(t) + \frac{2}{2\pi i} \frac{\partial H_2(f_1, f_2)}{\partial f_1} \Big|_{\substack{f_1=\nu_1 \\ f_2=\nu_1}} \dot{z}(t) z(t) \right] \quad (5.14)$$

$$= \frac{1}{2} \left[H_2(\nu) + 2f_m \frac{\partial H_2(\nu_1, \nu_1)}{\partial f_1} \right] z^2(t) \quad (5.15)$$

The error in taking the first term only is now defined as

$$\text{err}_1 = \frac{2f_m \frac{\partial H_2(\nu_1, \nu_1)}{\partial f_1}}{H_2(\nu) + 2f_m \frac{\partial H_2(\nu_1, \nu_1)}{\partial f_1}} \quad (5.16)$$

which is plotted in figure 5.3 as a function of frequency (carrier location) for $f_m = 6$ MHz and two values of the laser bias current. From 5.2 figure another definition for the error can be easily obtained as in the case where $H_2(\cdot)$ is assumed constant over the channel band the value of H_2 is taken at ν_1 , the carrier location, whereas the correct value should have been

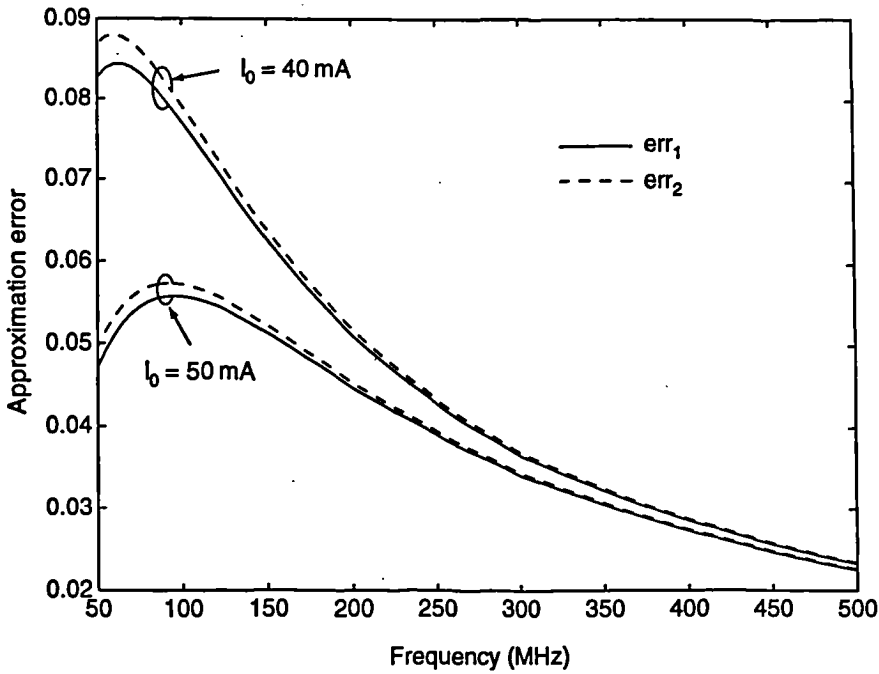


Figure 5.3: Approximation error on the evaluation of the second harmonic distortion resulting from taking the second-order transfer function constant over the channel band. AM single-tone modulation with frequency $f_m = 6$ MHz using a DFB-BH laser, parameters given in table 6.1

taken at $\nu_1 + f_m$. Thus, it follows that

$$\text{err}_2 = \frac{H_2(\nu_1 + f_m, \nu_1 + f_m) - H_2(\nu_1, \nu_1)}{H_2(\nu_1 + f_m, \nu_1 + f_m)} \quad (5.17)$$

This error is also plotted in figure 5.3 shown as a dashed line. First, it can be concluded that since the two errors are closely matched, the difference being negligible over most part of the spectrum range, the linear expansion of the transfer function at the carrier frequency is a good approximation to $H_2(f_1, f_2)$ over the channel band. Second, the simpler approximation of equation (5.10) is still reasonably accurate, the error being less than 9% in the worst case which occurs for low frequencies, decreasing rapidly with increasing frequency.

FM system

The same procedure will be used to estimate the error for FM single-tone modulation. The complex envelope of the FM signal is

$$z(t) = e^{i(\Delta f/f_m) \sin 2\pi f_m t} \quad (5.18)$$

where Δf is the FM frequency deviation. For FM systems operating in a single-octave at high frequencies the third-order distortion is dominant and this is the type of distortion we will consider. The complex envelope of the third harmonic is written as

$$q_{3\nu}(t) = \frac{3}{8} \left[H_3(\nu) + 2\Delta f \cos 2\pi f_m t \frac{\partial H_3(\nu_1, \nu_1, \nu_1)}{\partial f_1} \right] z^3(t) \quad (5.19)$$

The contribution of the derivative of H_3 now has a weighting coefficient that varies with time modulating the amplitude of $z^3(t)$. This modulation is however very small and we have taken

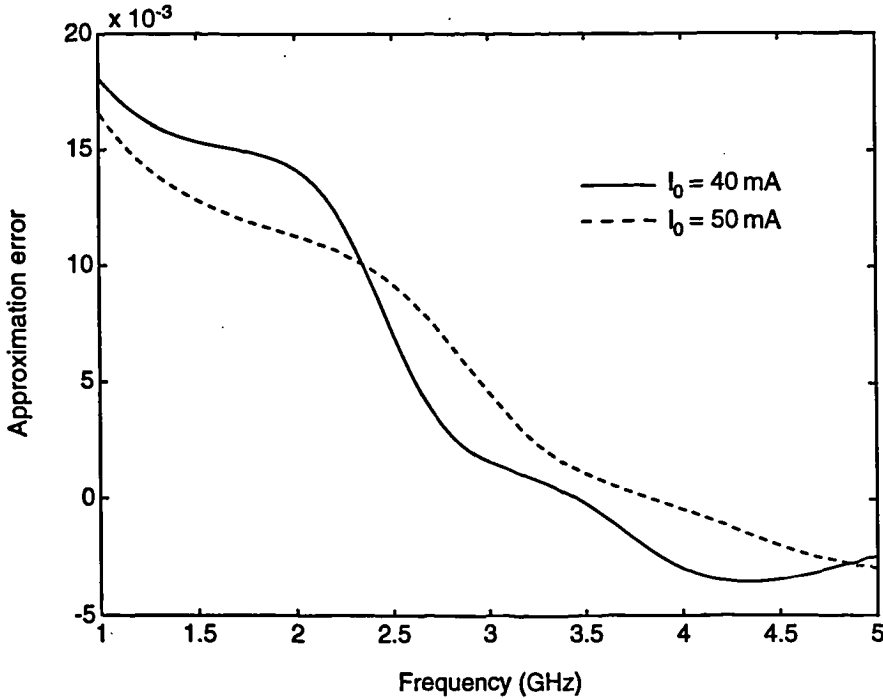


Figure 5.4: Approximation error on the evaluation of the third harmonic distortion resulting from taking the third-order transfer function constant over the channel band. FM single-tone modulation with frequency $\Delta f = 11.25$ MHz using a DFB-BH laser, parameters given in table 6.1

the error at $t = 0$ where it is maximum

$$\text{err} = \frac{2\Delta f \frac{\partial H_3(\nu_1, \nu_1, \nu_1)}{\partial f_1}}{H_3(\nu) + 2\Delta f \frac{\partial H_3(\nu_1, \nu_1, \nu_1)}{\partial f_1}} \quad (5.20)$$

It is interesting to note that the error increases with Δf , the frequency deviation of the FM signal, but does not depend on f_m . This error is plotted in figure 5.4 in the frequency range of 1 to 5 GHz for two values of the laser bias with parameters taken from a typical system. For $I_0 = 40$ mA and $I_0 = 50$ mA the resonance of the laser is at 7.5 and 9 GHz, respectively.

It shows that the error is much smaller than in the previous AM case, the reason being that at high frequencies the transfer functions vary slowly with frequency having zero derivative close to half the resonance oscillation frequency of the laser.

5.4 Carrier-to-intermodulation ratio

In order to quantify the affect of the intermodulation noise on the system performance we define the n th-order carrier-to-intermodulation ratio (CIR) for the r th channel located at frequency ν , due to input channels at f_{k_1}, \dots, f_{k_n} , as the ratio of the signal power to the n th-order intermodulation power at the output of the bandpass filter (BPF) (figure 5.1), with transfer function $H_{BP}(f)$. CIR is then written as

$$CIR_{nr}(f_{k_1}, \dots, f_{k_n}) = \frac{\int_B G_{p_{1\nu}}(f)df}{\int_B |H_{BP}(f)|^2 G_{p_{n\nu}}(f)df} \quad (5.21)$$

where the integrals are evaluated over the filter bandwidth B . Since the channels are independent the total n th-order CIR for channel r is obtained by summation of all the IMPs power terms of order n falling at frequency ν

$$CIR_{nr} = \frac{\int_B G_{p_{1\nu}}(f)df}{\sum_k \int_B |H_{BP}(f)|^2 G_{p_{n\nu}}(f)df} \quad (5.22)$$

where the summation over k includes all the distinct sets $\{k_1, \dots, k_n\}$ such that

$$f_{k_1} + \dots + f_{k_n} = m_{-N}f_{-N} + \dots + m_N f_N = \nu.$$

In the next chapter CIR will be calculated for three specific systems where the actual dependence of the intermodulation power with frequency is taken into account. Here, for the sake of simplicity, the application of Volterra series to the performance assessment of SCM systems will be given for the case of unmodulated subcarriers, which was treated previously in chapter 4. In this case the input is

$$j(t) = \frac{1}{2} \text{Re} \left\{ j_k e^{i2\pi f_k t} \right\} \quad (5.23)$$

and, after equation (4.52), CIR becomes

$$CIR_{nr} = \frac{|j_r H_1(\nu)|^2}{\sum_k B_{nm}^2 |j_{k_1} \dots j_{k_n} H_n(f_{k_1}, \dots, f_{k_n})|^2} \quad (5.24)$$

with $B_{nm} = n!/(m_{-N}! \cdots m_N!)$. Only second and third-order IMPs need be considered and the summation in the denominator of CIR can be expanded to

$$\begin{aligned}
 CIR^{-1} &= \sum_{\substack{f_{k_1}+f_{k_2} \\ -f_{k_3}=v}} \left(\frac{3}{2}\right)^2 \frac{|j_{k_1} j_{k_2} j_{k_3} H_3(f_{k_1}, f_{k_2}, -f_{k_3})|^2}{|j_r H_1(v)|^2} \\
 &+ \sum_{2f_{k_1}-f_{k_2}=v} \left(\frac{3}{4}\right)^2 \frac{|j_{k_1}^2 j_{k_2} H_3(f_{k_1}, f_{k_1}, -f_{k_2})|^2}{|j_r H_1(v)|^2} \\
 &+ \sum_{f_{k_1} \pm f_{k_2}=v} \frac{|j_{k_1} j_{k_2} H_2(f_{k_1}, \pm f_{k_2})|^2}{|j_r H_1(v)|^2} \\
 &+ \sum_{2f_{k_1}=v} \left(\frac{1}{2}\right)^2 \frac{|j_{k_1}^2 H_2(f_{k_1}, f_{k_1})|^2}{|j_r H_1(v)|^2}, \quad k_1 \neq k_2 \neq k_3 \quad (5.25)
 \end{aligned}$$

The subscripts in CIR have been dropped, remembering that this expression refers to a specific channel subject to third and second-order intermodulation. So far nothing has been said about the amplitudes of the carriers which relates to the per-channel optical modulation depth, m , at the laser output by

$$j_k = \frac{m(f_k) p_0}{H_1(f_k)} \quad (5.26)$$

Constant j

If the channels have the same amplitude and considering that, for a large number of channels, the number of third-order three-tone products and two-tone products increases as N^2 and N , respectively, and the number of second-order IMPs is proportional to N [72, 73] the CIR can be conveniently written as

$$CIR^{-1} = m^4 (D_{111} N^2 + D_{21} N) + m^2 (D_{11} + D_2) \quad (5.27)$$

where D_{111} , D_{21} , D_{11} and D_2 are the distortion coefficients, associated with each type of distortion, given by

$$D_{111} = \left(\frac{3}{2}\right)^2 \frac{p_0^4}{N^2} \sum_k \frac{|H_3(f_{k_1}, f_{k_2}, -f_{k_3})|^2}{|H_1(v)|^6} \quad (5.28)$$

$$D_{21} = \left(\frac{3}{4}\right)^2 \frac{p_0^4}{N} \sum_k \frac{|H_3(f_{k_1}, f_{k_1}, -f_{k_2})|^2}{|H_1(v)|^6} \quad (5.29)$$

$$D_{11} = \frac{p_0^2}{N} \sum_k \frac{|H_2(f_{k_1}, \pm f_{k_2})|^2}{|H_1(v)|^4} \quad (5.30)$$

$$D_2 = \left(\frac{1}{2}\right)^2 p_0^2 \sum_k \frac{|H_2(f_k, f_k)|^2}{|H_1(f_k)|^4} \quad (5.31)$$

and m corresponds to the modulation depth of the channel under consideration. Note that, since the amplitude of the electrical carriers is the factor which is taken as constant, m will be frequency dependent (varies between channels) if the laser transfer function H_1 is not flat within the transmission band.

Constant m

On the other hand, if we take the modulation depth of each channel as constant, equation (5.27) still remains valid but a different expression for the distortion coefficients is obtained, reflecting the fact that the input signal amplitudes are now scaled by the inverse of the first-order transfer function:

$$D_{111} = \left(\frac{3}{2}\right)^2 \frac{p_0^4}{N^2} \sum_k \frac{|H_3(f_{k_1}, f_{k_2}, -f_{k_3})|^2}{|H_1(f_{k_1})H_1(f_{k_2})H_1(-f_{k_3})|^2} \quad (5.32)$$

$$D_{21} = \left(\frac{3}{4}\right)^2 \frac{p_0^4}{N} \sum_k \frac{|H_3(f_{k_1}, f_{k_1}, -f_{k_2})|^2}{|H_1(f_{k_1})H_1(f_{k_1})H_1(-f_{k_2})|^2} \quad (5.33)$$

$$D_{11} = \frac{p_0^2}{N} \sum_k \frac{|H_2(f_{k_1}, \pm f_{k_2})|^2}{|H_1(f_{k_1})H_1(\pm f_{k_2})|^2} \quad (5.34)$$

$$D_2 = \left(\frac{1}{2}\right)^2 p_0^2 \sum_k \frac{|H_2(f_k, f_k)|^2}{|H_1(f_k)|^4} \quad (5.35)$$

The distortion coefficients are important in that they enable one to assess, independently of the number of channels, the impact of laser distortion and the influence on system performance of key parameters such as bias current (resonance frequency) and channel frequency allocation.

5.5 Overall system performance

Thus far only contributions from the laser nonlinearity have been considered. In the determination of the overall system carrier-to-noise ratio (CNR) relative intensity noise (RIN), receiver shot and thermal noise must also be taken into account. The CNR in the receiver may be expressed as:

$$CNR_r^{-1} = CNR_{Tx}^{-1} + CNR_{Rx}^{-1} \quad (5.36)$$

where CNR_{TX} is the ratio of the carrier power to the noise power generated by the laser diode and CNR_{RX} is the ratio of the carrier power to the noise power generated at the receiver. These ratios are relative to a specific channel r . For simplicity of notation we will drop the subscript r .

The ratios are given by

$$CNR_{TX}^{-1} = \frac{2BRIN}{m^2} + CIR^{-1} \quad (5.37)$$

$$CNR_{RX} = \frac{\frac{1}{2}(mgI)^2}{(2eI g^2 F + \langle I_r^2 \rangle)B} \quad (5.38)$$

with definitions as follows

RIN Relative Intensity noise

g APD gain

$\langle I_r^2 \rangle$ receiver noise spectral noise density A^2/Hz

I primary dc photocurrent

$F=g^x$ excess APD noise factor

e electronic charge

B signal bandwidth

The total CNR is then written as

$$CNR = \frac{\frac{1}{2}m^2 I^2 g^2}{\langle I_r^2 \rangle B + g^2 I^2 RIN B + 2eBI g^2 F + \frac{1}{2}g^2 I^2 \{m^6 C_1 + m^4 C_2\}} \quad (5.39)$$

with

$$C_1 = D_{111}N^2 + D_{21}N \quad (5.40)$$

$$C_2 = D_{11}N + D_2 \quad (5.41)$$

CNR may be bivariate maximised in m and g for a given I , equivalent to balancing the total contributions of signal-independent and signal-dependent noise terms [74]. The maximum CNR for an optimum modulation depth, m_{opt} , and a given I , obtained by differentiation of (5.39), is

$$CNR^{-1}(m_{opt}) = 3m_{opt}^4 [D_{111}N^2 + D_{21}N] + 2m_{opt}^2 [D_{11}N + D_2] \quad (5.42)$$

or, conversely, m_{opt} may be determined by specifying the required CNR

$$m_{opt}^2 = \frac{-C_2 + \sqrt{C_2^2 + 3C_1/CNR}}{3C_1}. \quad (5.43)$$

The optimum APD gain is given by the usual expression

$$g_{opt} = \left[\frac{\langle I_r^2 \rangle}{eIx} \right]^{1/(2+x)} \quad (5.44)$$

The maximum CNR for an optimum OMD and APD gain is then

$$CNR(m_{opt}, g_{opt}) = \frac{\frac{1}{2}m_{opt}^2 I^2 g_{opt}^2}{K_3 B \left\{ \langle I_r^2 \rangle \left[1 + \frac{2}{x} \right] + g_{opt}^2 I^2 RIN \right\}} \quad (5.45)$$

where

$$K_3 = \frac{3m_{opt}^2 C_1 + C_2}{2m_{opt}^2 C_1 + C_2} \quad (5.46)$$

The necessary primary dc photocurrent to achieve $CNR(m_{opt}, g_{opt})$ is readily obtained by combination of equations (5.44) and (5.45)

$$I_{APD} = \left[\frac{ex}{\langle I_r^2 \rangle} \right]^{\frac{1}{1+x}} \left[\frac{CNR(m_{opt}, g_{opt}) K_3 B \langle I_r^2 \rangle (1 + 2/x)}{\frac{1}{2}m_{opt}^2 - RIN K_3 B} \right]^{\frac{1+x/2}{1+x}} \quad (5.47)$$

For a PIN receiver the gain and the excess noise factor are both unity; the required photocurrent to achieve $CNR(m_{opt})$ is then

$$I_{PIN} = \frac{e + \sqrt{e^2 + W \langle I_r^2 \rangle}}{W} \quad (5.48)$$

with

$$W = \frac{m_{opt}^2}{2CNRK_3B} - RIN \quad (5.49)$$

where once again we have followed the notation of [74].

In practice we are interested in obtaining the receiver sensitivity for a desired CNR and a specific number of channels with the laser biased at a certain point. These last two parameters, number of channels and laser bias current, will determine the levels of distortion at the laser output and are included in the analysis through the distortion coefficients D . Once the system parameters are specified the distortion coefficients are determined and from these the optimum modulation depth for the desired CNR follows from equation (5.43). Depending whether the system uses a PIN or an APD, the receiver sensitivity ($I_{PIN(APD)}$) times the photodetector

responsivity R_0) is readily obtained from equation (5.47) or (5.48), respectively.

In cases where either only second or third-order intermodulation effects are significant considerable simplification of the previous equations is possible. If only second-order distortion is significant the optimum modulation depth (equation 5.42) may be reduced to

$$m_{opt} = \left[2 \cdot CNR \cdot (D_{11}N + D_2) \right]^{-1/2} \quad (5.50)$$

Similarly, for third-order distortion effects

$$m_{opt} = \left[3 \cdot CNR \cdot (D_{111}N^2 + D_{21}N) \right]^{-1/4} \quad (5.51)$$

The maximum allowable number of channels may be estimated by defining N_{max} as the number channels for zero shot and thermal noise, that is, the ideal situation when no additional noise is introduced at the detection process. If second-order distortion is dominant, then for both PIN and APD cases

$$N_{max} \simeq (4 \cdot CNR^2 D_{11} B \cdot RIN)^{-1} \quad (5.52)$$

whereas for third-order intermodulation

$$N_{max} \simeq \left[(3CNR)^{3/2} D_{111}^{1/2} RIN \cdot B \right]^{-1} \quad (5.53)$$

For example, if $CNR = 20$ dB, $D_{111} = 0.05$ and $D_{11} = 0.05$ [1, 74] with $RIN = -130$ dB/Hz and $B = 36$ MHz then N_{max} is 139 and 414 for the second and third-order cases. Note that, in accordance with the previous definition for the distortion coefficients, these equations are bias and frequency dependent: as the frequency channel allocation gets closer to the resonance frequency the distortion coefficients reach maxima that forces N_{max} to correspondingly lower values.

5.6 Receiver design considerations

It has been verified that the optimum modulation depth is determined by the intermodulation distortion. Therefore, for a certain amount of distortion (given by the distortion coefficients), the photocurrent I must increase if higher values of CNR are required. Shot noise and RIN then start to dominate. The associated APD gain will reduce towards unity for a fixed circuit noise and APD receivers do not provide any advantage. A PIN diode is then the preferred

choice. Even so APDs can improve performance for relatively low CNR particularly when circuit noise is dominant.

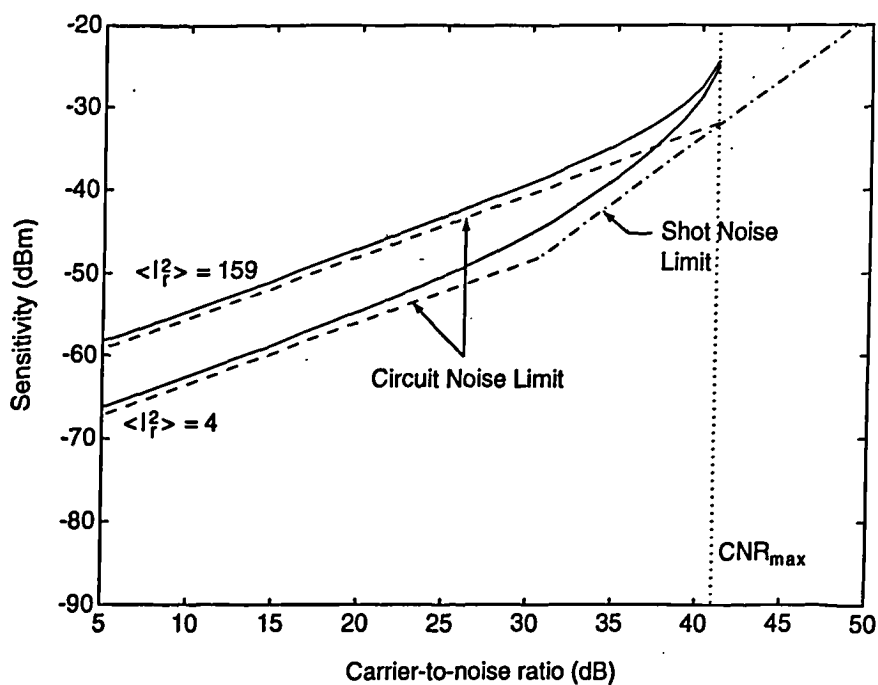


Figure 5.5: Sensitivity as a function of carrier-to-noise ratio using a PIN detector for two circuit noise levels. Parameters are $R_0 = 0.8 \text{ A/W}$, $N = 62$, $B = 36 \text{ MHz}$, $RIN = -155 \text{ dB/Hz}$ and $D_{111} = 0.02$

Figures 5.5 and 5.6 show the performance obtained with a PIN detector and an APD, respectively. We have consider an APD with $x = 0.7$, responsivity of $R_0 = 0.8 \text{ A/W}$ and two circuit noise levels corresponding to a tuned receiver with $\langle I_r^2 \rangle = 4 \text{ pA}^2/\text{Hz}$ [75] and a 50 Ohm low noise amplifier with a noise figure of 3 dB for which $\langle I_r^2 \rangle = 159 \text{ pA}^2/\text{Hz}$. Other parameters are number of channels $N = 62$, $B = 36 \text{ MHz}$, $RIN = -155 \text{ dB/Hz}$ and third-order intermodulation $D_{111} = 0.02$, corresponding to a system [52] operating in the frequency range of 2.7 to 5.2 GHz (see also chapter 6). The solid lines in figure 5.5 represent the relation between CNR and the optical power for the optimum modulation depth, derived from equation (5.48) (values of the optimum modulation depth can be read from figure 5.7 since m_{opt} is independent of the type of detector used). In this figure it is seen that when CNR ratios of less 25 dB are required the difference in sensitivity between the two circuits is approximately 8 dB, as both are operating in the circuit noise limit. Between 25 and 35 dB this difference is reduced and for CNR greater than 35 dB not only shot noise but also RIN

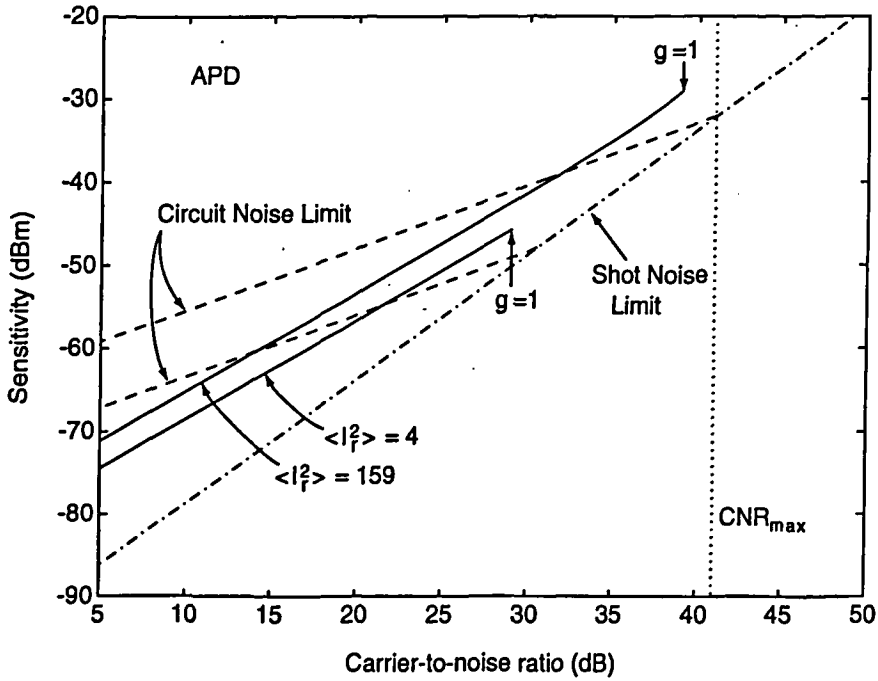


Figure 5.6: Sensitivity as a function of carrier-to-noise ratio using an APD with the same assumptions of figure 5.5: $R_0 = 0.8 \text{ A/W}$, $x = 0.7$, $N = 62$, $B = 36 \text{ MHz}$, $RIN = -155 \text{ dB/Hz}$ and $D_{111} = 0.02$

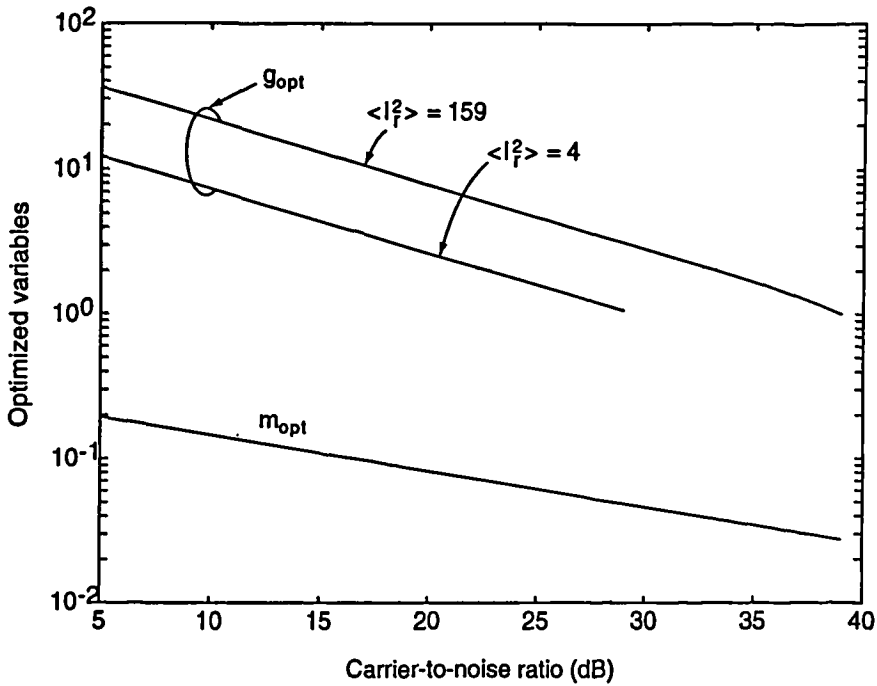


Figure 5.7: Optimum avalanche gain and optimum modulation depth associated with the curves of figure 5.6.

and intermodulation distortion become important until a point is reached above which no transmission is possible.

Figure 5.6 shows the relation between CNR and the received optical power for an APD detector. The asymptotic values of the circuit noise limit for the two amplifier noise levels (using a PIN) as well as shot noise limit are shown by dashed lines. The solid lines for the received optical power correspond to optimum avalanche gain and optimum modulation depth, these are shown in figure 5.7. At low CNR the optimum avalanche gain is large, decreasing as the CNR increases and reaching a value of 1 (PIN) close to the point where the circuit and shot noise asymptotes intersect. The power margin relative to a PIN detector, for a CNR of approximately 16 dB, is 3.5 dB for the tuned receiver and 8 dB for the 50 Ohm amplifier. Thus, the APD can improve system performance by providing significant reduction in the required optical power for low CNR, such as FM systems, but is ineffective for large CNR as required in AM systems.

5.7 Clipping distortion implications

We have seen that RIN and intermodulation distortion establish a limit to the maximum obtainable optical modulation depth or carrier-to-noise ratio. Recently, it has been shown that clipping effects determine a fundamental limit to the total modulation depth [61, 76]. Thus, even if the distortion coefficients are all zero a maximum CNR still exists. This limit imposed by clipping distortion will be determined based on the model by Saleh, which has been revised in Reference [77] and shown to agree with simulation results to within 2 dB for values of the effective modulation depth, $\mu = m\sqrt{N/2}$, greater than 0.25. In Saleh's analysis, the nonlinear distortion is calculated by approximating the sum of multiple randomly phased subcarriers as a Gaussian probability density of the amplitude. The total nonlinear distortion is then assumed to be proportional to the power in the Gaussian tail that falls below zero and to be distributed uniformly over all channels. The total mean-square value of the clipped portion of $I(t)$ is then [61, 77].

$$\langle I_{clip}^2 \rangle = \frac{1}{\sqrt{2\pi}} \frac{\mu^5}{1 + 6\mu^2} e^{-1/2\mu^2} \quad (5.54)$$

Additionally, a calculation by Mazo [78] indicated that over a wide range of μ most of the distortion is thrown out of the transmission band. Thus, the carrier to clipping distortion noise

ratio, CCR, becomes

$$CCR^{-1} = \Lambda \sqrt{\frac{2}{\pi}} \frac{\mu^3}{1 + 6\mu^2} e^{-1/2\mu^2} \quad (5.55)$$

where Λ represents the fraction of the clipping distortion power which falls in the transmission band, which for the US-CATV plan (50–500 MHz) takes the value $\Lambda = 1/2$ [78]. Rewriting (5.39) to include clipping noise we obtain

$$CNR^{-1} = \frac{KN}{\mu^2 I_r^2 g^2} + \Lambda \sqrt{\frac{2}{\pi}} \frac{\mu^3}{1 + 6\mu^2} e^{-1/2\mu^2} + 4\mu^4 D_{111} + 2\mu^2 D_{11} \quad (5.56)$$

where K includes all the other noise contributions

$$K = \langle I_r^2 \rangle B + g^2 I_r^2 RINB + 2eBIg^{2+x} \quad (5.57)$$

The CNR at optimum μ and APD gain, μ_{opt} and g_{opt} respectively, now becomes

$$CNR^{-1}(\mu_{opt}) = \Lambda \frac{e^{-1/2\mu_{opt}^2} \mu_{opt} + 11\mu_{opt}^3 + 18\mu_{opt}^5}{\sqrt{2\pi} (1 + 6\mu_{opt}^2)^2} + 12\mu_{opt}^4 D_{111} + 4\mu_{opt}^2 D_{11} \quad (5.58)$$

and g_{opt} remains unchanged. The relation between the photocurrent I and μ_{opt} is determined from the solution of the following equation

$$\left[\langle I_r^2 \rangle (1 + 2/x)BN + g_{opt}^2 I_r^2 RINBN \right] = \mu_{opt}^2 g_{opt}^2 I_r^2 \times \left[\Lambda \frac{e^{-1/2\mu_{opt}^2} \mu_{opt} + 9\mu_{opt}^3 + 6\mu_{opt}^5}{\sqrt{2\pi} (1 + 6\mu_{opt}^2)^2} + 8\mu_{opt}^4 D_{111} + 2\mu_{opt}^2 D_{11} \right] \quad (5.59)$$

Equation 5.58 may be used to compare the optimum CNR with and without clipping. Figure 5.8 plots the achievable CNR as a function of μ comparing the contribution of clipping distortion (dashed line) and third-order intermodulation distortion (dotted line) for the same system considered previously, corresponding to an FM system in the 2.7 to 5.2 GHz range. Over this frequency range the value of Λ is $\approx 1/4$ although the lower frequency channels suffer 2.5 dB more clipping distortion than the high frequency channels. The actual calculations are given in Appendix A. It is seen that laser intrinsic distortion dominates over a wide range of values of μ . The contribution of clipping distortion increases with increasing μ reaching a maximum at $\mu = 0.55$ where it degrades CNR, relative to the resonance distortion, by 1.3 dB. For $CNR = 16.5$ dB, the optimum μ equals 0.51 corresponding to a per-channel modulation depth of $m_{opt} = 9.2\%$ and the total modulation depth is $m_{tot} = mN = 5.7$ for a 62 channel system. That is, considerable overmodulation occurs, it being more advantageous

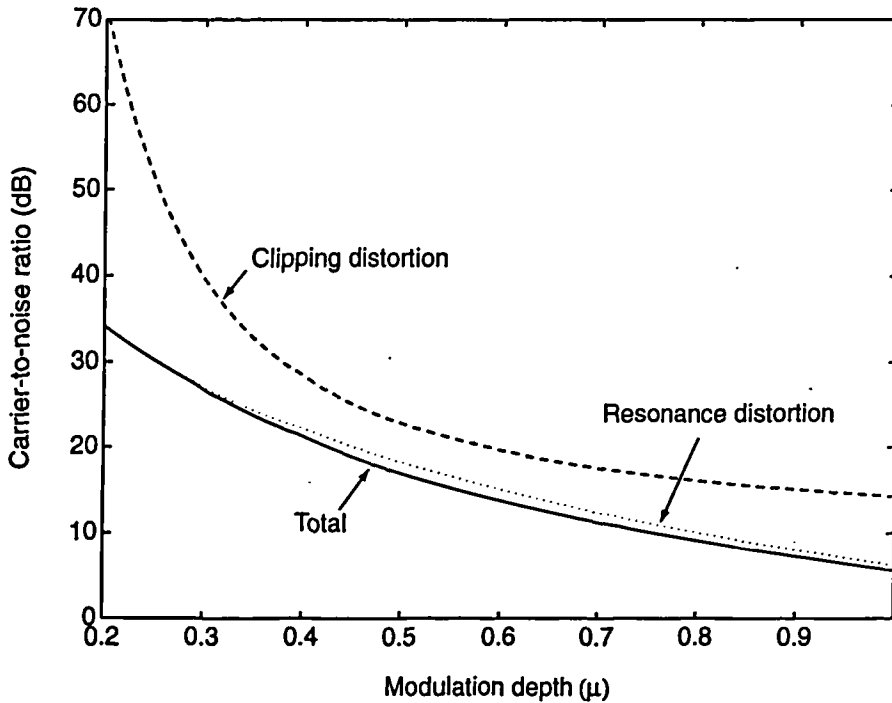


Figure 5.8: Contribution of clipping distortion and intermodulation distortion due to laser resonance distortion to the total carrier-to-noise ratio: $D_{111} = 0.02$, $D_{11} = 0$, $\Lambda = 1/4$ and $N = 62$.

to accept some distortion than constraining the total modulation depth to 100% [79]. An adequate measure of the total effective modulation depth is the r.m.s modulation defined as $m_{\text{rms}} = m\sqrt{N}$ [79] which, in the example given, takes the value of $m_{\text{rms}} = 72\%$.

For AM systems overmodulation is still advantageous. Clipping distortion, however, has a greater impact on system performance than in the example given, in spite of the high CNR and strict intermodulation distortion requirements. This latter case will be discussed in the following chapter.

5.8 Summary

The Volterra series analysis of laser distortion given in the previous chapter was here applied to assess the performance of SCM systems. The overall performance quantified in terms of the carrier-to-noise ratio was obtained for the case of unmodulated subcarriers. The case of modulated channels will be treated in the following chapter for specific systems. It has been shown that laser distortion can be quantified in terms of distortion coefficients which take into account the affect on system performance of key parameters such as bias current and

channel frequency allocation. Optimum performance was then identified corresponding to balancing the total contributions of signal dependent and independent noise contributions after the detection process. It was then shown that APD photodetectors can improve performance significantly for relatively low carrier-to-noise ratios, of which the FM system is a case, and for high values of circuit noise as occurs in the simple 50 Ohm amplifier. Finally, the impact of clipping distortion on the overall performance has been assessed and an illustrative case has been considered which shows that it is advantageous to accept overmodulation and the associated clipping distortion rather than constraining the total modulation depth to 100%. Even so, intermodulation distortion as a result of the intrinsic laser distortion is the dominant distortion mechanism for a large range of modulation depths for one octave systems operating in the GHz frequency interval.

Chapter 6

SCM system case studies

6.1 Introduction

The theoretical analysis of the previous chapter is here applied to study relevant systems in this area of research. Particular emphasis is given to laser nonlinear distortion (resonance and clipping distortion) and its contribution to the overall system performance. Two important system cases studies are first considered, FM broadcast and AM-CATV systems (sections 6.2 and 6.3, respectively), dealing with the transmission of high quality video signals. Although FM systems are very reliable, capable of tolerating the loss associated with a passive optical distribution network, AM systems are very attractive as they provide direct compatibility with present day residential video and CATV systems. As seen later, the requirements of these two systems are radically different.

The third case discussed in section 6.4 is a new evolving application concerned with the remote delivery, over optical fibres, of future mobile radio services and the provision of flexible customer access connections [80, 81]. Specifically, the performance of the return link is assessed where the existence of a wide dynamic variation of power levels due to range and fading associated with the mobile user imposes stringent requirements on laser linearity.

In the study presented the intermodulation power spectral density of the distortion products of interest is first determined. This enables one to assess accurately the impact of laser resonance distortion on system performance. The results of section 5.5 are then directly applied and illustrative results are given for each of the three systems mentioned above.

6.2 FM broadcast systems

6.2.1 Introduction

The performance of FM-SCM broadcast systems, for which many field trials have been reported [52, 10, 82, 83], is here accurately assessed. FM modulation is very reliable being more immune to noise than AM, with large improvements in signal-to-noise ratio (SNR) over carrier-to-noise ratio (CNR) at the expense of a wider bandwidth [48]. The basic FM-SCM system is shown in figure 5.1, the modulator being assumed to be of FM type.

The baseband video signal is converted to an FM subcarrier with a bandwidth typically of 30 to 40 MHz [52]. The increased bandwidth is exchanged for a considerable SNR improvement so that the SNR at the demodulator output is much larger than the input CNR. A 16.5 dB CNR yields a high quality signal with 56 dB SNR [48]. The FM signal bandwidth can be estimated using Carson's rule, $B = \Delta f_{pp} + 2f_m$, where Δf_{pp} is the peak-to-peak frequency deviation and f_m is the highest frequency of the composite video plus audio signal. Since the highest frequency of the composite video corresponds to the audio subcarrier, f_m is usually designated as the "top audio subcarrier frequency".

The intermodulation products (IMPs) generated from different uncorrelated signals can be considered to have equivalent deviations of $\sqrt{2}\Delta f_{pp}$ for second-order IMPs and $\sqrt{3}\Delta f_{pp}$ for third-order IMPs. Consequently, for the purpose of estimating the intermodulation power spectral we will consider the IMPs as wideband FM; this is also justified by the fact that a video signal contains little power in the high-frequency region.

6.2.2 Intermodulation power spectral density

The power spectral density of the intermodulation products for the wideband FM case will now be derived. The laser input current is considered to be a sum of N FM signals centered at ν_k

$$\begin{aligned} j(t) &= \sum_{k=1}^N A_k \cos[2\pi \nu_k t + \phi_k(t) + \psi_k] \\ &= \sum_{k=1}^N \operatorname{Re} \left\{ z_k(t) e^{i(2\pi \nu_k t)} \right\}. \end{aligned} \quad (6.1)$$

with

$$\begin{aligned} z_k(t) &= A_k e^{i(\phi_k(t) + \psi_k)}, \\ z_{-k}(t) &= z_k^*(t) \end{aligned} \quad (6.2)$$

and ψ_k is a uniform distributed random phase. We now assume $H_n(\nu_{k_1}, \dots, \nu_{k_n})$ to be constant around any set of frequencies $\nu = (\nu_{k_1}, \dots, \nu_{k_n})$ so that only the first term in the Taylor series expansion of H_n (equation 4.53) needs to be considered. The consequences of this approximation are discussed in the previous chapter. In this case the complex envelope of a particular intermodulation product falling at frequency ν due to signals centered at $\nu_{k_1}, \dots, \nu_{k_n}$ is

$$q_{n\nu}(t) = \frac{n!2^{-n+1}}{m_{-N}! \dots m_N!} H_n(\nu) \prod_{k=-N}^N z_k^{m_k}(t) \quad (6.3)$$

The calculation of the intermodulation power spectral density (IPSD) proceeds by evaluating the autocorrelation of $q_{n\nu}(t)$, $R_{q_{n\nu}}(\tau)$, which relates to the autocorrelation of $p_{n\nu}(t)$ by equation (5.8). The calculation of $R_{q_{n\nu}}(\tau)$ now follows

$$R_{q_{n\nu}}(\tau) = E \{ q_{n\nu}^*(t) q_{n\nu}(t + \tau) \} \quad (6.4)$$

$$\begin{aligned} &= E \left\{ B_{nm}^2 |H_n(\nu)|^2 \prod_{k=-N}^N [z_k^{m_k}(t)]^* z_k^{m_k}(t + \tau) \right\} \\ &= B_{nm}^2 |H_n(\nu)|^2 \left[\prod_{k=-N}^N A_k^{2m_k} \right] E \left\{ e^{im_k[\phi_k(t+\tau) - \phi_k(t)]} \right\} \end{aligned} \quad (6.5)$$

Noting that the last term equals the second-order characteristic function of the process ϕ_k

$$E \left\{ e^{i\omega_1 \phi_k(t+\tau) + i\omega_2 \phi_k(t)} \right\} = \Phi_{\phi_k}(\omega_1, \omega_2, \tau) \quad (6.6)$$

$R_{q_{n\nu}}(\tau)$ is compactly written as

$$R_{q_{n\nu}}(\tau) = B_{nm}^2 |H_n(\nu)|^2 \left[\prod_{k=-N}^N A_k^{2m_k} \right] \prod_{k=-N}^N \Phi_{\phi_k}(m_k, -m_k, \tau) \quad (6.7)$$

For an FM signal the phase equals the integral of the modulating signal $x_k(t)$

$$\phi_k(t) = 2\pi \Delta f \int_0^t x_k(\xi) d\xi, \quad \Delta f = \frac{\Delta f_{pp}}{2} \quad (6.8)$$

and

$$\Phi_{\phi_k}(m_k, -m_k, \tau) = E \left\{ \exp \left(im_k 2\pi \Delta f \int_t^{t+\tau} x_k(\xi) d\xi \right) \right\} \quad (6.9)$$

If $|t| \ll 1/f_m$ where f_m is the maximum frequency of the signal $x_k(t)$ then the integral in equation (6.8) can be written as

$$\int_0^t x_k(\xi) d\xi \simeq x_k(0)t, \quad |t| \ll 1/f_m \quad (6.10)$$

In this case the second-order characteristic function $\Phi_{\phi_k}(m_k, -m_k, \tau)$ can be approximated by the first-order characteristic function of x_k

$$\begin{aligned} \Phi_{\phi_k}(m_k, -m_k, \tau) &\simeq E \left\{ e^{i2\pi m_k \Delta f x(0)\tau} \right\}, \quad |\tau| \ll 1/f_m \\ &= \Phi_{x_k}(2\pi m_k \Delta f \tau) \end{aligned} \quad (6.11)$$

From this last relation and equation (6.7) it follows that

$$R_{q_{nv}}(\tau) = B_{nm}^2 |H_n(\nu)|^2 \left[\prod_{k=-N}^N A_k^{2m_k} \right] \prod_{k=-N}^N \Phi_{x_k}(2\pi m_k \Delta f \tau), \quad |\tau| \ll 1/f_m \quad (6.12)$$

If Δf is sufficiently large then equation (6.12) is a good approximation in the region where Φ_{x_k} takes significant values and if $x_k(t)$ has a uniform probability density function (p_{x_k}):

$$\prod_{k=-N}^N \Phi_{x_k}(2\pi m_k \Delta f \tau) = \prod_{k=-N}^N \text{sinc}(2m_k \Delta f \tau) \simeq 0, \quad \text{for } |\tau| > \tau_0 \quad (6.13)$$

Applying the Fourier transform to equation (6.12)

$$\begin{aligned} G_{q_{nv}}(f) &= B_{nm}^2 |H_n(\nu)|^2 \left[\prod_{k=-N}^N A_k^{2m_k} \right] \mathcal{F} \left\{ \prod_{k=-N}^N \Phi_{x_k}(2\pi m_k \Delta f \tau) \right\} \\ &= B_{nm}^2 |H_n(\nu)|^2 \left[\prod_{k=-N}^N A_k^{2m_k} \right] \\ &\quad \times \left[\frac{1}{m_{-N} \Delta f} p_{x_{-N}} \left(\frac{f}{m_{-N} \Delta f} \right) * \cdots * \frac{1}{m_N \Delta f} p_{x_N} \left(\frac{f}{m_N \Delta f} \right) \right] \end{aligned} \quad (6.14)$$

where the operation $*$ denotes convolution. Finally the n th-order intermodulation power spectral density, $G_{p_{nv}}$ given by equation (5.9), becomes

$$\begin{aligned} G_{p_{nv}}(f) &= \frac{1}{4} [G_{q_{nv}}(f - \nu) + G_{q_{nv}}(-f - \nu)] \\ &= \frac{1}{4} B_{nm}^2 |H_n(\nu)|^2 \left[\prod_{k=-N}^N A_k^{2m_k} \right] \\ &\quad \times \left\{ \frac{1}{m_{-N} \Delta f} p_{x_{-N}} \left(\frac{f - \nu}{m_{-N} \Delta f} \right) * \cdots * \frac{1}{m_N \Delta f} p_{x_N} \left(\frac{f - \nu}{m_N \Delta f} \right) \right\} \end{aligned}$$

$$+ \frac{1}{m_{-N}\Delta f} p_{x_{-N}} \left(\frac{-f - \nu}{m_{-N}\Delta f} \right) * \cdots * \frac{1}{m_N\Delta f} p_{x_N} \left(\frac{-f - \nu}{m_N\Delta f} \right) \} \quad (6.15)$$

with

$$p_{x_{-N}}(f) = p_{x_N}(-f) \quad (6.16)$$

Equation (6.15) is indeterminate when $m_k = 0$; we should note however that

$$\mathcal{F} \{ \Phi_{x_k}(2\pi m_k \Delta f \tau) \} |_{m_k=0} = \delta(f) \quad (6.17)$$

and so

$$\left[\frac{1}{m_k \Delta f} p_{x_k} \left(\frac{f - \nu}{m_k \Delta f} \right) \right] |_{m_k=0} = \delta(f). \quad (6.18)$$

The total intermodulation spectral density at frequency ν is the sum of all the terms given by equation (6.15) resulting from all possible combinations of the input channels.

6.2.3 Carrier-to-intermodulation ratio

The n th-order carrier-to-intermodulation ratio CIR for the r th channel centered at frequency ν is defined as the ratio of signal power to the intermodulation power at the output of the bandpass filter at the receiver (figure 5.1), with transfer function having unit gain over the signal bandwidth B

$$(CIR)_{nr} = \frac{\frac{1}{2} |H_1(\nu)|^2 A_r^2}{\frac{1}{2} B_{nm}^2 \left[\prod_{k=-N}^N A_k^{2m_k} \right] \alpha_n \sum_k |H_n(f_{k_1}, \dots, f_{k_n})|^2} \quad (6.19)$$

where the summation over k includes all the sets $\{k_1, \dots, k_n\}$ such that $f_{k_1} + \dots + f_{k_n} = \nu$ and

$$\alpha_n = \int_{-B/2\Delta f}^{B/2\Delta f} \frac{1}{m_{-N}} p_{x_{-N}} \left(\frac{f}{m_{-N}} \right) * \cdots * \frac{1}{m_N} p_{x_N} \left(\frac{f}{m_N} \right) df \quad (6.20)$$

if p_{x_k} is an even function. Assuming as before that x_k has uniform probability density between -1 and 1 , and that all channels have the same amplitude the third-order CIR becomes

$$(CIR)_{r111}^{-1} = \left(\frac{3}{2} \right)^2 (mp_0)^4 \alpha_{111} \sum_k \frac{|H_3(f_{k_1}, f_{k_2}, -f_{k_3})|^2}{|H_1(\nu)|^6} \quad (6.21)$$

The factor α_{111} denotes the fraction of the total intermodulation power that is passed by the filter

$$\alpha_{111} = \frac{1}{8} \int_{-B/2\Delta f}^{B/2\Delta f} \text{rect} \left(\frac{f}{2} \right) * \text{rect} \left(\frac{f}{2} \right) * \text{rect} \left(\frac{f}{2} \right) df$$

$$= \frac{1}{8} \left[\frac{1}{24} \zeta^3 - \frac{3}{4} \zeta^2 + \frac{9}{2} \zeta - 1 \right], \quad \zeta = \frac{B}{2\Delta f} \quad \text{and} \quad 1 < \zeta < 3 \quad (6.22)$$

The number of intermodulation products of type $f_i + f_j - f_k$ falling at the r th-channel in a sequence of N equally spaced carriers and for large N increases as N^2 so equation (6.21) can be expressed in terms of the distortion coefficient D_{111}

$$\begin{aligned} (CIR)_{r111}^{-1} &= D_{111} m^4 N^2 \\ D_{111} &= \left(\frac{3}{2} \right)^2 p_0^4 \frac{\alpha_{111}}{N^2} \sum_k \frac{|H_3(f_{k_1}, f_{k_2}, -f_{k_3})|^2}{|H_1(\nu)|^6} \end{aligned} \quad (6.23)$$

The other most important products besides the three-tone IMP are the two-tone third-order IMP ($2f_i - f_j$) and the second-order distortion products that have to be considered if the transmission band is not limited to one octave.

Following the same approach it is possible to show that the total CIR falling at channel r located at frequency ν is

$$(CIR)_r^{-1} = m^4 [D_{111} N^2 + D_{21} N] + m^2 [D_{11} N + D_2] \quad (6.24)$$

The indices of the distortion coefficients D identify the order and type of distortion products and are

$$D_{21} = \left(\frac{3}{4} \right)^2 p_0^4 \frac{\alpha_{21}}{N} \sum_k \frac{|H_3(f_{k_1}, f_{k_2}, -f_{k_3})|^2}{|H_1(\nu)|^6} \quad (6.25)$$

$$D_{11} = p_0^2 \frac{\alpha_{11}}{N} \sum_k \frac{|H_2(f_{k_1}, f_{k_2})|^2}{|H_1(\nu)|^4} \quad (6.26)$$

$$D_2 = \left(\frac{1}{2} \right)^2 p_0^2 \alpha_2 \sum_k \frac{|H_2(f_k, f_k)|^2}{|H_1(\nu)|^4} \quad (6.27)$$

The factors α are determined from equation (6.20)

$$\begin{aligned} \alpha_{21} &= \int_{-\zeta}^{\zeta} \frac{1}{2} p_{x_1} \left(\frac{f}{2} \right) * p_{x_2}(f) df, \quad \zeta = \frac{B}{2\Delta f} \\ &= \frac{1}{8} [\zeta^2 + 6\zeta + 1] \end{aligned} \quad (6.28)$$

$$\alpha_{11} = \int_{-\zeta}^{\zeta} p_{x_1}(f) * p_{x_2}(f) df = \left(\zeta - \frac{\zeta^2}{4} \right) \quad (6.29)$$

$$\alpha_2 = \int_{-\xi}^{\xi} \frac{1}{2} p_{x_1} \left(\frac{f}{2} \right) df = \frac{\xi}{2} \quad (6.30)$$

If the per-channel modulation depth is taken as constant for each channel the distortion coefficients are redefined accordingly as explained in section 5.3.

6.2.4 Results

The results given are for a typical SCM optical system where 62 FM video channels are multiplexed in the frequency band of 2.7 to 5.2 GHz. The video top baseband frequency is $f_m = 6.8$ MHz and the peak-to-peak frequency deviation is $\Delta f_{pp} = 22.5$ MHz. After modulation the signal bandwidth is estimated to be $B = 36.1$ MHz. A diagram of the multiplex structure is shown in figure 6.1. These parameters were taken from important

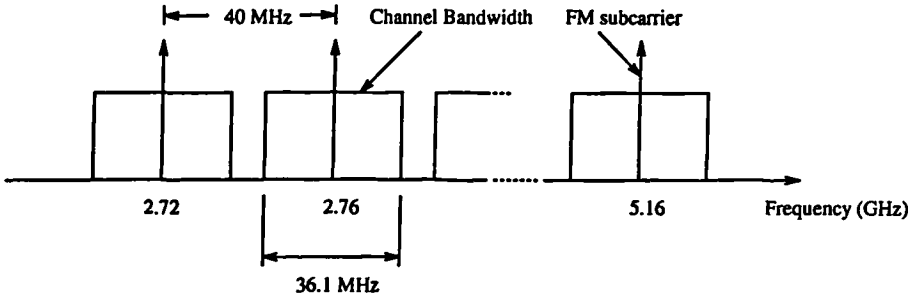


Figure 6.1: Diagram of the multiplex structure

reported experiments in this area of research [52, 48], so that the accuracy of our analytic results could be compared with actual experimental data.

Since the transmission bandwidth is limited to one octave the second-order IMPs and harmonics need not be considered. Also the third-order three-tone IMPs dominate [1, 48] for a large number of channels and these are the distortion products we will consider. For these IMPs the condition of equation (6.13) gives

$$\text{sinc}^3(2\Delta f\tau) \approx 0, \quad |\tau| > \frac{0.31}{\Delta f} \quad (6.31)$$

Since a video signal has little power at high-frequencies we relax somewhat the condition of equation (6.10) by taking $\tau < 1/(5f_m)$. From this and equation (6.31) there follows a condition on the ratio $\Delta f/f_m$

$$\frac{\Delta f}{f_m} > 5 \cdot 0.31 = 1.55 \quad (6.32)$$

In the system under study $\Delta f/f_m = 1.6$ so we can apply the quasi-static approximation given by equation (6.15). The system CNR is given by equations (5.29) and CIR defined by equations (6.23) to (6.30).

The laser parameters used, taken from Reference [33], are given in Table 6.1. As in [33], the laser model includes also a Butterworth filter with a 4 GHz 3 dB bandwidth to account for the laser drive circuit and laser parasitic shunt capacitance of 8 pF and series resistance of 5 Ω . Figures 6.2 and 6.3 plot the laser response and relative intensity noise, respectively, as a function of frequency.

Element	Value	Units
V: active region volume	$0.45 \cdot 10^{-16}$	m^3
g_0 : gain slope constant	$2.9 \cdot 10^{-12}$	$\text{m}^3 \text{s}^{-1}$
ϵ : gain compression factor	2.5^{-23}	m^3
N_{0m} : electron density at which net gain is zero	10^{24}	m^{-3}
β : fraction of spont. emission coupled into laser mode	10^{-4}	–
Γ : optical confinement factor	0.25	–
τ_p : photon lifetime	1	ps
τ_s : electron lifetime	1	ns
I_{th} : threshold current	17.13	mA

Table 6.1: Parameter values for a DFB-BH laser.

In figure 6.4 CIR is plotted versus the optical modulation depth per channel (m) for the first, middle and the last channels corresponding to a bias current of $I_0 = 50$ mA. Since the middle channel has the highest number of distortion products, 1365, compared to 900 for channel 62, we might have expected the middle channel to be more strongly affected by the intermodulation noise. Yet, as a consequence of the laser resonance ($f_0 = 9$ GHz), the last channel is in fact the most strongly affected by the laser distortion: as seen in the plot, $CIR_{62} < CIR_{31}$. The actual channel for which the distortion coefficient is maximum depends on the laser bias current and whether the input signal amplitude or the per-channel modulation depth is taken as the common factor between all the channels. These two cases are considered in figure 6.5 which plots the dependence of the maximum value of the distortion coefficient, between all channels, on the laser bias current. The arrows indicate the channel

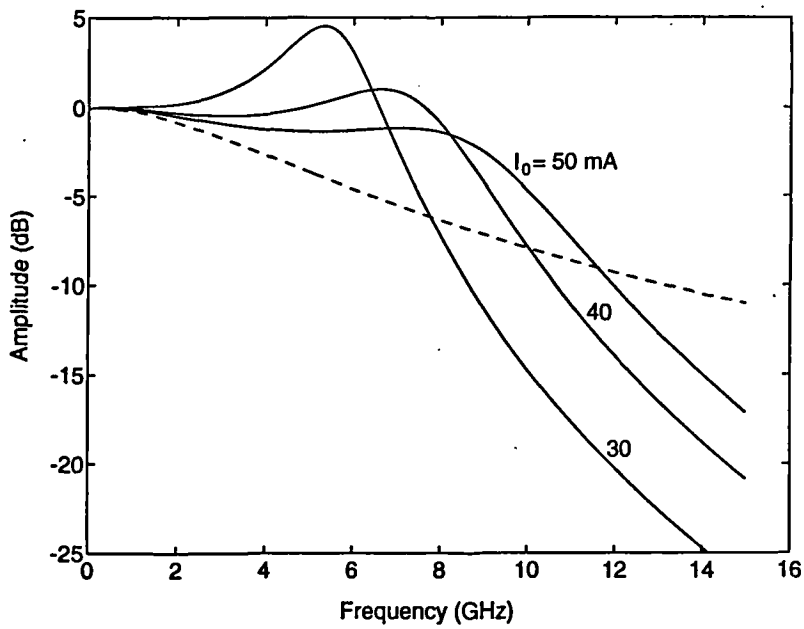


Figure 6.2: First-order transfer function (—) and parasitics response (---) for a DFB-BH laser diode.

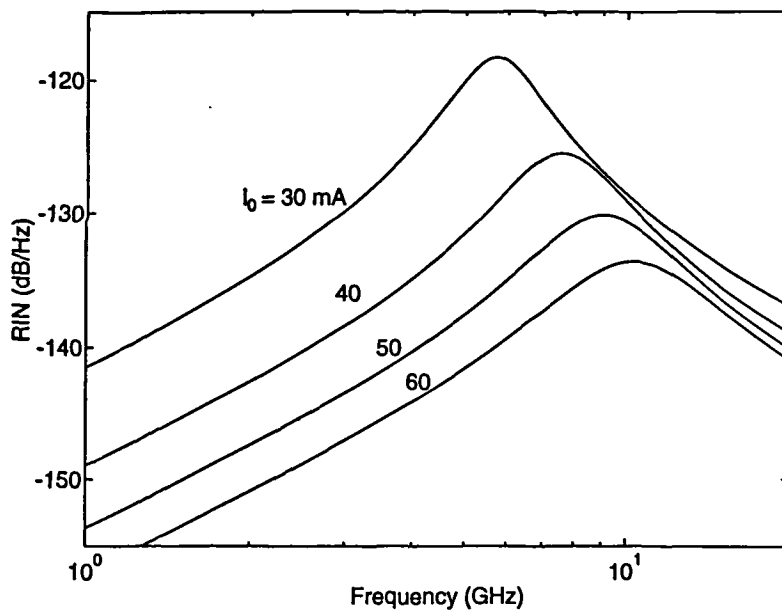


Figure 6.3: Relative intensity noise (RIN) for a DFB-BH laser diode.

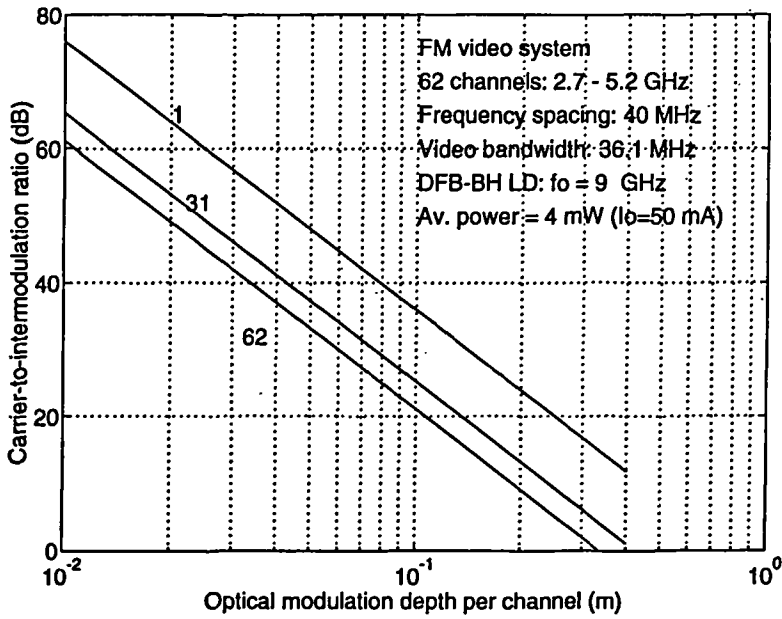


Figure 6.4: Carrier-to-intermodulation ratio for channels 1, 31 and 62

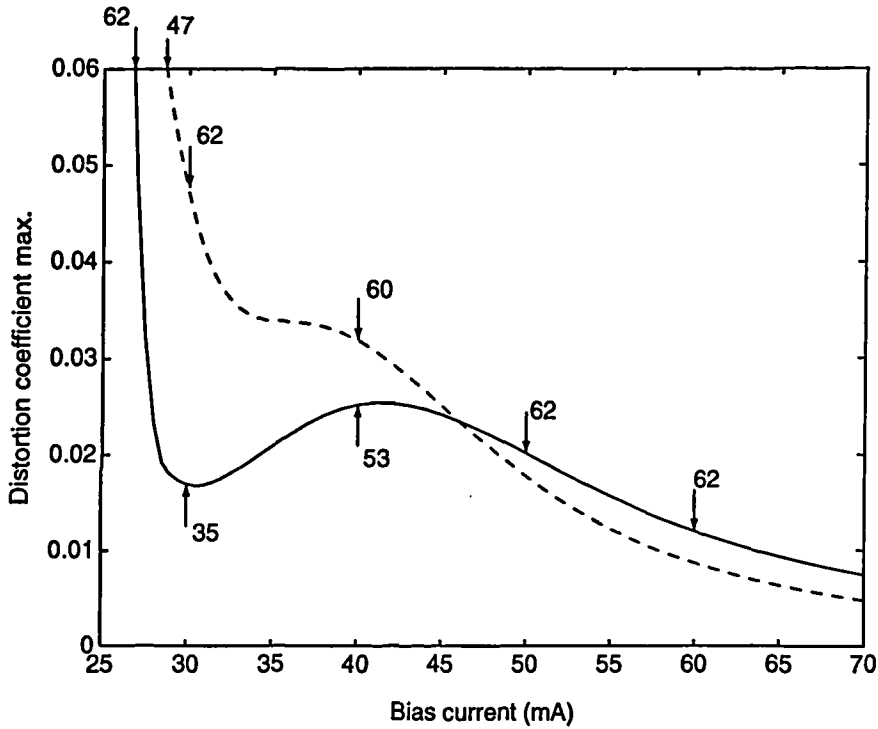


Figure 6.5: Maximum of the third-order distortion coefficient D_{111} as a function of laser bias current for constant input amplitude (—) and constant modulation depth (---) among all the channels. The numbers in the plot, for each curve, indicate the channel suffering maximum distortion ($\max(D_{111})$)

associated with the maximum of D_{111} . The minimum on the solid line curve is due to the affect of the laser parasitics on the laser transfer function which causes a depression to occur at ≈ 5 GHz for $I_0 = 42$ mA. This means that even if the channels have the same amplitude the modulation depth for the channels located at ≈ 5 GHz will be lower. To keep the optical modulation depth constant the input signal amplitude must be higher causing an increase in the levels of distortion (distortion coefficient) and the minimum to disappear (dashed line). If $I_0 = 50$ mA then $D_{111} = 0.020$ and $m_{opt} = 9.91\%$ for a CNR of 16.5 dB. This corresponds to a rms modulation depth of 78%.

The optimum OMD is also plotted in figure 6.6, for 3 values of CNR as a function of I_0 . These values of D_{111} and m_{opt} , for this number of channels, are in close agreement with previously published theoretical results [74] in which the estimated value for the distortion coefficient was based on experimental results [84]. Also in [84] an optimum modulation depth of $m_{opt} \approx 9\%$ was measured for a 60 channel FM system, which agrees well with our analysis.

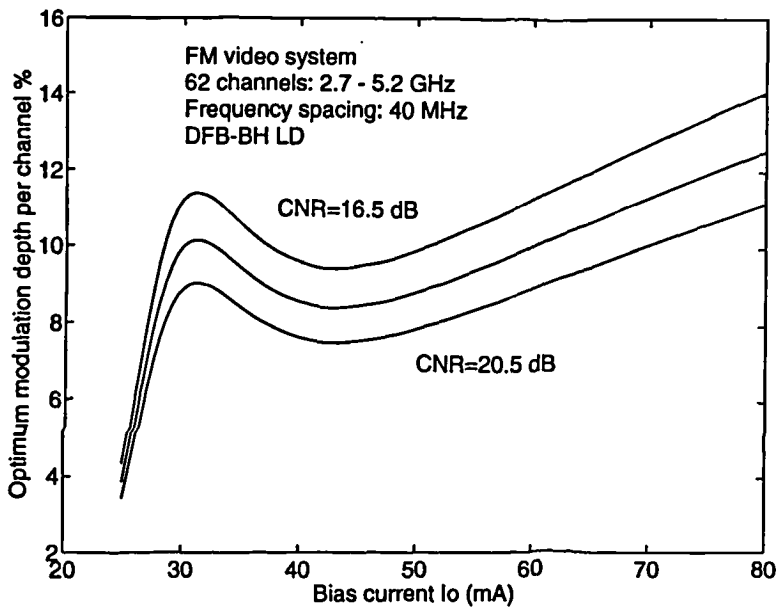


Figure 6.6: Optimum modulation depth per channel (m_{opt}) for three values of CNR (16.5, 18.5 and 20.5 dB).

The sensitivity for an APD and PIN receiver are shown respectively in figures 6.7 and 6.8, as a function of the receiver thermal noise. Figure 6.8, in contrast to figure 6.7, shows distinctively a region, for noise above ≈ 0.6 pA/ $\sqrt{\text{Hz}}$ on the graph, where signal independent receiver noise dominates and the sensitivity decreases as $\sqrt{\langle I_r^2 \rangle > B}$. For noise below this

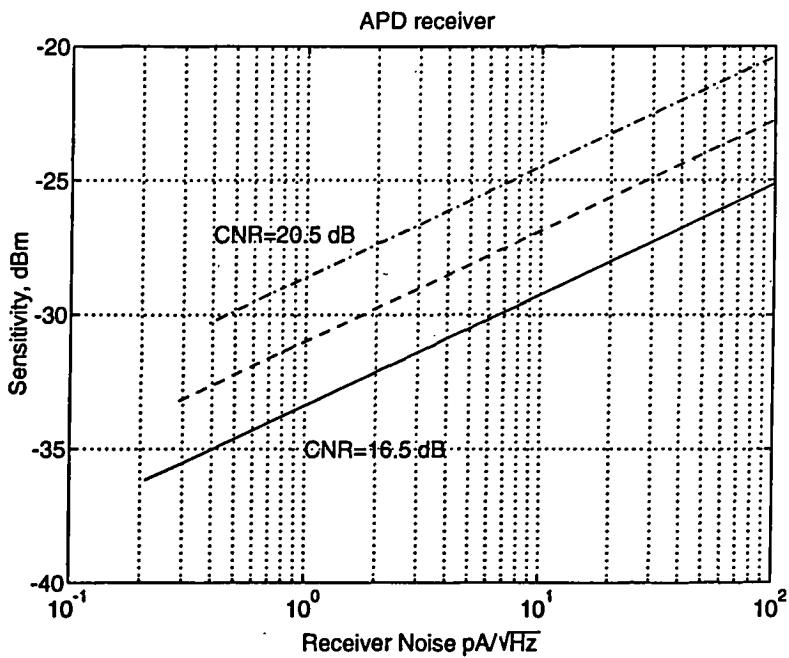


Figure 6.7: Sensitivity of an APD based receiver with APD gain ≥ 1 : 62 channel FM system with RIN= -150 dB/Hz and $I_0 = 50$ mA

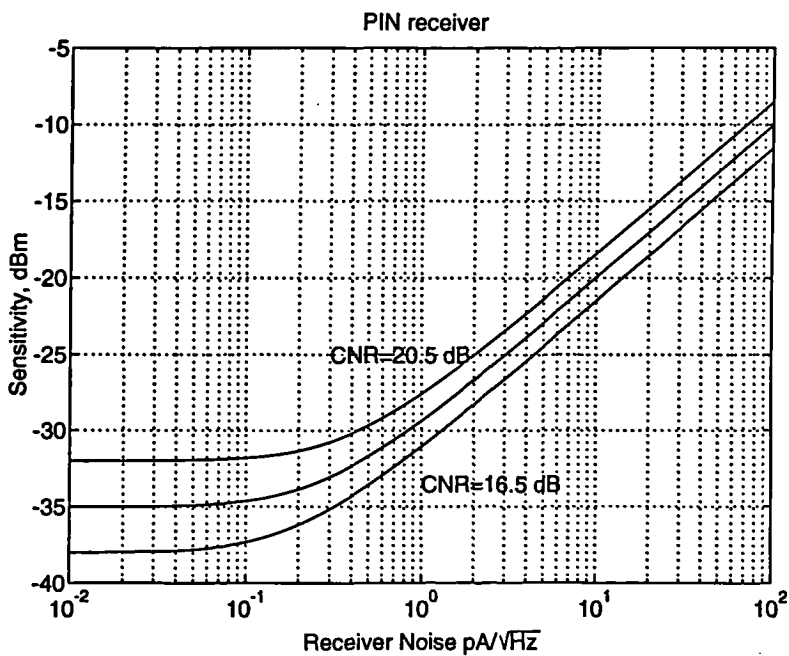


Figure 6.8: Sensitivity of a PIN based receiver: 62 channel FM system with RIN= -150 dB/Hz and $I_0 = 50$ mA

value shot noise starts dominating. For APD receivers, with gain > 1 , sensitivity decreases as $[\langle I_r^2 \rangle B]^{x/[2(1+x)]}$.

If the receiver noise is $\approx 10 \text{ pA}/\sqrt{\text{Hz}}$, for example, the required power to achieve $\text{CNR}=16.5 \text{ dB}$ is -21.5 dBm and -29.3 dBm for a PIN and APD, respectively. For 50 mA bias current the laser emitted power per facet is 4 mW and the coupled power into the fiber will be typically -2.4 dBm . The optical transmission loss budget will then be

$$P_{loss} = P_t - P_r \quad (6.33)$$

corresponding to 19.1 dB and 26.9 dB for the PIN and APD based receivers, respectively. Assuming a fibre attenuation of 0.5 dB/km and taking 7 dB for system margin the maximum transmission distances are then 24.2 and 39.8 km .

6.3 AM CATV systems

6.3.1 Introduction

Subcarrier multiplexing (SCM) has evolved as a convenient technique for multichannel video transmission taking advantage of the large modulation bandwidth of semiconductor lasers and availability of microwave components [4]. As the power and linearity of the lasers has increased attention has turned to amplitude modulated systems as they provide direct compatibility with CATV technology. However, stringent linearity and noise requirements must be met: AM-CATV signals require a carrier-to-noise ratio (CNR) of 56 dB for studio quality, which is partially eased by the small 6 MHz channel bandwidth.

While the AM signal needs a sufficiently large optical modulation depth (OMD) to achieve the higher CNR, the maximum OMD is limited by the increased nonlinear distortion. The number of intermodulation products (IMPs) are dominated by products of the type $f_i \pm f_j$ and $f_i + f_j - f_k$ for second and third-order products, respectively. With up to 40 channels separated by 6 MHz, occupying the 50–350 MHz bandwidth, tens of second-order and over five hundred third-order IMPs are generated within each channel [53]. This means that each product must be extremely small.

In this section the affect of laser intrinsic distortion on the performance of AM-SCM optical systems is assessed. The analysis presented here calculates the power spectral density of each type of IMP for an AM-SSB system. It then takes the fraction of the intermodulation power that falls in the channel bandwidth. Analytic expressions are given for the carrier-to-intermodulation ratio (CIR) which include the dependence of CIR on the frequency allocation and laser parameters including bias current. Illustrative results are given for a 42 channel system occupying the bandwidth of 50–350 MHz and channel bandwidth of 6 MHz. We show that the laser resonance frequency should be above 3 GHz if the laser intrinsic distortion is not to affect significantly system performance.

6.3.2 Intermodulation power spectral density

The input is considered to be a sum of N AM-SSB signals centred at ν_k

$$j(t) = \sum_{k=1}^N x_k(t) \cos(2\pi \nu_k t) - \hat{x}_k(t) \sin(2\pi \nu_k t). \quad (6.34)$$

where $\hat{x}_k(t)$ is the Hilbert transform of $x_k(t)$. The complex envelope of the n th-order output component at ν

$$\nu = \sum_{r=1}^n \nu_{k_r} = \sum_{k=-N}^N m_k \nu_k \quad (6.35)$$

generated by intermodulation of the input signals centred at ν_k , is given by

$$q_{n\nu}(t) = \frac{n!2^{-n+1}}{m_{-N}! \cdots m_N!} H_n(\nu) \prod_{k=-N}^N z_k^{m_k}(t) \quad (6.36)$$

in which $z_k(t)$ is the complex envelope of the input signals

$$z_k(t) = x_k(t) + i\hat{x}_k(t) \quad (6.37)$$

and, as before, $H_n(\nu_{k_1}, \dots, \nu_{k_n})$ is assumed to be constant around any set of frequencies $\nu = (\nu_{k_1}, \dots, \nu_{k_n})$.

To determine the intermodulation power spectral density (IPSD), $G_{q_{n\nu}}(f)$, of the equivalent low-pass process $q_{n\nu}(t)$, we start by calculating the autocorrelation $R_{q_{n\nu}}(\tau)$ of $q_{n\nu}(t)$ defined as

$$R_{q_{n\nu}}(\tau) = E \{ q_{n\nu}^*(t) q_{n\nu}(t + \tau) \}. \quad (6.38)$$

which yields the desired IPSD after Fourier transformation. Substitution of equations (6.36) and (6.37) into (6.38) gives

$$R_{q_{n\nu}}(\tau) = B_{nm}^2 |H_n(\nu)|^2 E \left\{ \prod_{k=-N}^N [x_k(t) - i\hat{x}_k(t)][x_k(t + \tau) + i\hat{x}_k(t + \tau)]^{m_k} \right\} \quad (6.39)$$

The most important intermodulation products are second-order terms of type $f_i \pm f_j$ and third-order products of type $f_i + f_j - f_k$ and $2f_i - f_j$. For second-order intermodulation $m_k = 1$, for all k and the above equation yields

$$R_{q_{11}}(\tau) = |H_2(f_i, \pm f_j)|^2 [R_a(\tau) + iR_{ab}(\tau)] \quad (6.40)$$

where

$$R_a(\tau) = 4 [R_{x_1}(\tau)R_{x_2}(\tau) - R_{x_1\hat{x}_1}(\tau)R_{x_2\hat{x}_2}(\tau)] \quad (6.41)$$

$$R_{ab}(\tau) = 4 [R_{x_1}(\tau)R_{x_2\hat{x}_2}(\tau) + R_{x_1\hat{x}_1}(\tau)R_{x_2}(\tau)] \quad (6.42)$$

and we have used the fact that the input signals satisfy the relations (5.6) and (5.7). After

Fourier transformation the second-order IPSD, $G_{11}(f)$, is obtained

$$G_{11}(f) = 4|H_2(f_i, \pm f_j)|^2 \left\{ G_{x_1}(f) * G_{x_2}(f) - [G_{x_1}(f)H_Q(f)] * [G_{x_2}(f)H_Q(f)] \right. \\ \left. + iG_{x_1}(f) * [G_{x_2}(f)H_Q(f)] + i[G_{x_1}(f)H_Q(f)] * G_{x_2}(f) \right\}. \quad (6.43)$$

$H_Q(f)$ is the quadrature filter transfer function defined as

$$H_Q(f) = -i \cdot \text{sgn}(f) \quad (6.44)$$

$\text{sgn}(f)$ being the sign function given by

$$\text{sgn}(f) = \begin{cases} -1, & f < 0 \\ 1, & f > 0 \end{cases} \quad (6.45)$$

Equation (6.43), after substitution of (6.44), can be simplified to

$$G_{11}(f) = 16|H_2(f_i, \pm f_j)|^2 [G_{x_1}(f)u(f)] * [G_{x_2}u(f)] \quad (6.46)$$

where $u(t)$ is the unit step function. For the sake of simplicity we take the PSD of the input signals to be identical for all the channels and to be uniform over the channel bandwidth B

$$G_{x_1}(f) = G_{x_2}(f) = G \cdot \text{rect}\left(\frac{f}{2B}\right) \quad (6.47)$$

with the rectangle function, $\text{rect}(f)$, defined as

$$\text{rect}\left(\frac{f}{B}\right) = \begin{cases} 0, & |f| > B/2 \\ 1, & |f| < B/2 \end{cases} \quad (6.48)$$

With these assumptions the second-order low-pass IPSD is finally written as

$$G_{11}(f) = 16G^2|H_2(f_i, \pm f_j)|^2 \text{rect}(f/B) * \text{rect}(f/B) * \delta(f - B) \quad (6.49)$$

which is a triangle of width $2B$ and height $16G^2B|H_2(f_i, \pm f_j)|^2$ centred at $f = B$. These calculations can be repeated for the third-order IMPSD of type $f_i + f_j - f_k$ yielding the spectral density

$$G_{111}(f) = 64(3/2)^2 G^3 |H_3(f_i, f_j, -f_k)|^2 \\ \times \text{rect}(f/B) * \text{rect}(f/B) * \text{rect}(f/B) * \delta(f - 3B/2) \quad (6.50)$$

A similar expression is obtained for the two-tone third-order IMP of type $2f_i - f_j$ with the difference that the transfer function is now evaluated at $H_3(f_i, f_i, -f_j)$

$$G_{21}(f) = 128(3/4)^2 G^3 |H_3(f_i, f_i, -f_j)|^2 \times \text{rect}(f/B) * \text{rect}(f/B) * \text{rect}(f/B) * \delta(f - 3B/2) \quad (6.51)$$

The derivation of this equation, however, is not as straightforward as in the previous cases and is left to Appendix B. The reason is that the complex envelope $q_{21}(t)$ involves the square of the input signal, $[x_i(t) + i\hat{x}_i(t)]^2$ and the autocorrelation function $R_{q_{21}}(\tau)$ of $q_{21}(t)$ requires the calculation of the autocorrelation and cross-correlation functions of the square and cross products of the signal $x_i(t)$ and the corresponding Hilbert transform $\hat{x}_i(t)$. In Appendix B these are obtained with the help of the moment generating function (MGF) assuming the input random processes are Gaussian.

6.3.3 Intermodulation noise

Figure 6.9 shows the channel allocation of a 42 channel system and the distribution of second and third-order IMPs. The maximum number of two-tone products occurs at the beginning of the transmission band, while the number of three-tone IMPs is higher for the centre channels. Due to the nonuniform frequency spacing, the products appear at several frequencies within each channel. This means that the power falling in the channel bandwidth depends not only on the type of distortion being considered but also on the channel frequencies which give rise to the distortion product and define its location. For a particular channel, we have to select those IMPs that make contribution to the noise power and take the fraction of the intermodulation power that falls in the channel bandwidth. Summing all these contributions yields the total intermodulation noise power (IMN) which will be calculated for second and third-order intermodulation products. Results will be given assuming a 6 MHz channel bandwidth and no guard space.

Second-order intermodulation

The second-order IPSD is given in equation (6.49). The corresponding band-pass spectral density, $G_{2\nu_c}$, of the intermodulation component $p_{2\nu_c}(t)$ due to the input components at

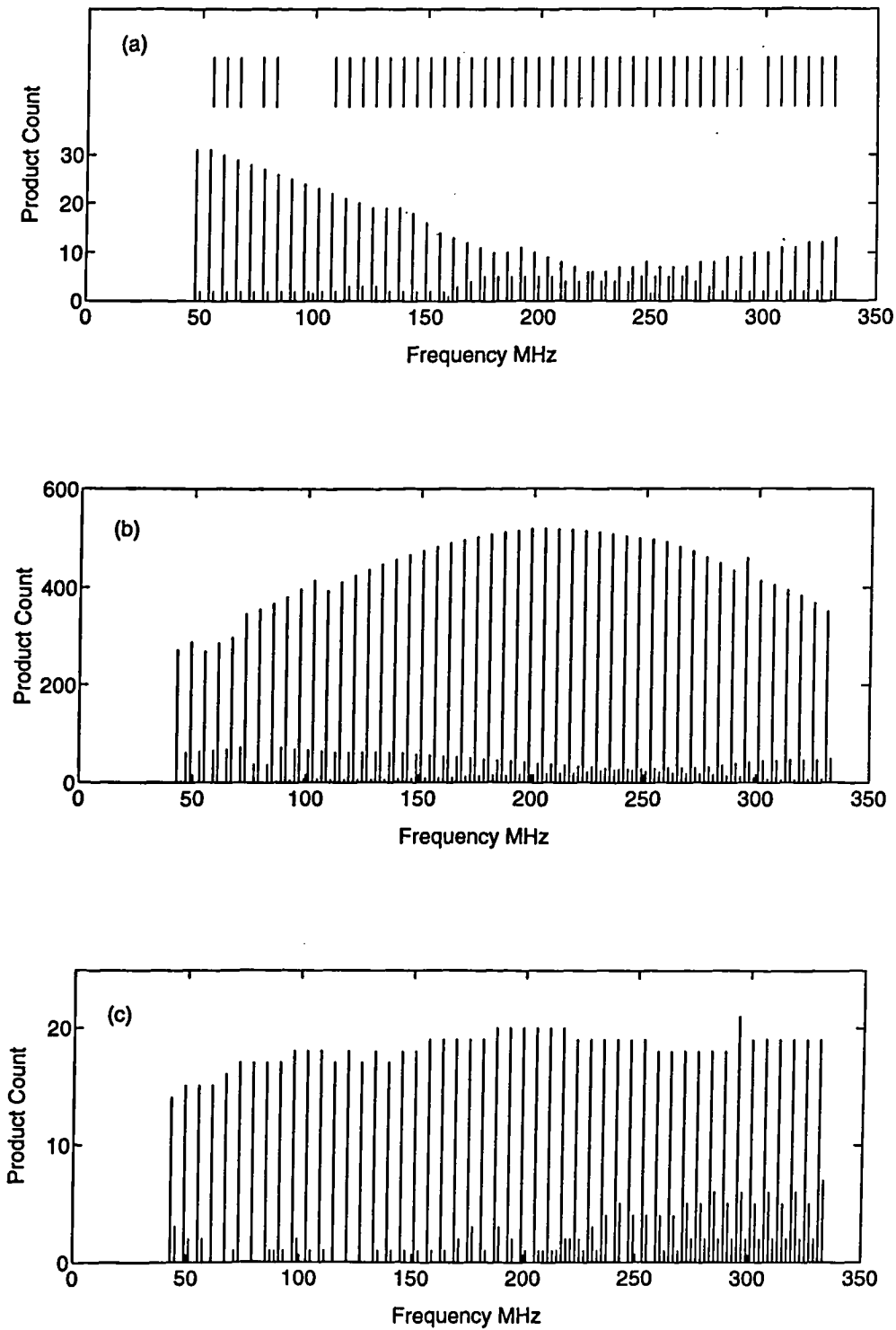


Figure 6.9: Distribution of (a) second-order distortion products and third-order products of type (b) $f_i + f_j - f_k$ and (c) $2f_i - f_k$ for a 42 channel system. The short markers on the top of (a) show the frequency location of the carriers.

$(f_{k_1}, \pm f_{k_2})$, such that $\nu_a = f_{k_1} \pm f_{k_2}$, is obtained by substitution of (6.49) into equation (5.9)

$$G_{2\nu_a}(f) = 4|H_2(\nu_a)|^2 B G^2 \left[\text{tri} \left(\frac{f - \nu_a - B}{B} \right) + \text{tri} \left(\frac{f + \nu_a + B}{B} \right) \right] \quad (6.52)$$

where $\text{tri}(f)$ is the triangle function defined by

$$\text{tri} \left(\frac{f - \nu}{B} \right) = \begin{cases} 1 - \left| \frac{f - \nu}{B} \right|, & |f - \nu| < B \\ 0, & |f - \nu| \geq B \end{cases} \quad (6.53)$$

The total second-order intermodulation noise, IMN_2^r , associated with channel located at f_r is then obtained by the integral of $G_{2\nu_a}(f)$ over the channel band and summing the contributions of all the intermodulation products

$$IMN_2^r = 8B G^2 \sum_{f_{k_1} + f_{k_2} = \nu_a}^k \sum_{\nu_a} |H_2(f_{k_1}, \pm f_{k_2})|^2 \int_{f_r}^{f_r+B} \text{tri} \left(\frac{f - \nu_a - B}{B} \right) df \quad (6.54)$$

The summation over k includes the intermodulation products that fall at frequency ν_a ; IMPs at different locations can contribute intermodulation noise to a particular channel which is accounted for by the summation over ν_a . Since the second-order power spectral density occupies a bandwidth of $2B$ centred at $\nu + B$ the possible contributions to the noise power arise from intermodulation products located at

$$f_r - 2B < \nu_a < f_r + B \quad (6.55)$$

Figure 6.10 shows a diagram of the possible second-order IMP locations, satisfying condition (6.55), for the 42 channel system with the frequency plan of figure 6.9(a), and channel bandwidth of 6 MHz. The location of these IMPs, identified by the carrier position, are

$$\nu_{a_i} = f_r + (2i - 13) \text{ MHz}, \quad i = 1, \dots, 9 \quad (6.56)$$

Also shown is the fraction of the intermodulation noise that falls in the channel band. Note that for some channels not all the IMPs shown in figure 6.10 exist. The total intermodulation noise power will be the sum of all these contributions, equivalent to expanding the sum over ν_a in equation (6.54), and for each ν_a taking the sum over k to account for all the possible combinations of the input components giving rise to the same IMP.

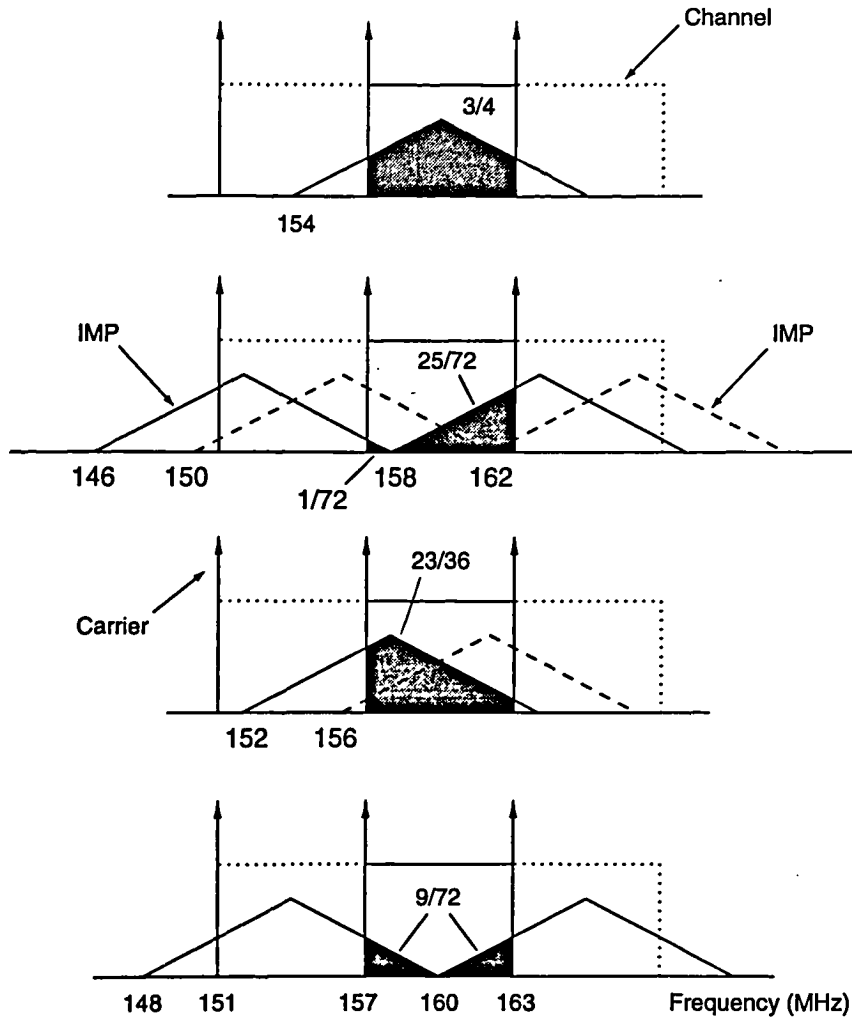


Figure 6.10: Power spectral density of second-order intermodulation products and their location within the band of channel at 157 MHz for a 42 channel AM system with the frequency plan of figure 6.9. The grey areas represent the fraction of the intermodulation power that falls in the channel band.

Third-order intermodulation

The procedure for the determination of the third-order intermodulation noise is similar to the one just presented. The three-tone and two-tone third-order band-pass IPSP, $G_{3\nu_b}(f)$ and $G_{3\nu_c}(f)$ respectively, located at $\nu_b = f_{k_1} + f_{k_2} - f_{k_3}$ and $\nu_c = 2f_{k_1} - f_{k_2}$ due to input components $(f_{k_1}, f_{k_2}, f_{k_3})$, are written as

$$G_{3\nu_b}(f) = 16(3/2)^2 G^3 B^2 \left[g \left(\frac{f - \nu_b - 3B/2}{B} \right) + g \left(\frac{f + \nu_b + 3B/2}{B} \right) \right] \quad (6.57)$$

$$G_{3\nu_c}(f) = 32(3/4)^2 G^3 B^2 \left[g \left(\frac{f - \nu_c - 3B/2}{B} \right) + g \left(\frac{f + \nu_c + 3B/2}{B} \right) \right] \quad (6.58)$$

where the function $g(f)$ is defined by

$$g(f) = \text{rect}(f)^{*3} = \begin{cases} 0, & f \leq -3/2 \\ (f^2 + 3f + 9/4)/2, & -3/2 < f \leq -1/2 \\ -f^2 + 3/4, & -1/2 < f \leq 1/2 \\ (f^2 - 3f + 9/4), & 1/2 < f \leq 3/2 \\ 0, & f > 3/2 \end{cases} \quad (6.59)$$

Integrating equations (6.57) and (6.58) over the channel band and summing all the IMP contributions yields for channel r

$$\begin{aligned} IMN_3^r &= \sum_k \sum_{\nu_b} 32(3/2)^2 |H_3(f_{k_1}, f_{k_2}, -f_{k_3})|^2 \alpha_{\nu_b} \\ &+ \sum_k \sum_{\nu_c} 64(3/4)^2 |H_3(f_{k_1}, f_{k_1}, -f_{k_2})|^2 \alpha_{\nu_c} \end{aligned} \quad (6.60)$$

where α_{ν_b} and α_{ν_c} are the fraction of the intermodulation power that fall in the channel bandwidth

$$\alpha_{\nu_{b(c)}} = \int_{f_r}^{f_r+B} g\left(\frac{f - \nu_{b(c)} - 3B/2}{B}\right) df \quad (6.61)$$

such that

$$f_r - 3B < \nu_{b(c)} < f_r + B \quad (6.62)$$

Figure 6.11 shows the location of the relevant third-order intermodulation products, identified by the carrier position $\nu_{b(c)}$, and the fraction of noise falling in a 6 MHz bandwidth. These IMPs which satisfy equation 6.62 are

$$\nu_{b_i(c_i)} = f_r + (2i - 18) \text{ MHz}, \quad i = 1, \dots, 11 \quad (6.63)$$

for the same frequency plan of figure 6.9(a).

6.3.4 Carrier-to-intermodulation ratio

Having determined the total intermodulation noise for a particular channel at frequency f_r , we proceed to calculate the carrier-to-intermodulation ratio (CIR). CIR, defined as the carrier power $S_r = 2GB|H_1(f_r)|^2$ over the total IMN power, $IMN^r = IMN_2^r + IMN_3^r$, can adequately be written as [85]

$$CIR_r^{-1} = m^4 [D_{111}N^2 + D_{21}N] + m^2 D_{11}N \quad (6.64)$$

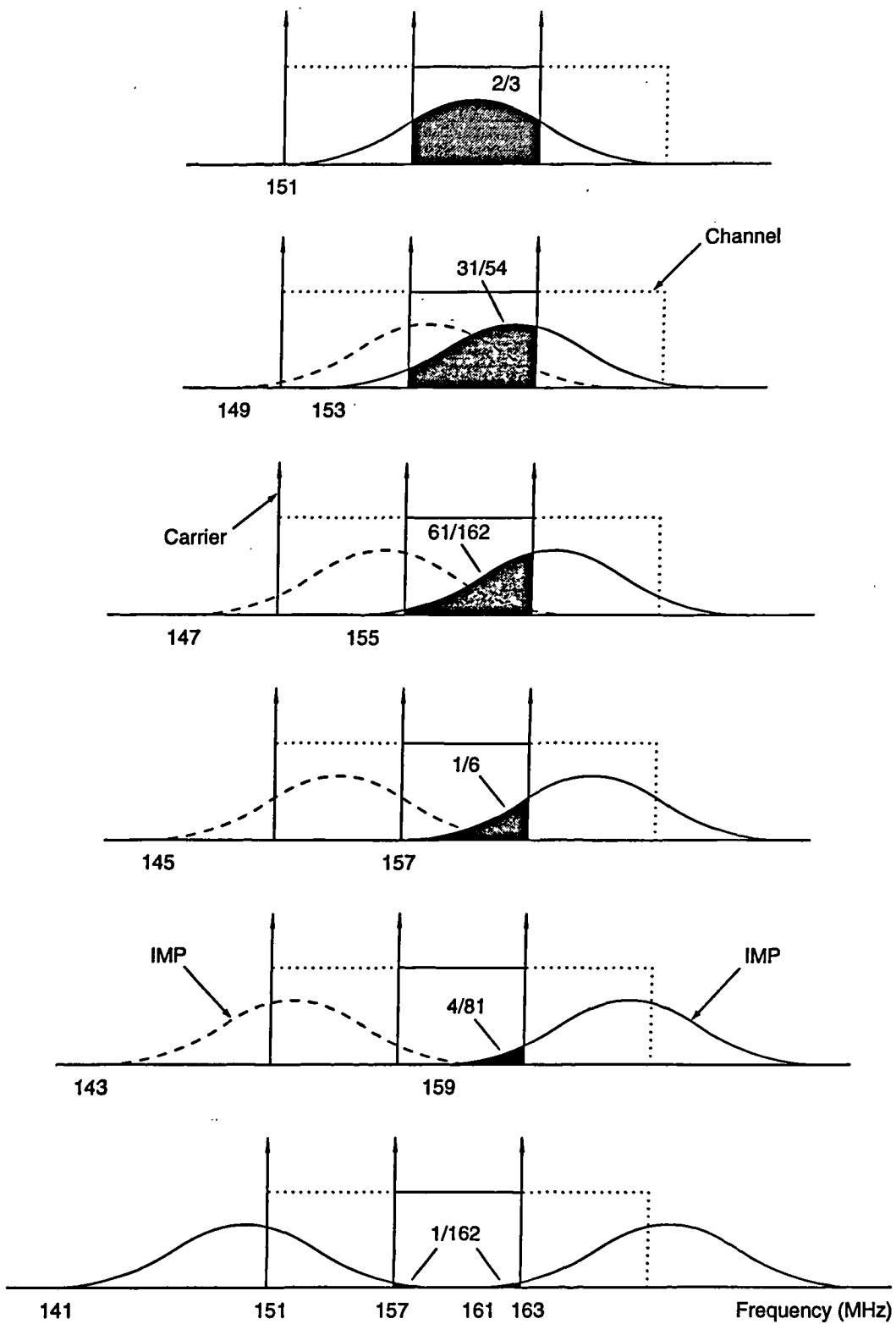


Figure 6.11: Power spectral density of third-order intermodulation products of type $f_i + f_j - f_k$ and their location within the band of channel at 157 MHz, for a 42 channel AM system with the frequency plan of figure 6.9. The grey areas represent the fraction of the intermodulation power that falls in the channel band.

Since the carrier does not have a constant amplitude the per-channel modulation, m , can not be defined in terms of the carrier amplitude. Instead, it must be defined in terms of the carrier power, S_c , as

$$S_c = \frac{1}{2} m^2 p_0^2 \quad (6.65)$$

after which the distortion coefficients D associated with the three types of distortion considered become

$$D_{11} = \frac{p_0^2}{N} \sum_k \sum_{\nu_a} \frac{|H_2(\nu_{k_1}, \pm \nu_{k_2})|^2}{|H_1(f_r)|^4} \alpha_{\nu_a} \quad (6.66)$$

$$D_{111} = \left(\frac{3}{2}\right)^2 \frac{p_0^4}{N^2} \sum_k \sum_{\nu_b} \frac{|H_3(\nu_{k_1}, \nu_{k_2}, -\nu_{k_3})|^2}{|H_1(f_r)|^6} \alpha_{\nu_b} \quad (6.67)$$

$$D_{21} = 2 \left(\frac{3}{4}\right)^2 \frac{p_0^4}{N} \sum_k \sum_{\nu_c} \frac{|H_3(\nu_{k_1}, \nu_{k_1}, -\nu_{k_2})|^2}{|H_1(f_r)|^6} \alpha_{\nu_c} \quad (6.68)$$

The CIR, as given by equations (6.64) to (6.68), is in a suitable form for the direct application of the results of the previous chapter to the assessment of the overall system performance.

6.3.5 System results

The previous analysis will be applied to assess the performance of a typical 42 channel AM system with the frequency allocation of figure 6.9(a), the channels having a 6 MHz bandwidth. The laser parameters for a DFB-BH laser, shown in table 6.1, are the same as used in the previous section.

The CIR, which must be higher than approximately 60 dB, is plotted in figure 6.12 for two values of laser bias as a function of the per-channel modulation depth. In both cases the last channel has a lower CIR and so is most affected by the laser distortion. Figure 6.13 plots the corresponding distortion coefficients. For values of m under 10% CIR exhibits a slope of 20 dB/decade which means the second-order IMPs are the main source of distortion. This occurs also for large I_0 (figure 6.13) since D_{11} increases rapidly with increasing current.

This is an important point as it implies the existence of an optimum bias current which, for the laser in question, occurs at $I_0/I_{th} \approx 3$. As a result, the capability of many laser structures to provide output powers of tens of milliwatts cannot be used in CATV systems. This phenomenon which has been observed experimentally by several authors [53, 60, 86, 55] is here explained by the fact that at high bias currents the factor $\sum_{k, \nu_a} |H_2(\nu_{k_1}, \pm \nu_{k_2})|^2 / |H_1(f_r)|^4$ approaches a

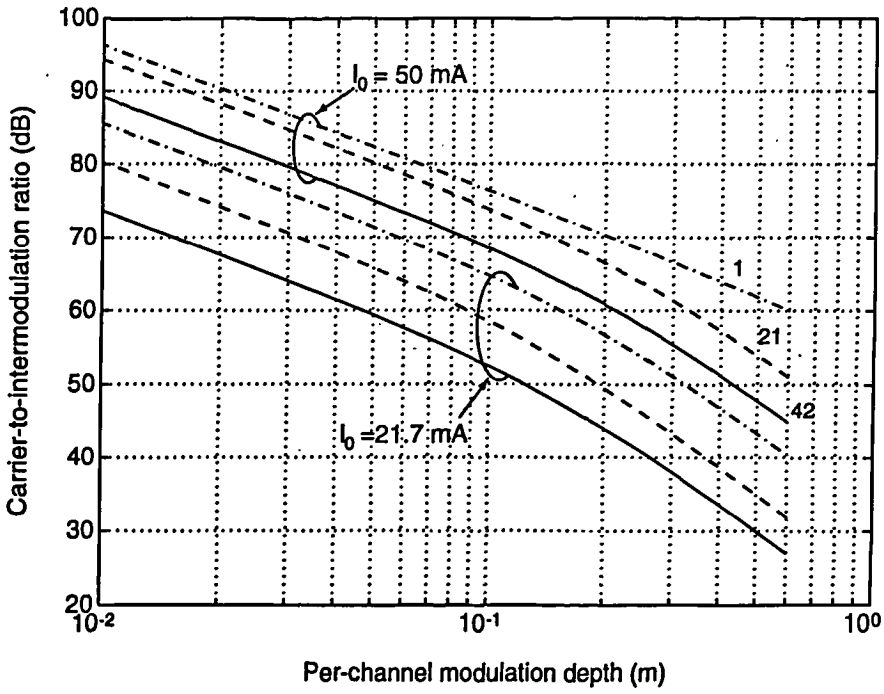


Figure 6.12: Carrier-to-intermodulation ratio of channels 1, 21 and 42 for two values of the laser bias current.

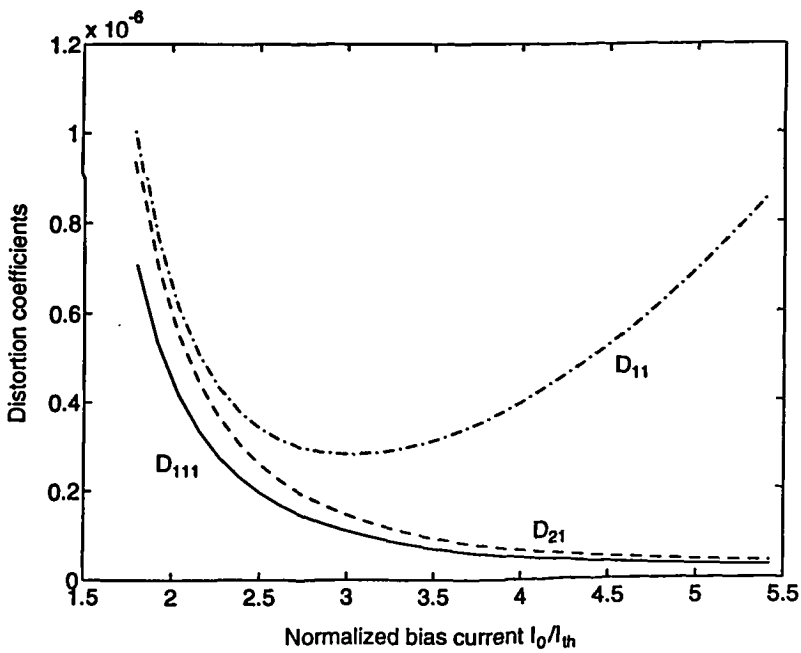


Figure 6.13: Second and third-order distortion coefficients of a 42 channel AM system: frequency plan of figure 6.9 and channel bandwidth of 6 MHz

constant value and D_{11} becomes directly proportional to p_0^2 . Note that if the modulation depth is

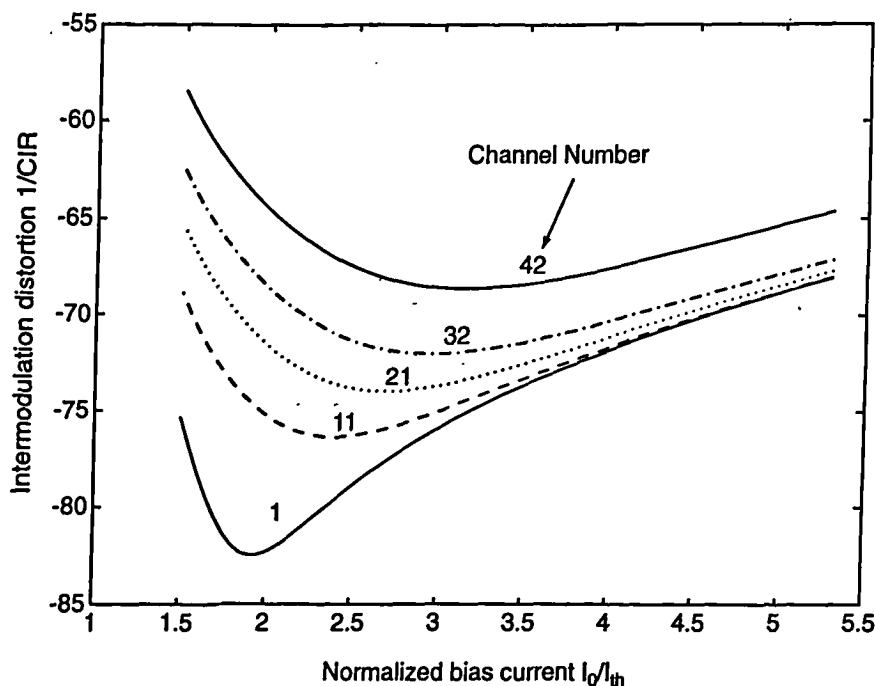


Figure 6.14: Distortion levels as a function of the laser bias current: modulation depth is $m = 0.1$. The distortion minimum occurs at lower bias currents for channels at the lower frequencies.

kept constant with increasing I_0 , by increasing the input signal amplitude, the same behaviour is observed for the carrier-to-intermodulation ratio, shown in figure 6.14, the minimum of CIR being shifted to lower bias levels for lower frequency channels in agreement with the experimental results of Kawamura et. al. [60]. However, if the input signal amplitude is kept constant a minimum for CIR does not occur. It has been shown [53], that even in this latter condition an increase in the distortion ratio ($1/CIR$) is observed. Thus, other distortion mechanisms must come into play, such as spatial hole burning (discussed in section 3.3, and diode leakage [55, 60], which have been used to explain the increased intermodulation distortion with I_0 at low frequencies.

Figure 6.12 shows that for a bias level of 21.7 mA, which corresponds to a laser resonance frequency of 3 GHz, the modulation depth is limited to values lower than 4% ($CIR > 60$ dB). Consequently, the laser resonance should be above 3 GHz if the laser intrinsic distortion is not to affect significantly system performance. If this is the case, clipping distortion, which imposes a fundamental limit on the minimum achievable nonlinear distortion, should be considered.

This limit, obtained from equation (5.58), is plotted in figure 6.15 taking $\Lambda = 1/2$, that is half of the distortion power falls outside the band [87], and assuming the in-band power is uniformly distributed between all channels. In fact, the low frequency channels may be affected by 1 dB

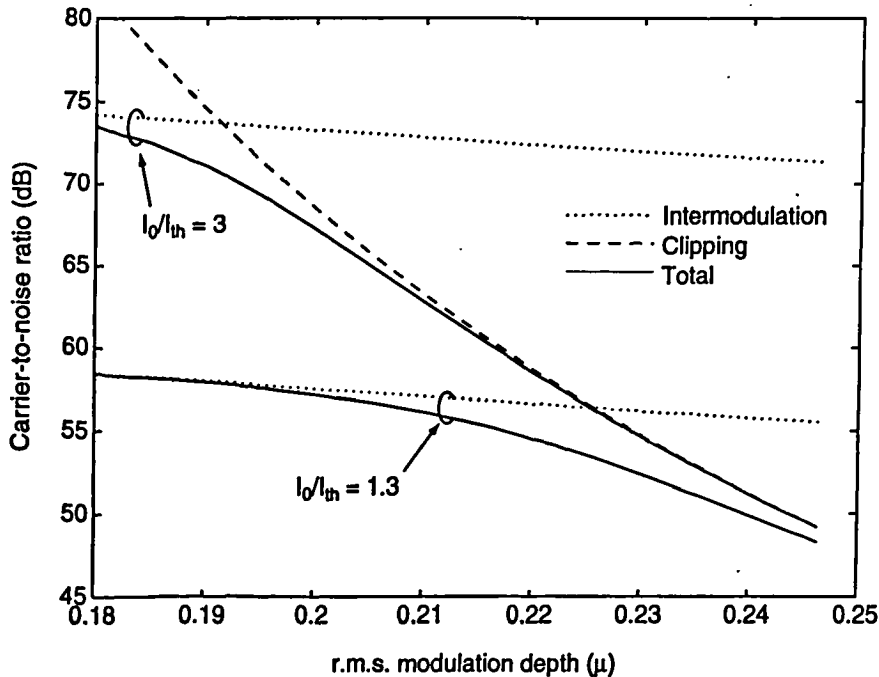


Figure 6.15: Carrier-to-intermodulation ratio as a function of the optimum r.m.s modulation depth, μ_{opt} , for two values of bias current, $I_0 = 21.7$ mA and $I_0 = 50$ mA, corresponding to two cases where laser intrinsic distortion and clipping distortion are dominant, respectively.

more than the high frequency channels [78]. For a bias current of $I_0/I_{th} = 1.3$ ($f_0 \approx 3$ GHz) and $CNR = 56$ dB ($\mu_{opt} = 0.211$), clipping distortion (dashed line) degrades CNR (solid line), relative to the intrinsic distortion (dotted line) only by 1.3 dB, whereas for $I_0/I_{th} = 3$ ($f_0 \approx 9$ GHz and $\mu_{opt} = 0.226$), corresponding to the minimum of $1/CIR$ for channel 42, the former dominates completely.

The expected sensitivity is given by the solution of equation (5.59). Using a PIN detector and a low noise 50Ω amplifier with a circuit noise of $12 \text{ pA}/\sqrt{\text{Hz}}$ and for $RIN = -155$ dB/Hz the sensitivity is approximately -10 dBm and -11 dBm, for the two extreme case bias levels of $I_0 = 21.7$ mA and $I_0 = 50$ mA considered in figures 6.12 and 6.15, respectively. The emitted power per facet for the latter is 4 mW which, upon assuming a 6 dB fibre coupling loss, 0.2 dB/Km fibre attenuation at $1.55 \mu\text{m}$ and a loss margin of 7 dB, corresponds to a possible length span of approximately 20 Km with a modulation depth per-channel of 5%.

Thus, a “window” of low distortion in the range of 0–500 MHz exists, at relatively high bias levels, permitting the transmission of analogue signals requiring high CNR values as needed for AM systems, clipping distortion being a more important factor than in FM systems analysed previously.

6.4 FSK Fibre-Radio return link

6.4.1 Introduction

Subcarrier multiplexing (SCM) techniques are very attractive for the remote delivery over optical fibres of future mobile radio services and for the provision of flexible customer access connections [81], offering advantages compared to copper or baseband optical systems. Specifically SCM allows the radio frequency carriers to modulate directly the laser and be transported over the optical fibre without the need for frequency conversion and multiplexing/demultiplexing functions. This will reduce the complexity of the radio distribution point and will facilitate the deployment of remote antennas whilst supporting the requisite multi-channel microwave signal format.

In the return optical link (figure 6.16) the off-air received signals are used to modulate the laser. Accordingly, the link must be capable of supporting a wide dynamic range of power levels arising from range variations and fading associated with the mobile user. This imposes severe restrictions on laser nonlinearity to ensure that in-band intermodulation products (IMPs), which rapidly increase with the number of channels, are sufficiently suppressed relative to the carrier.

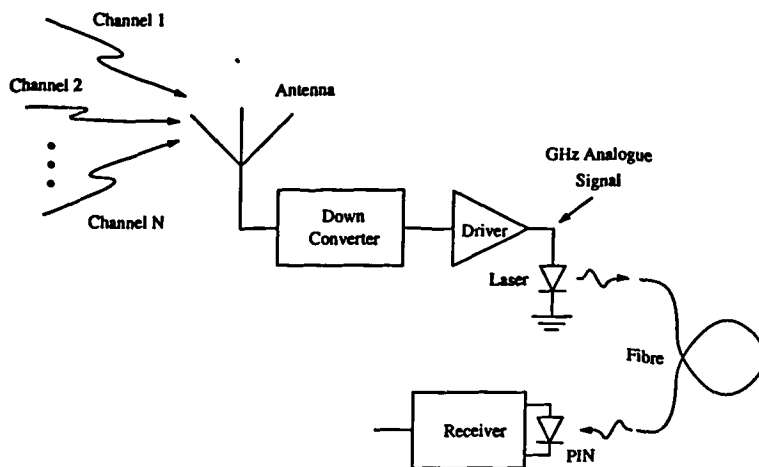


Figure 6.16: Block diagram of a frequency division multiple access (FDMA) fibre/radio return link.

Using the laser model of chapter 4, we show that the performance assessment of SCM systems having a wide dynamic range becomes tractable and also that the system can be optimised based on a worst case condition, which occurs when the channel most affected by

the laser distortion is at minimum power while the other channels are at their maximum. A system case study is given corresponding to a 50 channel CPFSK system having a dynamic range of 40 dB spanning the transmission band of 2 to 2.1 GHz, with channel bandwidth of 1 MHz and 2 MHz spacing between channels. This system is a constituent element of the RACE-II project MODAL-R2005 [80] concerned with the provision of a duplex optical link to a remote antenna

6.4.2 System description

A diagram of the return link of a SCM fibre-radio system is shown in figure 6.16. The received signal from the antenna is amplified following a down conversion operation, and used to modulate the laser diode. At the headend, after detection (optical-to-electrical conversion) a bandpass filter selects the desired channel and this is followed by the demodulation process. The carrier-to-noise ratio (CNR) is defined for each channel at the output of the bandpass filter. Due to the mobility range the link must support a wide range of power levels. The electrical dynamic range is defined as the difference between the achievable carrier-to-noise ratio and the minimum required CNR for a specified received optical power and channel modulation depth.

6.4.3 Intermodulation power spectral density

In this section we calculate the intermodulation power spectral density of three-tone ($f_i + f_j - f_k$) and two-tone ($2f_i - f_j$) third-order IMPs when the input signal consists of a sum of N CPFSK channels. The effect of the IMPs on each channel is accurately determined by taking the fraction of the IMP power that falls in the channel bandwidth B .

The laser input current is considered to be a sum of N , M -ary CPFSK signals centered at ν_l

$$j(t) = \sum_{l=1}^N j_l(t) \quad (6.69)$$

$$j_l(t) = \sum_{k=0}^{\infty} A_l \cos \{2\pi \nu_l t + 2\pi f_d [\phi_{kl} T + a_{kl}(t - kT)] + \theta_l\} p_T(t - kT) \quad (6.70)$$

where f_d is the peak frequency deviation, θ_l is a uniformly distributed initial phase of the l th carrier and $1/T$ equals the symbol rate; a_{kl} represents the k th symbol in the message sequence

of channel l , so the amplitudes belong to a set of M discrete values and ϕ_{kl} , defined as

$$\phi_{kl} = \sum_{r=0}^{k-1} a_{rl}, \quad (6.71)$$

represents the accumulation of all symbols up to the time $(k-1)T$ of the l th channel. It is also assumed that the unmodulated pulse $p_T(t)$ is a rectangular pulse of unit amplitude and duration of T seconds

$$p_T = \begin{cases} 1 & kT < t < (k+1)T \\ 0 & \text{otherwise} \end{cases} \quad (6.72)$$

The equivalent low-pass or complex envelope representation of the signal $j_l(t)$ is then written as

$$z_l(t) = \sum_{k=0}^{\infty} A_l e^{i2\pi f_d[\phi_{kl} + a_{kl}(t-kT)]} e^{i\theta_l} p_T(t-kT) \quad (6.73)$$

At the laser output the complex envelope of the n th-order intermodulation product falling at frequency ν due to signals centered at f_{k_1}, \dots, f_{k_n} is, after equation (5.10)

$$q_{n\nu}(t) = \frac{n!2^{-n+1}}{m_{-N}! \dots m_N!} H_n(\nu) \left[\prod_{k=-N}^N A_l^{m_l} \right] \sum_{k=0}^{\infty} e^{i2\pi f_d \sum_{l=-N}^N m_l[\phi_{kl} + a_{kl}(t-kT)]} p_T(t-kT) \quad (6.74)$$

The determination of the corresponding power spectral density $G_{q_{n\nu}}$ which follows the method of Reference [71] is left to Appendix C. The final result is

$$G_{q_{n\nu}}(f) = \frac{C_{nm}^2}{4T} E[|P_T(f-f_d I)|^2] + \frac{C_{nm}^2}{4T} 2\text{Re} \left\{ \frac{e^{-i2\pi f T}}{1 - \Phi_I(2\pi f_d T) e^{-i2\pi f T}} \right. \\ \left. \times E[P_T(f-f_d I)] E[P_T^*(f-f_d I)] e^{i2\pi f_d T I} \right\}, \quad |\Phi_I(2\pi f_d T)| < 1 \quad (6.75)$$

where $\Phi_I(2\pi f_d T)$ is the characteristic function of the discrete random variable I defined as

$$I_k = \sum_{l=-N}^N m_l a_{kl} \quad (6.76)$$

P_T is the Fourier transform of $p_T(t)$

$$P_T(f) = T e^{-i\pi f T} \frac{\sin \pi f T}{\pi f T}, \quad (6.77)$$

and

$$C_{nm} = \frac{n!2^{-n+1}}{m_{-N}! \dots m_N!} |H_n(\nu)| \left[\prod_{k=-N}^N A_l^{m_l} \right] \quad (6.78)$$

The condition $|\Phi_I(2\pi f_d T)| < 1$ means there are no discrete frequency components in the power density spectrum.

For binary CPFSK the information symbols take only 2 values, $a_k = 2k - 1$, $k = 0, 1$. If these occur with equal probability the three-tone and two-tone third-order IMPs due to input frequencies at $f_{k_1}, f_{k_2}, -f_{k_3}$ and $f_{k_1}, -f_{k_2}$, respectively, are given by

$$G_{111}(f) = \frac{T}{4} \left(\frac{3}{2}\right)^2 |H_3(f_{k_1}, f_{k_2}, -f_{k_3})|^2 (A_{k_1} A_{k_2} A_{k_3})^2 \left\{ \sum_{k=0}^3 \left(\frac{1}{2}\right)^3 \binom{3}{k} U_k^2(f) + 2 \sum_{j=0}^3 \sum_{k=0}^3 \binom{3}{j} \binom{3}{k} \left(\frac{1}{2}\right)^6 U_j(f) U_k(f) V_{jk}(f) \right\} \quad (6.79)$$

$$G_{21}(f) = \frac{T}{4} \left(\frac{3}{4}\right)^2 |H_3(f_{k_1}, f_{k_1}, -f_{k_2})|^2 (A_{k_1}^2 A_{k_3})^2 \times \left\{ \sum_{k=0}^3 \left(\frac{1}{4}\right)^2 U_k^2(f) + 2 \sum_{j=0}^3 \sum_{k=0}^3 \left(\frac{1}{4}\right)^2 U_j(f) U_k(f) V_{jk}(f) \right\} \quad (6.80)$$

where

$$U_k(f) = \frac{\sin \pi T [f - f_d(2k - 3)]}{\pi T [f - f_d(2k - 3)]} \quad (6.81)$$

$$V_{jk}(f) = \frac{\cos(2\pi f T - \varphi_{jk}) - \Phi \cos \varphi_{jk}}{1 + \Phi^2 - 2\Phi \cos(2\pi f T)} \quad (6.82)$$

$$\varphi_{jk} = 2\pi T f_d [(j + k) - 3] \quad (6.83)$$

$$\Phi = \begin{cases} \cos^3(2\pi f_d T), & \text{for eq. (6.79)} \\ \frac{1}{2} [\cos(6\pi f_d T) + \cos(2\pi f_d T)], & \text{for eq. (6.80)} \end{cases} \quad (6.84)$$

Figure 6.17 shows the power spectral density of the signal and third-order IMPs for $f_d T = 0.25$, usually designated as minimum shift keying (MSK). Integration of the above equations over the filter bandwidth, B , at the receiver end, gives the total intermodulation power in the signal band.

6.4.4 Carrier-to-intermodulation ratio

The affect of the intermodulation noise on system performance is quantified in terms of the carrier-to-intermodulation ratio, defined previously in chapter 5. The n th-order CIR for the r th channel located at frequency $\nu \equiv f_r$, due to input channels at f_{k_1}, \dots, f_{k_n} , is defined as the ratio of the signal power to the power of the corresponding intermodulation product at the output of the bandpass filter (BPF), figure 6.16. Assuming this filter to have a unit gain over

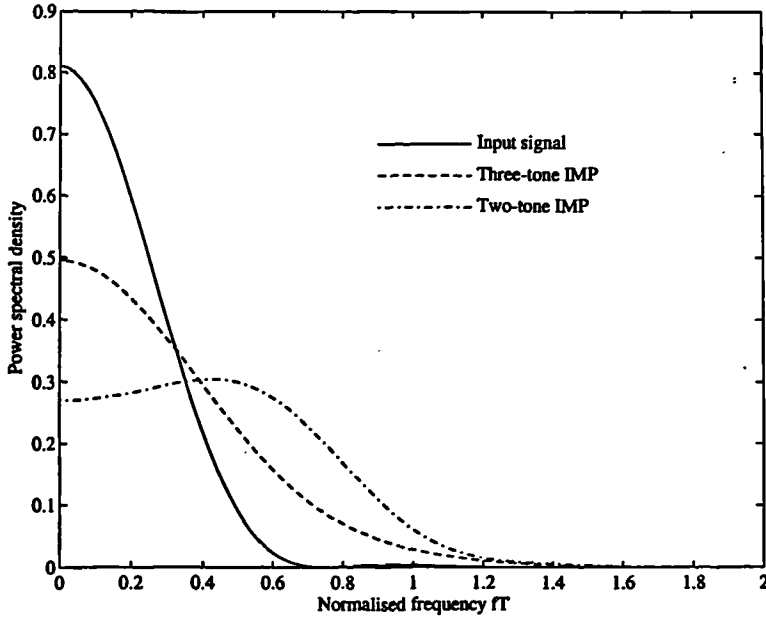


Figure 6.17: Power spectral density of input signal and of third-order intermodulation products. The frequency deviation is $f_d T = 0.5$ corresponding to minimum shift keying.

its bandwidth B , CIR is written as

$$(CIR)_{nr}(f_{k_1}, \dots, f_{k_n}) = \frac{\int_{-B/2}^{B/2} G_{q_{1\nu}}(f) df}{\int_{-B/2}^{B/2} G_{q_{n\nu}}(f) df} = \frac{|H_1(\nu)|^2 A_r^2}{B_{nm}^2 \alpha_n(m_{-N}, \dots, m_N) |H_n(f_{k_1}, \dots, f_{k_n})|^2 (A_{k_1} \dots A_{k_n})^2} \quad (6.85)$$

where $B_{nm} = n!/(m_{-N}! \dots m_N!)$ and $\alpha_n(m_{-N}, \dots, m_N)$ denotes the fraction of the intermodulation power relative to the signal power that is passed by the filter. We have also taken $B = 1/T$. The channels are uniformly spaced in frequency and so α_n does not depend on the specific frequencies which originate the distortion but only on the type of distortion product. For the three-tone IMPs $\alpha_3(1, 1, -1) = \alpha_{111} = 0.80$ while for the two-tone IMPs $\alpha_3(2, -1) = \alpha_{21} = 0.59$. Also since the channels are independent the total CIR for channel r is obtained by the summation of all the IMP power terms falling at frequency ν

$$CIR_{nr} = \frac{|H_1(\nu)|^2 A_r^2}{\sum_k B_{nm}^2 \alpha_n(m_{-N}, \dots, m_N) |H_n(f_{k_1}, \dots, f_{k_n})|^2 (A_{k_1} \dots A_{k_n})^2} \quad (6.86)$$

where the summation over k includes all the sets $\{k_1, \dots, k_n\}$ such that $f_{k_1} + \dots + f_{k_n} = m_{-N} f_{-N} + \dots + m_N f_N = \nu$. In the system under study only the third-order terms have to be

considered and we get

$$\begin{aligned} CIR^{-1} = & \left(\frac{3}{2}\right)^2 \alpha_{111} \sum_k \frac{|H_3(f_{k_1}, f_{k_2}, -f_{k_3})|^2 (A_{k_1} A_{k_2} A_{k_3})^2}{|H_1(\nu)|^2 A_r^2} \\ & + \left(\frac{3}{4}\right)^2 \alpha_{21} \sum_k \frac{|H_3(f_{k_1}, f_{k_1}, -f_{k_2})|^2 (A_{k_1}^2 A_{k_3})^2}{|H_1(\nu)|^2 A_r^2} \end{aligned} \quad (6.87)$$

6.4.5 Worst case condition

So far we have obtained general expressions for CIR. The case when the input channels have different power levels, defined by dynamic range dr , will now be derived based on a worst case condition. This condition occurs when the channel most affected by the laser distortion is at the minimum power A_{min} while the other channels are at their maximum A_{max} .

$$A_{max} = (10^{dr/20}) A_{min} \quad (6.88)$$

The channel most affected by the laser distortion is the one that has the lower CIR when all the channels have the same power. This depends not only on the number and type of IMPs falling at each channel but also on the channel allocation relative to the laser resonance, which defines the magnitude of the IMPs as described by the transfer functions. The closer the channel is to the resonance the higher the distortion. Although, as seen in chapter 3, the centre channel has a larger number of third-order distortion products, in general this is not the channel with the lowest CIR. For example, figure 6.18 shows that for a bias current of 50 mA (resonance $f_0 = 9$ GHz) channel 29 is most affected by the laser distortion. Here the CIR difference of this channel to the middle channel is small because the channels are closely spaced. In the discussion that follows we identify the channel most affected by the laser distortion as the reference channel r .

Consider now the first term in equation (6.87). This summation can be divided in two parts:

1. The IMPs do not include the reference channel $k_i \neq r$ ($i = 1, 2, 3$), where r identifies the reference channel.
2. The IMPs include the reference channel.

In the expression $f_{k_1} + f_{k_2} - f_{k_3}$, f_{k_3} is the frequency of the reference channel ($k_3 = r$),

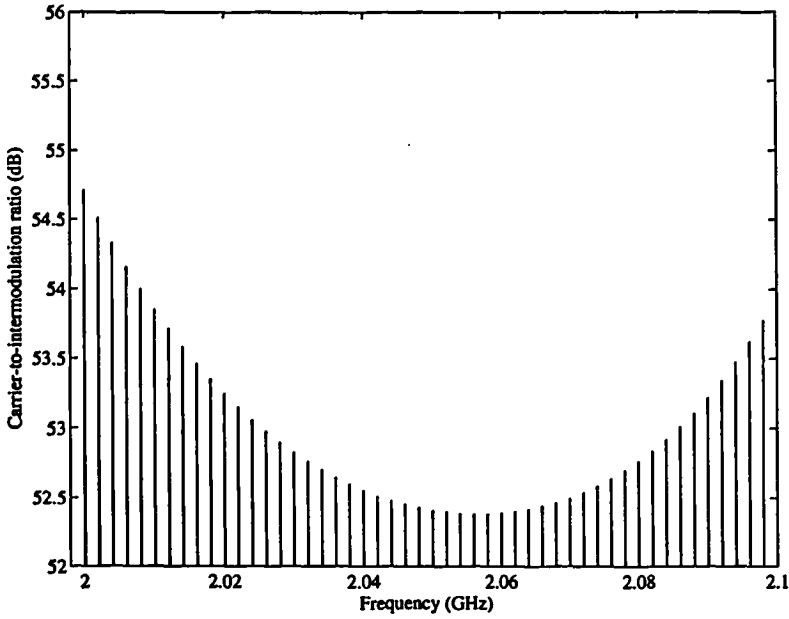


Figure 6.18: Carrier-to-intermodulation ratio; DFB-BH laser with a bias current of 50 mA and the channels have equal amplitudes. The optical modulation depth is (4.5%) for channel 29 (reference channel).

and the number of IMPs is given by

$$IM_r^N(f_k + f_{2r-k} - f_r) = \begin{cases} N - r & \text{for } r > N_c \\ r - 1 & \text{for } r \leq N_c \end{cases} \quad (6.89)$$

where N_c identifies the center channel

$$N_c = \begin{cases} N/2 & \text{if } N \text{ even} \\ (N + 1)/2 & \text{if } N \text{ odd} \end{cases} \quad (6.90)$$

Based on the above we write

$$\begin{aligned} & \sum_k (A_{k_1} A_{k_2} A_{k_3})^2 |H_3(f_{k_1}, f_{k_2}, -f_{k_3})|^2 \\ &= \sum_{k=N_1}^{N_2} (A_k A_{2r-k} A_{-r})^2 |H_3(f_k, f_{2r-k}, -f_r)|^2 \\ &+ \sum_{k, k_i \neq r} (A_{k_1} A_{k_2} A_{k_3})^2 |H_3(f_{k_1}, f_{k_2}, -f_{k_3})|^2 \end{aligned} \quad (6.91)$$

with N_1 and N_2 defined as

$$\begin{cases} N_1 = 1, N_2 = r - 1 & \text{if } r \leq N_c \\ N_1 = r + 1, N_2 = N & \text{if } r > N_c \end{cases} \quad (6.92)$$

Using the relation $A_k = (10^{dr/20})A_r$, for $k \neq r$, obtained from (6.88) we get

$$\begin{aligned} & \sum_k (A_{k_1} A_{k_2} A_{k_3})^2 |H_3(f_{k_1}, f_{k_2}, -f_{k_3})|^2 \\ &= \left[(10^{dr/20})^2 A_r^3 \right]^2 \sum_{k=N_1}^{N_2} |H_3(f_k, f_{2r-k}, -f_r)|^2 \\ &+ \left[(10^{dr/20})^3 A_r^3 \right]^2 \sum_{k, k_i \neq r} |H_3(f_{k_1}, f_{k_2}, -f_{k_3})|^2 \end{aligned} \quad (6.93)$$

For a large number of channels the second summation has a larger number of terms: for $N=50$ and $r = 29$ the first summation has 21 terms while the second summation has over 800 terms. Moreover, each of the latter terms is affected by the factor $(10^{dr/20})^2$ which, for a dynamic range of 40 dB, is 10^4 and so the first summation can be neglected. Using a similar approach the second summation in equation (6.87) can be written as

$$\begin{aligned} & \sum_{k, 2k_1 - k_2 = r} (A_{k_1}^2 A_{k_2})^2 |H_3(f_{k_1}, f_{k_1}, -f_{k_2})|^2 \\ &= (A_r 10^{dr/20})^6 \sum_{k, k_i \neq r} |H_3(f_{k_1}, f_{k_1}, -f_{k_2})|^2 \end{aligned} \quad (6.94)$$

Relating the signal amplitude to the per-channel optical modulation depth, m ,

$$A_r = \frac{m_r p_0}{|H_1(\nu)|} \quad (6.95)$$

the carrier-to-intermodulation ratio becomes

$$\begin{aligned} CIR^{-1} &= \frac{(10^{dr/20})^6 m_r^4 p_0^4}{|H_1(\nu)|^6} \left\{ \left(\frac{3}{2} \right)^2 \alpha_{111} \sum_{k, k_i \neq r} |H_3(f_{k_1}, f_{k_2}, -f_{k_3})|^2 \right. \\ &+ \left. \left(\frac{3}{4} \right)^2 \alpha_{21} \sum_{k, k_i \neq r} |H_3(f_{k_1}, f_{k_1}, -f_{k_2})|^2 \right\} \end{aligned} \quad (6.96)$$

For large N the number of IMPs, ${}_rIM_{111}^N$ and ${}_rIM_{21}^N$ increase as N^2 and N , respectively, and so the previous equation can be conveniently written in the form

$$CIR^{-1} = m_r^4 [D_{111} N^2 + D_{21} N] \quad (6.97)$$

where D is the distortion coefficient, the indices of which identify the type and order of the distortion products, and are

$$D_{111} = \left(\frac{3}{2} \right)^2 \frac{p_0^4 \alpha_{111}}{N^2} (10^{dr/20})^6 \sum_{k, k_i \neq r} \frac{|H_3(f_{k_1}, f_{k_2}, -f_{k_3})|^2}{|H_1(\nu)|^6}, \quad f_{k_1} + f_{k_2} - f_{k_3} = \nu \quad (6.98)$$

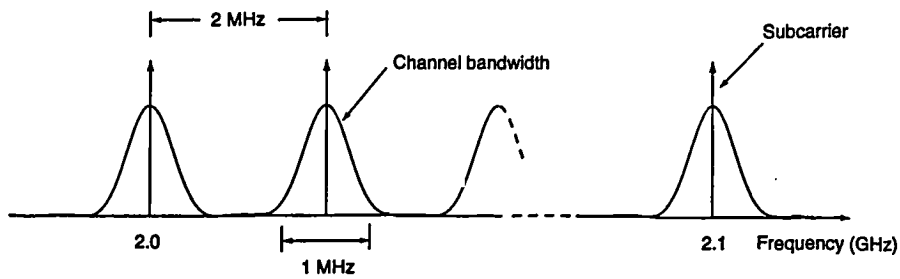


Figure 6.19: Multiplex frequency plan of a 50 channel CPFSK system.

$$D_{21} = \left(\frac{3}{4}\right)^2 \frac{p_0^4 \alpha_{21}}{N} (10^{dr/20})^6 \sum_{k, k_i \neq r} \frac{|H_3(f_{k_1}, f_{k_1}, -f_{k_2})|^2}{|H_1(\nu)|^6}, \quad 2f_{k_1} - f_{k_2} = \nu. \quad (6.99)$$

Here it is assumed that the system is limited to one octave. If this is not the case second-order distortion coefficients will have also to be determined using the same procedure.

The overall system performance can be assessed, including circuit noise, shot noise and RIN, upon application of the results derived in section 5.5. Illustrative results are given in the next section.

6.4.6 System results

The results given correspond to the 50 channel CPFSK system with the frequency plan of figure 6.19 and represented in figure 6.16. The laser parameters used, given in table 6.1, are the same as in previous sections for a DFB-BH laser.

As explained in the previous section, once the system parameters are defined the optimum performance can be obtained. This performance is based on the worst case condition which applies to the channel most affected by the laser distortion. We have found that this channel remains the same for a large range of bias currents, being strongly dependent on the spacing between the channels. For 2 MHz spacing the 29th channel always has the lower CIR for a bias current range of 35 to 80 mA. Thus, the results given in this section refer to this channel.

Figures 6.20 and 6.21 show the variation with bias current of the third-order distortion coefficients and the corresponding optimum modulation depth, respectively. The coefficient D_{111} is about four times larger than D_{21} and the contribution of two-tone third-order IMPs is small. For a bias current of 50 mA the distortion coefficients are $D_{111} = 2.4 \cdot 10^8$ and $D_{21} = 6.2 \cdot 10^7$ and the optimum modulation depth is $m_{opt} \approx 0.049\%$ for a carrier-to-noise ratio of 10 dB (bit error rate of 10^{-3}).

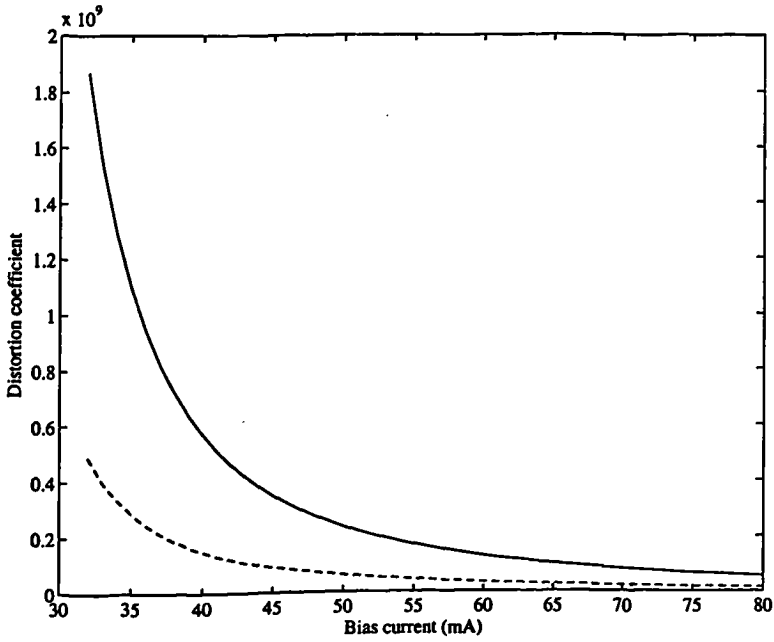


Figure 6.20: Third-order distortion coefficients D_{111} (—) and D_{21} (---).

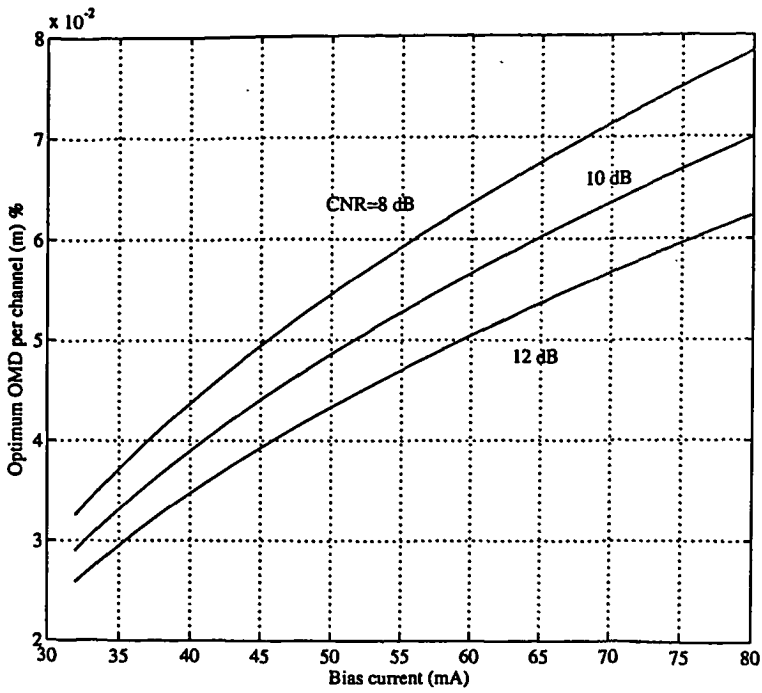


Figure 6.21: Dependence of the optimum modulation depth (m_{opt}) with laser bias current.

SCM systems are characterized by their ease of implementation and a PIN receiver is the usual choice, in some cases simply a PIN detector followed by a low-noise amplifier. Figure 6.22 shows the sensitivity for a PIN based receiver as a function of receiver noise for two values of bias current. A region is seen to exist, above $\approx 4\text{pA}/\sqrt{\text{Hz}}$ where signal independent receiver noise dominates and the sensitivity decreases as $\sqrt{\langle I_r^2 \rangle B}$.

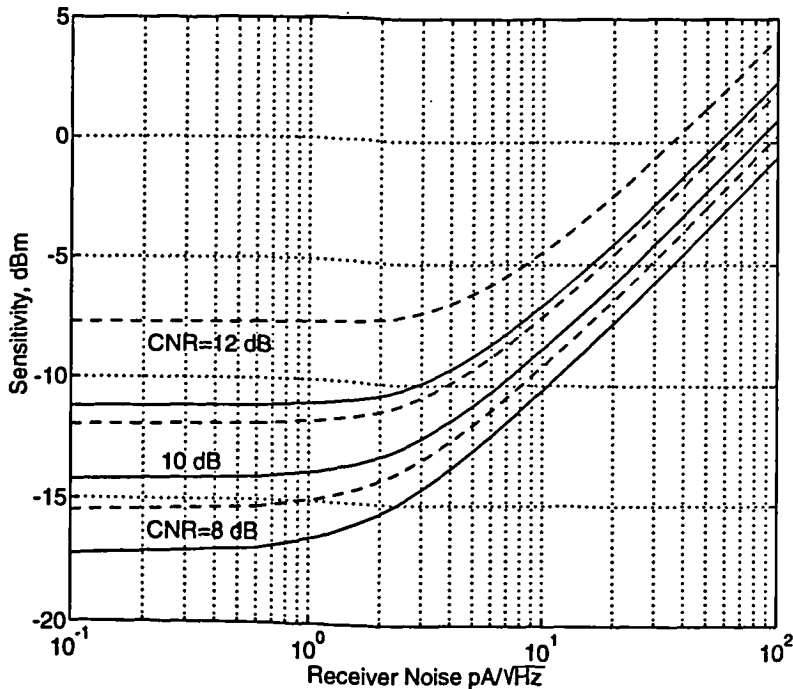


Figure 6.22: Sensitivity of a PIN based receiver: (—) $I_0=60\text{ mA}$, $\text{RIN}=-151\text{ dB/Hz}$; (---) $I_0 = 50\text{ mA}$, $\text{RIN}=-148\text{ dB/Hz}$

If the receiver noise is $\langle I_r^2 \rangle = 10\text{pA}/\sqrt{\text{Hz}}$ the required mean photocurrent I_{PIN} to achieve $\text{CNR}(m_{opt}) = 10\text{ dB}$ is 0.154 mA for a bias current of 50 mA , which for a photodetector responsivity of 0.8 corresponds to a sensitivity of -7.1 dBm . Such a high value of I_{PIN} means that an APD receiver can only provide a marginal improvement. In fact the sensitivity provided by an APD, for the same value of receiver noise, is -7.8 dBm , corresponding to an optimum APD gain of ≈ 1.8 . A tuned PIN receiver however is an appropriate choice for this type of application. A receiver of this type has been designed in GaAs specifically for this application [88]. The receiver has an equivalent noise current spectral density of $\approx 4\text{pA}/\sqrt{\text{Hz}}$, which falls in the limit where circuit noise ceases to be dominant, improving the sensitivity by 3 dB . Figure 6.23 shows the dependence of CNR with optical modulation depth and received optical

power (in figure 6.23.b the channels have equal amplitudes). The required dynamic range is achieved with the tuned receiver referred to above for a mean optical power of -10 dBm. Thus, span lengths of over 5 Km should be feasible with sufficient loss margin for 0 dBm optical power coupled into the fibre. Although shot noise is represented here as dominant, care must be taken to ensure RIN is low: for $RIN = -142$ dB/Hz it dominates circuit and shot noise by 10 dB.

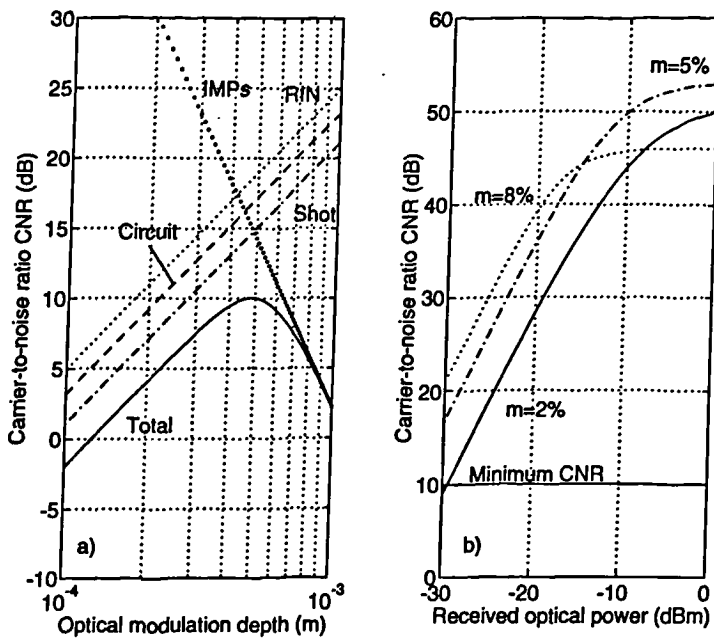


Figure 6.23: Various noise contributions and dependence of CNR with received optical power: $\langle I_r^2 \rangle = 4 \text{ pA}/\sqrt{\text{Hz}}$, $RIN = -148$ dB/Hz and laser bias 50 mA. Optimum performance is obtained for $m \approx 4.9\%$ and the dynamic range is achieved for a mean optical power of -10 dBm.

6.5 Summary

Subcarrier multiplexed system case studies have been discussed in some detail and illustrative results have been given corresponding to FM broadcast, AM-SSB and wide dynamic range Fibre/Radio systems. Using Volterra series given in chapter 4 and the system results of chapter 5 the impact of laser intrinsic distortion on system performance has been assessed. For FM systems usually operating at high frequencies this type of distortion was shown previously (chapter 5) to be dominant. For AM systems operating in the 50–500 MHz band it was here demonstrated that clipping distortion may be the dominant distortion mechanism. This is

certainly the case if the laser is biased at high bias currents which increases the resonance frequency of the laser. However, in agreement with previously reported experimental results, it was shown that an optimum bias current exists for which laser intrinsic distortion is minimum. This is a major drawback as it limits the capability of many laser structures, in AM-CATV applications, to provide output powers of tens of milliwatts. Even so a window of low distortion exists which makes possible the transmission of more than 40 channels over distances of typically < 20 Km, as required for CATV applications.

Another important SCM application was discussed concerned with the remote delivery of future mobile radio services over optical fibres. Specifically, the results given are for the return link of the RACE-II project MODAL (Microwave Optical Duplex Antenna Link) which proposes to provide a duplex optical link to a remote antenna. Due to the mobility range the return link must support a wide range of power levels. Even in this complex situation a worst case condition emerges from our analysis which is used to assess laser nonlinear distortion and provides a basis for system optimisation. The 50 channel system described with a dynamic range of 40 dB is, in terms of performance, practically identical to the AM system as both have optimum modulation depths of $\approx 5\%$ and the achieved receiver sensitivity is ≈ -10 dBm with a tuned receiver. This example clearly demonstrates that Volterra series is a powerful technique well suited for the performance assessment of multichannel SCM systems.

Chapter 7

Concluding remarks

The performance of subcarrier multiplexing has been investigated in this thesis as a means of realising multichannel optical systems supporting a wide range of analogue and digital services. The various impairments which may constrain the design and dimensioning of such systems have been detailed and quantified, with particular emphasis on the laser nonlinearities. The aim throughout has been to provide models and analytic techniques appropriate for the assessment of the nonlinearities and the associated intermodulation distortion, ensuring a sound, comprehensive platform for the design and optimisation of practical systems.

To achieve this, a number of extensions and new developments in the area of modelling and analysis of laser nonlinearity were required. Recourse has been made of the Volterra series, the tractability and applicability of the method being demonstrated via a set of system case studies.

The basic principles and characteristics of the semiconductor laser were reviewed in chapter 2. The single-mode rate equations provided an adequate basis for the analysis of laser intrinsic dynamic distortion and relative intensity noise and their dependence on device parameters and operating conditions.

The laser diode modulation characteristics were discussed in chapter 3, complemented by measurements of device characteristics and extraction of laser parameters for a commercial laser diode. Additionally, two analytic techniques for the analysis of the laser nonlinearity were presented: the perturbation technique was extended to accommodate three-tone intermodulation products; a previously reported method based on expansion in terms of Bessel functions was reformulated to include relaxation resonance effects and existing deficiencies were corrected.

The inadequacy of the existing techniques for system performance evaluation prompted the development, presented in chapter 4, of a detailed analytic nonlinear model based on the Volterra series method of nonlinear systems theory. With this method the dependence of laser distortion with channel frequency spacing is determined.

Attention is directed in chapter 5 to the assessment of the implications on system performance and the constraints on system design of laser intrinsic distortion and clipping effects. Laser intrinsic distortion was quantified in terms of distortion coefficients which take into account key parameters such as bias current and channel frequency allocation. The overall system performance is evaluated including the noise introduced in the detection process and optimum operation is identified. In particular, it was shown that APD detectors can improve performance significantly under conditions of high circuit noise and for relatively low carrier-to-noise ratios. Also, it was established that it is advantageous to accept overmodulation and the associated clipping rather than constrain the total modulation depth to 100%.

These results were applied in chapter 6 to study three relevant SCM systems and illustrative results were given for each case. It was demonstrated that for AM systems operating in the 50–500 MHz transmission band an optimum bias current exists for which laser intrinsic distortion is minimum in agreement with previously reported experimental results. At this optimum operation point clipping distortion is the dominant distortion mechanism. In systems requiring a wide-dynamic range of power levels a worst case condition was obtained from our analysis which was used to assess laser distortion and provided a basis for optimisation, this last example clearly demonstrating the applicability of the Volterra series method to the assessment of laser distortion in SCM applications.

The research summarised above suggests several possible directions for future investigation. Amongst these, the following deserve specific mention:

1. The Volterra series method provides a powerful means of analysing laser nonlinear distortion. There is however the need to further refine the rate equations which serve as a basis for the model as new effects are constantly being introduced. In particular, as mentioned in chapter 2, spatial hole burning and leakage current effects may be important for systems operating at low frequencies (50–500 MHz.) Moreover, practical systems are affected by optical feedback caused by reflections. Modelling of these

phenomena and their combined effect, which can be incorporated in the rate equations, to obtain a good match with experimental results is clearly an important area for further work.

2. In SCM applications special purpose, high linearity and hence high cost lasers are usually required. Realisation of truly low-cost systems calls for development of appropriately signal processing techniques and linearisation strategies, supported by experimental evidence as to their practicability, to enable the achievement of high linearity from low-cost lasers. The nonlinear model for the semiconductor laser here developed provides an appropriate framework within which to address this issue. Some work in this direction has been already started where possible linearisation techniques some of them borrowed from the microwave field [89, 90, 91, 92] have been investigated.
3. Recently there has been much interest in the “gain-lever” effect in single quantum well semiconductor lasers for RF and microwave applications as a means to substantially enhance the efficiency of direct intensity modulation and frequency modulation with only a marginal increase in RIN [93, 94]. Assessment of the distortion performance of such devices is therefore of importance. The analytic techniques presented in this thesis can be applied directly to this case and work is now under way on this at University College of London. Of course the technique may be applied to other laser structures, of which the “gain-lever” is but one case of interest.
4. Assessment of the linearity of semiconductor laser amplifiers (SOA) for analogue applications when used as modulators by controlling the bias current (optical gain), either in transmission or reflective modes.
5. Integration of the software written during this work in a MATLAB toolbox to provide “software tools” for system evaluation and optimisation by design engineers.
6. For systems that operate at $1.5\mu\text{m}$ to take advantage of the low attenuation of silica fibre, the coupling between laser chirp and fibre dispersion is an additional source of distortion [95, 96, 97]. Work already exists in the literature about the relative importance of this effect. Study of the interplay of fibre and laser nonlinearities in a multichannel

SCM system may be worthwhile investigating, perhaps including both phenomena in the same set of nonlinear transfer functions.

7. Most of the modelling work extant in the literature about semiconductor lasers is based on the rate equations. To apply these models, including the one described in this thesis, a set of laser parameters is needed. At this stage manufacturers still do not provide the required parameters as the fitting of parameters to measured data is usually a difficult and lengthy process. Thus, software and experimental techniques should be developed to facilitate the extraction of laser parameters. Furthermore, using distortion measurements to completely characterise the nonlinearity in the frequency domain, the present model may permit a self consistent set of parameters to be obtained particularly suited to analogue applications.

Appendix A

Clipped distortion power of an octave bandwidth FM system

The results of Reference [78] are used here to estimate the fraction of clipped distortion power falling in the transmission band of a 62 channel FM system operating in the frequency range of 2.72 to 5.2 GHz, each channel having a 36.1 MHz bandwidth. Mazo [78] has calculated the clipping distortion for the asymptotic case of small μ . The modulation of N carriers, each of modulation depth m , is assumed to result in a Gaussian random process of effective rms width

$$\mu = \sqrt{m^2 N / 2} \quad (\text{A.1})$$

which relates the ideal mean current at the photodetector I to the variance of the process, σ_I^2 through

$$\sigma_I = \mu I \quad (\text{A.2})$$

In these circumstances, over the band of frequencies $[f_a, f_b]$, the clipping events become a Poisson process with rate

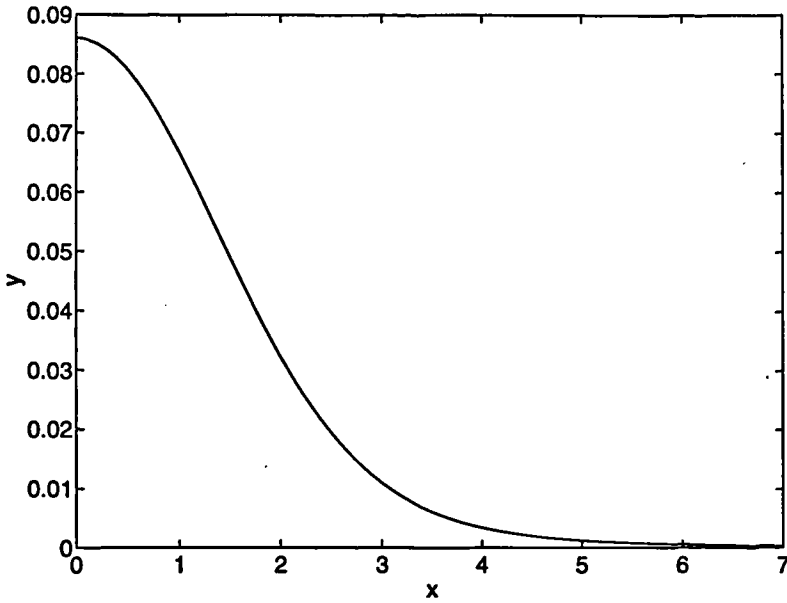
$$\lambda_I = \left[\frac{f_b^3 - f_a^3}{3(f_b - f_a)} \right]^{1/2} e^{-1/2\mu^2}. \quad (\text{A.3})$$

The duration of the clipping events τ approaches a Rayleigh distribution with mean

$$\bar{\tau} = \frac{1}{2} \frac{\text{erfc} \left(\sqrt{1/2\mu^2} \right)}{\lambda_I} \simeq \frac{\mu}{\sqrt{2\pi}} \left[\frac{3(f_b - f_a)}{f_b^3 - f_a^3} \right]^{1/2} \quad (\text{A.4})$$

and the time profile of the clipped signal approaches a parabola. From the Gaussian nature of the signal the total clipping distortion power is [78, 61]

$$\langle I_{clip}^2 \rangle = \frac{1}{\sigma_I \sqrt{2\pi}} \int_{-\infty}^0 u^2 e^{-(u-I)^2 / 2\sigma_I^2} du$$

Figure A.1: Normalized clipped distortion spectrum, $y(x)$.

$$= \frac{I^2}{2} \left[(1 + \mu^2) \operatorname{erfc} \left(\frac{1}{\sqrt{2}\mu} \right) - \sqrt{\frac{2}{\pi}} \mu e^{-1/2\mu^2} \right] \quad (\text{A.5})$$

In [78] a universal distortion spectrum curve is given from which one can calculate the ratio of distortion power in the transmission band to the total distortion power. The “flatness” of the distortion power across any band of interest may also be determined. The normalized spectrum curve $y(x)$ relating to the clipping distortion spectrum $S(f)$,

$$S(f) df = \sqrt{\frac{\pi}{2}} I^2 \mu^5 e^{-1/2\mu^2} y(x) dx \quad (\text{A.6})$$

is given by

$$y(x) = \frac{2}{\pi^2 x^3} \left[\sqrt{\pi} F \left(\frac{x}{\sqrt{\pi}} \right) - x + \frac{2x^2}{\sqrt{\pi}} F \left(\frac{x}{\sqrt{\pi}} \right) \right] \quad (\text{A.7})$$

where

$$x = 2\pi \bar{\nu} f \quad (\text{A.8})$$

$$F(t) = e^{-t^2} \int_0^t e^{u^2} du. \quad (\text{A.9})$$

A plot of the normalized asymptotic spectrum is shown in figure A.1.

Now, let us consider a FM system operating in the frequency range of 2.72 to 5.4 GHz.

Assuming a distortion power of 20 dB below the signal power σ_I^2 , we deduce from (A.5) that

$$\mu = 0.55 \quad \text{for} \quad \frac{\sigma_I^2}{\langle I_{clip}^2 \rangle} = 20 \text{ dB} \quad (\text{A.10})$$

Using this in (A.4), along with $f_a = 2.72$ GHz and $f_b = 5.2$ GHz, we get from (A.8)

$$x = 1.815 \frac{f}{f_b} \quad (\text{A.11})$$

and in figure A.1 the signal band is approximately the interval [0.93, 1.79]. The integral of $y(x)$ over this interval yields

$$\int_{0.93}^{1.79} y(x) dx = 0.046 \quad (\text{A.12})$$

which is proportional to the distortion power in the band of interest. Since the total distortion power is proportional to

$$\int_0^\infty y(x) dx = \frac{1}{2\pi} = 0.159 \quad (\text{A.13})$$

the fraction of this power that falls in the 2.72 to 5.2 GHz band being occupied by the channels is

$$\Lambda = \frac{0.046}{0.159} \cdot \frac{62 \cdot 0.0361}{5.2 - 2.72} \simeq \frac{1}{3.8} \quad (\text{A.14})$$

The second term in the above equation takes into account the fraction of distortion power that falls in the guard band between the channels. Since we have chosen $\sigma_I / \langle I_{clip}^2 \rangle = 20$ dB the distortion power in the band of interest is 25.8 dB below the signal power. It is also seen from figure A.1 that the lower frequency channels suffer about 2.5 dB more distortion power than the channels at the high end of the transmission band. Equation (A.14) is the desired result used in chapter 5 to assess the impact of clipping distortion on the performance of broadcast video FM-SCM systems.

Appendix B

Power spectral density of third-order two-tone IMP of an AM-SSB system

A method for the calculation of the power spectral density $G_{21}(f)$ of the intermodulation product of type $2f_1 - f_2$ of an AM-SSB system will be outlined here assuming the input signals are Gaussian. The method starts with the calculation of the autocorrelation function of the corresponding complex envelope

$$q_{21}(t) = (3/4)H_3(f_1, f_1, -f_3)[x_1(t) + i\hat{x}_1(t)]^2[x_2(t) + i\hat{x}_2(t)] \quad (\text{B.1})$$

where $x_1(t)$ and $x_2(t)$ are stationary random signals with zero mean that satisfy the relations

$$R_x(\tau) = R_{\hat{x}}(\tau) \quad (\text{B.2})$$

$$R_{x\hat{x}}(\tau) = -R_{\hat{x}x}(\tau) \quad (\text{B.3})$$

The fact that the calculation is carried out for a particular IMP $2f_1 - f_2 = \nu$ is not in any way restrictive as f_1 and f_2 may be replaced by any carrier frequency of the N channel system.

The autocorrelation $R_{q_{21}}(\tau) = E\{q_{21}^*(t)q_{21}(t + \tau)\}$ of $q_{21}(t)$ becomes

$$\begin{aligned} R_{q_{21}}(\tau) &= (3/4)^2 |H_3(\nu)|^2 \{ R_{x_1^2}(\tau) + R_{\hat{x}_1^2}(\tau) - R_{x_1^2 \hat{x}_1^2}(\tau) - R_{\hat{x}_1^2 x_1^2}(\tau) + 4R_{(x_1 \hat{x}_1)(x_1 \hat{x}_1)}(\tau) \\ &+ i2[R_{x_1^2(x_1 \hat{x}_1)}(\tau) - R_{\hat{x}_1^2(x_1 \hat{x}_1)}(\tau) - R_{(x_1 \hat{x}_1)x_1^2}(\tau) + R_{(x_1 \hat{x}_1)\hat{x}_1^2}(\tau)] \} \\ &\times 2[R_{x_2}(\tau) + iR_{x_2 \hat{x}_2}(\tau)] \end{aligned} \quad (\text{B.4})$$

It is seen that $R_{q_{21}}(\tau)$ involves autocorrelation and cross-correlation functions of the square and cross products of the signal $x_1(t)$ and the corresponding Hilbert transform $\hat{x}_1(t)$. These will now be evaluated using the moment generating function (MGF) [98] of a sum of random

variables assuming the input $x_1(t)$ is a Gaussian random process. Since $\hat{x}_1(t)$ is obtained by a linear operation on $x_1(t)$, $\hat{x}_1(t)$ is also Gaussian.

If V is a Gaussian random variable with zero mean the moment generating function, $M_V(s)$, of V is [70]

$$M_V(s) = E \{ e^{sV} \} = e^{\sigma_V^2 s^2 / 2} \tag{B.5}$$

σ_V^2 being the variance of V

$$\sigma_V^2 = E\{V^2\} \tag{B.6}$$

Let us now take V as the sum of the Gaussian random variables W, X, Y and Z having zero mean $V = s_1W + s_2X + s_3Y + s_4Z$. The MGF of the sum of the random variables is

$$\begin{aligned} M_{WXYZ}(s_1, s_2, s_3, s_4) &= E \{ e^{s_1W + s_2X + s_3Y + s_4Z} \} \\ &= e^{\sigma^2 / 2} \end{aligned} \tag{B.7}$$

where

$$\begin{aligned} \sigma^2 &= s_1^2 \sigma_W^2 + s_2^2 \sigma_X^2 + s_3^2 \sigma_Y^2 + 2C_{WX} s_1 s_2 + 2C_{WY} s_1 s_3 \\ &+ 2C_{XY} s_2 s_3 + 2C_{WZ} s_1 s_4 + 2C_{XZ} s_2 s_4 + 2C_{YZ} s_3 s_4 \end{aligned} \tag{B.8}$$

with σ_a and C_{ab} denoting the variance of a and the covariance of a and b ($a, b = W, X, Y, Z$), respectively. Expanding equation (B.7) in a Taylor series the following equality is obtained

$$\begin{aligned} M_{WXYZ}(s_1, s_2, s_3, s_4) &= \sum_{n=0}^{\infty} \frac{1}{n!} \sum_{k=0}^n \sum_{l=0}^k \sum_{m=0}^l \binom{n}{k} \binom{k}{l} \binom{l}{m} \\ &\times E \{ W^m X^{l-m} Y^{k-l} Z^{n-k} \} s_1^m s_2^{l-m} s_3^{k-l} s_4^{n-k} \end{aligned} \tag{B.9}$$

$$= \sum_{r=0}^{\infty} \frac{1}{r!} \left[\frac{\sigma^2}{2} \right]^r \tag{B.10}$$

which will be the basis for the calculation of the above correlation functions.

Consider the autocorrelation $R_{x_1^2}(\tau) = E\{x_1^2(t)x_1^2(t + \tau)\}$. In (B.9) there is a term in $s_1^2 s_2^2$ corresponding to $m = 2, l = k = n = 4$ with a coefficient

$$\binom{4}{2} \frac{1}{4!} E\{W^2 X^2\}. \tag{B.11}$$

Equating this coefficient to the corresponding coefficient in the expansion of $e^{\sigma^2/2}$ (equa-

tion (B.10)), yields

$$\frac{1}{4!} \binom{4}{2} E\{W^2 X^2\} = \frac{1}{4} [\sigma_w^2 \sigma_x^2 + 2C_{wX}^2] \quad (\text{B.12})$$

which gives

$$E\{W^2 X^2\} = 2E^2\{WX\} + E\{W^2\}E\{X^2\} \quad (\text{B.13})$$

Using this equality the autocorrelations $R_{x_1^2}(\tau)$ and $R_{x_1^2 \hat{x}_1^2}(\tau)$ become

$$\begin{aligned} R_{\hat{x}_1^2 \hat{x}_1^2}(\tau) &= R_{x_1^2}(\tau) \\ &= 2R_{x_1}^2(\tau) + R_{x_1}^2(0) \end{aligned} \quad (\text{B.14})$$

$$\begin{aligned} R_{x_1^2 \hat{x}_1^2}(\tau) &= R_{\hat{x}_1^2 x_1^2}(\tau) \\ &= 2R_{x_1 \hat{x}_1}^2(\tau) + R_{x_1}^2(0) \end{aligned} \quad (\text{B.15})$$

Proceeding with the same technique the other autocorrelation and cross-correlation functions appearing in equation (B.4) are simplified in terms of the autocorrelation function $R_{x_1}(\tau)$ and $R_{x_1 \hat{x}_1}(\tau)$. Generally, the coefficient of $s_1 s_2 s_3 s_4$ in (B.9) is

$$\frac{1}{4!} \binom{4}{3} \binom{3}{2} \binom{2}{1} E\{WXYZ\} \quad (\text{B.16})$$

Terms in $s_1 s_2 s_3 s_4$ appear in (B.10) for $n=2$ and are

$$C_{wz} C_{xy} + C_{wy} C_{xz} + C_{wx} C_{yz} \quad (\text{B.17})$$

Equating both coefficients results in:

$$E\{WXYZ\} = E\{WZ\}E\{XY\} + E\{WY\}E\{XZ\} + E\{WX\}E\{YZ\} \quad (\text{B.18})$$

from which the following simplifications are derived

$$\begin{aligned} R_{x_1^2(x_1 \hat{x}_1)}(\tau) &= E\{x_1^2(t) x_1(t+\tau) \hat{x}_1(t+\tau)\} \\ &= R_{(x_1 \hat{x}_1) \hat{x}_1^2}(\tau) \\ &= 2E\{x_1(t) x_1(t+\tau)\} E\{x_1(t) \hat{x}_1(t+\tau)\} \\ &= 2R_{x_1}(\tau) R_{x_1 \hat{x}_1}(\tau) \end{aligned} \quad (\text{B.19})$$

$$R_{(x_1 \hat{x}_1) x_1^2}(\tau) = E\{x_1(t) \hat{x}_1(t) x_1^2(t+\tau)\}$$

$$\begin{aligned}
 &= R_{\hat{x}_1^2(x_1\hat{x}_1)}(\tau) \\
 &= -2E\{x_1(t)x_1(t+\tau)\}E\{x_1(t)\hat{x}_1(t+\tau)\} \\
 &= -2R_{x_1}(\tau)R_{x_1\hat{x}_1}(\tau)
 \end{aligned} \tag{B.20}$$

Substituting equations (B.14), (B.15), (B.19) and (B.20) into (B.4) yields

$$\begin{aligned}
 R_{q_{21}}(\tau) &= (3/4)^2 16 \left\{ (R_{x_1}^2(\tau) - R_{x_1\hat{x}_1}^2(\tau)) R_{x_2}(\tau) - 2R_{x_1}(\tau) R_{x_1\hat{x}_1}(\tau) R_{x_2\hat{x}_2}(\tau) \right. \\
 &\quad \left. + i \left[(R_{x_1}^2(\tau) - R_{x_1\hat{x}_1}^2(\tau)) R_{x_2\hat{x}_2}(\tau) + 2R_{x_1}(\tau) R_{x_1\hat{x}_1}(\tau) R_{x_2\hat{x}_2}(\tau) \right] \right\}
 \end{aligned} \tag{B.21}$$

Taking the Fourier transform and after some simplification the power spectral density $G_{21}(f)$ of the IMP of type $2f_1 - f_2$ is written as

$$G_{21}(f) = (3/4)^2 128 [G_{x_1}(f)u(f)] * [G_{x_1}(f)u(f)] * [G_{x_2}(f)u(f)] \tag{B.22}$$

where $u(f)$ is the unit step function. If the power spectral density of the baseband signals is $G_{x_1}(f) = G_{x_2}(f) = G \times \text{rect}(f/2B)$ then the previous equation gives

$$(3/4)^2 128 G^3 \times \text{rect}^{*3}(f/B) * \delta(f - 3B/2) \tag{B.23}$$

with $\text{rect}^{*3}(f)$ denoting the triple convolution $\text{rect}(f) * \text{rect}(f) * \text{rect}(f)$.

Appendix C

Intermodulation power spectral density of CPFSK

In this appendix the second-order and third-order intermodulation power spectral density functions for a CPFSK system will be derived. The derivation follows closely the method given in Appendix 3A of Reference [71] and is given here for completeness.

The n -order complex envelope of the intermodulation component at ν due to the input components $(f_{k_1}, \dots, f_{k_n})$, is given by 6.74 as

$$q_{n\nu}(t) = \frac{n!2^{-n+1}}{m_{-N}! \dots m_N!} H_n(\nu) \left[\prod_{k=-N}^N A_l^{m_k} \right] \sum_{k=0}^{\infty} e^{i2\pi f_d \sum_{l=-N}^N m_l [\phi_{kl} + a_{kl}(t-kT)]} p_T(t-kT) \quad (\text{C.1})$$

where f_d is the frequency deviation, $p_T(t)$ is a rectangular pulse of unit amplitude and duration T

$$p_T(t) = \begin{cases} 1 & kT < t < (k+1)T \\ 0 & \text{otherwise} \end{cases} \quad (\text{C.2})$$

and ϕ_{kl} is defined as

$$\phi_{kl} = \sum_{r=0}^{k-1} a_{rl}, \quad (\text{C.3})$$

the amplitude a_{kl} being the k th symbol in the message sequence of channel l , belonging to a set of M discrete values.

The power spectral density of $q_{n\nu}(t)$ can be obtained by first calculating the corresponding autocorrelation function and then applying the Fourier transform, a method which has been described in chapter 5. There is an alternative procedure, which will be used here, for obtaining the power spectral density directly without having to determine the autocorrelation function. This approach, described in some detail in the book by Papoulis, [70] involves the direct

computation of the two dimensional Fourier transform

$$\begin{aligned}
 \Gamma_{q_{nv}}(f_1, f_2) &= \int_{-\infty}^{\infty} \int_{-\infty}^{\infty} R_{q_{nv}}(t_1, t_2) e^{-i2\pi(f_1 t_1 - f_2 t_2)} dt_1 dt_2 \\
 &= E \left[\int_{-\infty}^{\infty} q_{nv}(t_1) e^{-i2\pi f_1 t_1} dt_1 \int_{-\infty}^{\infty} q_{nv}(t_2) e^{-i2\pi f_2 t_2} dt_2 \right] \\
 &= E [Q_{nv}(f_1) Q_{nv}^*(f_2)] \tag{C.4}
 \end{aligned}$$

where $R_{q_{nv}}(t_1, t_2)$ and $Q_{nv}(f)$ are the autocorrelation function and Fourier transform of $q_{nv}(t)$, respectively. In general, $\Gamma_{q_{nv}}(f_1, f_2)$ can be expressed as a sum of two terms, namely,

$$\Gamma_{q_{nv}}(f_1, f_2) = G_{q_{nv}}(f_1) \delta(f_1 - f_2) + \Gamma'_{q_{nv}}(f_1, f_2) \tag{C.5}$$

The desired term in this decomposition is $G_{q_{nv}}(f)$, the power spectral density of intermodulation complex envelope q_{nv} . Thus, the desired power density spectrum is obtained directly by computing the expected value of $Q_{nv}(f_1) Q_{nv}^*(f_2)$ without going through the intermediate step of computing the autocorrelation function.

We now proceed by calculating the Fourier transform of $q_{nv}(t)$

$$Q_{nv}(f) = C_{nm} \sum_{k=0}^{\infty} P_T(f - f_d \sum_l m_l a_{kl}) e^{i2\pi T(f_d \sum_l m_l \alpha_{kl} - kf)} \tag{C.6}$$

$$= C_{nm} \sum_k P_T(f - f_d I_k) e^{i2\pi T(I'_k f_d - kf)} \tag{C.7}$$

where I_k and I'_k are random variables defined as

$$I_k = \sum_{l=-N}^N m_l a_{kl}, \quad I'_k = \sum_{l=-N}^N m_l \alpha_{kl} \tag{C.8}$$

From (C.4) the two-dimensional Fourier transform $\Gamma_{q_{nv}}(f_1, f_2)$ is

$$\begin{aligned}
 \Gamma_{q_{nv}}(f_1, f_2) &= [Q_{nv}(f_1) Q_{nv}^*(f_2)] \\
 &= |C_{nm}|^2 \sum_{j=0}^{\infty} \sum_{k=0}^{\infty} E \left\{ P_T(f_1 - f_d I_j) P_T^*(f_2 - f_d I_k) \right. \\
 &\quad \left. \times e^{i2\pi T[f_d(I'_j - I'_k) - jf_1 + kf_2]} \right\} \tag{C.9}
 \end{aligned}$$

the expectation being taken over the the set of information symbols $\{I_k, I'_k\}$. Let us separate this double sum into three terms corresponding to $j = k$, $j > k$ and $j < k$.

For $j = k$, we have

$$\widehat{kk}(f_1, f_2) = |C_{nm}|^2 \sum_{k=0}^{\infty} E [P_T(f_1 - f_d I_k) P_T^*(f_2 - f_d I_k)] e^{-i2\pi(f_1 - f_2)kT} \quad (\text{C.10})$$

The expected value of $P_T(f_1 - f_d I_k) P_T^*(f_2 - f_d I_k)$ is the same for all possible values of I_k because they are identically distributed (they have the same probability density function) yielding

$$\widehat{kk}(f_1, f_2) = |C_{nm}|^2 E \left[P_T(f_1 - f_d I) P_T^*(f_2 - f_d I) \sum_{k=0}^{\infty} e^{-2\pi(f_1 - f_2)kT} \right] \quad (\text{C.11})$$

The value of the sum in (C.11) is

$$\sum_{k=0}^{\infty} e^{-i2\pi(f_1 - f_2)kT} = \frac{1}{2} + \frac{1}{2T} \sum_{k=-\infty}^{\infty} \delta \left(f_1 - f_2 - \frac{k}{T} \right) - \frac{i}{2} \cot(f_1 - f_2)\pi T \quad (\text{C.12})$$

Therefore, for $j = k$ the contribution is

$$\begin{aligned} \widehat{kk}(f_1, f_2) &= |C_{nm}|^2 E [P_T(f_1 - f_d I) P_T^*(f_2 - f_d I)] \\ &\times \left[\frac{1}{2} + \frac{1}{2T} \sum_{k=-\infty}^{\infty} \delta \left(f_1 - f_2 - \frac{k}{T} \right) - \frac{i}{2} \cot(f_1 - f_2)\pi T \right] \end{aligned} \quad (\text{C.13})$$

When $j > k$ we have the term

$$\begin{aligned} \circ_{jk}(f_1, f_2) &= |C_{nm}|^2 \sum_{j=1}^{\infty} \sum_{k=0}^{j-1} e^{-i2\pi T(jf_1 - kf_2)} \\ &\times E \left\{ P_T(f_1 - f_d I_j) P_T^*(f_2 - f_d I_k) e^{i2\pi T f_d [\sum_l m_l (\alpha_{jl} - \alpha_{kl})]} \right\} \end{aligned} \quad (\text{C.14})$$

We now have

$$\begin{aligned} \sum_l m_l (\alpha_{jl} - \alpha_{kl}) &= \sum_l m_l \left[\sum_{r=0}^{j-1} a_{rl} - \sum_{r=0}^{k-1} a_{rl} \right] \\ &= \sum_l m_l \sum_{r=k}^{j-1} a_{rl} \\ &= \sum_l m_l [a_{kl} + a_{k+1,l} + \dots + a_{j-1,l}] \\ &= I_k + I_{k+1} + \dots + I_{j-1} \end{aligned} \quad (\text{C.15})$$

Since the symbols I_k are independent, the expected value of the product in (C.14) can be written as

$$E \left\{ P_T(f_1 - f_d I_j) P_T^*(f_2 - f_d I_k) e^{i2\pi T f_d [\sum_l m_l (\alpha_{jl} - \alpha_{kl})]} \right\}$$

$$= E[P_T(f_1 - f_d I_j)] E \left[P_T^*(f_2 - f_d I_k) e^{i2\pi f_d T I_k} \right] \prod_{r=k+1}^{j-1} E \left[e^{i2\pi f_d T I_r} \right] \quad (\text{C.16})$$

Note that

$$E \left[e^{i2\pi f_d T I_r} \right] = \Phi_I(2\pi f_d T) \quad (\text{C.17})$$

is the characteristic function of the random variable I . Also the expectation of $P_T(f_1 - f_d I_j)$ and $P_T(f_2 - f_d I_k) \exp(i2\pi f_d T I_k)$ is independent of j and k , respectively. Hence, the double sum in (C.14) can be expressed as

$$\begin{aligned} \circ_{jk}(f_1, f_2) &= |C_{nm}|^2 E[P_T(f_1 - f_d I)] E \left[P_T(f_2 - f_d I) e^{i2\pi f_d T I} \right] \\ &\times \sum_{j=1}^{\infty} \sum_{k=0}^{j-1} [\Phi_I(2\pi f_d T)]^{j-k-1} e^{-i2\pi T(jf_1 - kf_2)} \end{aligned} \quad (\text{C.18})$$

In evaluating the double sum we note that a characteristic function satisfies the condition $|\Phi(\omega)| \leq 1$. For the moment we assume $|\Phi_I(2\pi f_d T)| < 1$. In this case and after some analytical manipulation the double sum in (C.18), denoted as S , becomes

$$\begin{aligned} S &= \frac{1}{\Phi_I(2\pi f_d T) - e^{i2\pi f_2 T}} \left\{ \left[\frac{1}{1 - \Phi_I(2\pi f_d T) e^{-i2\pi f_1 T}} - 1 \right] \right. \\ &\left. - \left[-\frac{1}{2} + \frac{1}{2T} \sum_{j=-\infty}^{\infty} \delta(f_1 - f_2 - \frac{j}{T}) - \frac{i}{2} \cot(f_1 - f_2)\pi T \right] \right\} \end{aligned} \quad (\text{C.19})$$

and the contribution to $\Gamma_{q_{nv}}(f_1, f_2)$ for $j > k$ becomes

$$\circ_{jk}(f_1, f_2) = S |C_{nm}|^2 E[P_T(f_1 - f_d I)] E \left[P_T^*(f_2 - f_d I) e^{i2\pi f_d T I} \right] \quad (\text{C.20})$$

Repeating the above calculations for $j < k$ yields

$$+_{jk} = S^* |C_{nm}|^2 E \left[P_T(f_1 - f_d I) e^{-i2\pi f_d T I} \right] E \left[P_T^*(f_2 - f_d I) \right] \quad (\text{C.21})$$

Adding the three terms $\hat{k}_k(f_1, f_2)$, $\circ_{jk}(f_1, f_2)$ and $+_{jk}(f_1, f_2)$ corresponding to the terms $j = k$, $j > k$ and $j < k$, respectively, the two-dimensional Fourier transform of the autocorrelation function $R_{q_{nv}}(t_1, t_2)$ is obtained. From equations (C.4), (C.13), (C.20) and (C.21) and selecting the appropriate terms contained in $G_{q_{nv}}$ which are the coefficient of $\delta(f_1 - f_2)$, gives

$$\begin{aligned} G_{q_{nv}}(f) &= \frac{|C_{nm}|^2}{2T} E[|P_T(f - f_d I)|^2] + \frac{|C_{nm}|^2}{2T} 2 \operatorname{Re} \left\{ \frac{e^{-i2\pi f T}}{1 - \Phi_I(2\pi f_d T) e^{-i2\pi f T}} \right. \\ &\left. \times E[P_T(f - f_d I)] E \left[P_T^*(f - f_d I) e^{i2\pi f_d T I} \right] \right\} \end{aligned} \quad (\text{C.22})$$

Equation (C.22) applies for $|\Phi_I(2\pi f_d T)| < 1$, a condition for which the power spectral density contains no discrete frequency components. The case when $|\Phi_I(2\pi f_d T)| < 1$, also described in some detail in Appendix 3A of Reference [71] will not be considered here.

Binary CPFSK

The continuous intermodulation spectral density will now be evaluated when the information symbols take 2 possible values:

$$a_k = 2k - 1, \quad k = 0, 1 \quad (\text{C.23})$$

$$I_k = \sum_{l=-N}^N m_l a_{kl} \quad (\text{C.24})$$

the index l identifying the channel number.

Three-tone intermodulation:

Let us calculate the power spectral density of three-tone distortion products of type $f_1 + f_2 - f_3$. First, we determine the expectation $E[|P_T(f - f_d I)|^2]$ taking $m_l = 1$ for $l = 1, 2$ or -3 , and $m_l = 0$ otherwise.

$$\begin{aligned} E[|P_T(f - f_d I)|^2] &= E\left[|P_T(f - f_d 2(k_1 + k_2 - k_3 + 1) + 3f_d)|^2\right] \\ &= E\left[|P_T(f - f_d(2k - 3))|^2\right] \end{aligned} \quad (\text{C.25})$$

In the last expression $k = k_1 + k_2 - k_3 + 1$ is the sum of three independent random variables with possible values $k = 0, 1, 2, 3$. The probabilities P_k associated with these values may be obtained using the probability generating function (PGF) [98], $F_k(z)$ defined as

$$\begin{aligned} F_k(z) &= E[z^k] \\ &= E[z^{k_1}]E[z^{k_2}]E[z^{-k_3}]z \\ &= pq^2 + (q^3 + 2p^2q)z + (p^3 + 2pq^2)z^2 + p^2qz^3 \end{aligned} \quad (\text{C.26})$$

where q and p are the probabilities of $k_i = 0, 1$, respectively. The probabilities P_k given by

$$P_k = \frac{1}{k!} \left. \frac{d^k F_k(z)}{dz^k} \right|_{z=0} \quad (\text{C.27})$$

are

$$P_0 = pq^2 \quad (C.28)$$

$$P_1 = q^3 + 2p^2q \quad (C.29)$$

$$P_2 = p^3 + 2pq^2 \quad (C.30)$$

$$P_3 = p^2q \quad (C.31)$$

Thus, the expectation (C.25) becomes

$$E[|P_T(f - f_d I)|^2] = \sum_{k=0}^3 P_k T^2 \text{sinc}^2 T[f - f_d(2k - 3)] \quad (C.32)$$

In the same way we have

$$E[P_T(f - f_d I)] = \sum_{k=0}^3 P_k T \text{sinc} T[f - f_d(2k - 3)] e^{-i\pi T[f - f_d(2k - 3)]} \quad (C.33)$$

and

$$E[P_T^*(f - f_d I) e^{i2\pi f_d T I}] = \sum_{k=0}^3 P_k T \text{sinc} T[f - f_d(2k - 3)] e^{i\pi T[f + f_d(2k - 3)]} \quad (C.34)$$

Let us now evaluate $\Phi_I(2\pi f_d T)$

$$\begin{aligned} \Phi &\equiv \Phi_I(2\pi f_d T) = E[e^{i2\pi f_d T(2k-3)}] \\ &= P_0 e^{-i6\pi f_d T} + P_1 e^{-i2\pi f_d T} + P_2 e^{i2\pi f_d T} + P_3 e^{i6\pi f_d T} \end{aligned} \quad (C.35)$$

Substitution of equations (C.32), (C.33) and (C.34) into (C.22) and performing some algebraic manipulation yields the following expression for the three-tone intermodulation power spectrum

$$G_{111}(f) = \frac{T|C_{111}|^2}{2} \left\{ \sum_{k=0}^3 P_k U_k^2(f) + 2 \sum_{j=0}^3 \sum_{k=0}^3 P_j P_k U_j(f) U_k(f) V_{jk}(f) \right\} \quad (C.36)$$

where

$$C_{111} = (3/2) H_3(f_1, f_2, -f_3) A_1 A_2 A_3 \quad (C.37)$$

$$U_k(f) = \text{sinc} T[f - f_d(2k - 3)] \quad (C.38)$$

$$V_{jk}(f) = \frac{\cos(2\pi T f - \varphi_{jk}) - \text{Re}\{\Phi\} \cos \varphi_{jk} - \text{Im}\{\Phi\} \sin \varphi_{jk}}{1 + |\Phi|^2 - 2[\text{Re}\{\Phi\} \cos 2\pi f T + \text{Im}\{\Phi\} \sin 2\pi f T]} \quad (C.39)$$

$$\varphi_{jk} = 2\pi f_d T(j + k - 3) \quad (C.40)$$

the probabilities P_k being given by equations (C.28)–(C.31).

If both symbols occur with equal probabilities ($p = q = 1/2$) then

$$P_k = \left(\frac{1}{2}\right)^3 \binom{3}{k} \quad (\text{C.41})$$

and after some simplification we get

$$\Phi \equiv \Phi(2\pi f_d T) = \cos^3 2\pi f_d T \quad (\text{C.42})$$

$$V_{jk}(f) = \frac{\cos(2\pi f T - \varphi_{jk}) - \Phi \cos \varphi_{jk}}{1 + |\Phi|^2 - 2\Phi \cos 2\pi f T} \quad (\text{C.43})$$

Two-tone intermodulation:

The calculation of the intermodulation power spectral density of two-tone third-order distortion products of type $2f_1 - f_2$ follows a similar procedure as the one just presented. The random variable I is now written as

$$\begin{aligned} I &= \sum_{l=-N}^N m_l (2k_l - 1) = 2(k_1 - k_2 + 1) - 3 \\ &= 2k - 3 \end{aligned} \quad (\text{C.44})$$

where $k = 2k_1 - k_2 + 1$, for $k_i = 0, 1$ with $i = 1, 2$. Again the possible values for k are 0, 1, 2, 3.

The corresponding PGF is

$$F_k = pq + q^2 z + p^2 z^2 + pqz^3 \quad (\text{C.45})$$

and the associated symbol probabilities are

$$P_0 = pq \quad (\text{C.46})$$

$$P_1 = q^2 \quad (\text{C.47})$$

$$P_2 = p^2 \quad (\text{C.48})$$

$$P_3 = pq \quad (\text{C.49})$$

The final expression for the power spectral density is

$$G_{21}(f) = \frac{T|C_{21}|^2}{2} \left\{ \sum_{k=0}^3 P_k U_k^2(f) + 2 \sum_{j=0}^3 \sum_{k=0}^3 P_j P_k U_j(f) U_k(f) V_{jk}(f) \right\} \quad (\text{C.50})$$

with

$$C_{21} = (3/4) H_3(f_1, f_1, -f_2) A_1^2 A_2 \quad (\text{C.51})$$

equations (C 35), (C 38)–(C 40) being still applicable except for the probabilities P_k which are now given by (C 46)–(C 49)

If both symbols occur with equal probability then $P_k = 1/4$, $k = 0, 1, 2, 3$ and the characteristics function Φ simplifies to

$$\Phi = \frac{1}{2}[\cos 6\pi f_d T + \cos 2\pi f_d T] \quad (\text{C } 52)$$

Bibliography

- [1] T. E. Darcie, "Subcarrier multiplexing for multiple-access lightwave networks," *J. Lightwave Technol.*, vol. LT-5, pp. 1103–1110, Aug. 1987.
- [2] T. E. Darcie, P. P. Iannone, B. L. Kasper, J. R. Talman, C. A. Burrus and T. A. Baker, "Wide-band lightwave distribution system using subcarrier multiplexing," *J. Lightwave Technol.*, vol. 7, pp. 997–1005, June 1989.
- [3] R. Olshansky, V. A. Lanzisera and P. M. Hill, "Subcarrier multiplexed lightwave systems for broadband distribution," *J. Lightwave Technol.*, vol. 7, pp. 1329–1342, Sept. 1989.
- [4] T. E. Darcie, "Subcarrier multiplexing for lightwave networks and video distribution systems," *IEEE J. on Select. Areas in Commun.*, vol. 8, pp. 1240–1248, Sept. 1990.
- [5] C. B. Su, V. Lanzisera, R. Olshansky, W. Powazinik, E. Meland, J. Schlafer and R. B. Lauer, "15 GHz direct modulation bandwidth of vapour-phase regrown 1.3 μm InGaAsP buried-heterostructure lasers under CW operation at room temperature," *Electron. Lett.*, vol. 21, pp. 577–578, June 1985.
- [6] R. Olshansky, W. Powazinik, P. Hill, V. Lanzisera and R. B. Lauer, "InGaAsP buried heterostructure laser with 22 GHz bandwidth and high modulation efficiency," *Electron. Lett.*, vol. 23, pp. 839–841, July 1987.
- [7] C. N. Lo, "A hybrid lightwave transmission system for subcarrier multiplexed video and digital B-ISDN services in the local loop," *J. Lightwave Technol.*, vol. 7, pp. 1839–1846, Nov. 1989.
- [8] R. Olshansky, V. A. Lanzisera and P. Hill, "Simultaneous transmission of 100 Mbit/s at baseband and 60 FM video channels for a wideband optical communication-network," *Electron. Lett.*, vol. 24, pp. 1234–1235, Sept. 1988.

- [9] R. Gross, R. Olshansky and P. Hill, "20 channel coherent FSK system using subcarrier multiplexing," *IEEE Photonics Technol. Lett.*, vol. 1, pp. 224–226, Aug. 1989.
- [10] R. Olshansky, R. Gross and M. Schmidt, "Subcarrier multiplexed coherent lightwave system for video distribution," *IEEE J. on Select. Areas in Commun.*, vol. 8, pp. 1268–1275, Sept. 1990.
- [11] P. M. Hill and R. Olshansky, "8 Gb/s subcarrier multiplexed coherent lightwave system," *IEEE Photonics Technol. Lett.*, vol. 3, pp. 764–766, Aug. 1991.
- [12] K. W. Cheung, S. C. Liew and C. Lo, "Experimental demonstration of multiwavelength optical network with microwave subcarriers," *Electron. Lett.*, vol. 25, pp. 381–383, 1989.
- [13] S. C. Liew and K. Cheung, "A broad-band optical network based on hierarchical multiplexing of wavelenghts and RF subcarriers," *J. Lightwave Technol.*, vol. 7, pp. 1825–1838, Nov. 1989.
- [14] K. Y. Lau and A. Yariv, "Intermodulation distortion in a directly modulated semiconductor injection laser," *Appl. Phys. Lett.*, vol. 45, pp. 1034–1036, Nov. 1984.
- [15] T. E. Darcie, R. S. Tucker and G. J. Sullivan, "Intermodulation and harmonic distortion in InGaAsP lasers," *Electron. Lett.*, vol. 21, pp. 665–666, Aug. 1985.
- [16] P. Iannone and T. E. Darcie, "Multichannel intermodulation distortion in high-speed GaInAsP lasers," *Electron. Lett.*, vol. 23, pp. 1361–1362, Dec. 1987.
- [17] J. J. O'Reilly and H. M. Salgado, "Distortion analysis of semiconductor lasers: A caution," *Electron. Lett.*, vol. 27, pp. 946–947, May 1991.
- [18] H. M. Salgado and J. J. O'Reilly, "Tractable models of laser distortion in subcarrier multiplexed optical systems," *Digest of 3rd Bangor Symposium on Communications*, pp. 23–25, (Bangor, U.K.), 29–30 May 1991.
- [19] H. M. Salgado and J. J. O'Reilly, "Volterra series analysis of distortion in semiconductor laser diodes," *IEE Proc.-J*, vol. 138, pp. 379–382, Dec. 1991.

- [20] K. Petermann, *Laser Diode Modulation and Noise*. Advances in Optoelectronics, Kluwer Academic Publisher, 1988.
- [21] G. P. Agrawal and N. K. Dutta, *Long-Wavelength Semiconductor Lasers*. Electrical/Computer Science and Engineering Series, Van Nostrand Reinhold, 1986.
- [22] J. H. C. Casey and M. B. Panish, *Heterostructure Lasers*. Part A: *Fundamental Principles*. Quantum Electronics Series, Academic Press, Inc., 1978.
- [23] A. Yariv, *Quantum Electronics*. John Wiley & Sons, third edition ed., 1989.
- [24] J. F. S. H. C. Casey, "Concentration-dependent absorption and spontaneous emission of heavily doped GaAs," *J. Appl. Phys.*, vol. 47, pp. 631–643, Feb. 1976.
- [25] N. K. Dutta, "Calculated absorption, emission and gain in $\text{In}_{0.72}\text{Ga}_{0.28}\text{As}_{0.6}\text{P}_{0.4}$," *J. Appl. Phys.*, vol. 51, pp. 6095–6100, Dec. 1980.
- [26] L. D. Westbrook, "Measurements of dg/dN and dn/dN and their dependence of photon energy in $\lambda = 1.5 \mu\text{m}$ InGaAsP laser diodes," *IEE Proc.-J*, vol. 133, pp. 135–142, Apr. 1986.
- [27] D. Marcuse, "Classical derivation of the rate equation," *IEEE J. Quantum Electron.*, vol. QE-19, pp. 1228–1231, Aug. 1983.
- [28] H. Kogelnik and C. V. Shank, "Coupled-wave theory of distributed feedback lasers," *J. Appl. Phys.*, vol. 432, pp. 2327–2335, May 1972.
- [29] J. Wang, N. Schunk and K. Petermann, "Linewidth enhancement for DFB lasers due to longitudinal mode field dependence in the laser cavity," *Electron. Lett.*, vol. 23, pp. 715–717, July 1987.
- [30] K. Y. Lau and A. Yariv, "Ultrahigh speed semiconductor lasers," *IEEE J. Quantum Electron.*, vol. QE-21, pp. 121–137, Feb. 1985.
- [31] R. S. Tucker and I. P. Kaminow, "High-frequency characteristics of directly modulated InGaAsP ridge waveguide and buried heterostructures," *J. Lightwave Technol.*, vol. LT-2, pp. 385–393, Aug. 1984.

- [32] R. S. Tucker, "High-speed modulation of semiconductor lasers," *J. Lightwave Technol.*, vol. LT-3, pp. 1180–1192, Dec. 1985.
- [33] R. S. Vodhanel, A. F. Elrefaie, R. E. Wagner, M. Z. Iqbal, J. L. Gimlett and S. Tsuji, "10-to-20 gbit/s modulation performance of 1.5 μm distributed feedback lasers for frequency-shift-keying systems," *J. Lightwave Technol.*, vol. 7, pp. 1454–60, Oct. 1989.
- [34] C. Y. Kuo, "Fundamental second-order nonlinear distortion in analog AM CATV transport systems based on single frequency semiconductor lasers," *J. Lightwave Technol.*, vol. 10, pp. 235–243, Feb. 1992.
- [35] K. Y. Lau and A. Yariv, "High-frequency current modulation of semiconductor injection lasers," *Semiconductors and Semimetals*. Vol. 22, Part B: *Semiconductor Injection Lasers* (W. T. Tsang, ed.), Academic Press, Inc., 1985.
- [36] J. B. Moreno, "Volume-averaged rate equations for planar and disk-cavity lasers," *J. Appl. Phys.*, vol. 48, p. 4152, Oct. 1977.
- [37] R. S. Tucker and D. J. Pope, "Circuit modelling of diffusion on damping in a narrow-stripe semiconductor laser," *IEEE J. Quantum Electron.*, vol. LT-2, pp. 1179–1183, July 1983.
- [38] M. Asada and Y. Suematsu, "Density-matrix theory of semiconductor lasers with relaxation broadening and gain-suppression in semiconductor lasers," *IEEE J. Quantum Electron.*, vol. QE-21, pp. 434–442, May 1985.
- [39] K. Konnerth and C. Lanza, "Delay between current pulse and light emission of a Gallium Arsenide injection laser," *App. Phys. Lett.*, vol. 4, pp. 120–121, Apr. 1964.
- [40] R. W. Dixon and W. B. Joyce, "Generalized expressions for the turn-on delay in semiconductor lasers," *J. Appl. Phys.*, vol. 50, pp. 4591–4595, July 1979.
- [41] R. S. Tucker, "Large-signal switching transients in index-guided semiconductor lasers," *Electron. Lett.*, vol. 20, pp. 802–803, Sept. 1984.
- [42] D. E. McCumber, "Intensity fluctuations in the output of cw laser oscillators. i," *Phys. Rev.*, vol. 141, pp. 306–322, Jan. 1966.

- [43] M. Lax, "Quantum noise VII: The rate equations and amplitude noise in lasers," *IEEE J. Quantum Electron.*, vol. QE-3, pp. 37–46, Feb. 1967.
- [44] H. Haug, "Quantum-mechanical rate equations for semiconductor lasers," *Phys. Rev.*, vol. 184, pp. 338–348, Aug. 1969.
- [45] Y. Yamamoto, "AM and FM quantum noise in semiconductor lasers—part i: Theoretical analysis," *IEEE J. Quantum Electron.*, vol. QE-19, pp. 34–46, Jan. 1983.
- [46] M. Lax, "Classical noise IV: Langevin methods," *Rev. Mod. Phys.*, vol. 38, pp. 541–566, July 1966.
- [47] C. H. Henry, "Theory of the linewidth of semiconductor lasers," *IEEE J. Quantum Electron.*, vol. QE-18, pp. 259–264, Feb. 1982.
- [48] W. I. Way, "Subcarrier multiplexed lightwave system design considerations for subscriber loop applications," *J. Lightwave Technol.*, vol. 7, pp. 1806–1818, Nov. 1989.
- [49] M. T. Abuelma'atti, "Carrier-to-intermodulation performance of multiple FM/FDM carriers through a GaAlAs heterojunction laser diode," *IEEE Trans. on Commun.*, vol. COM-33, pp. 246–248, Mar. 1985.
- [50] R. J. Westcott, "Investigation of multiple f.m./f.d.m. carriers through a satellite t.w.t operating near saturation," *Proc IEEE*, vol. 114, pp. 726–740, June 1967.
- [51] T. E. Darcie, P. P. Iannone, B. L. Kasper, J. R. Talman, C. A. Burrus and T. A. Baker, "Bidirectional multichannel 1.44 Gb/s lightwave system using subcarrier multiplexing," *Electron. Lett.*, vol. 24, pp. 649–650, May 1988.
- [52] R. Olshansky and V. A. Lanzisera, "60 channel FM video subcarrier multiplexed optical communication system," *Electron. Lett.*, vol. 23, pp. 1196–1198, Oct. 1987.
- [53] T. E. Darcie and G. E. Bodeep, "Lightwave subcarrier CATV transmission systems," *IEEE Trans. Microwave Theory Tech.*, vol. 38, pp. 524–533, May 1990.
- [54] N. K. Dutta, P. Wilt and R. J. Nelson, "Analysis of leakage currents in 1.3 μm InGaAsP real-index-guided lasers," *J. Lightwave Technol.*, vol. LT-2, pp. 201–208, June 1984.

- [55] M.-S. Lin, S.-Y. Wang and N. K. Dutta, "Measurements and modeling of the harmonic distortion in InGaAsP distributed feedback lasers," *IEEE J. Quantum Electron.*, vol. 26, pp. 998–1004, June 1990.
- [56] K. Y. Lau and A. Yariv, "Nonlinear distortions in the current modulation of non-self-pulsing and weakly self-pulsing GaAs/GaAlAs injection lasers," *Opt. Commun.*, vol. QE-2134, pp. 424–428, Feb. 1985.
- [57] A. Takemoto, H. Watanabe, Y. Nakajima, Y. Sakakibara, S. Kakimoto, J. Yamashita, T. Hatta and Y. Miyake, "Distributed feedback laser diode and module for CATV systems," *IEEE J. on Select. Areas in Commun.*, vol. 8, pp. 1359–1364, Sept. 1990.
- [58] H. Soda, Y. Kotaki, H. Ishikawa and H. Imai, "Stability in single longitudinal mode operation in GaInAsP/InP phase-adjusted dfb lasers," *IEEE J. Quantum Electron.*, vol. QE-23, pp. 804–814, June 1987.
- [59] G. Morthier, F. Libbrecht, K. David, P. Vankwikelberge and R. G. Baets, "Theoretical investigation of the second-order harmonic distortion in the AM response of 1.55 μm F-P and DFB lasers," *IEEE J. Quantum Electron.*, vol. 27, pp. 1990–2002, Aug. 1991.
- [60] H. Kawamura, K. Kamite, H. Yonetani, S. Ogita, H. Soda and H. Ishikawa, "Effect of varying threshold gain on second-order intermodulation distortion in distributed feedback lasers," *Electron. Lett.*, vol. 26, pp. 1720–1721, Sept. 1990.
- [61] A. A. M. Saleh, "Fundamental limit on number of channels in subcarrier multiplexed lightwave CATV system," *Electron. Lett.*, vol. 25, pp. 776–777, June 1989.
- [62] K. Kamite, H. Sudo, M. Yano, H. Ishikawa and H. Imai, "Ultrahigh speed InGaAsP/InP DFB lasers emitting at 1.3 μm wavelength," *IEEE J. Quantum Electron.*, vol. QE-23, pp. 1054–1058, June 1987.
- [63] R. Olshansky, P. M. Fye, J. Manning and C. B. Su, "Effect of nonlinear gain on the bandwidth of semiconductor lasers," *Electron. Lett.*, vol. 21, pp. 721–722, June 1985.
- [64] R. S. Tucker and D. J. Pope, "Microwave circuit models of semiconductor injection lasers," *IEEE Trans. Microwave Theory Tech.*, vol. MTT-31, pp. 289–294, Mar. 1983.

- [65] H. Kressel and J. K. Butler, *Semiconductor Lasers and Heterojunction LEDs*. New York: Academic Press, 1977.
- [66] T. P. Biswas and W. F. McGee, "Volterra series analysis of semiconductor laser diode," *IEEE Photonics Technol. Lett.*, vol. 3, pp. 706–708, Aug. 1991.
- [67] W. Harth, "Large-signal direct modulation of injection lasers," *Electron. Lett.*, vol. 9, pp. 532–533, Nov. 1973.
- [68] J. J. Bussgang, L. Ehrman and J. W. Graham, "Analysis of nonlinear systems with multiple inputs," *Proc. IEEE*, vol. 62, pp. 1088–1119, Aug. 1974.
- [69] J. Helms, "Intermodulation distortions of broad-band modulated lasers," *J. Lightwave Technol.*, vol. 10, pp. 1901–1906, Dec. 1992.
- [70] A. Papoulis, *Probability, Random Variables, and Stochastic Processes*. Mathematics and Statistics Series, McGraw-Hill, second ed., 1984.
- [71] J. G. Proakis, *Digital Communications*. Electrical Engineering Series, McGraw-Hill, 1987.
- [72] W. R. Bennett, "Cross-modulation requirements on multichannel amplifiers below overload," *Bell Syst. Tech. J.*, vol. 19, pp. 587–610, Oct. 1940.
- [73] J. C. Daly, "Fiber optic intermodulation distortion," *IEEE Trans. on Commun.*, vol. COM-30, pp. 1954–1958, Aug. 1982.
- [74] S. D. Walker, M. Li, A. C. Boucouvalas, D. G. Cunningham and A. N. Coles, "Design techniques for subcarrier multiplexed broadcast optical networks," *IEEE J. on Select. Areas in Commun.*, vol. 8, pp. 1276–1284, Sept. 1990.
- [75] K. Alameh and R. A. Minasian, "Tuned optical receivers for microwave subcarrier multiplexed systems," *IEEE Trans. Microwave Theory Tech.*, vol. 38, pp. 546–551, May 1990.
- [76] K. Alameh and R. A. Minasian, "Optimum optical modulation index of laser transmitters in scm systems," *Electron. Lett.*, vol. 26, pp. 1273–1275, Aug. 1990.

- [77] M. R. Phillips and T. E. Darcie, "Numerical simulation of clipping-induced distortion in analog lightwave systems," *IEEE Photonics Technol. Lett.*, vol. 3, pp. 1153–1155, Dec. 1991.
- [78] J. E. Mazo, "Asymptotic distortion of clipped, dc-biased, gaussian noise," *IEEE Trans. on Commun.*, vol. 40, pp. 1339–1344, Aug. 1992.
- [79] F. Mendis and B. Tan, "Overmodulation in subcarrier multiplexed video FM broad-band optical networks," *IEEE J. on Select. Areas in Commun.*, vol. 8, pp. 1285–1289, Sept. 1990.
- [80] J. J. O'Reilly, P. M. Lane, M. H. Capstick, R. Heidemann, R. Hofstetter, J. da Rocha, N. Uzunoglu, C. Capsalis and L. Cupido, "Modal—A high bit rate wireless technology," *Digest of 4th Bangor Symposium on Communications*, pp. 315–318, (Bangor, U.K.), 27–28 May 1992.
- [81] A. J. Cooper, "Fibre/Radio for the provision of cordless/mobile telephony services in the access network," *Electron. Lett.*, vol. 26, pp. 1054–1056, Nov. 1990.
- [82] M. Maeda and M. Yamamoto, "FM-FDM optical CATV transmission experiment and system design for MUSE HDTV signals," *IEEE J. on Select. Areas in Commun.*, vol. 8, pp. 1257–1267, Sept. 1990.
- [83] J. R. Fox and S. T. Jewell, "A broad-band distributed-star network using subcarrier fiber transmission," *IEEE J. on Select. Areas in Commun.*, vol. 8, pp. 1223–1228, Sept. 1990.
- [84] G. R. Joyce, V. Lanzisera and R. Olshansky, "Improved sensitivity of 60 video channel fm-scm receiver with semiconductor optical amplifier," *Electron. Lett.*, vol. 25, pp. 499–501, Apr. 1989.
- [85] J. J. O'Reilly and H. M. Salgado, "Performance assessment of optical subcarrier multiplexing systems: Implications of laser distortion," *Proc. IEEE Global Telecommunications Conference*, pp. 1845–1848, (Phoenix, USA), 2–5 Dec. 1991.

- [86] M. S. Lin, S. J. Wang and N. K. Dutta, "Frequency dependence of the harmonic distortion in InGaAsP distributed feedback lasers," *Digest of Optical Fibre Communications Conference-OFC*, p. 215, (San Francisco, CA), 22-26 January 1990.
- [87] N. J. Frigo, M. R. Phillips and G. E. Bodeep, "Clipping distortion in lightwave CATV systems: Models, simulations and measurements," *J. Lightwave Technol.*, vol. 11, pp. 138-146, Jan. 1993.
- [88] P. Moreira, I. Darwazeh and J. O'Reilly, "Noise optimisation of tuned integrated GaAs receiver," *Digest of Int. Symposium on Fibre Optic Networks and Video Communications-SPIE*, Berlin, Apr. 1993.
- [89] R. G. Meyer, M. J. Shensa and R. Eschenbach, "Cross modulation and intermodulation in amplifiers at high frequencies," *IEEE J. of Solid-State Circ.*, vol. SC-7, pp. 16-23, Feb. 1972.
- [90] A. Javed, P. A. Goud and B. A. Syrett, "Analysis of a microwave feedforward amplifier using Volterra series representation," *IEEE Trans. on Commun.*, vol. COM-25, pp. 355-360, Mar. 1977.
- [91] R. E. Patterson, J. Straus, G. Blenman and T. Witkowicz, "Linearization of multichannel analog optical transmitters by quasi-feedforward compensation technique," *IEEE Trans. on Commun.*, vol. COM-27, pp. 582-588, Mar. 1979.
- [92] L. S. Fock and R. S. Tucker, "Reduction distortion in analogue modulated semiconductor lasers by feedforward compensation," *Electron. Lett.*, vol. 27, pp. 669-671, Apr. 1991.
- [93] K. J. Vahala, M. A. Newkirk and T. R. Chen, "The optical gain lever: A novel gain mechanism in the direct modulation of quantum well semiconductor lasers," *App. Phys. Lett.*, vol. 54, pp. 2506-2508, June 1989.
- [94] D. Gajic and K. Y. Lau, "Intensity noise in the ultrahigh efficiency tandem-contact quantum well lasers," *App. Phys. Lett.*, vol. 57, pp. 1837-1839, Oct. 1990.

- [95] G. J. Meslener, "Chromatic dispersion induced distortion of modulated monochromatic light employing direct detection," *IEEE J. Quantum Electron.*, vol. QE-20, pp. 1208–1216, Oct. 1984.
- [96] C. S. Ih and W. Gu, "Fiber induced distortions in a subcarrier lightwave system," *IEEE J. on Select. Areas in Commun.*, vol. 8, pp. 1296–1303, Sept. 1990.
- [97] M. R. Phillips, T. E. Darcie, D. Marcuse, G. E. Bodeep and N. J. Frigo, "Nonlinear distortion generated by dispersive transmission of chirped intensity-modulated signals," *IEEE Photonics Technol. Lett.*, vol. 3, pp. 481–483, May 1991.
- [98] K. W. Cattermole, "Generating-function methods in probability theory," *Mathematical Topics in Telecommunications. Vol. 2: Problems of Randomness in Communication Engineering* (K. W. Cattermole and J. J. O'Reilly, eds.), Pentech Press, 1984.